MOLECULAR COMPLEXES AT ELECTRODE INTERFACES FOR SUSTAINABLE ENERGY APPLICATIONS

Alexander Moore Lapides

A dissertation submitted to the faculty at the University of North Carolina at Chapel Hill in partial fulfillment of the requirements for the degree of Doctor of Philosophy in the Department of Chemistry in the College of Arts and Sciences.

Chapel Hill
2016

Approved by:

Thomas J. Meyer

Joseph L. Templeton

Alexander J. M. Miller

Maurice S. Brookhart

Marcey L. Waters

ABSTRACT

Alexander Moore Lapides: Molecular Complexes at Electrode Interfaces
for Sustainable Energy Applications
(Under the direction of Thomas J. Meyer and Joseph L. Templeton)

The development of sustainable, carbon-neutral energy sources is necessary to offset the environmental harm caused by the consumption of CO_2-releasing fossil fuels. Although solar irradiation is sufficient to satisfy worldwide energy demand, storage of this energy remains problematic. One storage method is the photolysis of water into oxygen and hydrogen. Burning hydrogen in the presence of oxygen unleashes the energy stored in its chemical bonds, forming only water as a byproduct. Long-term applications require the stable integration of molecules with semiconductor materials to facilitate photolysis. One method for attaching molecules to surfaces is reductive electropolymerization, in which vinyl-functionalized monomers are electrochemically reduced, inducing C–C bond formation. These polymers precipitate on the electrode surface – attached by physical adsorption. Substitutive coordination chemistry, influenced by electrochemical potential and the electrolytic solution, is possible in these polymer environments.

Electropolymerization is applicable in the formation of multi-component films as well. Electrochemical reduction of a semiconductor-bound, vinyl-derivatized chromophore in a solution containing a distinct vinyl-functionalized molecule results in spatially-separated, covalently-linked assemblies on the semiconductor surface. Transient absorption spectroscopy demonstrated that the chromophore undergoes electron injection to the semiconductor and hole

transfer to the second molecule. The polymer overlayer improves the photochemical interfacial stability of the underlying chromophore by ~30-fold. Multi-component film formation via electropolymerization allows for the incorporation of a molecular water oxidation catalyst as the outer layer. Chromophore-catalyst assemblies thusly formed demonstrate impressive electrochemical- and photo-stability with high electrocatalytic activity for oxygen formation.

Atomic layer deposition (ALD) of a metal oxide is known to stabilize covalent binding of molecules to semiconductor surfaces by "burying" the bonds; here it is demonstrated that embedding a chromophore in a metal oxide, attaching a catalyst, and additional metal oxide deposition is a method of forming stable chromophore-catalyst "mummies" that produce oxygen photoelectrochemically over multiple hours. Core/shell semiconductors with mismatched conduction band potentials are constructed using ALD. Sub-nanosecond injection and recombination processes are investigated, as are the effects of annealing on the core/shell interface. These findings are compared to device measurements.

ACKNOWLEDGEMENTS

I would first and foremost like to acknowledge my family, specifically my parents, Jeff and Emily, and my brother, Ben. Their support throughout the years has been unconditional and invaluable. Along the same lines I would like to thank Caitlin. Her support these past three years has meant more to me than I can express here.

I would next like to acknowledge my friends, acquaintances, and colleagues at the University of North Carolina at Chapel Hill. Although too numerous to name in full, I would specifically like to thank my fellow graduate students Dennis, Mike, Chris, Ross, and Katie from the Templeton lab for their collaboration and support. Too many postdocs and graduate students have come and gone over the years to mention by name, but to all those from the Meyer lab that supported me, both professionally and personally, thank you.

Finally I would like to acknowledge the chemistry faculty of the University of North Carolina at Chapel Hill, and specifically my advisers, Tom and Joe. Their support – scientific, academic, and personal – has been invaluable. I cannot express how fortunate I have been to have them as advisers, mentors, and teachers. Thank you both.

TABLE OF CONTENTS

LIST OF FIGURES

LIST OF TABLES

LIST OF EQUATIONS

LIST OF ABBREVIATIONS AND SYMBOLS

Å	Ångström (10^{-10} meters)
Γ	Surface coverage
Γ_{max}	Maximum surface coverage
Δ	Change in
ε	Molar absorptivity constant
η	Faradaic efficiency
$\eta_{collection}$	Collector electrode collection efficiency
λ	Wavelength
λ_{max}	Wavelength of maximum absorbance
λ_{pump}	Wavelength of pump pulse (transient absorption)
λ_{probe}	Wavelength of probe pulse (transient absorption)
μA	Microampere
μM	Micromolar
μm	Micrometer/micron
ν	Scan rate
$\Delta\nu_{1/2}$	Bandwidth at half height
τ	Lifetime
$\tau_{1/2}$	Half-life
Φ_{inj}	Injection yield
Ω	Ohm
A	Area
A	Absorbance
A	Ampere

ALD	Atomic layer deposition
AO	Aluminum oxide; Al_2O_3
Aux	Auxiliary electrode a.k.a. counter electrode
BET	Back electron transfer
BET	Brunauer-Emmett-Teller
°C	Degree Celsius
C	Coulomb
cm	Centimeter
CPE	Controlled potential electrolysis
CV	Cyclic voltammetry
DMSO	Dimethylsulfoxide
DSPEC	Dye-sensitized photoelectrosynthesis cell
DSSC	Dye-sensitized solar cell
e^-	Electron
E°	Standard reduction potential
$E°'$	Excited-state reduction potential
E_0	0-0 excited state energy
$E_{1/2}$	Average of $E_{p,a}$ and $E_{p,c}$
E_{app}	Applied potential
E_{cb}	Electrochemical potential of conduction band
E_{coll}	Potential at collector electrode
EDS	Energy-dispersive X-ray spectroscopy
E_{gen}	Potential at generator electrode

ΔE_p	Absolute value of the difference between $E_{p,a}$ and $E_{p,c}$
$E_{p,a}$	Potential at peak current for anodic sweep
$E_{p,c}$	Potential at peak current for cathodic sweep
EtOH	Ethanol
E_{vb}	Electrochemical potential of valence band
F	Faraday's constant (96,485 C mol^{-1})
FTO	Fluorine-doped tin oxide
fwhm	Full width at half maximum
g	Gram
GCE	Glass-like carbon electrode
ΔG_{ES}	Free energy content of excited state
GSB	Ground state bleach
h	Planck's constant
h^+	Electron-hole
$\hbar\omega_M$	Quantum spacing
H_2Q	Hydroquinone
HER	Hydrogen evolution reaction
HPLC	High performance liquid chromatography
HRMS	High-resolution mass spectrometry
Hz	Hertz (cycles s^{-1})
I	Light intensity
i	Current
i_c	Catalytic current

i_{cat}	Catalytic current
i_p	Peak current
$i_{p,a}$	Peak anodic current
i_{peak}	Peak current
$i_{p,c}$	Peak cathodic current
ITO	Tin-doped indium(III) oxide
j	Current density (current area^{-1})
K	Kelvin
K_{ad}	Binding constant for adsorption
k_B	Boltzmann's constant
k_{BET}	Rate constant of back electron transfer
k_{des}	Rate constant of desorption
kg	Kilogram
k_{obs}	Observed rate constant
kV	Kilovolt
kW	Kilowatt
kW-h	Kilowatt-hour
L	Liter
LSV	Linear sweep voltammetry
M	Molar (mol L^{-1})
mA	Milliampere
MeCN	Acetonitrile
mg	Milligram

MHz	Megahertz
mL	Milliliter
MLCT	Metal-ligand charge transfer
mM	Millimolar
mm	Millimeter
mmol	Millimole
mOD	Milli-optical density
mol	Mole
MOx	Metal oxide
mV	Millivolt
mW	Milliwatt
m/z	Mass-to-charge ratio
n	Number of electrons
nA	Nanoampere
*nano*ITO	Nanoparticles of tin-doped indium(III) oxide
nanoSnO_2	Nanoparticles of tin(IV) oxide
nanoTiO_2	Nanoparticles of titanium dioxide
nanoZrO_2	Nanoparticles of zirconium(IV) oxide
n_{cat}	Number of electrons in catalysis
NHE	Normal hydrogen electrode
nm	Nanometer
NMR	Nuclear magnetic resonance
OEC	Oxygen-evolving complex

OER	Oxygen evolution reaction
pA	Picoampere
PC	Propylene carbonate
PEC	Photoelectrochemical
PCET	Proton-coupled electron transfer
pK_a	Acid dissociation constant
ppm	parts per million
PSI	Pounds per square inch
Q	Charge passed
Q	Quinone
$Q_{p,a}$	Charge passed through anodic wave
$Q_{p,c}$	Charge passed through cathodic wave
Ref	Reference electrode
RHE	Reversible hydrogen electrode
s	Second
SCE	Saturated calomel electrode
SEM	Scanning electron microscopy
S_M	Electron-vibrational coupling constant
T	Temperature
t	Time
TA	Transient absorption
TiTDMA	tetrakis(dimethylamido)titanium(IV)
TMA	Trimethylaluminum

TOF	Turnover frequency
TW	Terawatt
TW-h	Terawatt-hour
UV	Ultraviolet
V	Volt
W	Watt
XPS	X-ray photoelectron spectrometry

CHAPTER 1: SOLAR FUELS – (INTER)FACING THE CHALLENGE

1.1. Introduction

Developing sustainable, carbon-neutral energy sources is a necessity as fossil fuel supplies fall and the environmental concerns caused by the use of fossil fuels are amplified. As exemplified by recent crude oil prices (Brent Crude priced at $37 per barrel on December 31, 2015, down 67% from two years prior) and predictions of availability (from 40 to 150 years of oil remaining),[1] fossil fuels will be an unstable and unreliable energy source in the coming years. Perhaps more important are the extreme environmental changes for which fossil fuel use is responsible. **Figure 1.1** shows atmospheric CO_2 concentration (in ppm by volume) dating back to approximately 400,000 B.C. Despite natural fluctuations in atmospheric CO_2 concentration observed over the past several hundred millennia, 2015 saw the highest CO_2 concentration of the past 400,000 years – a 34% higher concentration (400.8 ppm) than the pre-modern high (298.7 ppm) around 320,000 B.C. Additionally, this dramatic increase has occurred over the past hundred or so years, with 1912 being the last year that atmospheric CO_2 was below 300 ppm. To offset this rapid increase in atmospheric CO_2 concentration, carbon-neutral energy sources are required.

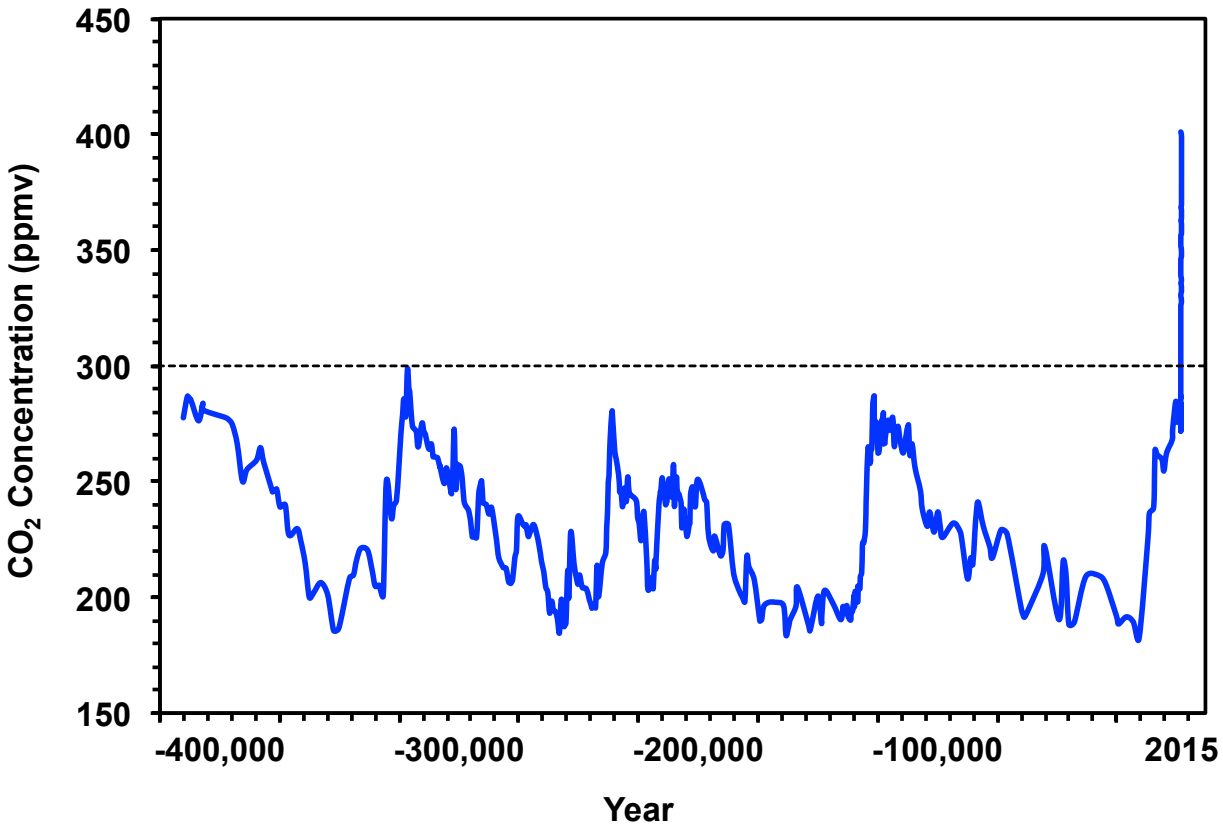

Figure 1.1. Plot of atmospheric CO_2 concentration (in parts per million by volume) over the past 400+ millennia. The dashed line represents 300 ppmv. (Data Source: Vostok 400,000-plus-year record: J.R.Petit, Laboratoire de Glaciologie et Geophysique de l'Environnement, Grenoble, France and Dr. Pieter Tans, NOAA/ESRL (www.esrl.noaa.gov/gmd/ccgg/trends/) and Dr. Ralph Keeling, Scripps Institution of Oceanography (scrippsco2.ucsd.edu/)).

Among a multitude of carbon-neutral energy sources, solar energy is the best option. For practical purposes, its supply is infinite, and it is perhaps the only carbon-neutral energy source truly available worldwide. **Figure 1.2** shows that Germany has consumed more solar energy annually (without normalizing for population) than the United States since 2005, despite the fact that it receives roughly the same annual solar irradiation as Alaska.[2] Sunlight resource is not a limiting factor in solar adoption. At 1.2×10^5 TW, the solar energy that hits the earth's surface in one day exceeds the total energy consumed worldwide in a decade.[1] Yet despite the enormous potential for satisfying global energy demand with sunlight, solar energy remains a small

percentage of the global energy footprint, with only 186 TW-h (rate = 0.02 TW) provided by solar-generated fuel out of approximately 5.7×10^4 TW-h (rate = 6.5 TW) consumed in 2014.[3]

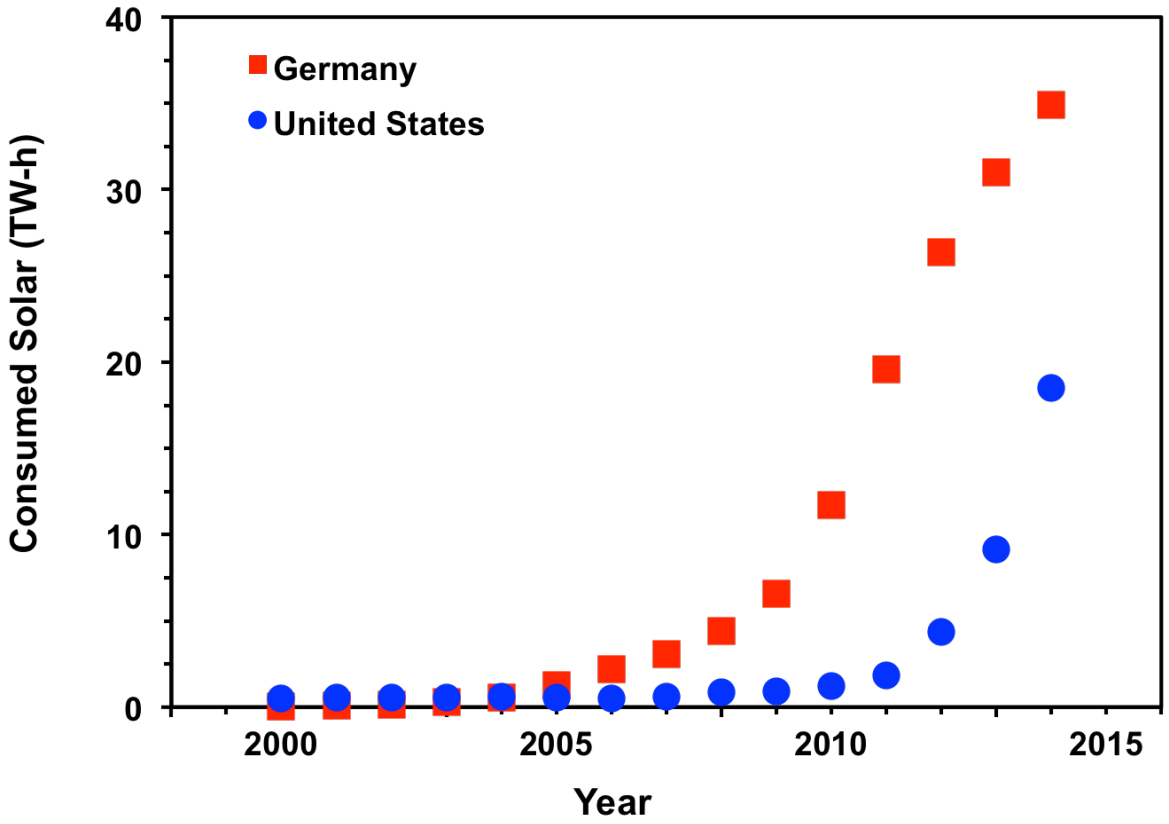

Figure 1.2. Consumed solar electricity (in TW-h) for the United States and Germany since the year 2000. (Data Source: BP Statistical Review of World Energy June 2015).

One reason for this discrepancy is that solar energy requires capture, conversion, and storage.[1] While many techniques exist for the first two requirements, implementation is still limited by the diffuseness of solar energy. Solar arrays covering an area approximately the size of Nevada (assuming 10% efficiency) would be needed to power the planet. Such implementation would require a large investment in materials, and a shift in infrastructure. However, the third issue, that of solar energy storage, is just as problematic (if not more so) as

the first two. The sun is an inherently intermittent energy source; it sets at night and it is often shielded by clouds. Photovoltaic energy, or direct conversion of solar energy to electricity, is a point-of-use power source – the energy that is not used is lost. Therefore, storage of solar energy is critical.

While several methods for storing solar energy are possible, two have legitimate claim to being globally implementable: storing solar energy in batteries and using solar energy to form chemical bonds that are later broken to release the stored energy (i.e. fuel). Although battery technology (in particular lithium-ion battery technology) has improved dramatically over recent years, several considerations favor fuel storage. Without considering production cost and disposal complications, the specific energy density in chemical bonds is higher than that of lithium-ion batteries. For example, gasoline has a specific energy density of ~12 kW-h kg^{-1}, hydrogen gas has an even higher one of 32.5 kW-h kg^{-1}, but a typical lithium-ion battery has a specific energy density of only ~0.2 kW-h kg^{-1}.[4,5] Implementing solar fuel is more compatible with current infrastructure. In the United States in 2014, 1.0×10^4 TW-h of fuel were consumed (largely as oil, coal, and natural gas) whereas only 4.3×10^3 TW-h of electricity were generated.[3] The generation of a carbon-based solar fuel (e.g. ethanol or butanol) from atmospheric CO_2, water, and sunlight would minimize interruption of economic activity during implementation. Fuel is a more versatile energy source than batteries are. It can exist in many forms, from H_2 gas to butanol to gasoline. Several commodity chemicals, including carbon monoxide and formic acid, can also be generated by the reduction of atmospheric CO_2.

1.2. Artificial Photosynthesis

Despite the enormous potential for converting water, CO_2, and sunlight into fuel, the overall process for doing so is challenging. Using sunlight to generate fuel mirrors the natural photosynthetic process by which plants generate O_2 and carbohydrates from water and carbon

dioxide. The term “artificial photosynthesis” is the widely adopted moniker for scientists’ attempts to mimic the reaction. The most fundamental approach to artificial photosynthesis is known as water splitting, in which water is broken down into its component parts: oxygen and hydrogen. In the case of water splitting, hydrogen is the desired fuel, while oxygen is a byproduct. The overall reaction, $2H_2O \rightarrow 2H_2 + O_2$, can be broken down into two half-reactions: the oxygen evolution reaction (OER, also known as water oxidation) and the hydrogen evolution reaction (HER, also known as water or proton reduction). The half-reaction and thermodynamic potential are shown in **Equation 1.1** (OER) and **Equation 1.2** (HER).

Equation 1.1

$2H_2O \rightarrow O_2 + 4H^+ + 4e^-$ $\quad E° = 1.23 – (pH)(0.059)$ V vs. NHE

Equation 1.2

$4H^+ + 4e^- \rightarrow 2H_2$ $\quad E° = 0 – (pH)(0.059)$ V vs. NHE

It is important to note that the potentials in **Equation 1.1** and **Equation 1.2** are dependent on H^+ concentration; each potential shifts negatively 0.059 V per pH unit increase. The difference between them is always 1.23 V, which represents the minimum potential input required to drive the formation of O_2 and two H_2.

Simplifying water splitting into its component half-reactions also highlights the separation of four electrons and four oxidative equivalents (a.k.a. holes). These electrons and holes must remain separated for O_2 evolution to occur; therefore the electrons and holes tend to accumulate on the electrode interfaces. The accumulation of electrons and holes reduces the likelihood of a subsequent separation occurring, which increases the overpotential (or the amount

of potential required above the thermodynamic value) needed to drive the two half-reactions simultaneously. The accumulation of four holes on the anode (oxidative) side is especially problematic. For this reason, light-induced water splitting remained elusive for some time.

In a seminal 1972 *Nature* report, Honda and Fujishima first demonstrated light-assisted water oxidation catalysis.[6] They connected n-type TiO_2 as a photoanode to a platinum black dark cathode in aqueous solution. Upon illumination at $\lambda < 415$ nm (i.e. ultraviolet light), O_2 was evolved at TiO_2 and H_2 was evolved at Pt. These results were later confirmed, with the recognition that an applied potential bias (as low as 0.25 V but often 0.5 V to 2.0 V) is required to drive production of both products.[7] Following this report, other systems were developed to reduce or remove the applied bias requirement.[8-13] The majority of these systems use planar, bulk-material electrodes to effect water splitting. These materials often act as both light-absorber and catalytic surface, although catalysts and/or protective layers can be added to increase catalytic rates and to improve the lifetime of the systems.

The first molecular catalyst for water oxidation was the "blue dimer" reported by Meyer in the early 1980s (**Figure 1.3**a).[14,15] Since its emergence, many other molecular catalysts for water oxidation have been developed and investigated.[16-23] One example is particularly promising.[24] Sun's Ru^{II} 6,6′-dicarboxylic acid-2,2′-bipyridine-type catalysts (**Figure 1.3**b) have achieved turnover frequencies (TOFs) exceeding 300 s^{-1}. While catalyst longevity remains a critical issue, the high TOFs observed with these molecular catalysts demonstrate their potential in solar fuel production.

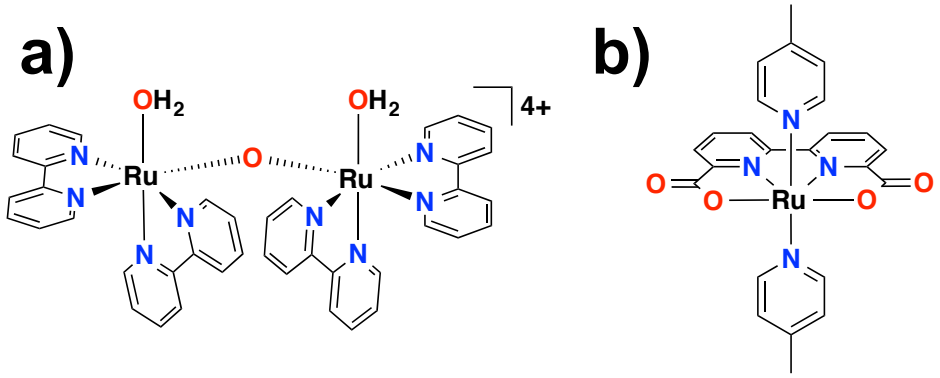

Figure 1.3. a) Meyer's "blue dimer," $[(bpy)_2(OH_2)Ru^{III}ORu^{III}(OH_2)(bpy)_2]^{4+}$; b) Sun's bis(picoline) catalyst, Ru(6,6'-dicarboxylate-2,2'-bipyridine)(4-picoline)$_2$.

One benefit of molecular systems is their ability to utilize proton-coupled electron transfer (PCET). In 1978, Meyer reported that the one-electron oxidation of $[Ru^{II}(bpy)_2(py)(OH_2)]^{2+}$ (bpy = 2,2'-bipyridine; py = pyridine) in aqueous solution above pH 1 does not result in $[Ru^{III}(bpy)_2(py)(OH_2)]^{3+}$, but instead concertedly releases a proton to form $[Ru^{III}(bpy)_2(py)(OH)]^{2+} + H^+$ (**Figure 1.4**).[25] A subsequent oxidation releases another proton, resulting in $[Ru^{IV}(bpy)_2(py)(O)]^{2+} + H^+$. This observation has important implications. First, the oxidation of $[Ru(bpy)_2(py)(OH_2)]^{2+}$ is pH-dependent. A one-electron, one-proton oxidation will shift 59 mV negatively per pH unit increase. This pH-dependent redox behavior is true across several molecular species in which an aquo ligand is coordinated to a metal center. Another implication is that the overall charge on the complex remains +2 for the first two oxidation events due to the release of two protons. As noted previously, one of the challenges of water oxidation catalysis is the accumulation of four holes for catalysis to occur. Typically this build-up results in a +4 increase in charge on the complex. However, because the complex is able to shed protons as oxidation occurs, the accumulation of excessive charge is largely avoided. Molecular catalysts also allow for mechanistic study and systematic variation of the catalytic

environment via alterations of the metal center and ligand framework of the molecules. Such modifications are not as straightforward in bulk systems.

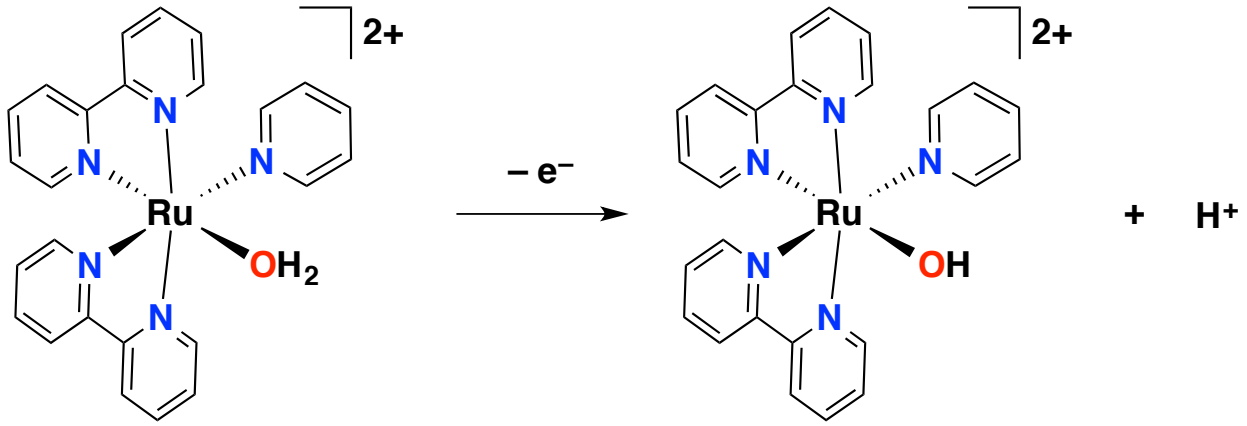

Figure 1.4. Schematic depiction of proton-coupled electron transfer in single-electron oxidation of $[Ru(bpy)_2(py)(OH_2)]^{2+}$.

1.3. Dye-Sensitized Photoelectrosynthesis Cells (DSPECs)

Despite the promising activity of these molecular species as water oxidation catalysts, they address only the conversion and storage issues of solar fuels production. Capture of sunlight is still required. The molecular light-absorber $[Ru(bpy)_3]^{2+}$ was observed to undergo excited-state electron transfer to a methyl viologen quencher, resulting in the one-electron reduced species of methyl viologen and $[Ru(bpy)_3]^{3+}$.[26] This quenching behavior suggested that $[Ru(bpy)_3]^{2+}$ could be used for light-induced electron transfer events.[27] Given correctly-positioned redox potentials for a catalyst, $[Ru(bpy)_3]^{3+}$ ($E(Ru^{III/II})$ = 1.26 V vs. NHE) can be used to oxidize a molecular catalyst following excited-state electron injection into the conduction band of a wide bandgap metal oxide semiconductor ($E(Ru^{III/II}*)$ = –0.87 V vs. NHE).

This reactivity was realized in 1999 with Meyer's report of the first dye-sensitized photoelectrosynthesis cell (DSPEC) for the light-assisted dehydrogenation of 2-propanol to

acetone (**Figure 1.5**).[28] In this study, a covalently-linked chromophore-catalyst assembly (with each component a Ru^{II}-polypyridyl complex, the light-absorber a $[Ru(bpy)_3]^{2+}$ derivative) was bound to nanoparticles of crystalline TiO_2 (*nano*TiO_2) via carboxylate linkers. Upon illumination, subsequent electron injection and charge transfer events resulted in the Ru^{IV}=O form of the catalyst, which is capable of oxidizing 2-propanol to acetone. In 2009, Mallouk employed a similar photoanode design to that of Meyer, using hydrated iridium oxide (IrO_2 • nH_2O) as the catalyst bound to a $[Ru(bpy)_3]^{2+}$ derivative through carboxylate attachment for water oxidation catalysis, the key half-reaction of water splitting.[29] Multiple reports of DSPEC photoanodes for water oxidation have emerged since then,[22,30-35] and different strategies for coupling semiconductors, chromophores, and catalysts have emerged as well, each with its own set of advantages and disadvantages.

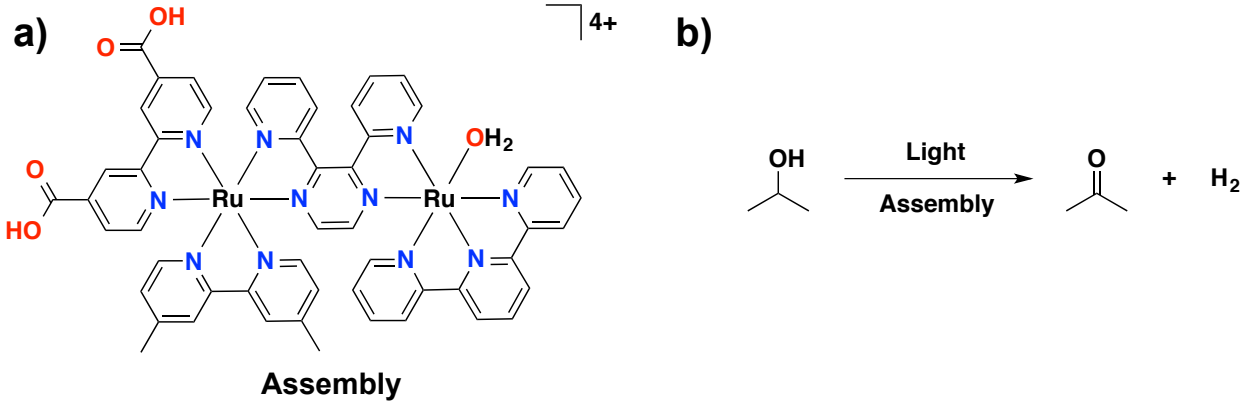

Figure 1.5. a) Chromophore-catalyst assembly employed in the first report of a DSPEC. b) Scheme of first-reported DSPEC reaction.

In the simplest scheme, a DSPEC photoanode requires a wide bandgap semiconductor, a molecular chromophore, and a catalyst, along with a means of binding the latter two to the former. An ideal DSPEC has a series of desired, forward charge transfer events that occur

sequentially (**Figure 1.6**). The forward processes are (numbered as in **Figure 1.6**): (1) light absorption by the chromophore promoting a metal-to-ligand charge transfer (MLCT); (3) electron injection from the excited state of the chromophore to the conduction band of the metal oxide semiconductor; (4) hole transfer from the oxidized chromophore to the catalyst; and (6) diffusion of the injected electron to the back contact (to prevent recombination). These processes are shown in green in **Figure 1.6**. These processes must occur four times in order to liberate one molecule of O_2 from H_2O.

A series of backward processes, in which the electron-hole charge separated pair recombines, can also occur. The deleterious (backward) processes are (numbered as in **Figure 1.6**): (2) relaxation of the excited-state chromophore to the ground state; (5) BET from the semiconductor to the oxidized chromophore; and (7) BET from the semiconductor to the oxidized catalyst. These processes are shown in red in **Figure 1.6**.

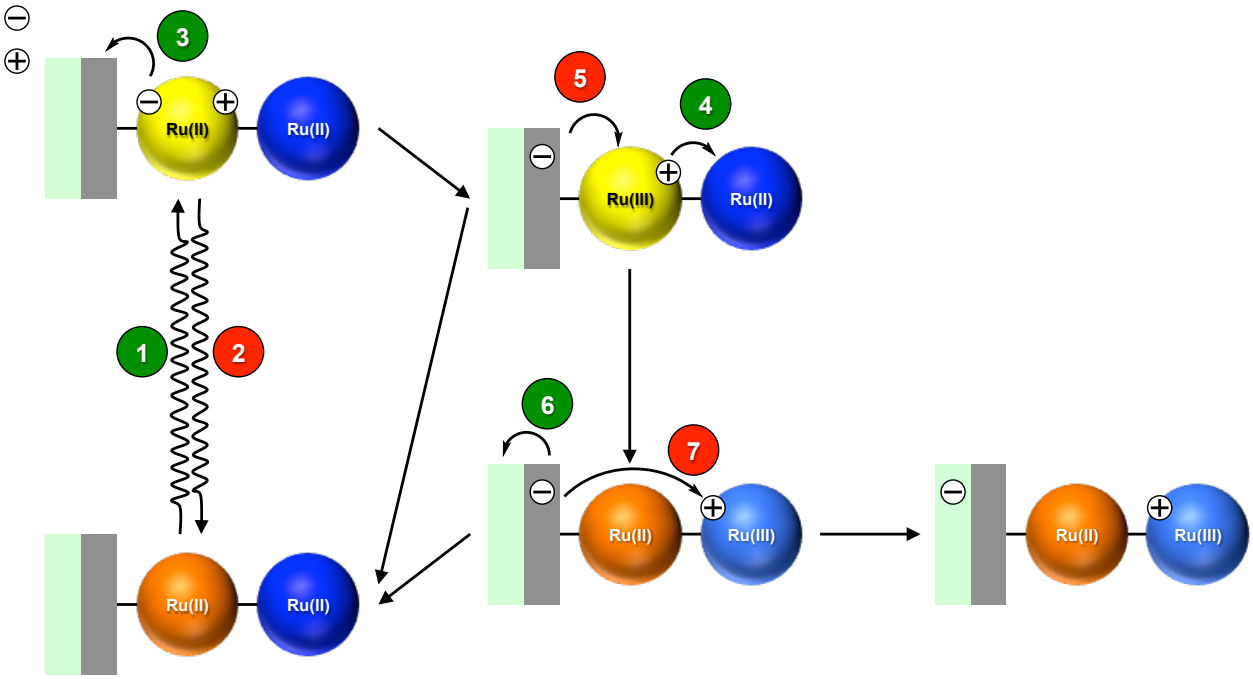

Figure 1.6. A simplified scheme for photochemical activation and charge transfer in a chromophore-catalyst assembly bound to a transparent, wide bandgap semiconductor. Please refer to the text for a discussion of charge transfer events.

The balance of forward and backward charge transfer events is determined by the relative rates at which these reactions occur. The critical timescales for a photoanode were summarized in a recent review by the UNC Energy Frontier Research Center (EFRC).[33] Following light absorption, electron injection (sub-picosecond) and hole transfer (typically sub-nanosecond) occur quickly, while catalysis (millisecond to second, depending on conditions) occurs more slowly. Two competing events, electron diffusion to the back contact and BET, both occur on the microsecond to millisecond timescale, and this competition ultimately hinders DSPEC efficiency. Ideally, BET would be several orders of magnitude slower than diffusion, which would allow for accumulation of holes on the catalyst prior to (typically slow) catalysis.

Strict energetic requirements are placed on the components of the photoanode. The excited-state reduction potential of the chromophore must be positioned more negative than the

conduction band of the semiconductor. This arrangement allows for electron injection from the excited state into the conduction band. The redox potential for the oxidized chromophore (i.e. the chromophore following electron injection) must be positioned more positive than the redox couples of the catalyst. This arrangement allows for hole transfer from the oxidized chromophore to the catalyst. Each oxidation of the catalyst tends to shift the new oxidation potential more positive; therefore it is important that the potential to oxidize the catalyst to its active state (typically a $Ru^{V/IV}$=O event for Ru^{II}-polypyridyl catalysts) remains negative of the redox potential of the oxidized chromophore.

As mentioned above, a DSPEC requires the integration of a chromophore and catalyst with a wide bandgap metal oxide semiconductor. Typically, binding groups are required for immobilization on a metal oxide surface. These groups consist of one (or more) of several functional groups, including carboxylic acids, phosphonic acids, sulfonic acids, siloxanes, alcohols, amides, acetyl acetonates, and nitriles.[33,36-39] These functional groups are typically moieties on ligands. The simplest method of integrating the three components is co-deposition (**Figure 1.7**a).[34,35,40,41] The chromophore and catalyst, functionalized with binding groups (most often carboxylic or phosphonic acids), are loaded from solution to the metal oxide. These assemblies require lateral hole transfer from the oxidized chromophore to the catalyst, and they might suffer fast BET since both the chromophore and catalyst are localized on the semiconductor interface. Furthermore, they have inherently limited surface coverage due to binding two species.

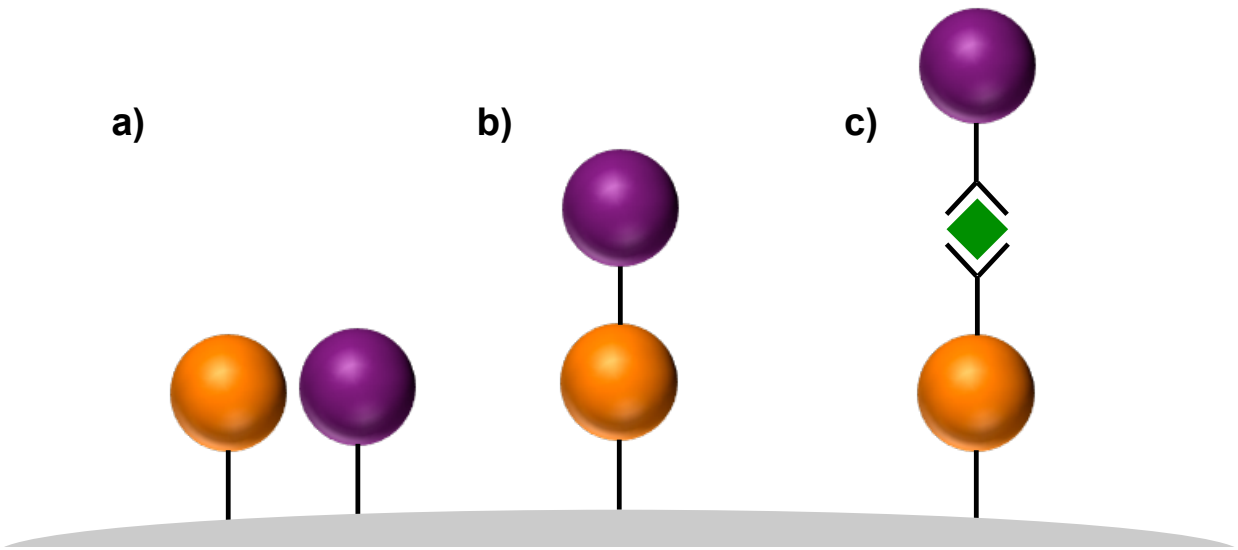

Figure 1.7. Schematic depiction of a) co-deposition; b) covalent-linked assembly attachment; and c) layer-by-layer assembly of a chromophore and catalyst on a metal oxide surface. In this scheme, the chromophore is shaded orange and the catalyst is shaded purple. The green diamond in c) is a coordination linker (e.g. Zr^{IV}).

The chromophore and catalyst can be covalently linked prior to loading (**Figure 1.7**b). These pre-formed chromophore-catalyst assemblies have several advantageous properties, including constant chromophore-catalyst ratios (typically 1:1), close spatial (and occasionally electronic) coupling, and consistency among samples.[22,33,42-46] They also have drawbacks, including low surface coverage due to higher charge and larger size,[47,48] tedious and time-consuming synthetic preparation,[49,50] and the requirement of functionalizing the chromophore for binding (via carboxylic or phosphonic acid linkers), increasing the complexity of synthesis.[51,52]

A simpler assembly technique, with many of the same advantages but few of the drawbacks, is layer-by-layer formation achieved by sequentially soaking a metal oxide electrode in solutions containing: 1) a chromophore; 2) a coordination linker (e.g. Zr^{IV}); and 3) a catalyst (**Figure 1.7**c).[53-55] The chromophore requires at least two binding groups: one for surface attachment, one for coordination to the linker. The catalyst requires only one binding group for

coordination to the linker. The formation of these assemblies can be easily monitored by UV-visible absorption spectroscopy, as well as sweep voltammetry measurements.

Despite the different manners in which chromophores and catalysts can be assembled on semiconductor surfaces, each method suffers a common set of disadvantages. Decomposition is a critical issue facing DSPEC applications. In natural photosynthesis, the oxygen-evolving complex (OEC) must regenerate itself approximately every 30 minutes due to oxidative damage.[56] Artificial photosynthesis shares the same fate, with chromophore and catalyst decomposition regular occurrences.[16,27,29,57-60] Another issue critical to DSPEC application is desorption. The acid groups (both carboxylic and phosphonic) used for surface binding are susceptible to detachment under a myriad of conditions, notably under illumination, applied electrochemical potential, and in aqueous solution – the exact conditions of DSPEC operation.[59-63] Two immediate solutions could ameliorate these issues: 1) stabilization of the binding groups; or 2) removal of the binding groups.

1.4. Electropolymerization

One method for eliminating surface binding groups is electropolymerization.[36,37,64-77] The technique of electropolymerization (a.k.a. electro-assembly) requires a moiety capable of undergoing C-C coupling under an applied potential. Typically, these functional groups are vinyl groups capable of electropolymerization upon reduction. The mechanism of this coupling has been investigated.[78] Surface anchoring is due to precipitation and physical adsorption of the polymer – the molecules are not attached chemically. Due to this manner of binding, adsorption to the semiconductor surface should be pH-independent. Multi-component films have also been demonstrated using electropolymerization, suggesting the technique can be used to form chromophore-catalyst assemblies on semiconductor surfaces.[65,75,79,80]

Electropolymerization can also be used in conjunction with other surface-binding techniques. Meyer showed that a $[Ru(bpy)_3]^{2+}$ derivative functionalized with both vinyl and carboxylic acid groups (on different bpy ligands) would first bind on *nano*TiO_2 via the carboxylate linkers, and was then capable of undergoing reductive coupling with a vinyl-functionalized $[Ru(bpy)_3]^{2+}$ derivative in solution.[81,82] Not only did electropolymerization of these overlayers result in covalent-coupling to a surface bound chromophore, but the polymer overlayers also improved the binding stability of the carboxylic acid-bound chromophore. No desorption was observed thermally from pH 1 to 14 over periods of weeks; however the photoelectrochemical stability was not investigated at the time.[82] These studies demonstrated the possibility of using electropolymerization to form photoelectrochemically-stable multi-component films for DSPEC applications.

1.5. Atomic Layer Deposition (ALD)

Another method of stabilizing surface binding sites is protecting them using atomic layer deposition (ALD). ALD has emerged in recent years as a leading technique for thin film deposition in a precise and controlled manner.[83] It is a self-limiting process that alternates exposures of a metal source and oxygen source to a substrate. Using ALD, a variety of thin films can be deposited on high aspect ratio substrates. The most common metal oxide deposited is Al_2O_3, but many others, including TiO_2, SnO_2, ZrO_2, ZnO, HfO_2, Ta_2O_5, and Fe_2O_3 are deposited routinely.[84,85]

A sample ALD procedure is outlined in **Figure 1.8** for the deposition of aluminum oxide from trimethylaluminum (TMA) and water. A hydroxide-terminated substrate (e.g. a metal oxide surface) is placed in a reaction chamber under a steady flow of an inert gas (typically N_2 at 5 – 20 sccm) and dynamic vacuum. TMA is quickly pulsed into the chamber and allowed to react with substrate. For planar substrates, the pulse itself is typically sufficient for a complete

reaction; for high aspect ratio substrates, the chamber might be isolated temporarily from vacuum to provide a longer exposure time. Following exposure, residual TMA and the methane byproduct are purged from the chamber via vacuum. When the first reactant is fully removed, water is then pulsed into the chamber, hydrolyzing the remaining Al-CH_3 bonds. Excess water is then purged from the chamber with the methane byproducts. The new surface consists of Al-OH bonds, which are capable of reacting with more TMA, continuing the process in a layer-by-layer fashion. ALD has several advantages over other coating methods (e.g. dip-coating, electrodeposition, spray pyrolysis, etc.). It is a gas-to-surface reaction, which allows for uniform coating of high aspect ratio films (typically up to 1,000 depending on the precursors). It provides tremendous control of thickness, depositing a sub-monolayer amount with each cycle (Al_2O_3 is known to deposit 1.1 Å $cycle^{-1}$; a monolayer of amorphous Al_2O_3 is ~3.8 Å thick).[84]

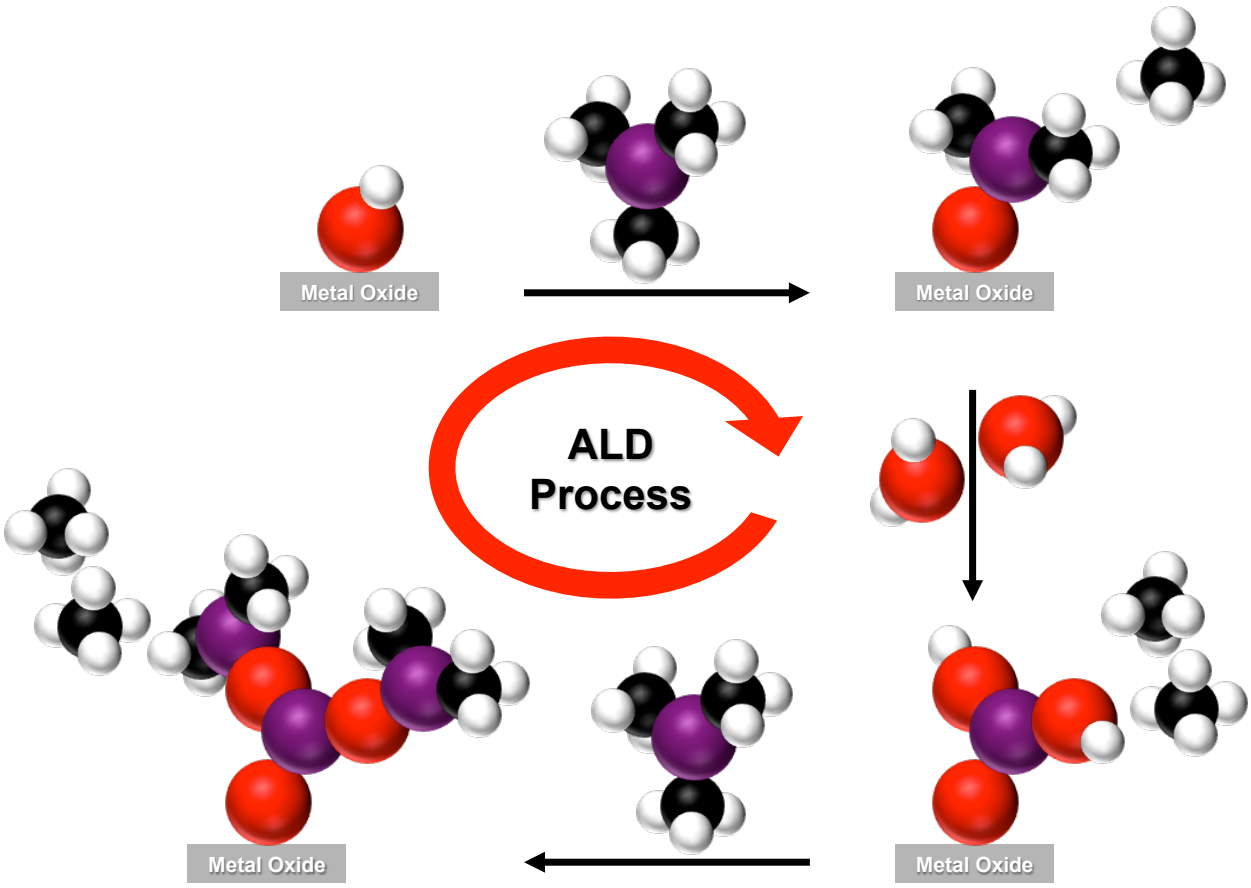

Figure 1.8. Scheme depicting the atomic layer deposition of aluminum oxide via: (1) exposure of surface-terminating hydroxide to trimethylaluminum; (2) removal of excess trimethylaluminum; (3) exposure of methyl-aluminum termini to water; (4) removal of excess water; and (5) repetition of (1) – (4) until the desired thickness of aluminum oxide is achieved.

The effects of ALD on binding stabilization of the well-studied molecular chromophore $[Ru(4,4'\text{-dpbpy})(2,2'\text{-bipyridine})_2][Cl]_2$ (**RuP^{2+}**; 4,4'-dpbpy = [2,2'-bipyridine]-4,4'-diylbis(phosphonic acid)) has been characterized in recent years.[61,62] Increased thicknesses of Al_2O_3 and TiO_2 deposited on *nano*TiO_2|-**RuP^{2+}** have been shown to increase the photochemical interfacial stability relative to an unprotected sample albeit with some deleterious effects on electron injection (**Figure 1.9**). Other molecules, including a water oxidation catalyst, have also been surface stabilized using ALD.[63,86,87] ALD is also used to stabilize planar photoanodes for water oxidation catalysis with promising results.[88]

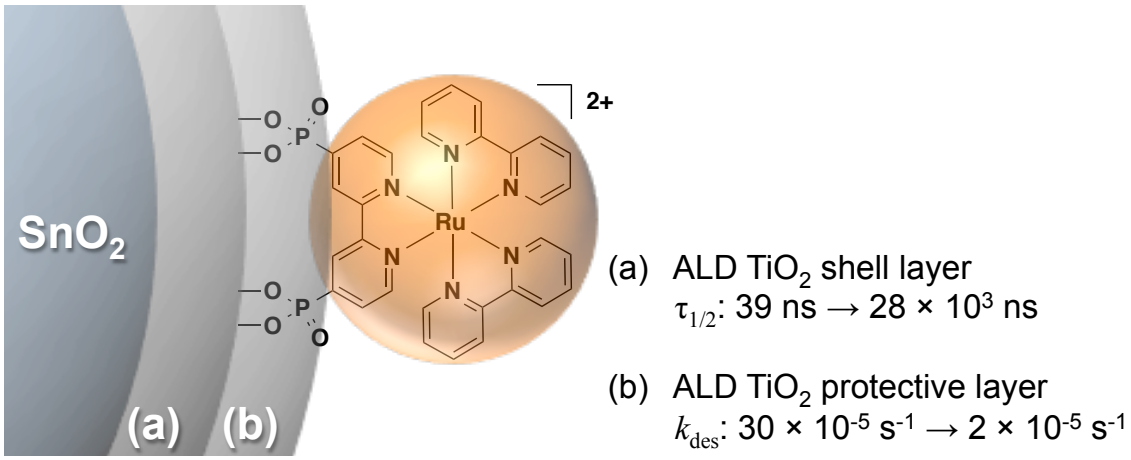

Figure 1.9. Diagram depicting the use of ALD in (a) forming core/shell structures for slowing back electron transfer;[89] and (b) protecting the binding to metal oxide surfaces of covalently-attached molecular species.[62]

Another application of ALD in DSPECs is the fabrication of core/shell structures. Core/shell structures are constructed such that there is a favorable energy gradient for electron transfer from the outer (shell) semiconductor to the inner (core) semiconductor due to misaligned conduction band potentials. ALD is used to deposit the shell atop the core substrate. The primary benefit of employing a core/shell structure is that the energy gradient between the core and the shell makes BET an uphill process, which dramatically slows BET (**Figure 1.9**a).[89] From a practical standpoint, longer-lived charge separation results in an increased level of photocurrent, allowing for more efficient light-to-fuel DSPECs.[30,32,77]

This dissertation discusses multiple strategies for assembling molecules on high surface area, nanoparticular semiconductor surfaces. Methods include electropolymerization of single-site catalyst precursors, electropolymerization of chromophore-electron donor assemblies, electropolymerization of chromophore-catalyst assemblies for electrochemical water oxidation catalysis, and ALD-assembly of chromophore-catalyst assemblies for photoelectrochemical

water oxidation catalysis. Finally, the use of ALD as a means of constructing core/shell structures (in which directional electron transfer cascade events are achieved to increase charge separation lifetime) was investigated on the ultrafast timescale by transient absorption spectroscopy. Ultimately, these strategies demonstrate the feasibility of building stabilization into assembly formation. Long-term stability is essential for these devices to achieve light-driven water splitting.

REFERENCES

(1) Lewis, N. S.; Nocera, D. G. *Proc. Natl. Acad. Sci. U. S. A.* **2006**, *103*, 15729.

(2) Schwabe, P. *Solar Energy Prospecting in Remote Alaska: An Economic Analysis of Solar Photovoltaics in the Last Frontier State*, National Renewable Energy Laboratory, 2016.

(3) BP Statistical Review of World Energy June 2015: BP p.l.c., 2015.

(4) Goodenough, J. B.; Park, K.-S. *J. Am. Chem. Soc.* **2013**, *135*, 1167.

(5) Lewis, N. S. *Chem. Rev.* **2015**, *115*, 12631.

(6) Fujishima, A.; Honda, K. *Nature* **1972**, *238*, 37.

(7) Wrighton, M. S.; Ginley, D. S.; Wolczanski, P. T.; Ellis, A. B.; Morse, D. L.; Linz, A. *Proc. Natl. Acad. Sci. U. S. A.* **1975**, *72*, 1518.

(8) Wrighton, M. S.; Ellis, A. B.; Wolczanski, P. T.; Morse, D. L.; Abrahamson, H. B.; Ginley, D. S. *J. Am. Chem. Soc.* **1976**, *98*, 2774.

(9) Khaselev, O.; Turner, J. A. *Science* **1998**, *280*, 425.

(10) Nocera, D. G. *Acc. Chem. Res.* **2012**, *45*, 767.

(11) Walter, M. G.; Warren, E. L.; McKone, J. R.; Boettcher, S. W.; Mi, Q.; Santori, E. A.; Lewis, N. S. *Chem. Rev.* **2010**, *110*, 6446.

(12) Grätzel, M. *Nature* **2001**, *414*, 338.

(13) Luo, J.; Im, J.-H.; Mayer, M. T.; Schreier, M.; Nazeeruddin, M. K.; Park, N.-G.; Tilley, S. D.; Fan, H. J.; Grätzel, M. *Science* **2014**, *345*, 1593.

(14) Gersten, S. W.; Samuels, G. J.; Meyer, T. J. *J. Am. Chem. Soc.* **1982**, *104*, 4029.

(15) Gilbert, J. A.; Eggleston, D. S.; Murphy, W. R.; Geselowitz, D. A.; Gersten, S. W.; Hodgson, D. J.; Meyer, T. J. *J. Am. Chem. Soc.* **1985**, *107*, 3855.

(16) Youngblood, W. J.; Lee, S.-H. A.; Maeda, K.; Mallouk, T. E. *Acc. Chem. Res.* **2009**, *42*, 1966.

(17) Concepcion, J. J.; Jurss, J. W.; Brennaman, M. K.; Hoertz, P. G.; Patrocinio, A. O. T.; Murakami Iha, N. Y.; Templeton, J. L.; Meyer, T. J. *Acc. Chem. Res.* **2009**, *42*, 1954.

(18) Sala, X.; Romero, I.; Rodriguez, M.; Escriche, L.; Llobet, A. *Angew. Chem., Int. Ed.* **2009**, *48*, 2842.

(19) Duan, L.; Tong, L.; Xu, Y.; Sun, L. *Energy Environ. Sci.* **2011**, *4*, 3296.

(20) Andreiadis, E. S.; Chavarot-Kerlidou, M.; Fontecave, M.; Artero, V. *Photochem. Photobiol.* **2011**, *87*, 946.

(21) Lv, H.; Geletii, Y. V.; Zhao, C.; Vickers, J. W.; Zhu, G.; Luo, Z.; Song, J.; Lian, T.; Musaev, D. G.; Hill, C. L. *Chem. Soc. Rev.* **2012**, *41*, 7572.

(22) Joya, K. S.; Vallés-Pardo, J. L.; Joya, Y. F.; Eisenmayer, T.; Thomas, B.; Buda, F.; de Groot, H. J. M. *ChemPlusChem* **2013**, *78*, 35.

(23) Blakemore, J. D.; Crabtree, R. H.; Brudvig, G. W. *Chem. Rev.* **2015**, *115*, 12974.

(24) Duan, L.; Bozoglian, F.; Mandal, S.; Stewart, B.; Privalov, T.; Llobet, A.; Sun, L. *Nature Chem.* **2012**, *4*, 418.

(25) Moyer, B. A.; Meyer, T. J. *J. Am. Chem. Soc.* **1978**, *100*, 3601.

(26) Young, R. C.; Meyer, T. J.; Whitten, D. G. *J. Am. Chem. Soc.* **1975**, *97*, 4781.

(27) Thompson, D. W.; Ito, A.; Meyer, T. J. *Pure Appl. Chem.* **2013**, *85*, 1257.

(28) Treadway, J. A.; Moss, J. A.; Meyer, T. J. *Inorg. Chem.* **1999**, *38*, 4386.

(29) Youngblood, W. J.; Lee, S.-H. A.; Kobayashi, Y.; Hernandez-Pagan, E. A.; Hoertz, P. G.; Moore, T. A.; Moore, A. L.; Gust, D.; Mallouk, T. E. *J. Am. Chem. Soc.* **2009**, *131*, 926.

(30) Alibabaei, L.; Sherman, B. D.; Norris, M. R.; Brennaman, M. K.; Meyer, T. J. *Proc. Natl. Acad. Sci. U. S. A.* **2015**, *112*, 5899.

(31) Song, W.; Vannucci, A. K.; Farnum, B. H.; Lapides, A. M.; Brennaman, M. K.; Kalanyan, B.; Alibabaei, L.; Concepcion, J. J.; Losego, M. D.; Parsons, G. N.; Meyer, T. J. *J. Am. Chem. Soc.* **2014**, *136*, 9773.

(32) Alibabaei, L.; Brennaman, M. K.; Norris, M. R.; Kalanyan, B.; Song, W.; Losego, M. D.; Concepcion, J. J.; Binstead, R. A.; Parsons, G. N.; Meyer, T. J. *Proc. Natl. Acad. Sci. U. S. A.* **2013**, *110*, 20008.

(33) Ashford, D. L.; Gish, M. K.; Vannucci, A. K.; Brennaman, M. K.; Templeton, J. L.; Papanikolas, J. M.; Meyer, T. J. *Chem. Rev.* **2015**, *115*, 13006.

(34) Gao, Y.; Ding, X.; Liu, J.; Wang, L.; Lu, Z.; Li, L.; Sun, L. *J. Am. Chem. Soc.* **2013**, *135*, 4219.

(35) Fan, K.; Li, F.; Wang, L.; Daniel, Q.; Gabrielsson, E.; Sun, L. *PCCP* **2014**, *16*, 25234.

(36) Murray, R. W. *Acc. Chem. Res.* **1980**, *13*, 135.

(37) Abruña, H. D. *Coord. Chem. Rev.* **1988**, *86*, 135.

(38) Heimer, T. A.; D'Arcangelis, S. T.; Farzad, F.; Stipkala, J. M.; Meyer, G. J. *Inorg. Chem.* **1996**, *35*, 5319.

(39) Ardo, S.; Meyer, G. J. *Chem. Soc. Rev.* **2009**, *38*, 115.

(40) Moore, G. F.; Blakemore, J. D.; Milot, R. L.; Hull, J. F.; Song, H.-e.; Cai, L.; Schmuttenmaer, C. A.; Crabtree, R. H.; Brudvig, G. W. *Energy Environ. Sci.* **2011**, *4*, 2389.

(41) Li, F.; Fan, K.; Xu, B.; Gabrielsson, E.; Daniel, Q.; Li, L.; Sun, L. *J. Am. Chem. Soc.* **2015**, *137*, 9153.

(42) Alstrum-Acevedo, J. H.; Brennaman, M. K.; Meyer, T. J. *Inorg. Chem.* **2005**, *44*, 6802.

(43) Concepcion, J. J.; Jurss, J. W.; Hoertz, P. G.; Meyer, T. J. *Angew. Chem. Int. Ed.* **2009**, *48*, 9473.

(44) Concepcion, J. J.; House, R. L.; Papanikolas, J. M.; Meyer, T. J. *Proc. Natl. Acad. Sci. U. S. A.* **2012**, *109*, 15560.

(45) Frischmann, P. D.; Mahata, K.; Wurthner, F. *Chem. Soc. Rev.* **2013**, *42*, 1847.

(46) Kärkäs, M. D.; Johnston, E. V.; Verho, O.; Åkermark, B. *Acc. Chem. Res.* **2014**, *47*, 100.

(47) Rawling, T.; Austin, C.; Buchholz, F.; Colbran, S. B.; McDonagh, A. M. *Inorg. Chem.* **2009**, *48*, 3215.

(48) Kleverlaan, C. J.; Indelli, M. T.; Bignozzi, C. A.; Pavanin, L.; Scandola, F.; Hasselman, G. M.; Meyer, G. J. *J. Am. Chem. Soc.* **2000**, *122*, 2840.

(49) Ashford, D. L.; Stewart, D. J.; Glasson, C. R.; Binstead, R. A.; Harrison, D. P.; Norris, M. R.; Concepcion, J. J.; Fang, Z.; Templeton, J. L.; Meyer, T. J. *Inorg. Chem.* **2012**, *51*, 6428.

(50) Norris, M. R.; Concepcion, J. J.; Harrison, D. P.; Binstead, R. A.; Ashford, D. L.; Fang, Z.; Templeton, J. L.; Meyer, T. J. *J. Am. Chem. Soc.* **2013**, *135*, 2080.

(51) Ashford, D. L.; Song, W.; Concepcion, J. J.; Glasson, C. R. K.; Brennaman, M. K.; Norris, M. R.; Fang, Z.; Templeton, J. L.; Meyer, T. J. *J. Am. Chem. Soc.* **2012**, *134*, 19189.

(52) Norris, M. R.; Concepcion, J. J.; Fang, Z.; Templeton, J. L.; Meyer, T. J. *Angew. Chem. Int. Ed.* **2013**, *52*, 13580.

(53) Ishida, T.; Terada, K.-i.; Hasegawa, K.; Kuwahata, H.; Kusama, K.; Sato, R.; Nakano, M.; Naitoh, Y.; Haga, M.-a. *Appl. Surf. Sci.* **2009**, *255*, 8824.

(54) Haga, M.-a.; Kobayashi, K.; Terada, K. *Coord. Chem. Rev.* **2007**, *251*, 2688.

(55) Hanson, K.; Torelli, D. A.; Vannucci, A. K.; Brennaman, M. K.; Luo, H.; Alibabaei, L.; Song, W.; Ashford, D. L.; Norris, M. R.; Glasson, C. R. K.; Concepcion, J. J.; Meyer, T. J. *Angew. Chem., Int. Ed.* **2012**, *51*, 12782.

(56) Meyer, T. J. *Nature* **2008**, *451*, 778.

(57) Ghosh, P. K.; Brunschwig, B. S.; Chou, M.; Creutz, C.; Sutin, N. *J. Am. Chem. Soc.* **1984**, *106*, 4772.

(58) Hara, M.; Waraksa, C. C.; Lean, J. T.; Lewis, B. A.; Mallouk, T. E. *J. Phys. Chem. A* **2000**, *104*, 5275.

(59) Hanson, K.; Brennaman, M. K.; Luo, H.; Glasson, C. R.; Concepcion, J. J.; Song, W.; Meyer, T. J. *ACS Appl. Mater. Interfaces* **2012**, *4*, 1462.

(60) Hyde, J. T.; Hanson, K.; Vannucci, A. K.; Lapides, A. M.; Alibabaei, L.; Norris, M. R.; Meyer, T. J.; Harrison, D. P. *ACS Appl. Mater. Interfaces* **2015**, *7*, 9554.

(61) Hanson, K.; Losego, M. D.; Kalanyan, B.; Ashford, D. L.; Parsons, G. N.; Meyer, T. J. *Chem. Mater.* **2013**, *25*, 3.

(62) Hanson, K.; Losego, M. D.; Kalanyan, B.; Parsons, G. N.; Meyer, T. J. *Nano Lett.* **2013**, *13*, 4802.

(63) Vannucci, A. K.; Alibabaei, L.; Losego, M. D.; Concepcion, J. J.; Kalanyan, B.; Parsons, G. N.; Meyer, T. J. *Proc. Natl. Acad. Sci. U. S. A.* **2013**, *110*, 20918.

(64) Oyama, N.; Anson, F. C. *J. Am. Chem. Soc.* **1979**, *101*, 3450.

(65) Abruña, H. D.; Denisevich, P.; Umaña, M.; Meyer, T. J.; Murray, R. W. *J. Am. Chem. Soc.* **1981**, *103*, 1.

(66) Cosnier, S.; Deronzier, A.; Moutet, J. C. *J. Electroanal. Chem. Interfacial Electrochem.* **1985**, *193*, 193.

(67) Cosnier, S.; Deronzier, A.; Moutet, J. C. *J. Mol. Catal.* **1988**, *45*, 381.

(68) Hurrell, H. C.; Mogstad, A. L.; Usifer, D. A.; Potts, K. T.; Abruña, H. D. *Inorg. Chem.* **1989**, *28*, 1080.

(69) Arana, C.; Keshavarz, M.; Potts, K. T.; Abruña, H. D. *Inorg. Chim. Acta* **1994**, *225*, 285.

(70) Ramos Sende, J. A.; Arana, C. R.; Hernandez, L.; Potts, K. T.; Keshevarz-K, M.; Abruña, H. D. *Inorg. Chem.* **1995**, *34*, 3339.

(71) Nie, H.-J.; Yao, J.; Zhong, Y.-W. *J. Org. Chem.* **2011**, *76*, 4771.

(72) Nie, H.-J.; Shao, J.-Y.; Wu, J.; Yao, J.; Zhong, Y.-W. *Organometallics* **2012**, *31*, 6952.

(73) Harrison, D. P.; Lapides, A. M.; Binstead, R. A.; Concepcion, J. J.; Méndez, M. A.; Torelli, D. A.; Templeton, J. L.; Meyer, T. J. *Inorg. Chem.* **2013**, *52*, 4747.

(74) Torelli, D. A.; Harrison, D. P.; Lapides, A. M.; Meyer, T. J. *ACS Appl. Mater. Interfaces* **2013**, *5*, 7050.

(75) Ashford, D. L.; Lapides, A. M.; Vannucci, A. K.; Hanson, K.; Torelli, D. A.; Harrison, D. P.; Templeton, J. L.; Meyer, T. J. *J. Am. Chem. Soc.* **2014**, *136*, 6578.

(76) Ashford, D. L.; Sherman, B. D.; Binstead, R. A.; Templeton, J. L.; Meyer, T. J. *Angew. Chem. Int. Ed.* **2015**, *54*, 4778.

(77) Sherman, B. D.; Ashford, D. L.; Lapides, A. M.; Sheridan, M. V.; Wee, K.-R.; Meyer, T. J. *J. Phys. Chem. Lett.* **2015**, *6*, 3213.

(78) Calvert, J. M.; Schmehl, R. H.; Sullivan, B. P.; Facci, J. S.; Meyer, T. J.; Murray, R. W. *Inorg. Chem.* **1983**, *22*, 2151.

(79) Gould, S.; O'Toole, T. R.; Meyer, T. J. *J. Am. Chem. Soc.* **1990**, *112*, 9490.

(80) Li, M.; Zhang, J.; Nie, H.-J.; Liao, M.; Sang, L.; Qiao, W.; Wang, Z. Y.; Ma, Y.; Zhong, Y.-W.; Ariga, K. *Chem. Commun.* **2013**, *49*, 6879.

(81) Moss, J. A.; Stipkala, J. M.; Yang, J. C.; Bignozzi, C. A.; Meyer, G. J.; Meyer, T. J.; Wen, X.; Linton, R. W. *Chem. Mater.* **1998**, *10*, 1748.

(82) Moss, J. A.; Yang, J. C.; Stipkala, J. M.; Wen, X.; Bignozzi, C. A.; Meyer, G. J.; Meyer, T. J. *Inorg. Chem.* **2004**, *43*, 1784.

(83) Parsons, G. N.; George, S. M.; Knez, M. *MRS Bull.* **2011**, *36*, 865.

(84) George, S. M. *Chem. Rev.* **2010**, *110*, 111.

(85) Martinson, A. B. F.; DeVries, M. J.; Libera, J. A.; Christensen, S. T.; Hupp, J. T.; Pellin, M. J.; Elam, J. W. *J. Phys. Chem. C* **2011**, *115*, 4333.

(86) Son, H.-J.; Prasittichai, C.; Mondloch, J. E.; Luo, L.; Wu, J.; Kim, D. W.; Farha, O. K.; Hupp, J. T. *J. Am. Chem. Soc.* **2013**, *135*, 11529.

(87) Son, H.-J.; Kim, C. H.; Kim, D. W.; Jeong, N. C.; Prasittichai, C.; Luo, L.; Wu, J.; Farha, O. K.; Wasielewski, M. R.; Hupp, J. T. *ACS Appl. Mater. Interfaces* **2015**, *7*, 5150.

(88) Hu, S.; Shaner, M. R.; Beardslee, J. A.; Lichterman, M.; Brunschwig, B. S.; Lewis, N. S. *Science* **2014**, *344*, 1005.

(89) Knauf, R. R.; Kalanyan, B.; Parsons, G. N.; Dempsey, J. L. *J. Phys. Chem. C* **2015**, *119*, 28353.

CHAPTER 2: COORDINATION CHEMISTRY OF SINGLE-SITE CATALYST PRECURSORS IN REDUCTIVELY ELECTROPOLYMERIZED VINYLBIPYRIDINE FILMS

Reprinted with permission from Harrison, D. P.; Lapides, A. M.; Binstead, R. A.; Concepcion, J. J.; Méndez, M. A.; Torelli, D. A.; Templeton, J. L.; Meyer, T. J. *Inorg. Chem.* **2013**, *52*, 4747.

2.1. Introduction

Well-established procedures are available for the electropolymerization of vinyl-[1-10] and pyrrole-derivatized[11-14] metal complexes on a variety of conducting substrates. The electron transfer,[2,9] photochemical,[3,5,10] diffusional,[12] and related properties of the resulting films, including electrocatalysis,[6-8,11,14] have also been investigated. Electropolymerization offers significant advantages over other approaches to modifying surfaces. Multiple polymerizable functional groups allows for cross-linking and formation of relatively high molecular weight polymers, which leads to film formation by physical adsorption to the electrode surface. The resulting film structures have interfacial stability in a variety of media and over an extended pH range in water. In contrast, surface binding of carboxylate- or phosphonate-derivatized complexes to oxide surfaces is only stable in water below pH 5.[15,16]

Electrochemistry allows for the design of interfaces for electrocatalytic and photoelectrocatalytic applications. In one strategy, electropolymerization is used to form films on electrode surfaces from monomer-based catalyst precursors; recent examples have appeared based on oxidatively-induced pyrrole polymerization.[13,14] Here we report our initial findings on reductive electropolymerization of the catalyst precursor complexes $[Ru^{II}$(Ph-tpy)(5,5′-dvbpy)(Cl)$][PF_6]$ (**1**) and $[Ru^{II}$(Ph-tpy)(5,5'-dvbpy)(MeCN)$][PF_6]_2$ (**2**), where Ph-tpy is 4'-phenyl-2,2':6',2"-terpyridine and 5,5'-dvbpy is 5,5'-divinyl-2,2'-bipyridine (**Figure 2.1**), and the

behavior of the resulting interfacial films, poly-**1** and poly-**2**. Earlier strategies relied on multiple polymerizable ligands and cross-linking, which limited the generality of the coordination chemistry. We report here that the doubly derivatized 5,5'-dvbpy ligand in these complexes is sufficient to achieve stable interfacial film structures, as reported earlier by Nie and co-workers.[17]

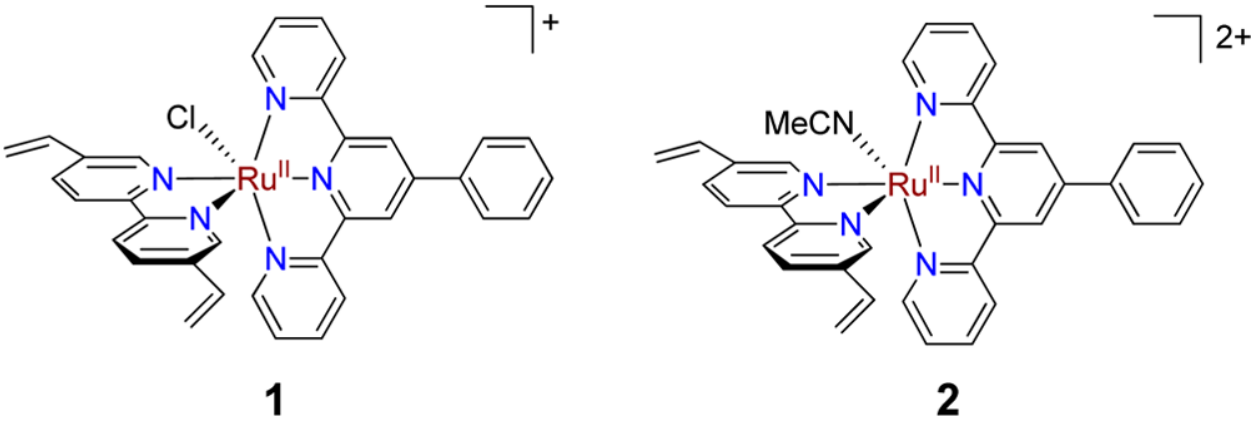

1 **2**

Figure 2.1. Structures of single-site ruthenium complex catalyst precursors to poly-**1** and poly-**2**.

2.2. Results and Discussion

Electropolymerization of **1** and **2** to give poly-**1** and poly-**2** was induced by controlled potential electrolysis or cyclic voltammetry (CV) scans at (or up to) potentials sufficiently negative to reduce the ligands and initiate polymerization (**Figure 2.2**). Either technique produces surface coverages (Γ in mol cm^{-2}; **Equation 2.1** and **Equation 2.2**) that increase linearly with the number of reductive scan cycles or with time spent at potential (**Figure 2.3**). Electropolymerized films of poly-**1** ($E_{1/2}(Ru^{III/II})$ = +0.56 V vs. Ag/$AgNO_3$; see Experimental for details) and poly-**2** ($E_{1/2}(Ru^{III/II})$ = +0.99 V vs. Ag/NO_3) on 0.071-cm^2 glass-like carbon electrodes (GCEs) in 0.1 M [TBA]PF_6/MeCN ([TBA]PF_6 is tetra-n-butylammonium hexafluorophosphate) display peak-to-peak separations (ΔE_p) of 22 and 21 mV (**Figure 2.4**a),

respectively, at a scan rate, ν, of 100 mV s^{-1}. ΔE_p approaches 0 as the scan rate is decreased, as expected for a surface wave (**Figure 2.4**b). UV-visible absorption spectra of poly-**1** and poly-**2** on semitransparent fluorine-doped tin oxide (FTO) surfaces closely resemble those of **1** and **2** in solution (**Figure 2.5**).

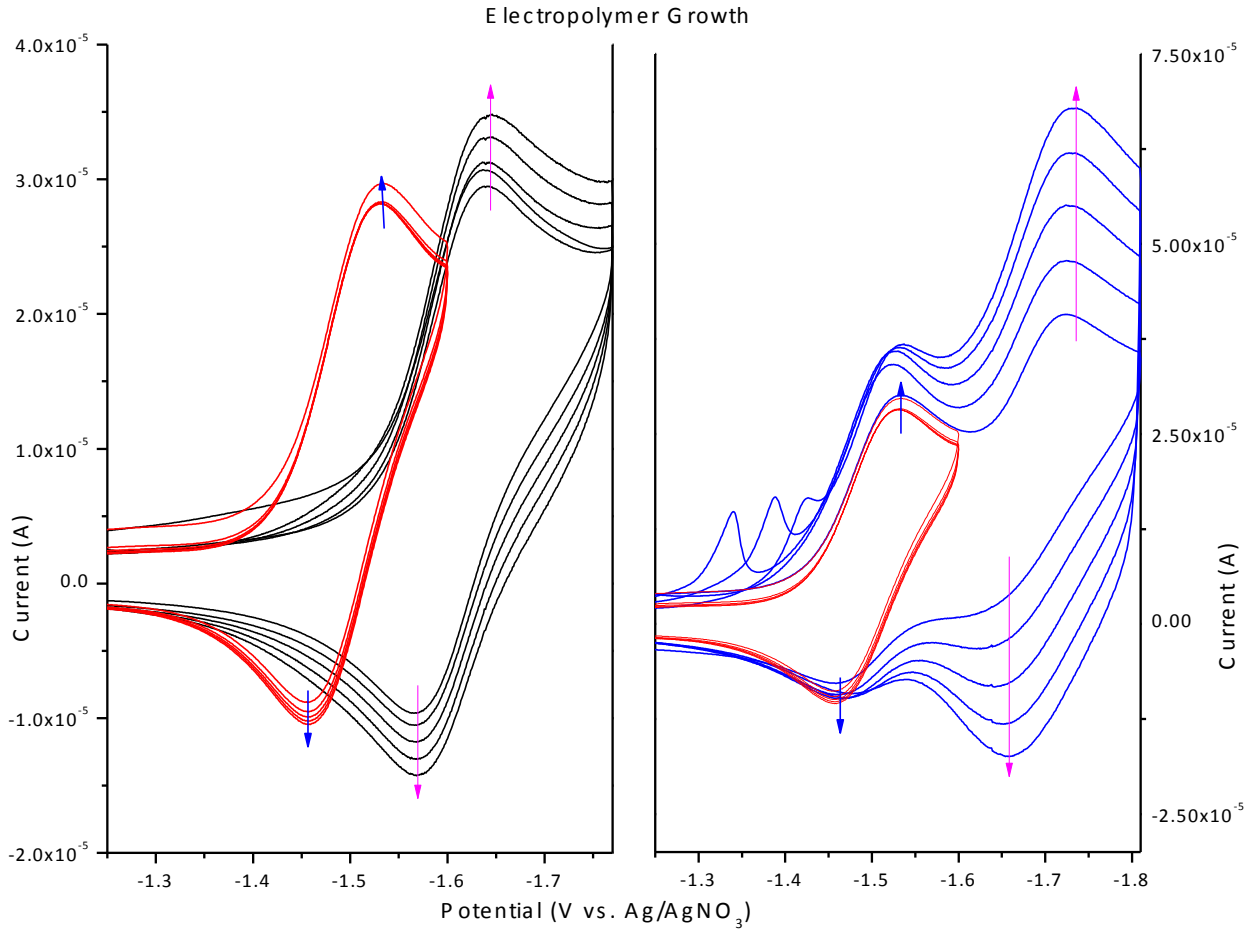

Figure 2.2. Relative rates of electropolymerization of 1.3 mM solutions of **1** and **2** in 0.1 M [TBA]PF_6/MeCN at 100 mV s^{-1} scan rates on a 0.071-cm^2 glass-like carbon disk electrode. Left plot shows 5 cycles past the first ligand-centered reduction of **1** (black) and **2** (red). Right plot shows the difference in the rate of polymerization resulting from cycling past the first ligand centered reduction of **2** (red) vs. cycling past the second ligand based reduction (blue).

Equation 2.1

$$\Gamma = \frac{Q}{nFA}$$

Equation 2.2

$$Q = \frac{Q_{p,a} + Q_{p,c}}{2}$$

Electropolymer growth is obvious by the increased current that is observed as the number of cycles through a wave increases. The rates of electropolymerization for **1** and **2** are notably different when polymerization is initiated via one-electron reduction. Electropolymerization in 1.3 mM solutions of **1** and **2** induced either by cycling past the first reduction or by applying a potential equal to the first reduction $E_{1/2}$ value both indicate that **1** polymerizes at least five times faster than **2**. For example, five CVs at a scan rate of 100 mV s^{-1} between 0 and –1.77 V (**1**) and –1.60 V (**2**) produces Γ of 2.33×10^{-9} mol cm^{-2} and 1.77×10^{-10} mol cm^{-2}, respectively, while applying a potential at –1.59 V (**1**) and –1.52 V (**2**) for 30 seconds, produces Γ of 1.23×10^{-9} mol cm^{-2} and 2.32×10^{-10} mol cm^{-2}, respectively. The accelerated rate of electropolymerization for **1** likely results from a close match in the vinyl reduction potential to that of the first reduction potential of **1**. Electropolymer growth is greatly accelerated by passing through the second reduction wave of **2**, as evidenced by the increasing current between successive cycles between 0 and –1.80 V (**Figure 2.2**). These observations hold true for **1** as well.

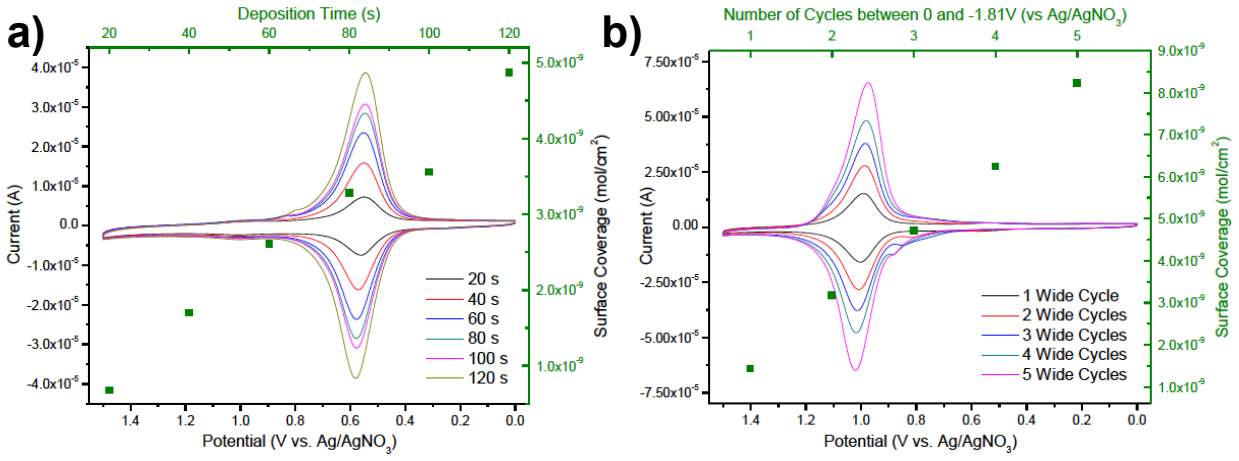

Figure 2.3. a) Linear relationship ($r^2 = 0.9697$) between Γ and controlled potential electrolysis (CPE) deposition time (–1.59 V) produced from a 1.3 mM solution of **1** in 0.1 M [TBA]PF_6/MeCN on a 0.071-cm^2 glass-like carbon disk electrode. Inlaid is an overlay of the 9th oxidative cycle for each experiment. b) Linear relationship ($r^2 = 0.9972$) between Γ and number of CV cycles between 0 and –1.81 V used to electropolymerization **2** from a 1.3 mM solution of **2** in 0.1 M [TBA]PF_6/MeCN on a 0.071-cm^2 glass-like carbon disk electrode. Inlaid is an overlay of the 9th oxidative cycle for each experiment.

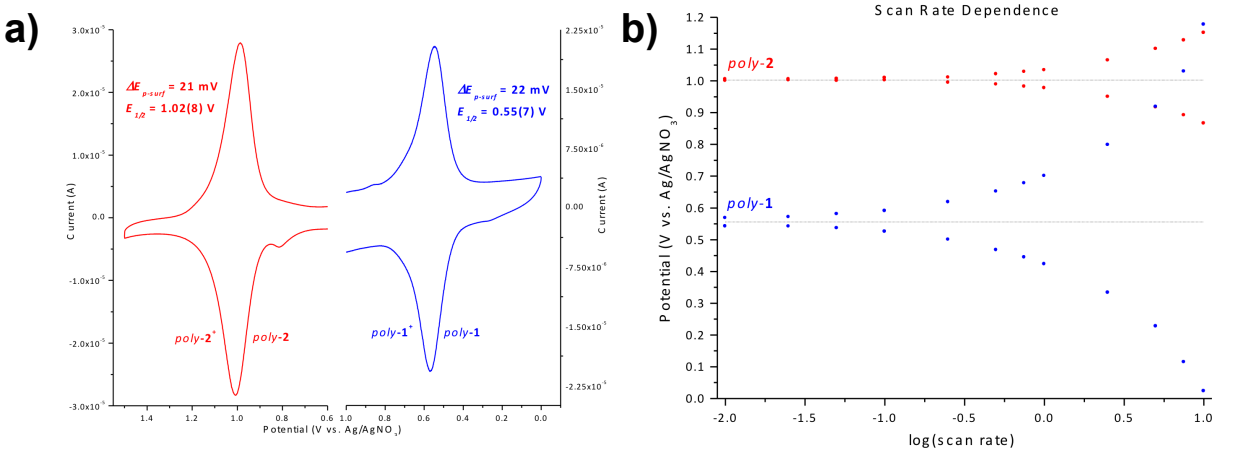

Figure 2.4. a) Oxidative CVs of poly-**1** (blue; $\Gamma = 2.8 \times 10^{-9}$ mol cm^{-2}) and poly-**2** (red; $\Gamma = 2.1 \times 10^{-9}$ mol cm^{-2}) in a fresh solution of 0.1 M [TBA]PF_6/MeCN after electropolymerization on a 0.071-cm^2 GCE; $\nu = 100$ mV s^{-1}. b) $E_{p,a}$'s and $E_{p,c}$'s for poly-**1** ($\Gamma = 3.90 \times 10^{-10}$ mol cm^{-2}; blue) and poly-**2** ($\Gamma = 1.04 \times 10^{-9}$ mol cm^{-2}; red) as a function of scan rate. CVs were performed in 0.1 M [TBA]PF_6/MeCN with electropolymers deposited on a 0.071-cm^2 glass-like carbon electrode.

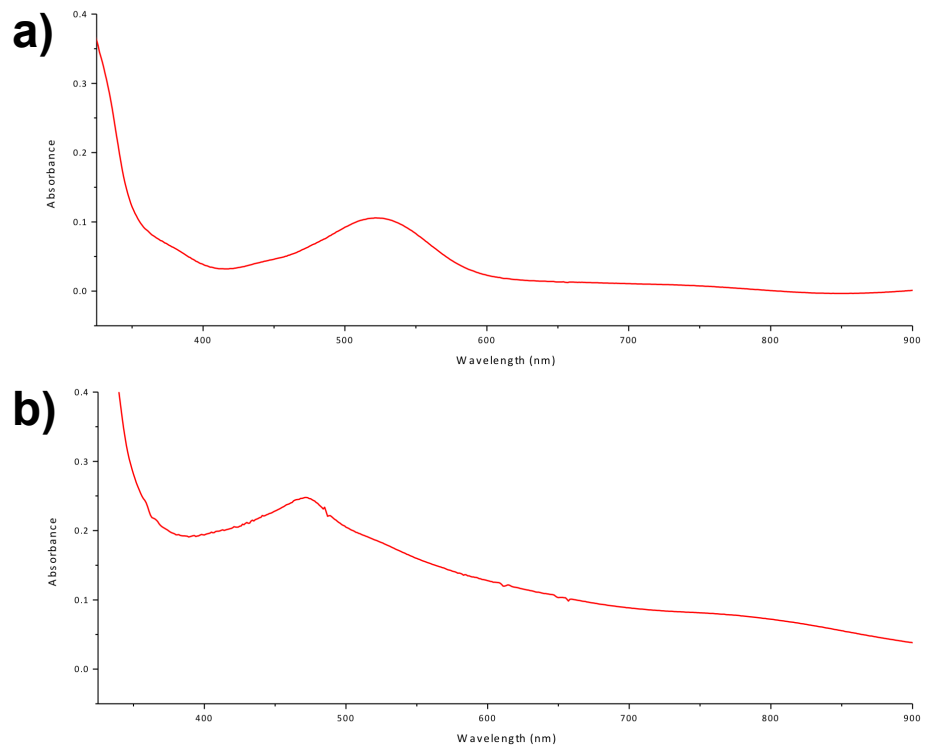

Figure 2.5. a) UV-visible absorption spectrum of poly-**1** on a 1-cm^2 FTO slide prepared by applied potential (–1.59 V vs. Ag/$AgNO_3$) deposition of a 1.3 mM solution of **1** for 150 s. b) UV-visible absorption spectrum of poly-**2** on a 1-cm^2 FTO slide prepared by reductive cyclic voltammetry (4 cycles from 0 to –1.81 V vs. Ag/$AgNO_3$) of a 1.3 mM solution of **2**. The λ_{max} values for poly-**1** and poly-**2** resemble their solution-based analogs.

2.2.1. Oxidatively Induced Ligand Substitution

Oxidative cycling of poly-**2** through the $Ru^{III/II}$ wave in a 1 mM solution of $[TBA]NO_3$ (in 0.1 M $[TBA]PF_6$/MeCN) produces a new surface couple at $E_{1/2}$ = +0.68 V (**Figure 2.6**). Interconversion from poly-**2** to the new couple is complete after 20 scans from 0 to +1.5 V (**Figure 2.7**a). A characteristic pre-wave appears at $E_{p,c}$ = +0.80 V because of changes in the film structure arising from ion transport.[18] The negative shift of $\Delta E_{1/2}$ = −0.34 V is consistent with oxidation to Ru^{III}, followed by substitution of MeCN by NO_3^- to give poly-Ru^{III}-ONO_2^{2+} (poly-Ru^{II}-ONO_2^+ = poly-ONO_2; **Equation 2.3** and **Equation 2.4**). UV-visible absorption spectral data

are consistent with this conclusion (**Figure 2.8**a). Oxidative cycling-induced substitution of MeCN for NO_3^- in $[Ru(tpy)(bpy)(NCMe)]^{2+}$ also occurs in solution under the same conditions.

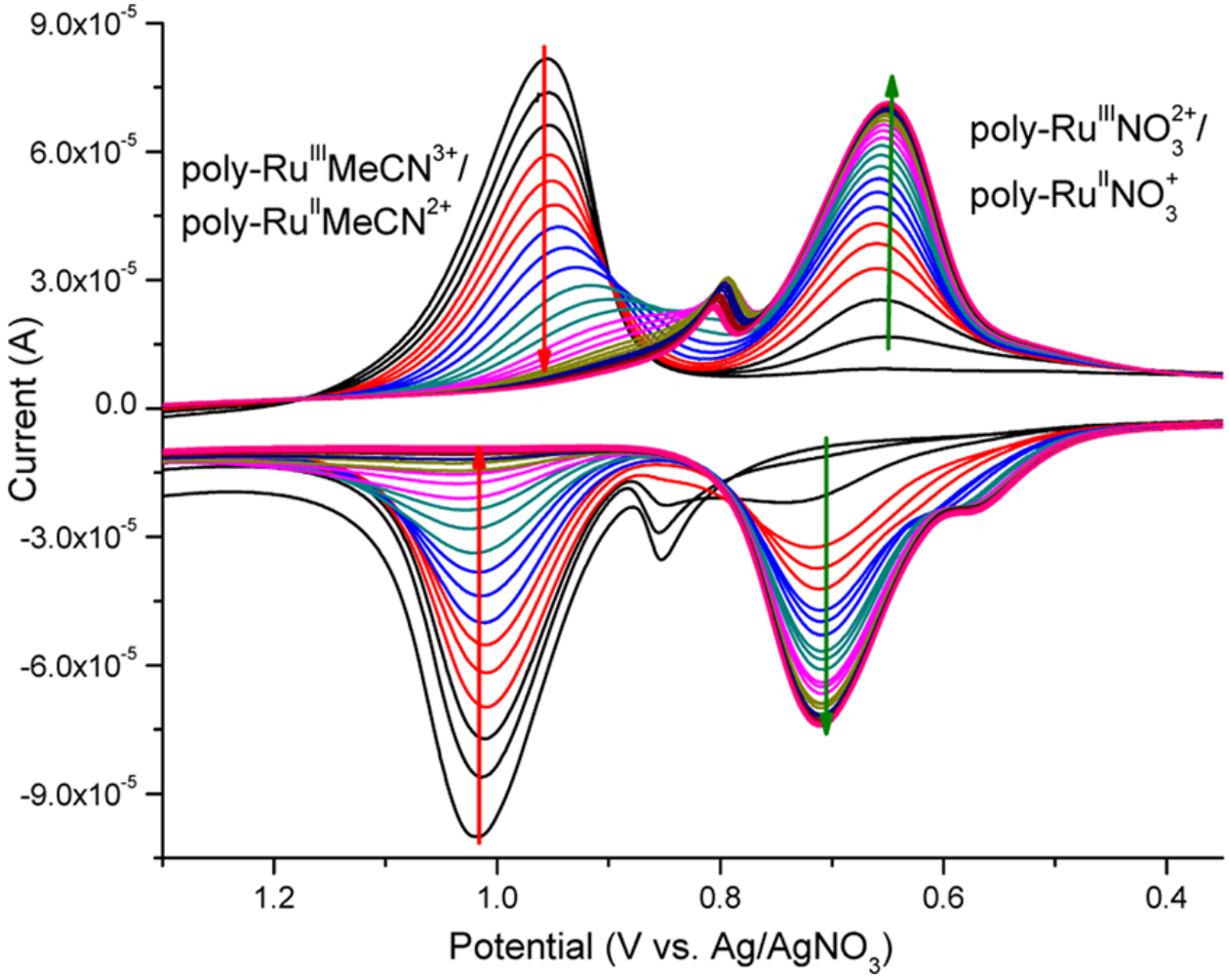

Figure 2.6. Oxidative CVs of poly-**2** on a GCE in 1 mM $[TBA]NO_3$ (ν = 250 mV s^{-1}), illustrating the loss of poly-**2** (red arrows; $\Gamma = 3.7 \times 10^{-9}$ mol cm^{-2}) and the appearance of poly-ONO_2 (green arrows). The shoulder at +0.55 V vs. $Ag/AgNO_3$ appears to be poly-OH_2, arising from trace water in the initial solution (see below).

Equation 2.3

$poly\text{-}Ru^{II}NCMe^{2+} \rightarrow e^- + poly\text{-}Ru^{III}NCMe^{3+}$

Equation 2.4

$$\text{poly-Ru}^{III}\text{NCMe}^{3+} + NO_3^- \rightarrow \text{poly-Ru}^{III}\text{ONO}_2^{2+} + \text{MeCN}$$

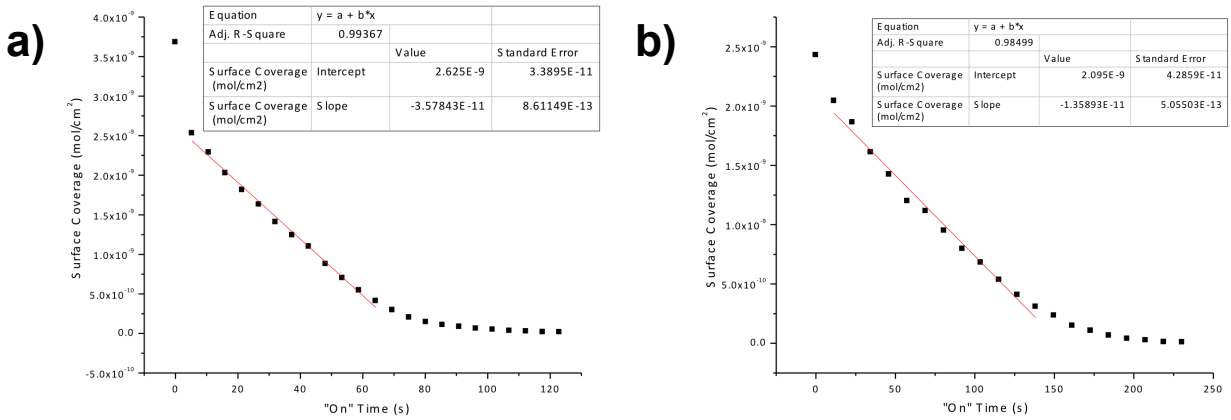

Figure 2.7. a) Plot of Γ vs. time following the substitution of NO_3^- for MeCN in poly-**2** to generate poly-ONO_2. The surface coverage for loss of poly-**2** is calculated by integrating the charge under the $E_{p,a}$ of the $Ru^{III/II}$ couple in poly-**2**. Zero-order rate constant: 3.6×10^{-11} mol cm^{-2} s^{-1}. b) Plot of Γ vs. time following the substitution of H_2O for MeCN in poly-**2** to generate poly-OH_2. The surface coverage for loss of poly-**2** is calculated by integrating the charge under the $E_{p,c}$ of the $Ru^{III/II}$ couple in poly-**2**. Zero-order rate constant: 1.4×10^{-11} mol cm^{-2} s^{-1}. The "on" time was estimated using the scan rate and $E_{1/2}$ values (see text).

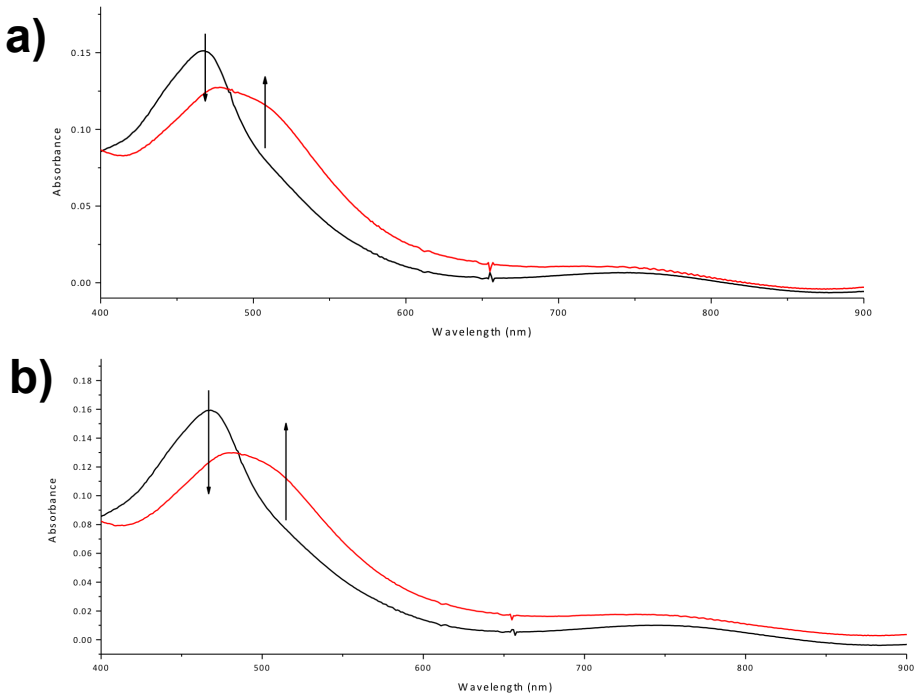

Figure 2.8. a) UV-visible absorption spectra of poly-**2** on FTO before (black) and after cycling (red) in 1 mM [TBA]NO_3. The red-shift in the spectrum is consistent with nitrate entering the coordination sphere of Ru. Note: there is a mixture of poly-**2** and poly-ONO_2 due to inconsistencies in the FTO polymer arising from the large surface area of the electrode. b) UV-visible absorption spectra of poly-**2** on FTO before (black) and after (red) cycling in a 0.1 M $HClO_4$ solution. The red-shift in the spectrum is consistent with water entering the coordination sphere of Ru. Note: there is a mixture of poly-**2** and poly-OH_2 due to inconsistencies in the FTO polymer arising from the large surface area of the electrode.

The poly-$Ru^{III/II}$-$ONO_2^{2+/+}$ couple was not present following a single oxidative sweep of 0 to +1.5 V or after soaking of a GCE–poly-**2** electrode in [TBA]NO_3 for 72 hours. There was no sign of coordination of HSO_4^-, ClO_4^-, or OTf^- by oxidative cycling of poly-**2** under comparable conditions. Cl^- is preferred over NO_3^- in the coordination spheres of both Ru^{III} and Ru^{II}. There was no evidence for substitution of Cl^- for NO_3^- in poly-**1**. In MeCN 5 mM in [Cl^-], substitution of NO_3^- occurs, converting poly-ONO_2 to poly-**1** by the reaction, poly-Ru^{III}-ONO_2^{2+} + Cl^- → poly-**1** + NO_3^- with oxidative cycling with slow substitution (hours) occurring without cycling.

Similarly, oxidative cycling of poly-**2** in 0.1 M $HClO_4$ between 0 and +1.5 V gives poly-Ru^{III}-OH_2^{3+} (poly-Ru^{II}-OH_2^{2+} = poly-OH_2; **Equation 2.3** and **Equation 2.5**), with $E_{1/2}$ = +0.80 V compared to $E_{1/2}$ = +0.79 V vs. SCE (to calculate: E(SCE) = E(Ag/AgCl) – 0.045 V) for the $[Ru^{III/II}(tpy)(bpy)OH_2]^{3+/2+}$ couple at pH 1 (**Figure 2.9**; tpy is 2,2':6',2"-terpyridine; bpy is 2,2'-bipyridine).[19] UV-visible absorption spectral data corroborate these results (**Figure 2.8**b). The reaction is complete after 20 cycles (**Figure 2.7**b). There was no sign of aquation when poly-**2** was soaked in 0.1 M $HClO_4$ for 72 hours. Careful inspection of the scan sequence in **Figure 2.9** reveals that a smaller wave at $E_{1/2} \approx$ +0.68 V vs. SCE appears during the first few scan cycles. This wave may arise from sites near the film–solution interface that undergo substitution more rapidly than sites in the film interior.

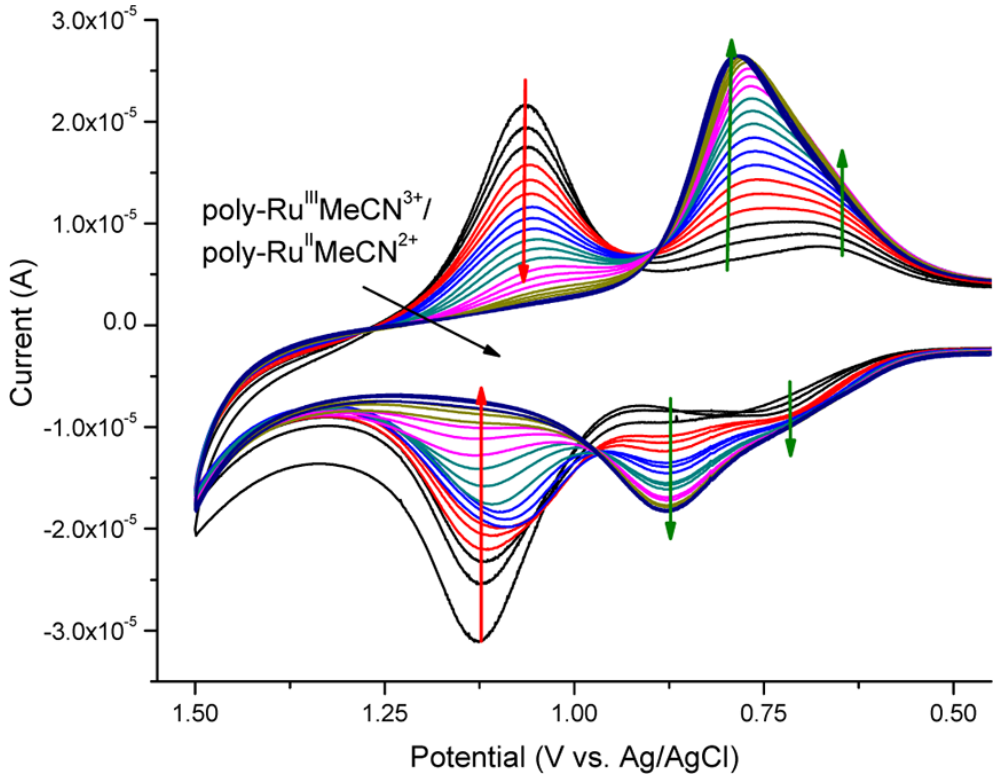

Figure 2.9. Formation of poly-H_2O following oxidative scan cycles of poly-**2** (red arrows; $\Gamma_{initial}$ = 2.7 × 10^{-9} mol cm^{-2}) in 0.1 M $HClO_4$; GCE, 0.071-cm^2, ν = 100 mV s^{-1}.

Equation 2.5

$$poly\text{-}Ru^{III}\text{-}NCMe^{3+} + H_2O \rightarrow poly\text{-}Ru^{III}\text{-}OH_2^{3+} + MeCN$$

Appearance of the aqua complex is significant given the known pH-dependent proton-coupled electron-transfer (PCET) properties of $[Ru(tpy)(bpy)(OH_2)]^{2+}$ and the oxidative reactivity of higher oxidation-state $Ru^{IV}(O)$ and $Ru^{V}(O)$ forms.[15,16,20,21] In MeCN, $[Ru(tpy)(bpy)(OH_2)]^{2+}$ undergoes substitution of H_2O by MeCN in minutes. By contrast, there is no evidence for poly-**2** when poly-OH_2 is soaked in $[TBA]PF_6$/MeCN for extended periods or after oxidative cycling. NO_3^- is lost from poly-ONO_2 to give poly-OH_2 upon oxidative cycling in 0.1 M $HClO_4$ or upon soaking in 0.1 M $HClO_4$. It is noteworthy that the substitution kinetics of MeCN in poly-**2** for H_2O or NO_3^- are zero-order over an extensive dynamic range consistent with a non-complex rate-limiting step, namely, diffusion into the film (**Figure 2.7**).

The reaction substitution time was estimated based upon sequential CVs. The reaction was assumed to proceed in the forward direction when the film was oxidized (i.e. when the ligands in the film are labile and susceptible to substitution). Knowledge of the scan rate and the potentials at which the film is in its oxidized form allows the reaction time for substitution during the CVs to be estimated. Zero-order rate constants were determined by sampling the majority of the polymer, not initial or final minority sites due to possible inconsistencies in the film environment.

2.2.2. Reductively Induced Substitution

Ligand substitution is also induced by reductive cycling following reduction at the π*(polypyridyl) levels of the ligands. The results of three reductive scan cycles of poly-**1** at 100 mV s^{-1} in 0.1 M $[TBA]PF_6$/MeCN from 0 to −1.97 V under N_2 are shown in **Figure 2.10**A.[22] On

the first scan, a pre-wave appears at $E_{p,c} = -1.27$ V followed by surface waves at $E_{1/2} = -1.66$ V (Ph-tpy reduction) and at $E_{1/2} = -1.87$ V (5,5'-poly-dvbpy reduction).

Following the first scan through both ligand-based reductions, a new surface-based couple appears at $E_{p,c} = -1.49$ V, which coincides with $E_{p,c}$ for the first Ph-tpy-based reduction in poly-**2**. A subsequent oxidative scan and the appearance of a wave at $E_{1/2} = +1.02$ V for the poly-$Ru^{III/II}$-$NCMe^{3+/2+}$ couple reveals that ligand-based reduction induces conversion of poly-**1** into poly-**2** (**Equation 2.6**, **Equation 2.7**, **Figure 2.10**B). UV-visible absorption spectral data corroborate these results (**Figure 2.11**). The substitution mechanism, following π*(Ph-tpy)/π*(5,5'-poly-dvbpy) reduction, is presumably by thermal population of Ru-based dσ* levels, which induces ligand labilization.

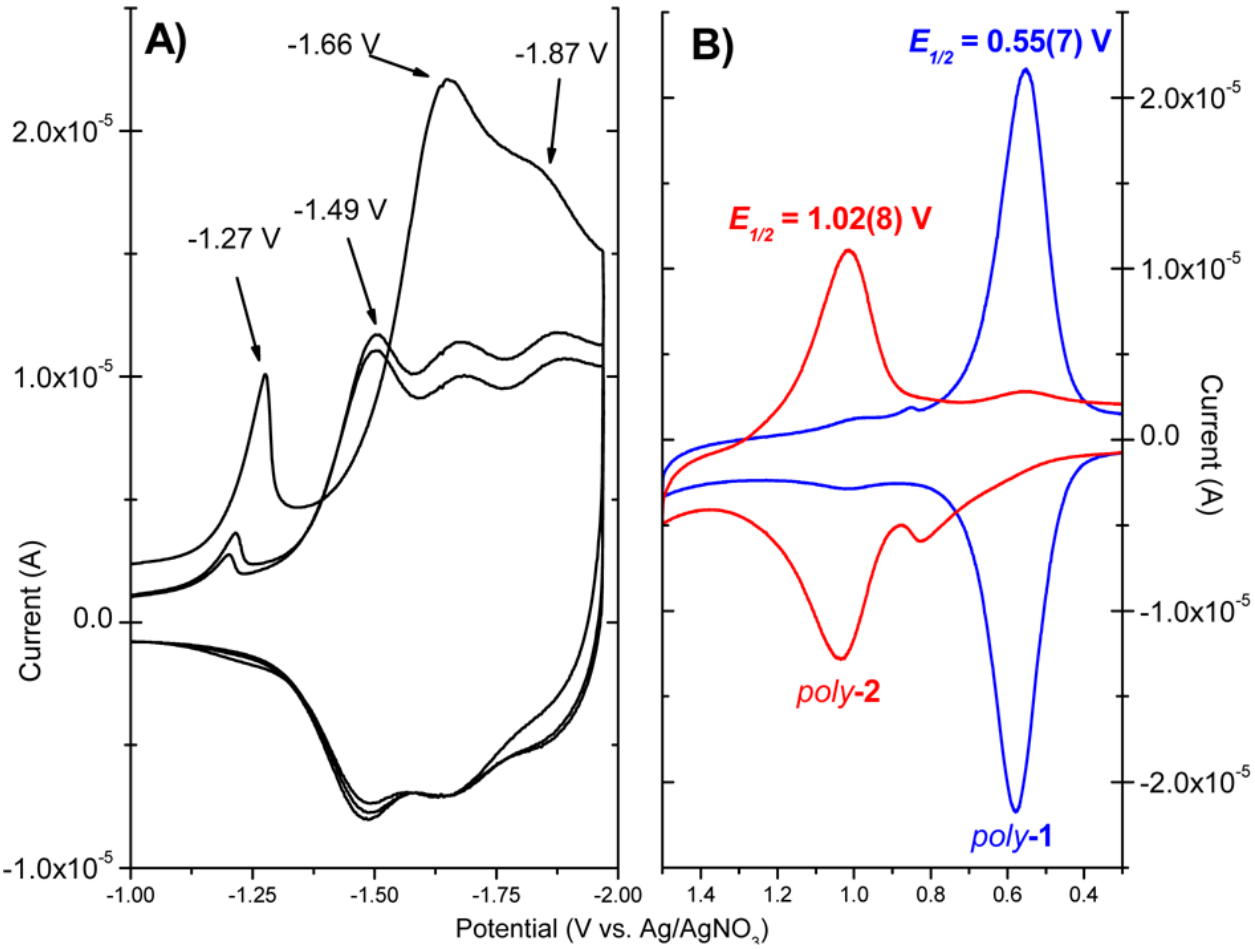

Figure 2.10. (A) Reductive CVs of poly-**1** under N_2 (black). (B) Oxidative CVs of a poly-**1** electrode prior to reductive cycling (blue; $\Gamma = 1.7 \times 10^{-9}$ mol cm^{-2}) and after reductive cycling (red). CVs in both (A) and (B) were obtained in fresh solutions of 0.1 M [TBA]PF_6/MeCN after electropolymerization on a 0.071-cm^2 GCE.

Equation 2.6

poly-Ru^{II}(Ph-tpy)(5,5'-dvbpy)$(Cl)^+ + 2e^- + MeCN \rightarrow$
poly-Ru^{II}(Ph-$tpy^{\bullet-}$)(5,5'-$dvbpy^{\bullet-}$)$(NCMe)^0 + Cl^-$

Equation 2.7

poly-Ru^{II}(Ph-$tpy^{\bullet-}$)(5,5'-$dvbpy^{\bullet-}$)$(NCMe)^0 - 2e^- \rightarrow$ poly-Ru^{II}(Ph-tpy)(5,5'-dvbpy)$(NCMe)^{2+}$

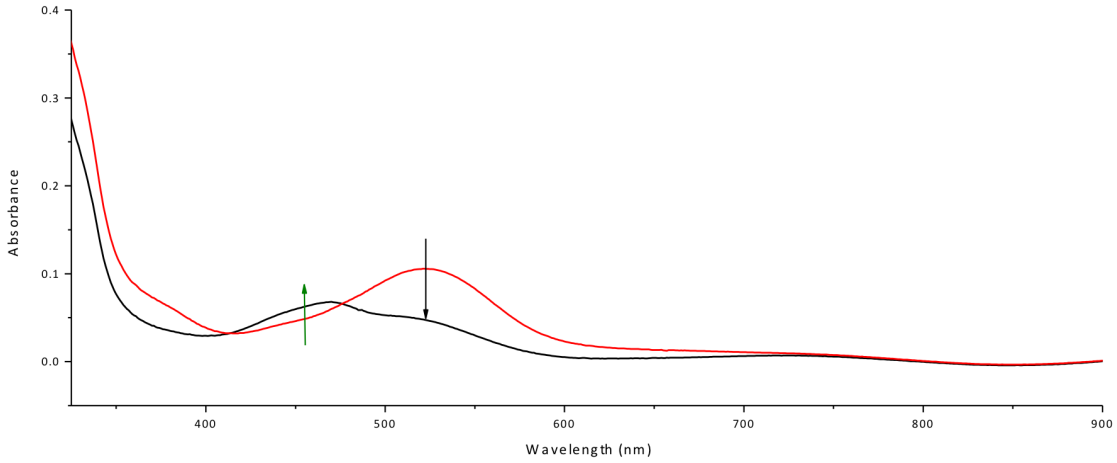

Figure 2.11. FTO slide (1-cm^2) of poly-**1** before (red) and after (black) reductive cycling under an atmosphere of N_2 between 0 and –1.97 V (vs. Ag/$AgNO_3$) three times. The black spectrum is a mixture of poly-**2** generated by ejection of the Cl^- ligand upon reduction and some residual poly-**1**.

Ligand-based reduction and substitution are accompanied by a loss of Faradaic response, with $\Gamma = 1.7 \times 10^{-9}$ mol cm^{-2} for the initial poly-**1** $Ru^{III/II}$ wave at $E_{1/2} = +0.56$ V decreasing to $\Gamma = 9.3 \times 10^{-10}$ mol cm^{-2} for the poly-**2** wave at $E_{1/2} = +1.03$ V. In addition, a new, distorted pre-wave appears at $E_{p,a} = +0.82$ V (**Figure 2.10**B). This observation points to a 46% decrease in the redox response at the end of three reductive scan cycles. A related response was observed for a thinner film of poly-**1** with $\Gamma = 4.5 \times 10^{-10}$ mol cm^{-2} before a reductive cycle and $\Gamma = 3.2 \times 10^{-10}$ mol cm^{-2} for poly-**2**, a 29% loss. Reductive cycling of poly-ONO_2 and poly-OH_2 both result in poly-**2** with comparable decreases in Γ (**Figure 2.12**). It is noteworthy that, after the initial exchange occurs with a loss of electroactivity, further decreases are greatly ameliorated upon additional reductive scan cycles.

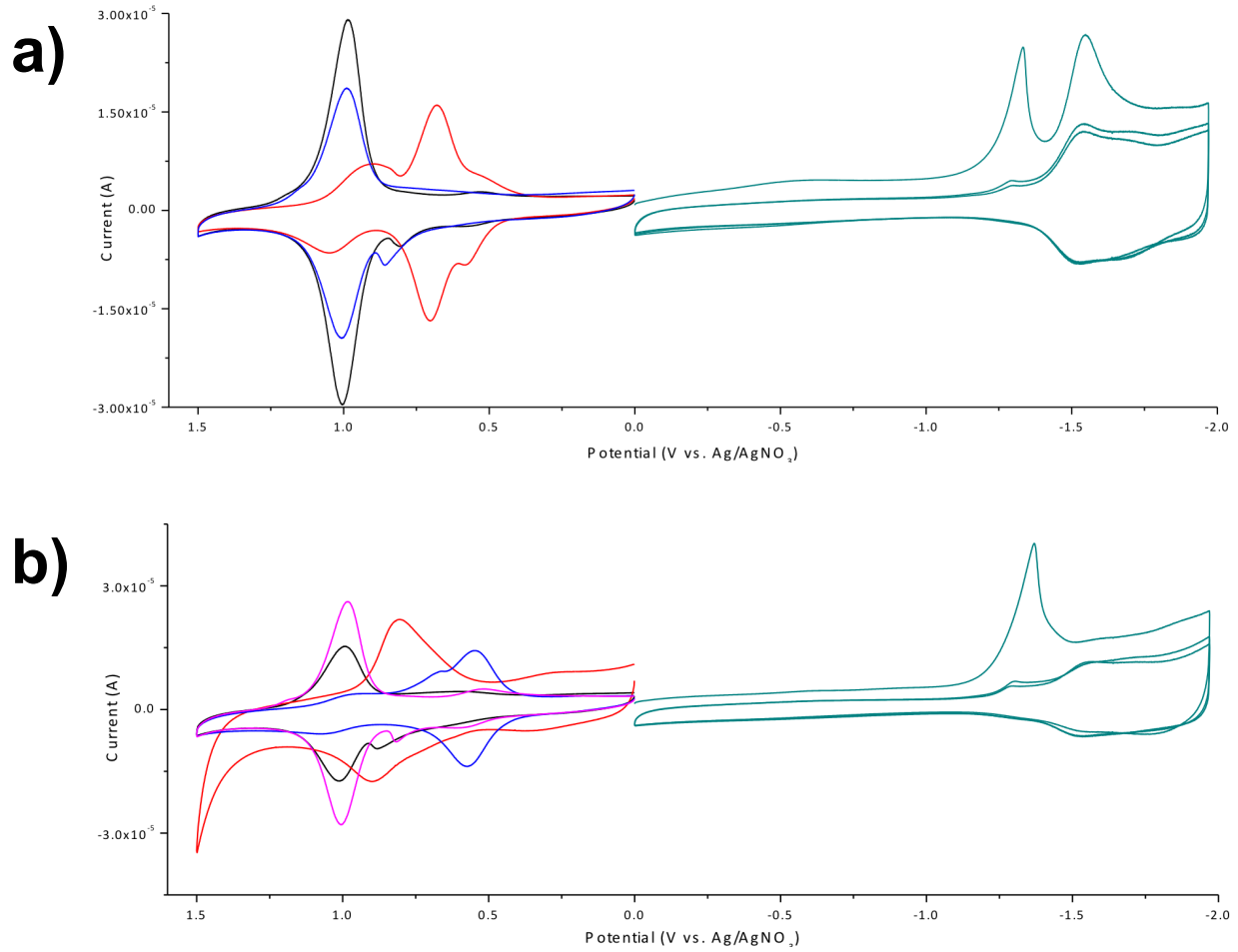

Figure 2.12. a) Reductive exchange of poly-ONO_2. Overlay of oxidative cycle of poly-**2** after electropolymerization (black), oxidative cycle of poly-ONO_2 (red) after nitrate exchange, reductive cycle of poly-ONO_2 under N_2 (turquoise), and oxidative cycle after regeneration of poly-**2** induced by reductive cycling of poly-ONO_2 (blue). b) Reductive exchange of poly-OH_2. Overlay of poly-**2** after electropolymerization (pink), oxidative cycle in 0.1 M $HClO_4$ after MeCN exchange for H_2O to generate poly-OH_2 (red), oxidative cycle of poly-OH_2 in MeCN (blue), reductive cycle of poly-OH_2 under N_2 (turquoise), and regeneration of poly-**2** after reductive cycling of poly-OH_2 (black). These experiments were performed at 100 mV s^{-1} scan rates on a 0.071-cm^2 GCE.

2.3. Conclusions

Our results are important in revealing systematic and synthetically exploitable features in the film-based coordination chemistries of poly-**1** and poly-**2** with significant differences between film and solution behavior. Polypyridyl complexes of $d\pi^6$ Ru^{II} typically undergo slow

loss of nitrile ligands. Nitrile ligands are weak σ donors and derive coordinative stability from dπ–π* back-bonding from Ru^{II}. With oxidation to Ru^{III}, back-bonding stabilization is no longer a factor, and nitriles become good leaving groups. Nitrile labilization was exploited here to convert poly-**2** into poly-ONO_2 and poly-OH_2.

The film environment also plays an important role. Following conversion of poly-**2** into poly-OH_2, there is no sign of substitution of H_2O for MeCN in poly-OH_2 or poly-Ru^{III}-OH_2^{3+} even over extended soaking or oxidative cycling periods in MeCN. This is a potentially important observation for possible applications in organic electrocatalysis based on Ru-oxo forms of poly-OH_2 with MeCN as the external solvent.[22] Oxidatively induced anation and aquation provide a basis for systematic manipulation of the coordination environment at the redox-active Ru^{II} sites in films. Ligand-based reduction offers a route to loss of anions or water in MeCN to return the films to the initial poly-**2** state.

2.4. Experimental

2.4.1. Materials

Solvents and chemicals were used as received unless otherwise noted. Solvents were obtained from Fisher Scientific; [TBA]PF_6 – Oakwood Products Inc.; [TEA]P – GFS Chemicals (TEA = tetra-n-ethylammonium); $RuCl_3$ - Pressure Chemical Company; $AgBF_4$ – Sigma-Aldrich Corporation; FTO – Hartford Glass Co. Inc.; Deuterated solvents were used as received from Cambridge Isotopes. Deionized water was further purified using a Milli-Q Ultrapure water purification system.

2.4.2. Instrumentation

Electrochemical measurements were conducted with a CH Instruments 660D potentiostat. UV-visible absorption spectra were recorded on an Agilent Technologies model 8453 diode-array spectrophotometer. ^1H and ^{13}C NMR spectra were collected on Bruker 400 (100), 500

(125), or 600 (150) MHz spectrometers. Elemental analyses (EA) were obtained from Atlantic Microlabs and agree to within 0.4 % for C. High resolution mass spectra (HRMS) were collected with an Agilent Technologies 6520, Accurate – Mass QTOF LCMS with 1200 series LC and Dual Spray ESI source with flow injection in positive ion mode. All values fall within the acceptable 5 ppm limit.

2.4.3. Electrochemical Analysis

Electrochemical experiments were performed in a three-compartment glass cell separated by medium or fine porosity frits. Unless otherwise noted, a glass-like carbon electrode was suspended in the center compartment with a septum containing two pre-drilled holes – one for the glass-like carbon electrode and one for the deaerating tube. In one outer compartment, a reference electrode was suspended in a septum containing two pre-drilled holes – one for the reference electrode and one for a deaerating tube. In the remaining outer compartment, platinum wire or gauze was threaded through a septum adjacent to a deaerating tube and served as the counter electrode. Prior to use, the cells were cleaned by sonication in MeCN for 15 minutes, rinsed with MeCN, and dried with a heat gun. Upon cooling, the appropriate solutions were placed in their respective compartments. For solutions where reductive potentials were applied (i.e. during electropolymerizations or film reductive cycling), fresh electrolytic solutions were prepared by dissolving the appropriate amount of [TBA]PF_6 (tetra-n-butylammonium hexafluorophosphate) or [TEA]P (tetra-n-ethylammonium perchlorate) to make 0.1 M solutions in MeCN (Optima), dried over 3 Å molecular sieves. The solutions were deaerated with Ar for a minimum of 5 minutes after the Ar flowed through gas washers containing MeCN. For solutions where oxidative cycling was needed, no special drying was used for the 0.1 M electrolyte solution and the experiments were performed open to the air. For this report, two glass-like carbon electrodes purchased from CH Instruments were used for all experiments. At the end of

the experiments, the glass-like carbon electrodes were polished for ~10 seconds with 0.3 μm alumina polish on a polishing pad, rinsed with water followed by MeCN, and allowed to air dry prior to the next polymerization that was performed. Electrochemical experiments performed in non-aqueous media (i.e. MeCN) employed a $Ag/AgNO_3$ reference electrode; those in aqueous media (i.e. 0.1 M $HClO_4$) employed a Ag/AgCl which was shifted to SCE (E(SCE) = +0.045 V vs. Ag/AgCl). Prior to performing non-aqueous electrochemical experiments, the Ag wire reference electrode solution was replaced with a stock solution of 10 mM $AgNO_3$ in 0.1 M [TBA]PF_6/MeCN. The $E_{1/2}$ of 1 mM $FeCp_2$ in 0.1 M [TBA]PF_6/MeCN with this reference electrode was +0.094 V (ΔE_p = 75 mV); thus, subtract 94 mV of the reported potentials to reference vs. $FeCp_2$.

Surface coverage (Γ) was calculated via **Equation 2.1**, where n is the number of electrons passed per redox couple (moles e^-), F is Faraday's constant (96,485 C mol^{-1}), A is the area of the electrode (cm^2), and Q is the accumulated charge (i.e. integrated charge) for the surface couples (in C) after nine oxidative cycles in 0.1 M [TBA]PF_6/MeCN calculated via **Equation 2.2**.

Fluorine-doped tin oxide (FTO) was cleaned by four cycles of sonication of 20 minutes each (isopropanol, isopropanol, water, water), followed by drying under air.

2.4.4. Synthetic Procedures

5,5'-divinyl-2,2'-bipyridine (5,5'-dvbpy). 5,5'-dvbpy was prepared with slight modification of a previously-published procedure.[23] In a 100-mL round-bottom flask, 5,5'-bis(bromomethyl)-2,2'-bipyridine (2.5 g, 7.3 mmol) and triphenylphosphine (5.0 g, 19 mmol) were stirred in *N,N'*-dimethylformamide (40 mL) under a nitrogen atmosphere at 90 °C for 8 hours. After cooling, the tan precipitate was collected and washed with diethyl ether. This

precipitate was added to a clean 100-mL round-bottom flask, along with 37% aqueous formaldehyde (13 mL) and dichloromethane (40 mL). This solution was cooled to 0 °C. Using a pressure equilibrating addition funnel under a nitrogen atmosphere, 10% aqueous NaOH (21 mL) was added over 1 hour. The solution was brought to room temperature, covered with aluminum foil, and left to stir overnight under a nitrogen atmosphere. The yellow mixture was diluted with water (50 mL) and extracted with dichloromethane (3 × 30 mL). The organic fractions were combined and washed with a saturated brine solution (2 × 30 mL) before being dried over anhydrous $MgSO_4$. Excess solid was removed by gravity filtration, and the solvent was removed to dryness. Concentration of the first band following silica gel column chromatography (petroleum ether:ethyl acetate 1:1) gave the light-yellow product (0.51 g, 2.4 mmol, 34% yield).

4'-phenyl-2,2':6',2''-terpyridine (Ph-tpy). Ph-tpy was synthesized according to a two-part procedure modified from the literature.[24] Part 1 (Synthesis of 3-phenyl-1,5-di(pyridin-2-yl)pentane-1,5-dione, **Int1**): Benzaldehyde (12.2 mL, 12.7 g, 0.120 mol) was added to a flask containing 126 mL of absolute EtOH and 90 mL of H_2O followed by 2-acetylpyridine (30.1 mL, 32.5 g, 0.268 mol). NaOH (7.2 g, 0.18 mol) was added to the reaction solution and the solution rapidly turned red. Within one to two minutes a white solid began to precipitate. After stirring the heterogeneous solution for 1 hour the white precipitate was collected on a 2 L medium porosity fritted funnel, washed with cold (–78 °C) EtOH, and air-dried (**Int1**, 35.0 g, 0.106 mol, 88% yield). Part 2 (Ph-tpy synthesis): **Int1** (17.5 g, 0.0530 mol) was added to a solution of EtOH (500 mL) followed by NH_4OAc (35 g, 0.45 mol). The heterogeneous solution was brought to reflux and allowed to stir. After 37 hours, the solution became homogeneous and yellow. It was allowed to cool and a yellow precipitate formed. The precipitate was collected on a medium porosity fritted funnel, washed with EtOH, and air-dried (7.8 g, 0.025 mol, 48% yield). The

filtrate was diluted with 500 mL H_2O and more yellow precipitate formed. The solid was collected on a medium porosity fritted funnel, rinsed with a minimal amount of EtOH, and air-dried (1.5 g, 4.8 mmol, 9% yield). Both crops were pure via NMR and matched previously published chemical shifts.[24]

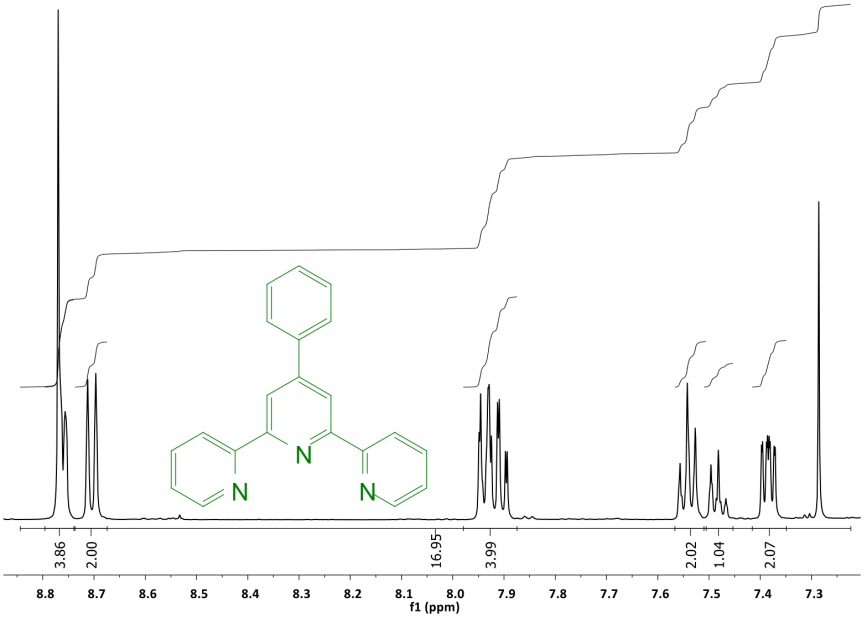

*[Ru(Ph-tpy)(5,5'-dvbpy)(Cl)][PF_6], **1***. In a CEM HP-500 Plus Teflon-coated microwave vessel, [(Ph-tpy)Ru(Cl)(μ-Cl)]$_2$ (50.6 mg, 0.0526 mmol) and 5,5'-dvbpy (23.7 mg, 0.114 mmol) were suspended in an EtOH (44 mL) and H_2O (14 mL) mixture. This suspension was placed in a microwave reactor where, following a ramping period (5 minutes), it was heated at 150 °C for 15 minutes. After cooling, the solution was transferred to a 100-mL round-bottom flask, and concentrated aqueous NH_4PF_6 (approximately 2 mL) was added to the flask. The solution was concentrated on a rotary evaporator until a precipitate was observed to form. The mixture was filtered, washed with water (twice), followed by diethyl ether (thrice) before being collected (63.4 mg, 76%). ^{1}H NMR (400 MHz, CD_3CN): δ 10.24 (d, 1H, J = 2 Hz), 8.75 (s, 2H), 8.55-8.50

(m, 3H), 8.36-8.34 (dd, 1H, J = 8.5 Hz, 2 Hz), 8.25-8.23 (d, 1H, J = 8.5 Hz), 8.13-8.10 (m, 2H), 7.90-7.86 (dt, 2H, J = 8 Hz, 1.5 Hz), 7.82-7.79 (dd, 1H, J = 8.6 Hz, 2 Hz), 7.72-7.68 (m, 4H), 7.62-7.59 (m, 1H), 7.29-7.23 (m, 3H), 7.13-7.06 (dd, 1H, J = 17 Hz, 11 Hz), 6.37-6.30 (dd, 1H, J = 17.6 Hz, 11 Hz), 6.28-6.23 (d, 1H, J = 17.6 Hz), 5.72-5.66 (m, 2H), 5.30-5.27 (d, 1H, J = 11 Hz). ^{13}C $\{^{1}H\}$ NMR (125.8 MHz, CD_3CN): δ 159.8, 159.0, 158.5, 155.9, 153.4, 151.7, 151.1, 147.1, 138.1, 137.9, 137.0, 136.3, 133.5, 132.2, 132.0, 130.9, 130.4, 128.6, 128.1, 124.7, 124.2, 124.0, 121.6, 120.1, 120.1. Elemental Analysis: Predicted C 52.61, H 3.41, N 8.76. Found C 52.37, H 3.66, N 8.91; HR-MS: Expected $[M - PF_6]^+$ = 654.1006, Found $[M - PF_6]^+$ = 654.0998, ppm diff: 1.2. E-chem: $E_{1/2}(Ru^{III/II})$ = +0.49(9) V vs. $Ag/AgNO_3$, ΔE_p = 72 mV. UV-Vis: λ_{MLCT} = 528 nm (ε = 12,450 L mol^{-1} cm^{-1}).

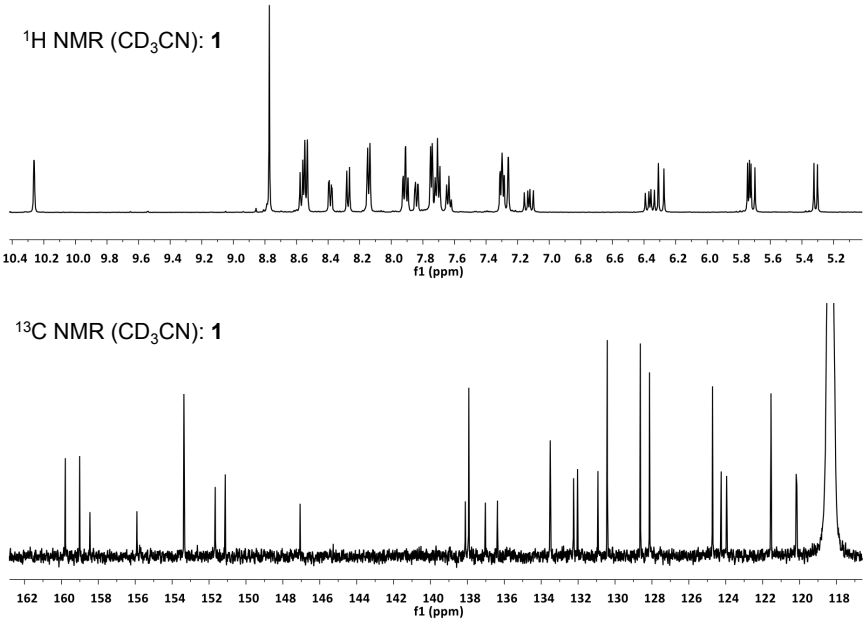

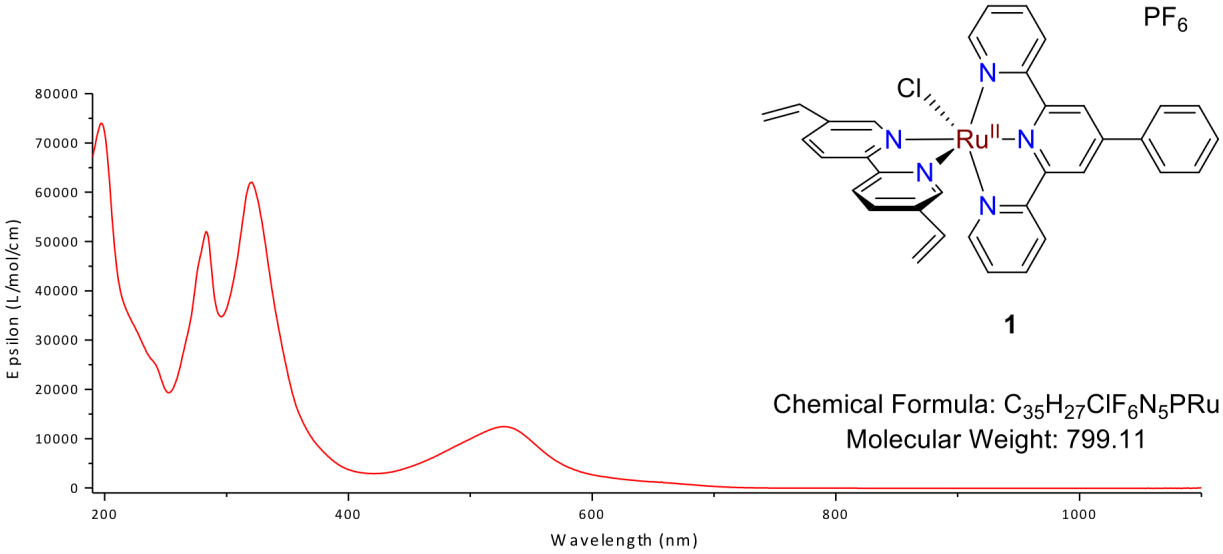

*[Ru(Ph-tpy)(5,5'-dvbpy)(CH$_3$CN)][PF$_6$]$_2$, **2**:* In a 25-mL round-bottom flask, Ru(Ph-tpy)(5,5'-dvbpy)(Cl)[PF$_6$] (58.8 mg, 0.0736 mmol) was dissolved in acetonitrile (7 mL). The solution was deaerated with argon (10 minutes). A solution of AgBF$_4$ (43 mg, 3 equivalents) in acetonitrile (1 mL) was added to the flask. The flask was covered and heated at reflux overnight. The solution was filtered hot over Celite. Aqueous NH$_4$PF$_6$ (1.0 g in 15 mL H$_2$O) was added to the filtrate. The volume of the solution was reduced on a rotary evaporator, and the remaining volume was cooled overnight. The mixture was filtered, and the orange precipitate washed with water and ether before being collected (51.9 mg, 0.0547 mmol, 74%). ^{1}H NMR (600 MHz, CD$_3$CN): δ 9.53-9.52 (d, 1H, J = 1.8 Hz), 8.83 (s, 2H), 8.60-8.57 (m, 3H), 8.46-8.44 (dd, 1H, J = 8.6 Hz, 2.0 Hz), 8.32-8.31 (d, 1H, J = 8.6 Hz), 8.16-8.15 (dd, 2H, J = 7.2 Hz, 1.3 Hz), 8.06-8.03 (td, 2H, J = 7.8 Hz, 1.4 Hz), 7.96-7.95 (dd, 1H, J = 8.5 Hz, 1.8 Hz), 7.77-7.73 (m, 4H), 7.68-7.66 (m, 1H), 7.39-7.36 (m, 2H), 7.22 (d, 1H, J = 1.8 Hz), 7.16-7.12 (dd, 1H, J = 17.7 Hz, 11.0 Hz), 6.41-6.33 (m, 2H), 5.78-5.71 (m, 2H), 5.35-5.33 (d, 1H, J = 11.1 Hz), 2.11 (s, 3H, CH$_3$- of CH$_3$CN). ^{13}C {1H} NMR (150.9 MHz, CD$_3$CN): δ 159.5, 158.7, 157.3, 155.5, 154.3, 151.8,

150.2, 139.5, 137.8, 137.6, 136.9, 134.4, 134.0, 132.9, 131.9, 131.5, 130.6, 128.8, 128.8, 126.2, 125.5, 124.9, 124.3, 122.6, 121.1, 120.6, 4.6. Elemental Analysis: **2**·0.5H_2O: Predicted C 46.35, H 3.26, N 8.77. Found C 46.49, H 3.32, N 8.62; HR-MS: Expected $[M - 2PF_6 - MeCN]^{2+}$ = 619.1321, Found $[M - 2PF_6 - MeCN]^{2+}$ = 619.1310, ppm diff: 1.7. E-chem: $E_{1/2}(Ru^{III/II})$ = +0.99(2) V vs. $Ag/AgNO_3$, ΔE_p = 73 mV. UV-Vis: λ_{MLCT} = 472 nm (ε = 13,300 L mol^{-1} cm^{-1}).

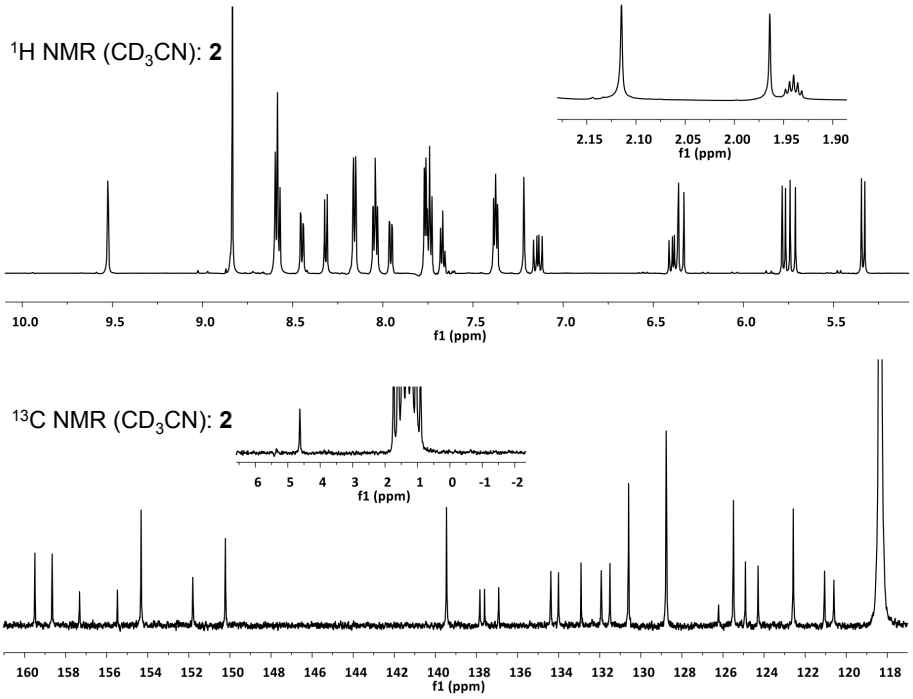

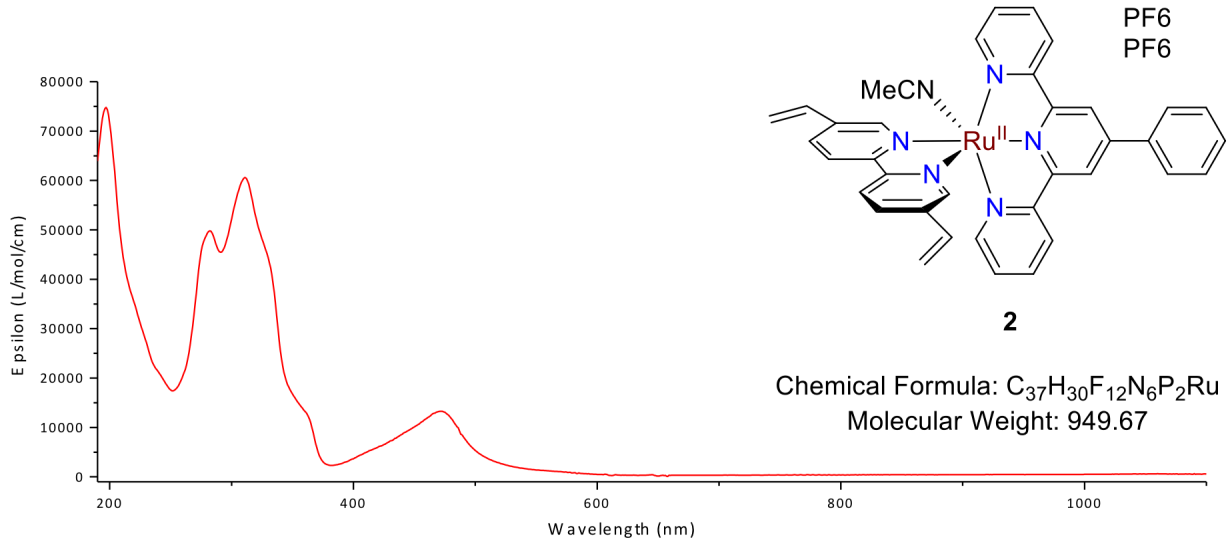

2.5. Acknowledgements

D.P.H. acknowledges support from the U.S. Department of Energy Office of Science, Office of Basic Energy Sciences, under Award DE-FG02-06ER15788 and the Virginia Military Institute. A.M.L., R.A.B., and J.J.C. acknowledge support from the UNC Energy Frontier Research Center (EFRC): Center for Solar Fuels, an Energy Frontier Research Center funded by the U.S. Department of Energy, Office of Science, Office of Basic Energy Sciences, under Award DE-SC0001011. M.A.M. acknowledges support by the Center for Catalytic Hydrocarbon Functionalization, an EFRC, funded by the U.S. Department of Energy, Office of Science, Office of Basic Energy Sciences, under Award DE-SC0001298. We also acknowledge support for the purchase of instrumentation from the UNC EFRC: Center for Solar Fuels (award DE-SC0001011), and from UNC SERC ("Solar Energy Research Center Instrumentation Facility" funded by the US Department of Energy – Office of Energy Efficiency & Renewable Energy under Award Number DE-EE0003188).

REFERENCES

(1) Calvert, J. M.; Schmehl, R. H.; Sullivan, B. P.; Facci, J. S.; Meyer, T. J.; Murray, R. W. *Inorg. Chem.* **1983**, *22*, 2151.

(2) Gould, S.; Gray, K. H.; Linton, R. W.; Meyer, T. J. *Inorg. Chem.* **1992**, *31*, 5521.

(3) Devenney, M.; Worl, L. A.; Gould, S.; Guadalupe, A.; Sullivan, B. P.; Caspar, J. V.; Leasure, R. L.; Gardner, J. R.; Meyer, T. J. *J. Phys. Chem. A* **1997**, *101*, 4535.

(4) Moss, J. A.; Argazzi, R.; Bignozzi, C. A.; Meyer, T. J. *Inorg. Chem.* **1997**, *36*, 762.

(5) Moss, J. A.; Yang, J. C.; Stipkala, J. M.; Wen, X.; Bignozzi, C. A.; Meyer, G. J.; Meyer, T. J. *Inorg. Chem.* **2004**, *43*, 1784.

(6) O'Toole, T. R.; Margerum, L. D.; Westmoreland, T. D.; Vining, W. J.; Murray, R. W.; Meyer, T. J. *J. Chem. Soc., Chem. Commun.* **1985**, 1416.

(7) Ramos Sende, J. A.; Arana, C. R.; Hernandez, L.; Potts, K. T.; Keshevarz-K, M.; Abruna, H. D. *Inorg. Chem.* **1995**, *34*, 3339.

(8) Cosnier, S.; Deronzier, A.; Moutet, J. C. *J. Mol. Catal.* **1988**, *45*, 381.

(9) Abruña, H. D.; Denisevich, P.; Umana, M.; Meyer, T. J.; Murray, R. W. *J. Am. Chem. Soc.* **1981**, *103*, 1.

(10) Yang, J.; Sykora, M.; Meyer, T. J. *Inorg. Chem.* **2005**, *44*, 3396.

(11) Cosnier, S.; Deronzier, A.; Moutet, J. C. *J. Electroanal. Chem. Interfacial Electrochem.* **1986**, *207*, 315.

(12) Deronzier, A.; Eloy, D.; Jardon, P.; Martre, A.; Moutet, J. C. *J. Electroanal. Chem.* **1998**, *453*, 179.

(13) Mola, J.; Mas-Marza, E.; Sala, X.; Romero, I.; Rodríguez, M.; Viñas, C.; Parella, T.; Llobet, A. *Angew. Chem., Int. Ed.* **2008**, *47*, 5830.

(14) Cheung, K. C.; Guo, P.; So, M. H.; Zhou, Z. Y.; Lee, L. Y. S.; Wong, K. Y. *Inorg. Chem.* **2012**, *51*, 6468.

(15) Concepcion, J. J.; Jurss, J. W.; Brennaman, M. K.; Hoertz, P. G.; Patrocinio, A. O. v. T.; Murakami Iha, N. Y.; Templeton, J. L.; Meyer, T. J. *Acc. Chem. Res.* **2009**, *42*, 1954.

(16) Chen, Z.; Concepcion, J. J.; Jurss, J. W.; Meyer, T. J. *J. Am. Chem. Soc.* **2009**, *131*, 15580.

(17) Nie, H. J.; Shao, J. Y.; Wu, J.; Yao, J.; Zhong, Y. W. *Organometallics* **2012**, *31*, 6952.

(18) Abruña, H. D. *Coord. Chem. Rev.* **1988**, *86*, 135.

(19) Takeuchi, K. J.; Thompson, M. S.; Pipes, D. W.; Meyer, T. J. *Inorg. Chem.* **1984**, *23*, 1845.

(20) Meyer, T. J.; Huynh, M. H. V. *Inorg. Chem.* **2003**, *42*, 8140.

(21) Gagliardi, C. J.; Vannucci, A. K.; Concepcion, J. J.; Chen, Z.; Meyer, T. J. *Energy Environ. Sci.* **2012**, *5*, 7704.

(22) Vannucci, A. K.; Chen, Z.; Concepcion, J. J.; Meyer, T. J. *ACS Catal.* **2012**, *2*, 716.

(23) Liu, Y.; Zhang, S.; Miao, Q.; Zheng, L.; Zong, L.; Cheng, Y. *Macromolecules* **2007**, *40*, 4839.

(24) Moya, S. A.; Pastene, R.; Le Bozec, H.; Baricelli, P. J.; Pardey, A. J.; Gimeno, J. *Inorganica Chimica Acta* **2001**, *312*, 7.

CHAPTER 3: STABILIZATION OF A RUTHENIUM(II) POLYPYRIDYL DYE ON NANOCRYSTALLINE TiO_2 BY AN ELECTROPOLYMERIZED OVERLAYER

3.1. Introduction

Stable surface binding of chromophores, catalysts, and chromophore-catalyst assemblies on metal oxide surfaces is an essential element in dye-sensitized photoelectrosynthesis cells (DSPECs) for solar fuel production.[1-5] In a DSPEC for water oxidation, photoexcitation of a chromophore, or dye, followed by excited-state electron injection into the conduction band of a wide bandgap semiconductor, typically TiO_2 or SnO_2, provides the basis for a photoanode.[2] Oxidative equivalents (a.k.a. holes) produced by electron injection are subsequently transferred to a catalyst for water oxidation. The injected electrons are transferred to a cathode for reduction of either water to H_2 or CO_2 to carbon-containing fuels.[6,7] The design of water oxidation DSPEC photoanodes is particularly challenging because of the need to integrate both light absorption and catalysis at the oxide interface. The resulting interfacial structures must be stable under irradiation while supporting high numbers of turnovers in aqueous environments.[8,9]

A number of strategies for binding chromophores and catalysts to metal oxide surfaces have been reported. They include co-deposition,[10,11] preformed assemblies,[12,13] and self-assembled bilayers.[14] These strategies are often limited by difficult synthetic procedures. The stability of the films, critical in all applications, is limited by the nature of the link to the surface. Although often used successfully in non-aqueous solvents, carboxylate-surface binding is

unstable in water. Phosphonate-surface binding is far more robust but typically subject to hydrolysis from the surface at pH 5 and above.[8,9,15]

Oxidative or reductive electropolymerization provides a potentially useful strategy for preparing stable, multiple component films.[16-21] Reductive electropolymerization of vinyl-derivatized monomers is especially well developed.[22-29] In these reactions, electrochemical reduction of the vinyl-group induces radical polymerization and C–C coupling and bond formation.[23] On planar electrode surfaces, two or more redox carriers have been incorporated into spatially-segregated co-polymeric films by sequential reductive cycling in distinct monomer solutions, and into integrated co-polymeric films prepared by cycling in a single solution containing multiple monomers.[22,24,30]

Despite the impressive background on planar electrodes, few reports have appeared describing electropolymerization on nanocrystalline metal oxide films.[26,27] In one notable example, Moss et al. demonstrated reductive electropolymerization of an overlayer of $[Ru(vbpy)_3]^{2+}$ (vbpy = 4-vinyl-4'-methyl-2,2'-bipyridine) on $[Ru(4,4'\text{-dcbpy})(vbpy)_2]^{2+}$ (4,4'-dcbpy = 2,2'-bipyridine-4,4'-dicarboxylic acid) that had been prebound to nanocrystalline TiO_2 (*nano*TiO_2). Significant increases in thermal stability for the surface-bound complex were observed even in basic media with no loss of chromophore over a three week period under conditions where the unprotected surface-bound complex underwent complete desorption in minutes.[26] The photostability and photophysical properties of the resulting overlayer structures were relatively unexplored.[9]

The electropolymerized overlayer approach to surface assembly stabilization is promising. We report here the synthesis and characterization, including photostability and photophysical measurements, on multicomponent films on mesoporous *nano*TiO_2 prepared by

reductive overlayer electropolymerization. The films were prepared by first derivatizing mesoporous *nano*TiO_2 with [Ru(5,5'-divinyl-2,2'-bipyridine)$_2$(4,4'-dpbpy)]$^{2+}$ (**RuPdvb** in **Figure 3.1**a, 4,4'-dpbpy = [2,2'-bipyridine]-4,4'-diylbis(phosphonic acid)) followed by reductive electropolymerization of [Fe(4'-vinyl-2,2':6':2"-terpyridine)$_2$]$^{2+}$ ([**Fe(v-tpy)$_2$**]$^{2+}$ in **Figure 3.1**a) to generate an electropolymerized overlayer. A scheme illustrating the formation of the *nano*TiO_2|-**RuPdvb**-*poly*-[**Fe(v-tpy)$_2$**]$^{2+}$ overlayer structure is shown in **Figure 3.1**b.

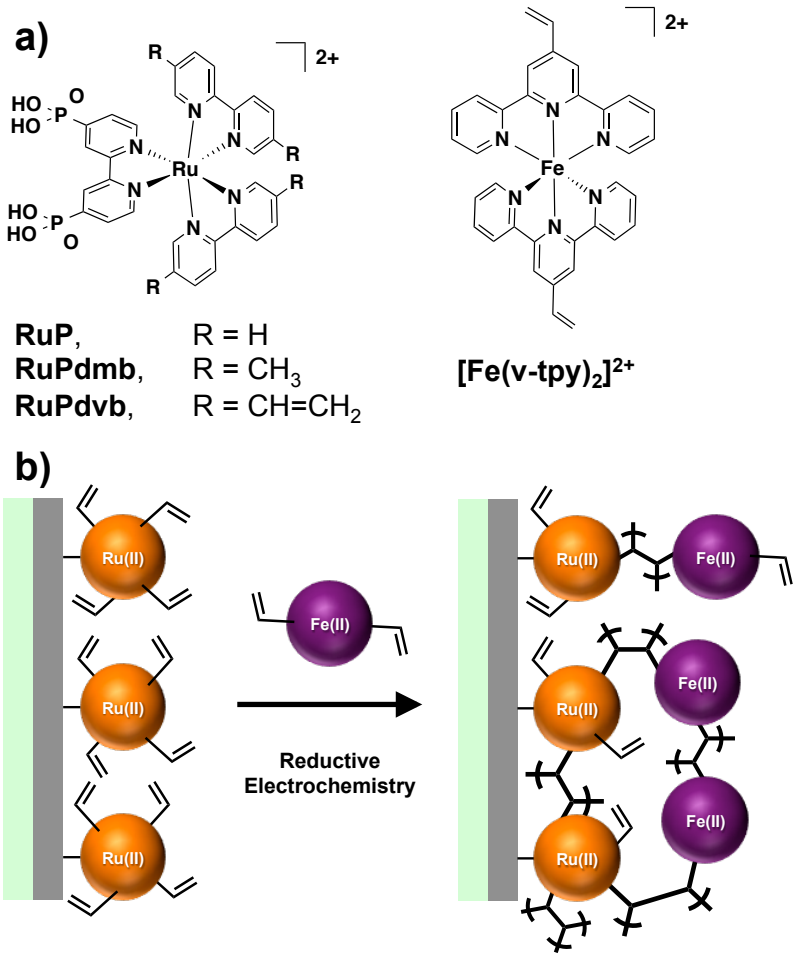

Figure 3.1. (a) Structures of **RuP**, **RuPdmb**, **RuPdvb**, and [**Fe(v-tpy)$_2$**]$^{2+}$. (b) Schematic diagram of the surface structure following reductive electropolymerization of [**Fe(v-tpy)$_2$**]$^{2+}$ on *nano*TiO_2|-**RuPdvb**.

3.2. Results and Discussion

3.2.1. Monomer Synthesis and Characterization

The structures of the complexes investigated in this study are shown in **Figure 3.1**a. They were synthesized as chloride (Ru^{II} complexes) and hexafluorophosphate ($[\mathbf{Fe(v\text{-}tpy)_2}]^{2+}$) salts. $[\mathbf{Fe(v\text{-}tpy)_2}]^{2+}$ and **RuP** were synthesized by previously reported procedures.[25,31] **RuPdvb** and **RuPdmb** were synthesized by literature procedures with minor modification.[31] The starting complex, $Ru(5,5'\text{-}(R)_2\text{-}bpy)_2Cl_2$ (R = CH_3 or $CH{=}CH_2$) was synthesized by heating $[Ru(1,4\text{-}cyclooctadiene)Cl_2]_n$ and the bipyridine precursors in *o*-dichlorobenzene to 160 °C. The dichloride complexes were subsequently reacted with one equivalent of tetraethyl [2,2'-bipyridine]-4,4'-diylbis(phosphonate) in a microwave reactor. The ethyl esters were then hydrolyzed using bromotrimethylsilane in anhydrous acetonitrile to give the unprotected phosphonic acids. **RuPdvb** and **RuPdmb** were isolated as their chloride salts in 86% and 80% yield, respectively.

RuPdvb contains one phosphonated bipyridine ligand for binding to metal oxide surfaces and two bipyridine ligands with vinyl groups in the 5,5' positions for electropolymerization. $[\mathbf{Fe(v\text{-}tpy)_2}]^{2+}$ was selected as the monomer precursor for the polymer overlayer because of its readily discernible photophysical and electrochemical properties compared to **RuPdvb**. Following electropolymerization the vinyl groups of **RuPdvb** are converted by C–C coupling into saturated alkyl substituents.[23] Alkyl-substituted **RuPdmb** (R = CH_3 in **Figure 3.1**a) was used as a model for the surface bound chromophore following electropolymerization. **RuP** was used as the benchmark chromophore for transient absorption and photostability experiments because its properties are well understood.[8,9]

In aqueous solutions, the absorption spectra for **RuP**, **RuPdvb** and **RuPdmb** all feature characteristic, intense π–π^* absorptions below 350 nm and lower energy metal-to-ligand charge-

transfer (MLCT) absorptions from 400 to 500 nm (**Table 3.1**, **Figure 3.2**). The slight blue-shift in absorption for **RuPdvb** and red-shift in absorption for **RuPdmb** relative to **RuP** is due to stabilization/destabilization effects in the $d\pi^5\pi^*$ MLCT excited states by the electron-withdrawing vinyl and -donating methyl groups, respectively. $[\mathbf{Fe(v\text{-}tpy)_2}]^{2+}$ has an MLCT absorption band maximum at 565 nm (ε = 15,500 M^{-1} cm^{-1}, **Figure 3.2**).

Table 3.1. Photophysical and Surface Binding Parameters for **RuP**, **RuPdvb**, **RuPdmb**, and $[\mathbf{Fe(v\text{-}tpy)_2}]^{2+}$ in Solution and on Metal Oxide Films.

Complex	MLCT, λ_{max} (nm) (ε, M^{-1} cm^{-1})[a]	Γ_{max} (mol cm^{-2})	K_{ad} (M^{-1})
RuP	458 (12,700)	8.5×10^{-8}	3.9×10^{4}
RuPdvb	476 (13,300)	6.7×10^{-8}	2.2×10^{4}
RuPdmb	453 (13,500)	5.2×10^{-8}	5.2×10^{4}
$[\mathbf{Fe(v\text{-}tpy)_2}]^{2+}$	565 (15,500)	–	–

[a] In H_2O.

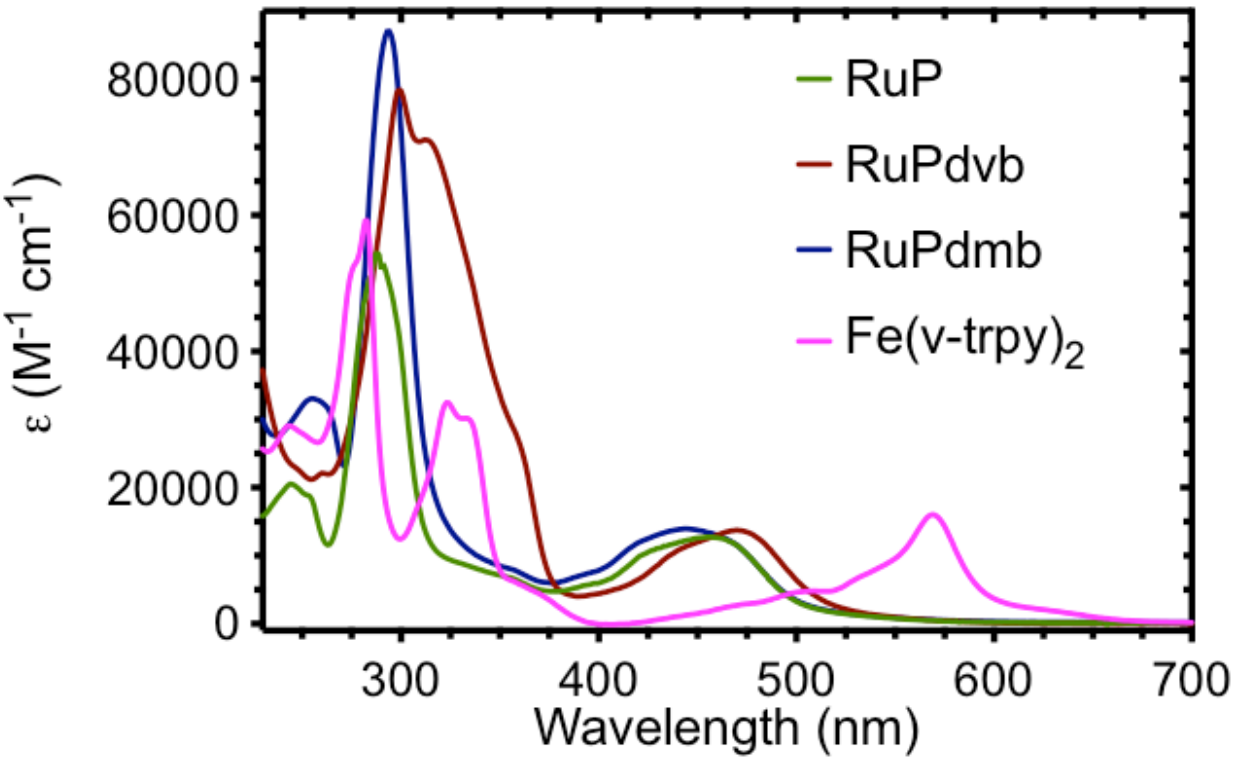

Figure 3.2. UV-visible absorption spectra of **RuP**, **RuPdvb**, **RuPdmb**, and $[\mathbf{Fe(v\text{-}tpy)_2}]^{2+}$ in H_2O.

Table 3.2. Photophysical and Electrochemical Parameters for **RuP**, **RuPdvb**, **RuPdmb**, and $[\mathbf{Fe(v\text{-}tpy)_2}]^{2+}$ on Metal Oxide Films.

Complex	$E_{1/2}$ ($Ru^{III/II}$) (V vs. $Ag/AgNO_3$)[a]	$E_{1/2}$ ($Ru^{III/II}$) (V vs. NHE)[b]	ΔG_{ES} (eV)[c]	$E^{\circ\prime}$ ($Ru^{III/II*}$)[e] (V vs. NHE)
RuP	1.02	1.28	2.04	-0.76
RuPdvb	1.12	1.34	2.02	-0.68
RuPdmb	0.94	1.22	2.06	-0.84
$[\mathbf{Fe(v\text{-}tpy)_2}]^{2+}$	0.79 ($Fe^{III/II}$)	–	*d*	–

[a]In 0.1 M $[TBA]PF_6/CH_3CN$; planar FTO working, Pt counter, and $Ag/AgNO_3$ (–0.09 V vs. $Fc^{0/+}$) reference electrodes. [b]In aqueous 0.1 M $HClO_4$, *nano*TiO_2 working, Pt counter, and Ag/AgCl (0.198 V vs. NHE) reference electrodes. [c]ΔG_{ES} from spectral fitting of emission on ZrO_2 in aqueous 0.1 M $HClO_4$. [d]Emission was not observed. [e]$E^{\circ\prime}(Ru^{III/II*}) = E_{1/2}(Ru^{III/II}) - \Delta G_{ES}$.

3.2.2. Surface Loading

Adsorption isotherms were measured by immersing *nano*TiO_2 films (~7 μm thickness) in 10 mL solutions of 10, 20, 50, 100, 150, and 200 μM **RuP**, **RuPdvb**, and **RuPdmb** in methanol. Adsorption isotherms (**Figure 3.3**) were analyzed by the Langmuir isotherm model **Equation 3.1**; details in Experimental).[32] Adsorption constants (K_{ad}) and maximum surface coverages (Γ_{max}) were similar for all three complexes; the results are summarized in **Table 3.1**.

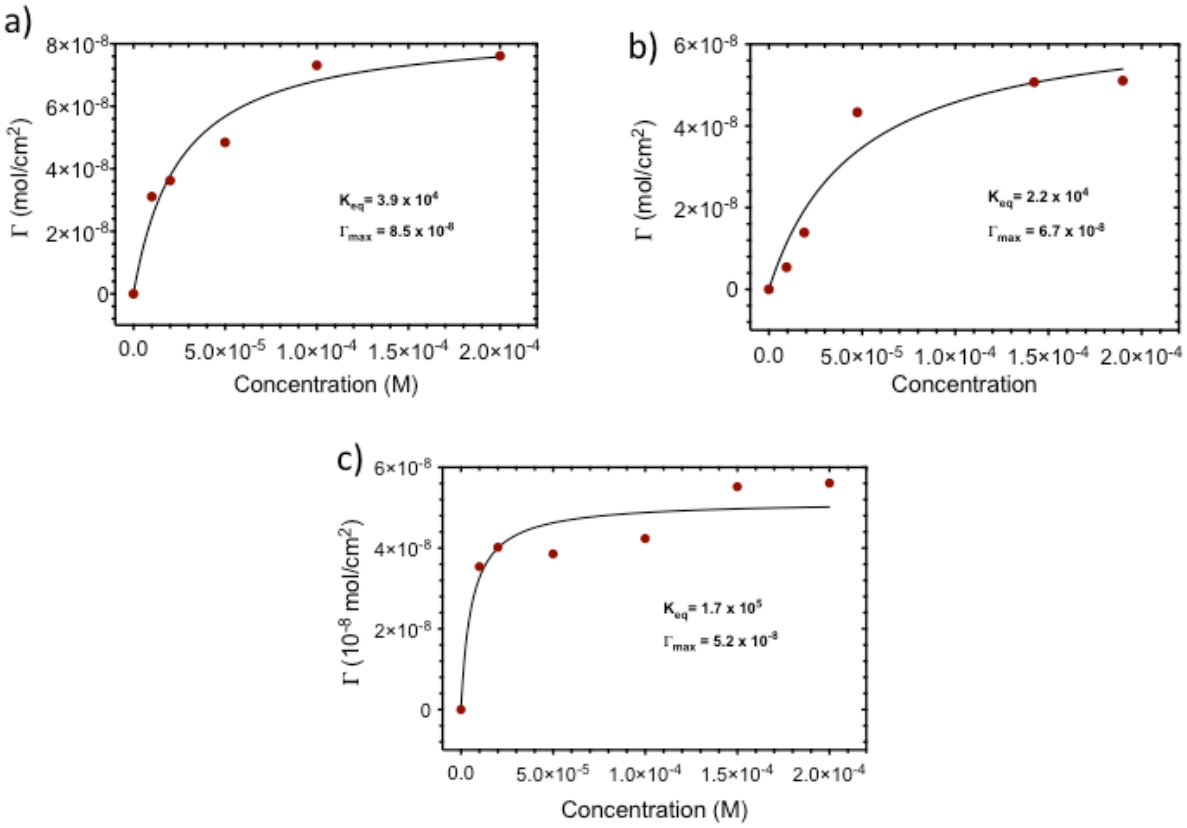

Figure 3.3. Adsorption isotherm for a) **RuP**, b) **RuPdvb**, and c) **RuPdmb** on *nano*TiO_2 (~7 μm) loaded from 10, 20, 50, 100, 150, 200 mM solutions in methanol. The black lines are the best fits to the Langmuir isotherm equation.

Equation 3.1

$$\Gamma = \Gamma_{max} \frac{K_{ad}[X]}{1 + K_{ad}[X]}$$

3.2.3. Surface Characterization

The electrochemical properties of **RuP**, **RuPdvb**, and **RuPdmb** on *nano*TiO_2 were examined by cyclic voltammetry (CV) and square-wave voltammetry (SWV) in CH_3CN (0.1 M [TBA]PF_6 electrolyte) and in aqueous 0.1 M $HClO_4$. The values are reported in **Table 3.2**. All complexes exhibit reversible $Ru^{III/II}$ couples with $E_{1/2}$ values of 1.28, 1.34, and 1.22 V (vs. NHE in aqueous 0.1 M $HClO_4$) for **RuP**, **RuPdvb**, and **RuPdmb**, respectively (**Figure 3.4**). Similar to the trends observed in absorption and emission spectra, the positive and negative shifts in $E_{1/2}$ for **RuPdvb** and **RuPdmb**, relative to **RuP**, can be attributed to the electron-withdrawing vinyl and electron-donating methyl groups, respectively.

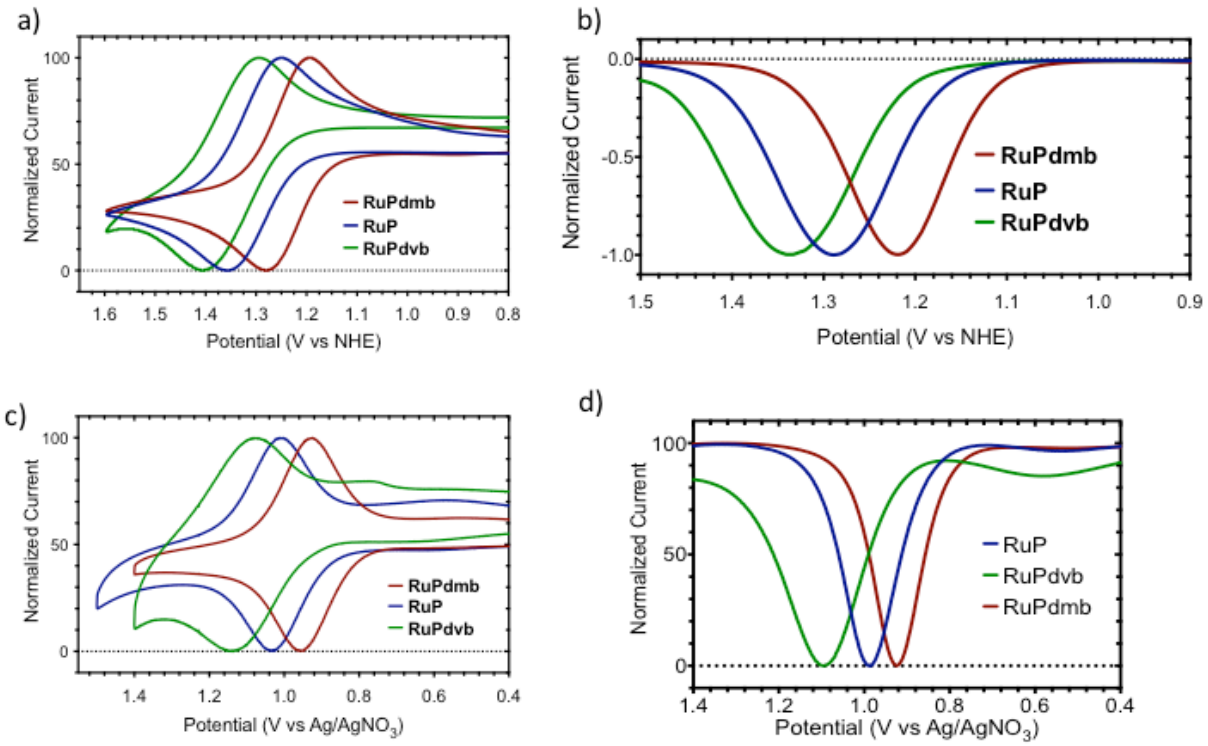

Figure 3.4. a,c) Cyclic voltammograms and b,d) square-wave voltammograms of all three chromophores immobilized on *nano*TiO_2 as the working electrode, with a Pt counter electrode, and a Ag/AgCl or $Ag/AgNO_3$ reference electrode in a,b) aqueous 0.1 M $HClO_4$ and c,d) in CH_3CN (0.1 M $[TBA]PF_6$).

Emission spectra for **RuP**, **RuPdvb**, and **RuPdmb** on *nano*ZrO_2 in aqueous 0.1 M $HClO_4$ were obtained (**Figure 3.5**). The trends in emission parallel those observed for absorption. The emission spectra were analyzed by application of a one-mode Franck-Condon analysis with the procedure described elsewhere.[8,33,34] The free energy content of the thermally equilibrated ^{3}MLCT excited states (ΔG_{ES}) are given in **Table 3.2** with the remaining spectral fitting parameters reported in **Table 3.3**. Excited-state reduction potentials for the couples, $Ru^{III} + e^- \rightarrow Ru^{II*}$ ($E°'(Ru^{III/II*})$), were calculated from $E°'(Ru^{III/II*}) = E_{1/2}(Ru^{III/II}) - \Delta G_{ES}$. Based on these values, all three complexes are sufficiently reducing (−0.68 to −0.84 V) to inject into the conduction band of TiO_2 (approximately −0.5 V vs. NHE) in aqueous pH 1 $HClO_4$.[35]

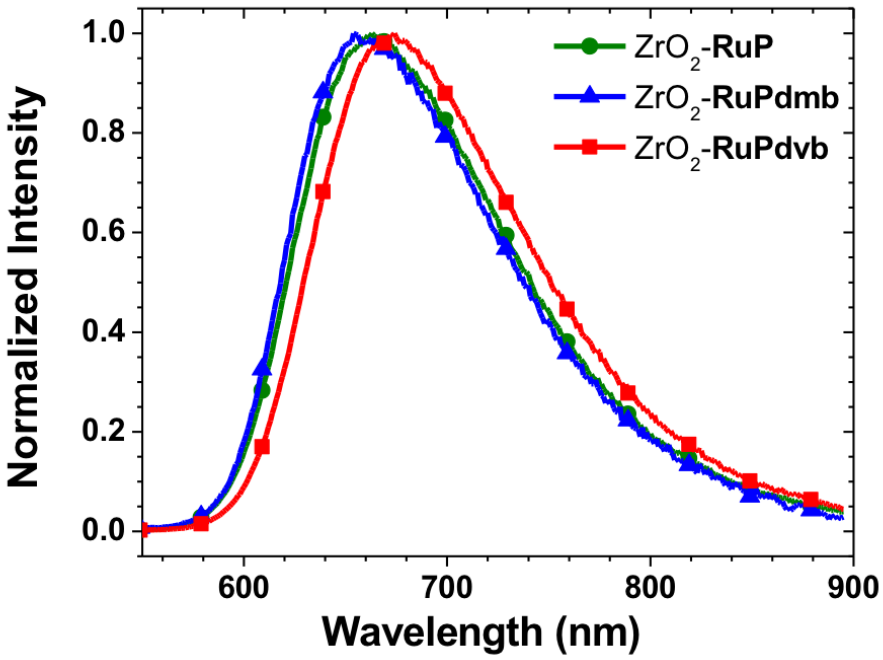

Figure 3.5. Emission spectra of **RuP**, **RuPdvb**, and **RuPdmb** on *nano*ZrO_2 in Ar-deaerated aqueous 0.1 M $HClO_4$ at room temperature (Excitation at 450 nm).

Table 3.3. Emission spectral fitting parameters for the MLCT excited states of **RuP**, **RuPdvb**, and **RuPdmb** on *nano*ZrO_2 in 0.1 M $HClO_4$ aqueous solution.

Sample	E_0 (cm^{-1})	$\Delta\nu_{1/2}$ (cm^{-1})	$\hbar\omega_M$ (cm^{-1})	S_M	ΔG_{ES}[a]
RuP	15,200	1,720	1,250	1.03	16,500
RuPdvb	15,100	1,650	1,250	1.09	16,300
RuPdmb	15,400	1,680	1,250	1.08	16,600

[a] $\Delta G_{ES} = E_0 + (\Delta\nu_{1/2})^2/(16k_BT\ln(2))$, where k_B is Boltzmann's constant and T is the temperature (25 °C).

3.2.4. Polymerization of $[Fe(v\text{-}tpy)_2]^{2+}$ on FTO

It has previously been demonstrated that $[\mathbf{Fe(v\text{-}tpy)_2}]^{2+}$ will undergo reductive electropolymerization on planar electrodes if the applied potential is more negative than the first

v-tpy-based reduction potential (approximately –1.5 V vs. $Ag/AgNO_3$).[25,36] As a control experiment, we initially investigated the electropolymerization of $[\mathbf{Fe(v\text{-}tpy)_2}]^{2+}$ on a planar fluoride-doped tin oxide (FTO) slide. In these experiments FTO was used as the working electrode, platinum as the counter electrode and $Ag/AgNO_3$ as the reference electrode with $[\mathbf{Fe(v\text{-}tpy)_2}]^{2+}$ in dry acetonitrile and 0.1 M $[TBA]PF_6$ as the electrolyte. The surface coverage (Γ in mol cm^{-2}) of redox active complex was calculated by using **Equation 3.2** where Q is the integrated current under the $Fe^{III/II}$ redox couple, F is Faraday's constant (96,485 C), n is the number of electrons transferred ($n = 1$), and A is the area of the electrode (~1 cm^2).

Equation 3.2

$$\Gamma = \frac{Q}{nFA}$$

The applied potential was cycled from 0 to −1.8 V (vs. $Ag/AgNO_3$), and FTO surface coverage was monitored as a function of both scan rate (50, 100, and 200 mV s^{-1}) and $[\mathbf{Fe(v\text{-}tpy)_2}]^{2+}$ concentration (0.5, 1.0, and 2.0 mM). Surface coverage was found to increase linearly as scan rate decreased or as the $[\mathbf{Fe(v\text{-}tpy)_2}]^{2+}$ concentration was increased (not shown).

3.2.5. Polymerization of $[\mathbf{Fe(v\text{-}tpy)_2}]^{2+}$ on *nano*$\mathbf{TiO_2}$

Under sufficiently reducing potentials (more negative than −0.5 V vs. NHE at pH = 1)[35] *nano*TiO_2 can readily transport electrons from the FTO electrode, through the metal oxide film, to the *nano*TiO_2/electrolyte interface providing a basis for reductive electropolymerization of $[\mathbf{Fe(v\text{-}tpy)_2}]^{2+}$. The high effective surface area of *nano*TiO_2 allows for monitoring the surface coverage of *poly*-$[\mathbf{Fe(v\text{-}tpy)_2}]^{2+}$ ($\varepsilon_{565\ nm}$ = 15,500 M^{-1} cm^{-1}) by UV-visible absorption

measurements. Absorption changes during an electropolymerization on a *nano*TiO_2 film cycled from 0 to −1.8 V vs. Ag/$AgNO_3$ are shown in **Figure 3.6**.

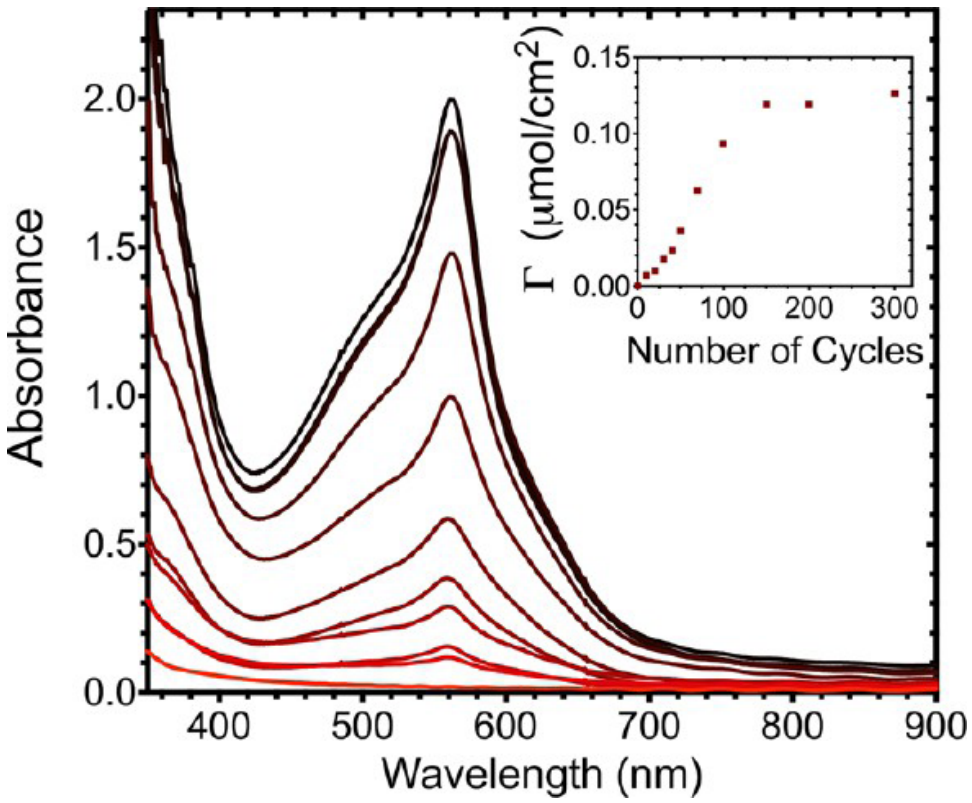

Figure 3.6. Changes in UV-visible absorption spectra for *nano*TiO_2 (dry slide) as the number of reductive cycles from 0 to –1.8 V (vs. Ag/$AgNO_3$) is increased (0, 10, 20, 30, 40, 50, 70, 100, 150, 200, and 300; red to black) in an acetonitrile solution of 0.5 mM $[\mathbf{Fe(v\text{-}tpy)_2}]^{2+}$ (0.1 M [TBA]PF_6 electrolyte); Pt counter electrode, and Ag/$AgNO_3$ reference electrode. Inset: Surface coverage of *poly*-$[\mathbf{Fe(v\text{-}tpy)_2}]^{2+}$ versus the number of reductive cycles.

For the first 70 cycles the surface coverage of *poly*-$[\mathbf{Fe(v\text{-}tpy)_2}]^{2+}$ increases linearly with the number of cycles (inset, **Figure 3.6**) and continues to increase, albeit at a slower rate, from 70 to 150 cycles. Further polymerization was minimal after 150 cycles. At 70 cycles, a single monolayer of *poly*-$[\mathbf{Fe(v\text{-}tpy)_2}]^{2+}$ was deposited on the *nano*TiO_2 surface (~7×10^{-8} mol cm^{-2}) as determined by UV-visible absorption measurements. The decreased deposition rate for [**Fe(v-**

tpy)$_2$]$^{2+}$ from 70 to 150 cycles may be due to a decrease in the rate of electron transfer from *nano*TiO_2 to [**Fe(v-tpy)$_2$**]$^{2+}$ or a decrease in the available volume within the internal voids of the nanostructured films. In any case, electropolymerization is hindered after the deposition of approximately two monolayers (150 cycles), **Figure 3.6**, inset.

No change in absorption was observed for a *nano*TiO_2 electrode cycled in [**Fe(v-tpy)$_2$**]$^{2+}$ solution from 0 V to −1.0 V (vs. $Ag/AgNO_3$). This potential range is more positive than that required for reductive electropolymerization, and this result shows that physical adsorption of [**Fe(v-tpy)$_2$**]$^{2+}$ to *nano*TiO_2 prior to electropolymerization does not occur.

3.2.6. Polymerization of [Fe(v-tpy)$_2$]$^{2+}$ on *nano*TiO_2|-RuPdvb

Electropolymerized films of *nano*TiO_2|-**RuPdvb**-*poly*-[**Fe(v-tpy)$_2$**]$^{2+}$ were prepared by first derivatizing TiO_2 with a monolayer of **RuPdvb** (*nano*TiO_2|-**RuPdvb**) by loading from methanol. The *nano*TiO_2|-**RuPdvb** film was then used as the working electrode during reductive cycling in an acetonitrile solution of 0.5 mM [**Fe(v-tpy)$_2$**]$^{2+}$ (0.1 M [TBA]PF_6 electrolyte). The changes in the UV-visible absorption spectra of *nano*TiO_2|-**RuPdvb** with increasing number of reductive cycles from 0 to −1.8 V (vs. $Ag/AgNO_3$) are shown in **Figure 3.7**.

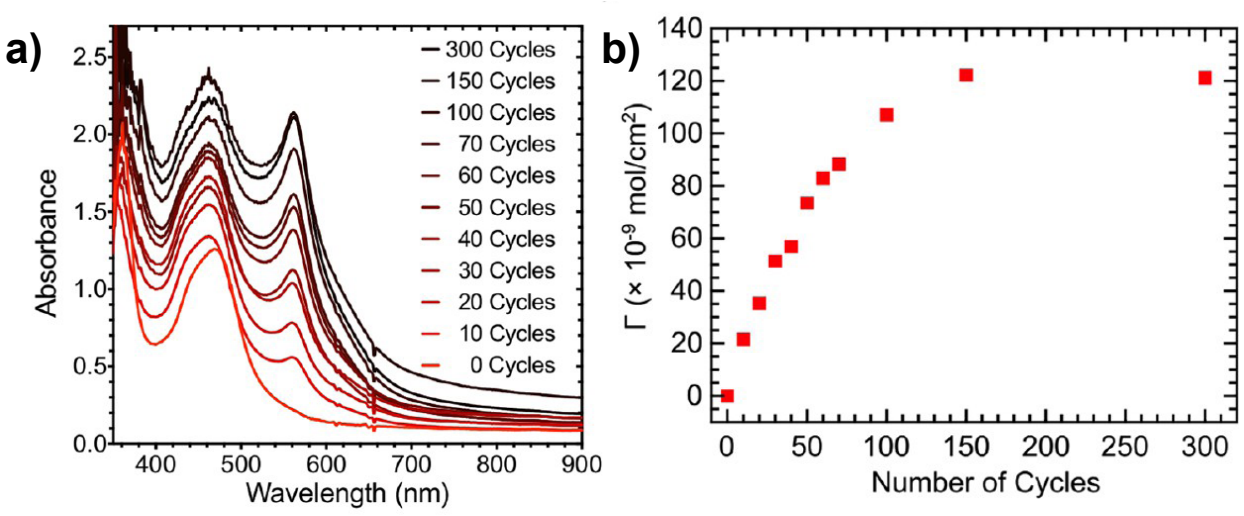

Figure 3.7. (a) Changes in UV-visible absorption spectra for *nano*TiO_2|-**RuPdvb** (dry slide) with an increase in the number of reductive scan cycles from 0 to –1.8 V (vs. $Ag/AgNO_3$) in an acetonitrile solution 0.5 mM in $[\mathbf{Fe(v\text{-}tpy)_2}]^{2+}$ (0.1 M $[TBA]PF_6$ electrolyte); Pt counter electrode, and $Ag/AgNO_3$ reference electrode. (b) Surface coverage of *poly*-$[\mathbf{Fe(v\text{-}tpy)_2}]^{2+}$ versus the number of scan cycles.

UV-visible absorption spectra of the polymerized films showed that the MLCT band for **RuPdvb** did not diminish in intensity following reductive polymerization of $[\mathbf{Fe(v\text{-}tpy)_2}]^{2+}$ (**Figure 3.7**a). As with non-derivatized *nano*TiO_2 (see above) the surface coverage of *poly*-$[\mathbf{Fe(v\text{-}tpy)_2}]^{2+}$ increases approximately linearly from 0 to 70 cycles, slows from 70 to 150 cycles, then remains constant above 150 cycles (**Figure 3.7**b). The surface coverage of *poly*-$[\mathbf{Fe(v\text{-}tpy)_2}]^{2+}$ on *nano*TiO_2|-**RuPdvb** after 70 and 150 cycles corresponds to approximately one and two monolayers, respectively.

A blue-shift (~9 nm) in the MLCT band for **RuPdvb** was observed after the first 10 cycles of electropolymerization (**Figure 3.7**a). A similar blue-shift (**Figure 3.8**) is also observed for *nano*TiO_2|-**RuPdvb** after reductive cycling in 0.5 mM *p*-divinylbenezene (absorption <350 nm) showing that the shift in Ru^{II}-based absorption in *nano*TiO_2|-**RuPdvb**-*poly*-$[\mathbf{Fe(v\text{-}tpy)_2}]^{2+}$ is not due to $[\mathbf{Fe(v\text{-}tpy)_2}]^{2+}$. The absorption spectrum of *nano*TiO_2|-**RuPdvb** after

electropolymerization closely resembles that of *nano*TiO_2|-**RuPdmb**, suggesting that the shift is due to conversion of the electron-withdrawing vinyl groups in **RuPdvb** to saturated alkane groups formed during the polymerization process.[23]

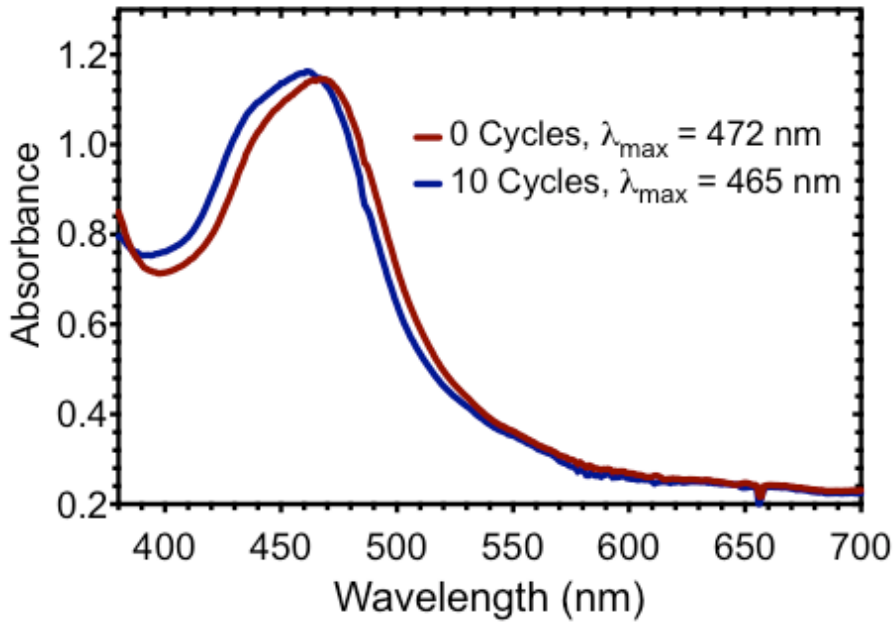

Figure 3.8. UV-visible absorption spectra of *nano*TiO_2|-**RuPdvb** before (red) and after (blue) 10 cycles from 0 to –1.8 V (vs. $Ag/AgNO_3$) in an acetonitrile solution of 0.5 mM *p*-divinylbenezene (0.1 M $[TBA]PF_6$ electrolyte); Pt counter electrode, and $Ag/AgNO_3$ reference electrode.

The electrochemical properties of *nano*TiO_2|-**RuPdvb** were monitored before and after reductive polymerization by cyclic voltammetry. Oxidative scans from 0 to 1.5 V (vs. $Ag/AgNO_3$) in CH_3CN (0.1 M $[TBA]PF_6$) following successive reductive cycles from 0 to −1.8 V (vs. $Ag/AgNO_3$) are shown in **Figure 3.9**. TiO_2 is a wide bandgap semiconductor with $E_{vb} \approx$ 2.8 V at pH = 7, and Ru^{II} oxidation to Ru^{III} on the surface is initiated by electron transfer at the FTO interface followed by cross-TiO_2 surface $Ru^{II} \rightarrow Ru^{III}$ electron transfer hopping with associated counter-ion diffusion.[35,37]

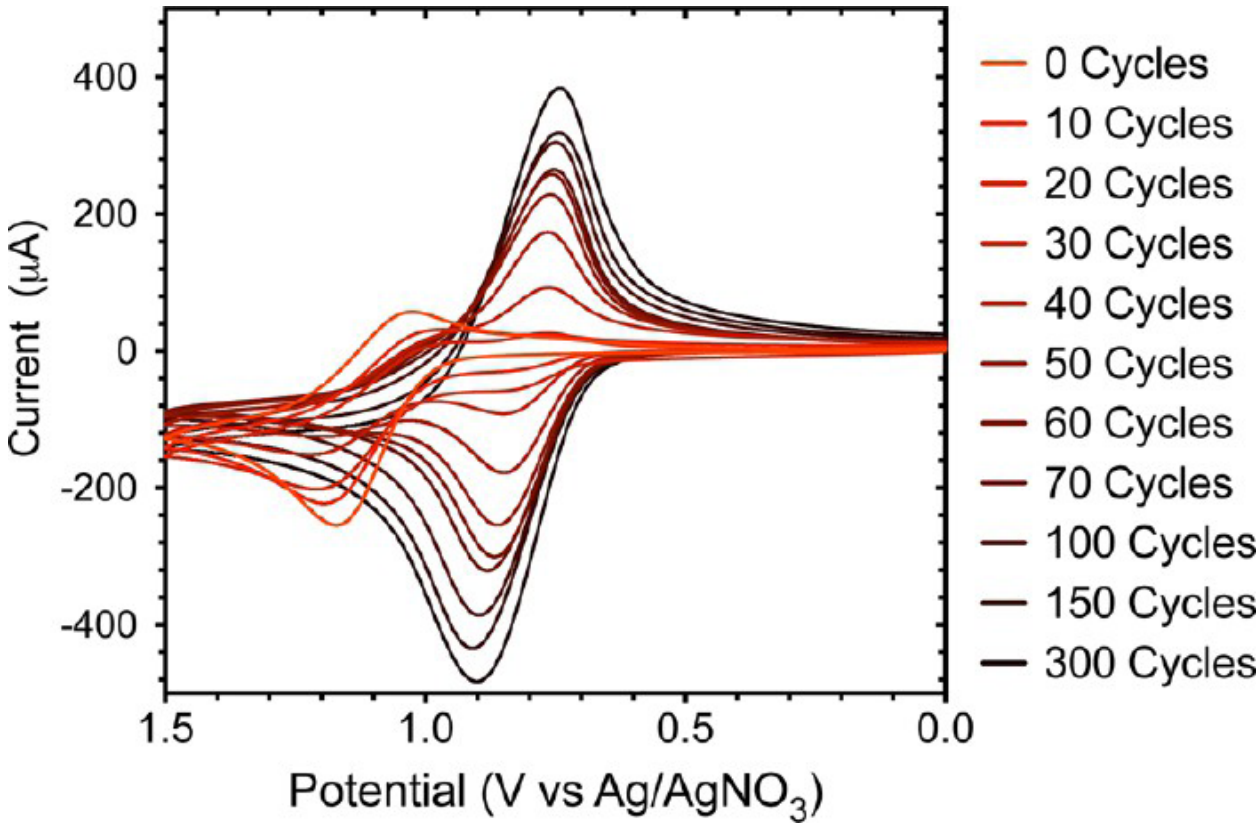

Figure 3.9. Cyclic voltammograms for *nano*TiO_2|-**RuPdvb** from 0 to 1.5 V (vs. $Ag/AgNO_3$) in acetonitrile (0.1 M [TBA]PF_6 electrolyte) after successive reductive scan cycles (ν = 100 mV s^{-1}) in an acetonitrile solution 0.5 mM in $[\mathbf{Fe(v\text{-}tpy)_2}]^{2+}$ (0.1 M [TBA]PF_6 electrolyte); Pt counter electrode, and $Ag/AgNO_3$ reference electrode.

Before overlayer electrodeposition, $E_{1/2}(Ru^{III/II})$ appeared at 1.16 V (vs. $Ag/AgNO_3$). Upon electropolymerization of the overlayer, the peak current for the $Ru^{III/II}$ couple decreased and the peak-to-peak splitting increased. Past ~50 cycles from 0 to 1.5 V (vs. $Ag/AgNO_3$) at 50 mV s^{-1}, the couple is no longer observed. Nonetheless, after 50 cycles the MLCT absorption band for **RuPdvb** is relatively unchanged in UV-visible absorption spectra (**Figure 3.7**a), indicating that it is still on the surface. A likely explanation for the decrease and ultimate loss in current for the $Ru^{III/II}$ wave is a blocking effect by the growing *poly*-$[\mathbf{Fe(v\text{-}tpy)_2}]^{2+}$ overlayer film which inhibits diffusion of counter-ions to the Ru^{II} sites on the surface. The lack of counter-ion

diffusion, and thus charge balance, for oxidation of Ru^{II} to Ru^{III} potentially inhibits cross-surface electron transfer.

After polymerization, a new reversible $Fe^{III/II}$ couple, due to *poly*-[**Fe(v-tpy)$_2$**]$^{2+}$, is observed at $E_{1/2}$ = 0.85 V (vs. $Ag/AgNO_3$). The integrated current for the $Fe^{III/II}$ wave increases with each successive reductive cycle.

3.2.7. Morphology Characterization

The morphology and composition of the *nano*TiO_2|-**RuPdvb**-*poly*-[**Fe(v-tpy)$_2$**]$^{2+}$ films were examined by scanning electron microscopy (SEM) and energy-dispersive X-ray spectroscopy (EDS). SEM images of *nano*TiO_2|-**RuPdvb** following 50 and 300 cycles of reductive polymerization can be seen in **Figure 3.10**. The SEM image of *nano*TiO_2|-**RuPdvb**-*poly*-[**Fe(v-tpy)$_2$**]$^{2+}$ after 50 reductive cycles resembles that of *nano*TiO_2|-**RuPdvb** in that the porosity of the *nano*TiO_2 is retained after polymerization (**Figure 3.10**a and **Figure 3.10**c). In contrast, after 300 reductive cycles, the porosity of the film is reduced and a film of *poly*-[**Fe(v-tpy)$_2$**]$^{2+}$ has formed on top of the mesoporous *nano*TiO_2 film (**Figure 3.10**b and **Figure 3.10**d). Presumably, as noted above, the surface layer inhibits both substrate and electrolyte diffusion into the film, with the latter resulting in the decrease in current for the $Ru^{III/II}$ couple.

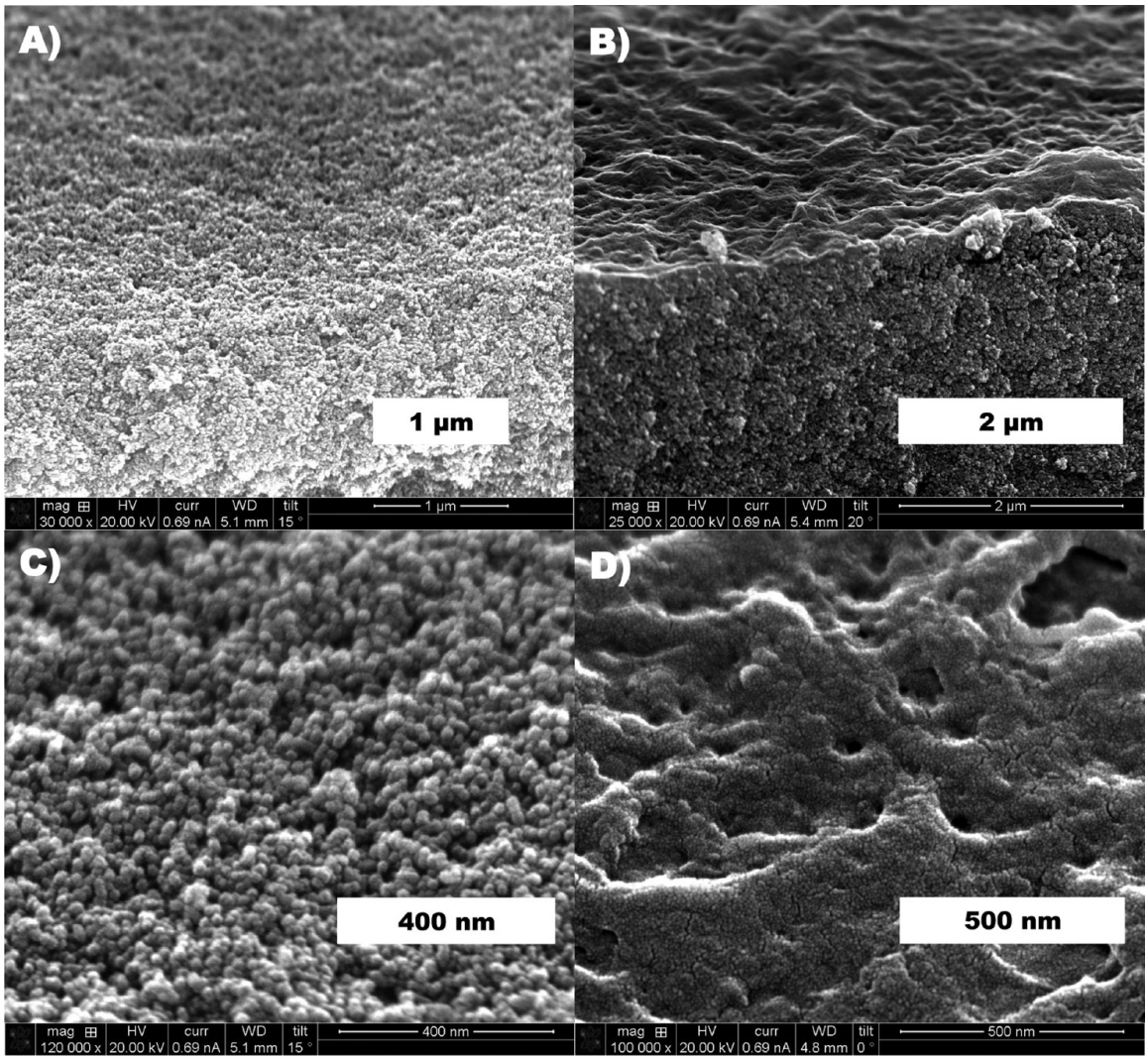

Figure 3.10. Cross-sectional (A and B) and surface (C and D) SEM images of the *nano*TiO_2|-**RuPdvb** film following 50 (A and C) and 300 (B and D) reductive scan cycles (ν = 100 mV s^{-1}) in an acetonitrile solution containing 0.5 mM in $[\mathbf{Fe(v\text{-}tpy)_2}]^{2+}$ (0.1 M $[TBA]PF_6$ electrolyte).

EDS was used to determine the concentrations of ruthenium and iron at different depths within the *nano*TiO_2 films. The results are summarized in **Table 3.4**. The EDS data for *nano*TiO_2|-**RuPdvb**-*poly*-$[\mathbf{Fe(v\text{-}tpy)_2}]^{2+}$ films prepared from 50 and 300 reductive cycles both reveal inhomogeneities throughout the mesoporous structure and a gradient in ruthenium complex content as well. The concentration of surface-bound Ru^{II} complex is highest at the TiO_2/solution interface decreasing with depth toward the FTO surface. This result is consistent

with those of O'Regan et al., which demonstrated that standard dye loading procedures on *nano*TiO_2 do not uniformly coat the films, but instead result in greater dye loading near the surface.[38]

Table 3.4. The Atomic % and Ru:Fe Ratios at the Top, Middle, and Bottom of *nano*TiO_2|-**RuPdvb** Films After 50 and 300 Reductive Cycles (ν = 100 mV s^{-1}) in an Acetonitrile Solution Containing 0.5 mM in $[\mathbf{Fe(v\text{-}tpy)_2}]^{2+}$ (0.1 M [TBA]PF_6 Electrolyte).

Sample	Ru (Atomic %)	Fe (Atomic %)	Ru:Fe
50 cycles (top)	1.54	1.05	1:0.7
50 cycles (middle)	1.31	0.62	1:0.5
50 cycles (bottom)	0.88	0.43	1:0.5
300 cycles (top)	0.50	1.20	1:2.4
300 cycles (middle)	0.51	0.75	1:1.5
300 cycles (bottom)	0.43	0.60	1:1.4

The EDS results also show that the Fe:Ru ratio is higher at the TiO_2/solution interface (top) compared to the interior of the film. This result suggests that electropolymerization of $[\mathbf{Fe(v\text{-}tpy)_2}]^{2+}$ occurs rapidly at the TiO_2/solution interface but is limited by diffusion of $[\mathbf{Fe(v\text{-}tpy)_2}]^{2+}$ into the mesoporous *nano*TiO_2 network. As a result the Fe:Ru ratios determined by UV-visible absorption measurements represent averages of actual ratios throughout the inhomogeneously loaded films. The Ru:Fe ratios in *nano*TiO_2|-**RuPdvb**-*poly*-$[\mathbf{Fe(v\text{-}tpy)_2}]^{2+}$ after 50 and 300 cycles, as determined by UV-visible absorption measurements, were 1:1 and 1:1.7, respectively. A film with a more uniform ratio of Fe:Ru was prepared by soaking a *nano*TiO_2|-**RuPdvb** slide in a $[\mathbf{Fe(v\text{-}tpy)_2}]^{2+}$ solution (0.5 mM in 0.1 M [TBA]PF_6/CH_3CN) overnight, stirring the solution during the electropolymerization process, and pausing 60 s between each

electropolymerization cycle. This suggests that diffusion of **[Fe(v-tpy)$_2$]$^{2+}$** through the mesoporous *nano*TiO_2 is a significant factor when controlling the distribution of the ratio of bound dye to electropolymer overlayer in the formation of these films.

3.2.8. Photostability

The photostabilities of *nano*TiO_2|-**RuPdvb**-*poly*-[**Fe(v-tpy)$_2$**]$^{2+}$ relative to **RuP** and **RuPdvb** on *nano*TiO_2 were evaluated by a previously published procedure with constant irradiation at 455 nm (fwhm ~30 nm, 475 mW cm^{-2}, ~135 suns at 455 nm).[8,9] Absorption spectra (360–800 nm) of the films were obtained every 15 minutes during 16 hours of irradiation. Results for *nano*TiO_2|-**RuPdvb** with ~2 monolayers of *poly*-[**Fe(v-tpy)$_2$**]$^{2+}$ (150 cycles) in aqueous 0.1 M $HClO_4$ (pH 1) are shown in **Figure 3.11**. The time-dependent changes in absorption at 480 nm were fit with the biexponential function in **Equation 3.3** and are presented as a single average rate constant (k_{des}) calculated as the inverse of the weighted average lifetime ($k_{des} = \langle\tau\rangle^{-1}$) for the time-dependent absorption changes, **Equation 3.4**. The results are summarized in **Table 3.5** and **Table 3.6**.

Equation 3.3

$$k_{obs} = A_1 e^{-k_1 t} + A_2 e^{-k_2 t}$$

Equation 3.4

$$\frac{1}{k_{des}} = \langle\tau\rangle = \frac{\sum_i A_i \tau_i^2}{\sum_i A_i \, \tau_i}$$

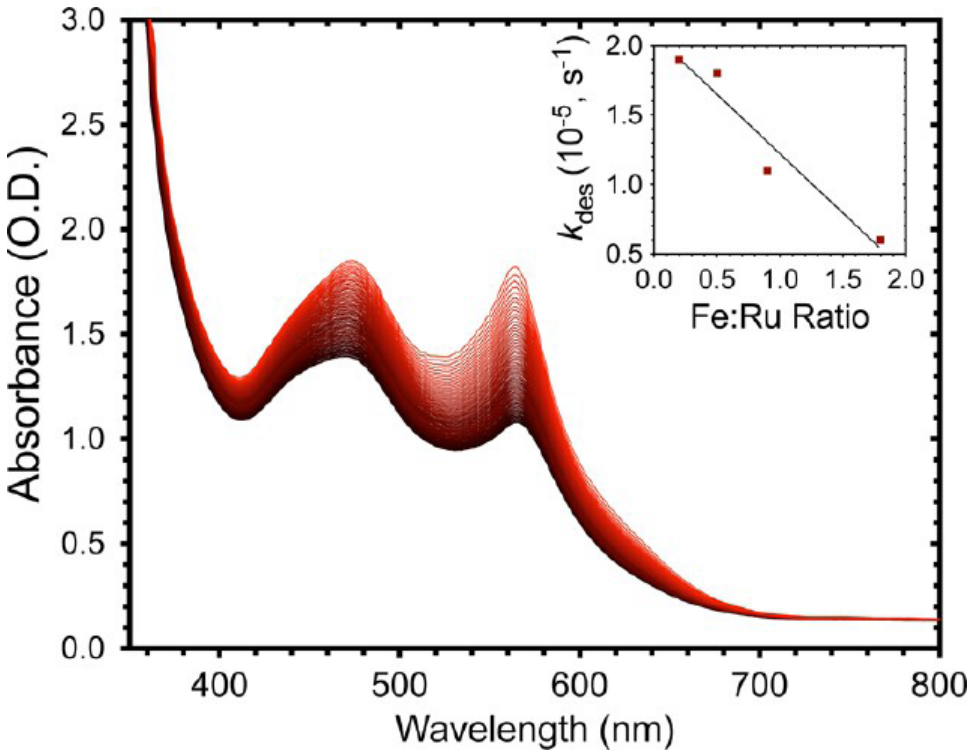

Figure 3.11. Changes in the absorption spectrum of *nano*TiO_2|-**RuPdvb**-*poly*-[**Fe(v-tpy)$_2$**]$^{2+}$ (150 cycles, 1:1.8 Ru:Fe) in aqueous 0.1 M $HClO_4$ under constant 455 nm irradiation (475 mW cm^{-2}) from 0 (red) to 16 hours (black) recorded every 15 minutes. Inset: Desorption rate constant (k_{des}) as a function of the number of reductive cycles.

Table 3.5. Summary of Desorption Rate Constants (k_{des}) in Aqueous 0.1 M $HClO_4$ for **RuP**, **RuPdvb**, and **RuPdmb** on *nano*TiO_2 and *nano*TiO_2|-**RuPdvb** Films after 10, 30, 70, and 150 Reductive Cycles in $[\mathbf{Fe(v\text{-}tpy)_2}]^{2+}$ Solution.

Sample	Ru:Fe	k_{des} ($\times 10^{-5}$ s^{-1})
RuP	1:0	4.8
RuPdmb	1:0	5.6
RuPdvb	1:0	5.9
RuPdvb + 10 cycles	1:0.2	1.9
RuPdvb + 30 cycles	1:0.5	1.8
RuPdvb + 70 cycles	1:0.9	1.1
RuPdvb + 150 cycles	1:1.8	0.6

Table 3.6. Summary of Desorption Rate Constants (k_{des}) for *nano*TiO_2|-**RuP**, *nano*TiO_2|-**RuP** Stabilized by ~3.3 Å of Al_2O_3, and *nano*TiO_2|-**RuPdvb**-*poly*-$[\mathbf{Fe(v\text{-}tpy)_2}]^{2+}$ Films (150 cycles, 1:1.8 Ru:Fe) under Various Conditions.

Solvent	k_{des} ($\times 10^{-5}$ s^{-1})		
	nanoTiO_2|-**RuP**	*nano*TiO_2|-**RuP** + 3.3 Å of Al_2O_3	*nano*TiO_2|-**RuPdvb**-*poly*-$[\mathbf{Fe(v\text{-}tpy)_2}]^{2+}$
pH 1[a]	4.8	–	0.6
pH 5[b]	>20	2.3	1.3
H_2O	>30	3.2	0.9
pH 7[c]	–	9.5	5.5
CH_3CN[d]	0.8	<0.01	0.07

[a]In 0.1 M $HClO_4$. [b]In 10 μM $HClO_4$. [c]In 0.1 M Na_3PO_4 buffer. [d]In 0.1 M $LiClO_4$.

Desorption rate constants for the unprotected surface-bound chromophores increase slightly in the order **RuP** (4.8×10^{-5} s^{-1}), **RuPdvb** (5.6×10^{-5} s^{-1}), and **RuPdmb** (5.8×10^{-5} s^{-1}). All three complexes share a similar surface binding motif based on the 4,4'-dpbpy ligand, and the slight differences in k_{des} are presumably due to the differences in surface packing and morphology/local structure.

The photochemical desorption rate constants for *nano*TiO_2|-**RuPdvb** in aqueous 0.1 M $HClO_4$ as a function of Ru:Fe ratios are summarized in **Table 3.5** and shown in **Figure 3.12**. With 10 reductive cycles, 1:0.2 (Ru:Fe), k_{des} is three times slower than for unprotected *nano*TiO_2|-**RuPdmb** or **RuPdvb**. From 10 cycles (1:0.2 Ru:Fe) to 150 cycles, 1:1.8 (Ru:Fe), there was an approximately linear decrease in k_{des} from 4.8×10^{-5} s^{-1} to 0.6×10^{-5} s^{-1} (inset, **Figure 3.11**). The desorption rate constant was similar from 400 to 600 nm, showing that desorption from the surface, and not photodecomposition of **RuPdvb** or $[\mathbf{Fe(v\text{-}tpy)_2}]^{2+}$, is occurring.

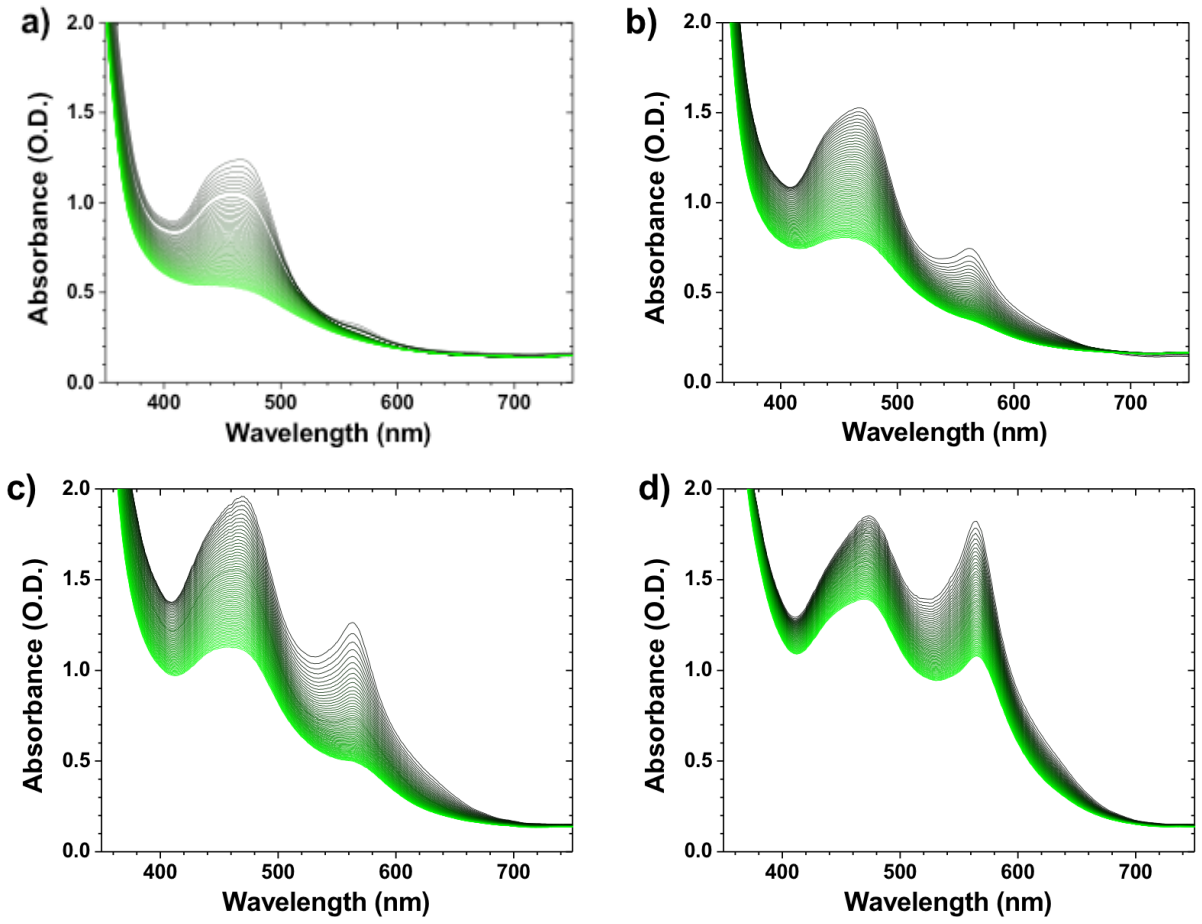

Figure 3.12. Changes in the absorption spectrum of *nano*TiO_2|-**RuPdvb** in aqueous 0.1 M $HClO_4$ under constant 455 nm irradiation (475 mW cm^{-2}) after (a) 10, (b) 30, (c) 70, and (d) 150 reductive cycles in an acetonitrile solution containing 0.5 mM $[\mathbf{Fe(v\text{-}tpy)_2}]^{2+}$. Spectra are shown from t = 0 (black) to t = 16 hours (green) with traces every 15 minutes.

The mechanism of photoinduced chromophore desorption from the metal oxide surface is not fully understood, but mechanisms have been proposed.[9] Increased stability after polymerization may arise from a number of factors including: (1) increased steric bulk provided by the polymer, which inhibits hydroxide/water attack at the phosphonate groups on the surface; (2) cross-linking of the film, which mechanically prevents desorption of individual chromophores; and (3) the newly formed hydrophobic alkyl linkers, which reduce the solubility

of the film in the external aqueous medium. Similar factors have been suggested for dye-sensitized solar cells that have been stabilized by cross-linking polymerization.[39]

It is also important to note that under irradiation a photostationary state exists that is dictated by photoexcitation, electron injection, and back electron transfer rates. For **RuP**, **RuPdvb**, and **RuPdmb** on *nano*TiO_2 under irradiation the surface-bound complex exists as Ru^{III}.[40] Conversely for *nano*TiO_2|-**RuPdvb**-*poly*-[**Fe(v-tpy)$_2$**]$^{2+}$ there is a ~300 mV driving force for electron transfer from *poly*-[**Fe(v-tpy)$_2$**]$^{2+}$ to **Ru^{III}Pdvb**, and at the steady state Fe^{III} dominates (see below).

The desorption rate constant for the *nano*TiO_2|-**RuPdvb**-*poly*-[**Fe(v-tpy)$_2$**]$^{2+}$ films (150 cycles, 1:1.8 Ru:Fe) was investigated in a variety of solvents, and the results are summarized in **Table 3.6** and shown in **Figure 3.13**. In previous experiments, the photostability of *nano*TiO_2|-**RuP** was maximized in 0.1 M $HClO_4$ with k_{des} (5.0×10^{-5} s^{-1}) increasing at higher pHs and in buffered solutions.[9] It is notable that at pH 5 (1.3×10^{-5} s^{-1}) and in H_2O (0.9×10^{-5} s^{-1}) the desorption rate constant for *nano*TiO_2|-**RuPdvb**-*poly*-[**Fe(v-tpy)$_2$**]$^{2+}$ is lower than for *nano*TiO_2|-**RuP** at pH 1 in water. Even in solutions buffered at pH 7 (0.1 M Na_3PO_4 buffer), the polymerized films have desorption rate constants (5.5×10^{-5} s^{-1}) comparable to *nano*TiO_2|-**RuP** in 0.1 M $HClO_4$. In solutions buffered at pH 7, desorption of **RuP** occurs with $k_{des} > 30 \times 10^{-5}$ s^{-1}.

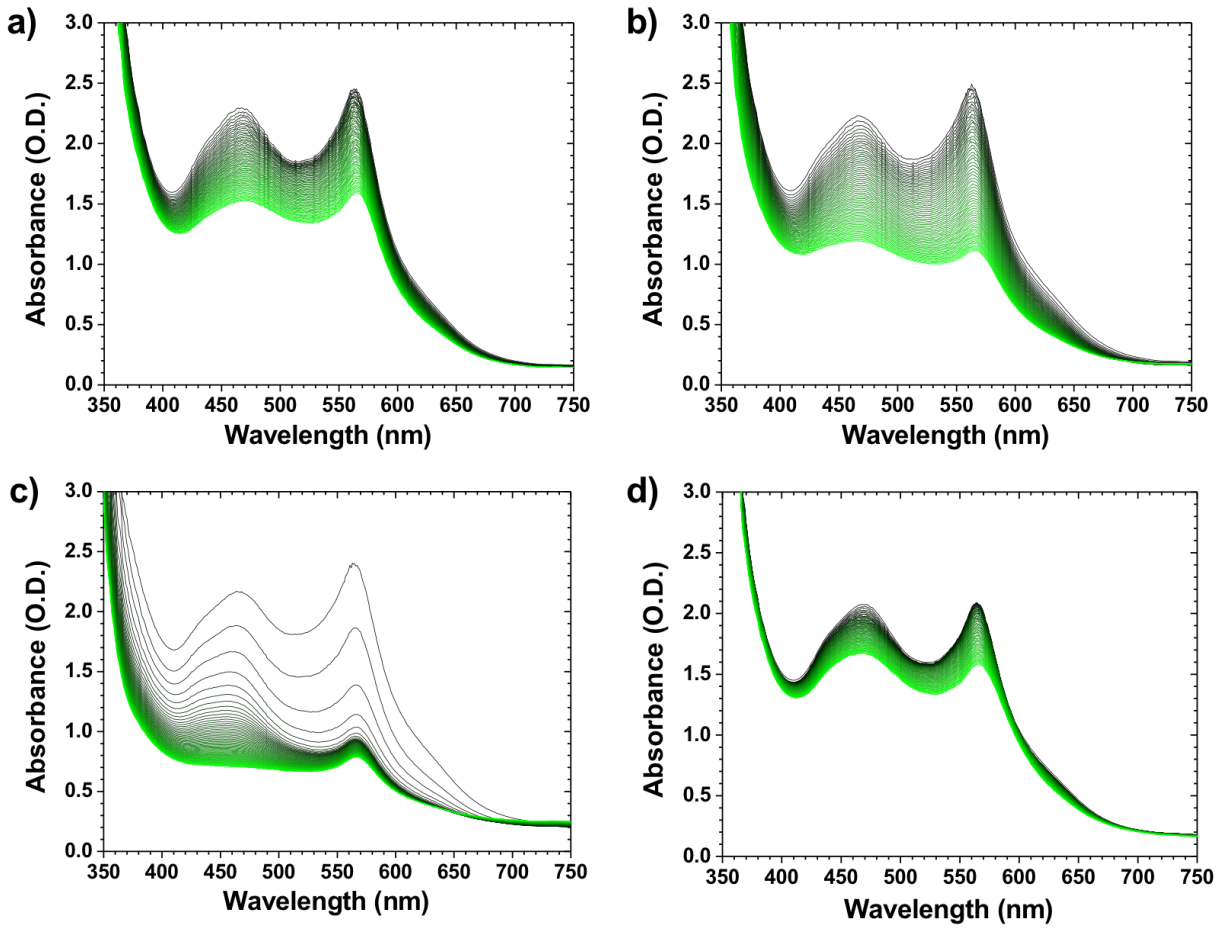

Figure 3.13. Changes in the absorption spectrum of *nano*TiO_2|-**RuPdvb**-*poly*-[**Fe(v-tpy)$_2$**]$^{2+}$ (150 cycles, 1:1.8 Ru:Fe) in (a) H_2O, (b) pH 5 $HClO_4$, (c) pH 7 phosphate buffer and (d) CH_3CN with 0.1 M $LiClO_4$ under constant 455 nm irradiation (475 mW cm^{-2}). Spectra are shown from t = 0 (black) to t = 16 hours (green) with traces every 15 minutes.

The use of the standard stability measurement protocol allows for comparison between surface stabilization strategies. For example, we recently demonstrated that atomic layer deposition (ALD) of Al_2O_3 on a *nano*TiO_2 surface derivatized with **RuP** significantly increases the stability of the surface-bound complex in water.[41] A comparison of k_{des} for untreated *nano*TiO_2|-**RuP**, *nano*TiO_2|-**RuP** stabilized by ~3.3 Å of ALD Al_2O_3, and *nano*TiO_2|-**RuPdvb**-*poly*-[**Fe(v-tpy)$_2$**]$^{2+}$ films (150 cycles, 1:1.8 Ru:Fe) is shown in **Table 3.6**. Under aqueous conditions the polymerized films are almost twice as stable as the ALD films and 10 times more

stable than the untreated films. This result suggests that reductive electropolymerization is a viable strategy for increasing stability of surface-bound complexes under aqueous conditions.

3.2.9. Transient Absorption

Interfacial electron transfer dynamics for *nano*TiO_2|-**RuP,** *nano*TiO_2|-*poly*-[**Fe(v-tpy)$_2$**]$^{2+}$, and *nano*TiO_2|-**RuPdvb** with 10, 30, 70, and 150 cycles of *poly*-[**Fe(v-tpy)$_2$**]$^{2+}$ overlayer were investigated by nanosecond transient absorption measurements in aqueous 0.1 M $HClO_4$. It has previously been demonstrated that photoexcitation of phosphonate-derivatized ruthenium polypyridyl complexes on *nano*TiO_2, **Equation 3.5**, is followed by efficient electron injection into the conduction band of TiO_2, **Equation 3.6**, with Φ_{inj} = 100% for *nano*TiO_2|-**RuP** at pH 1.[8] The electron injection process is accompanied by a bleach of the MLCT absorption features from 400 to 520 nm.

For *nano*TiO_2|-*poly*-[**Fe(v-tpy)$_2$**]$^{2+}$ (70 cycles, ~1 monolayer), a negligible transient absorption response (<10 mOD at 580 nm) was observed upon photoexcitation at 450 nm (**Figure 3.14**). The relatively small transient absorption amplitude suggests that the injection yield for excited *poly*-[**Fe(v-tpy)$_2$**]$^{2+}$ on *nano*TiO_2 is <1%, consistent with the known photophysics of related complexes in solution. As shown by McCusker, MLCT excitation is followed by rapid interconversion to low-lying dd states and rapid nonradiative decay.[42]

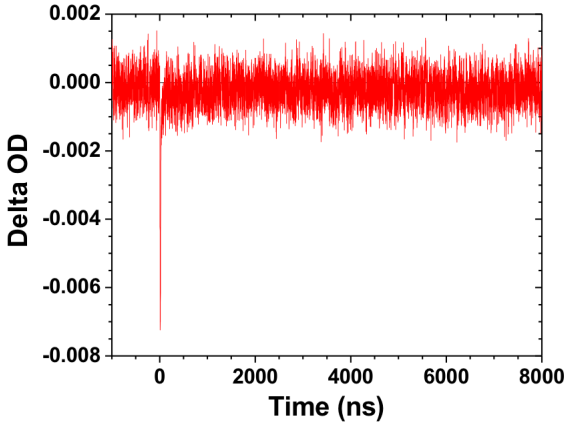

Figure 3.14. Absorption-time trace for *nano*TiO_2|-*poly*-[**Fe(v-tpy)$_2$**]$^{2+}$ (70 cycles) in Ar-deaerated 0.1 M $HClO_4$ aqueous solution measured at 580 nm. (Excitation at 450 nm, 5.0 mJ pulse^{-1}).

Equation 3.5

TiO_2|-**Ru^{II}** + hν → TiO_2|-**Ru^{II*}**

Equation 3.6

TiO_2|-**Ru^{II*}** → $TiO_2(e^-)$|-**Ru^{III}**

Time-resolved absorption difference spectra for **RuPdvb** with 10, 30, 70, and 150 cycles of *poly*-[**Fe(v-tpy)$_2$**]$^{2+}$ following photoexcitation at 425 nm were constructed from multiple single-wavelength measurements from 440 to 640 nm, acquired every 10 nm. The results are shown in **Figure 3.15**.

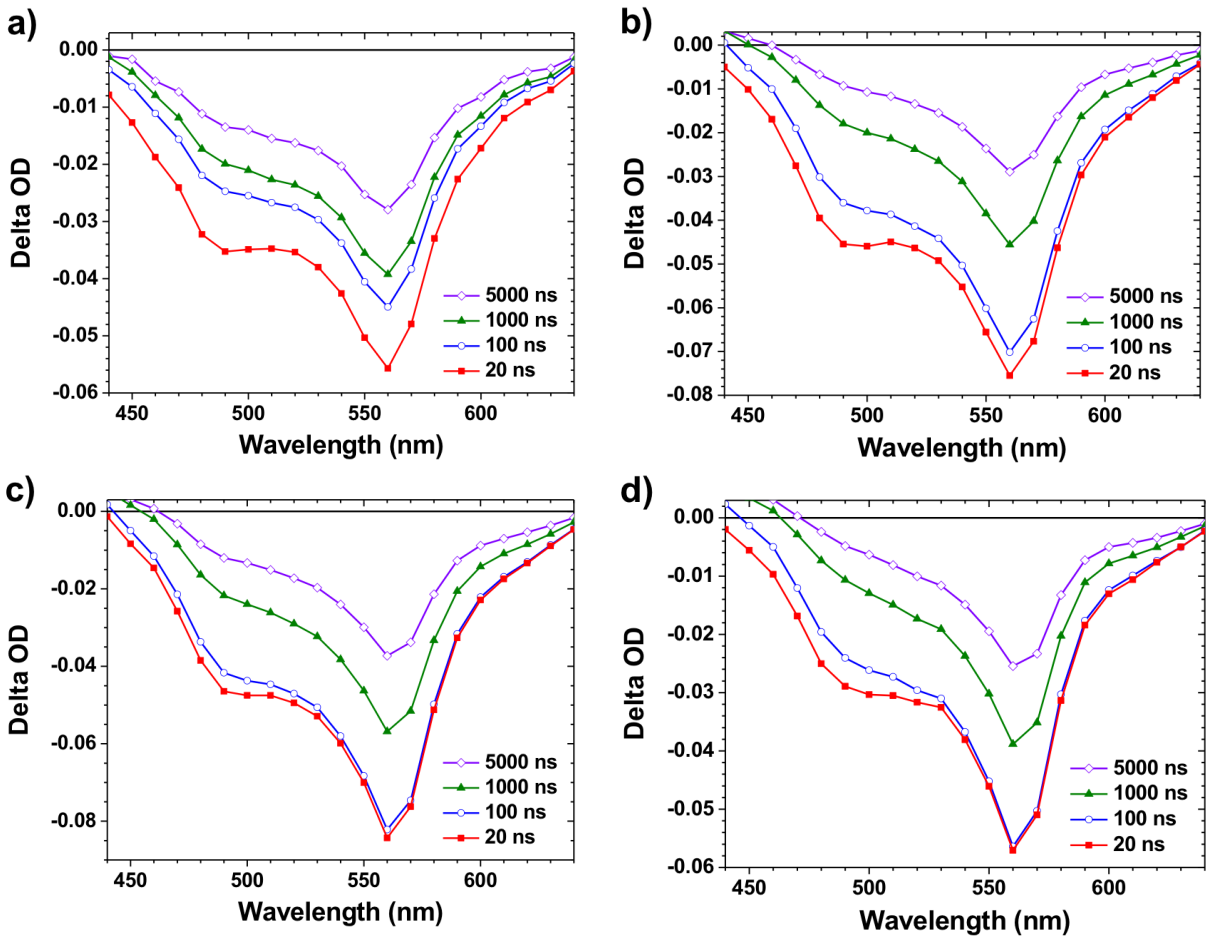

Figure 3.15. Time-resolved absorption difference spectra from for *nano*TiO_2|-**RuPdvb** with (a) 10, (b) 30, (c) 70 and (d) 150 cycles of $[\mathbf{Fe(v\text{-}tpy)_2}]^{2+}$ in Ar-deaerated aqueous 0.1 M $HClO_4$. (Excitation at 425 nm, 5.0 mJ $pulse^{-1}$).

In the difference spectra for *nano*TiO_2|-**RuPdvb**-*poly*-$[\mathbf{Fe(v\text{-}tpy)_2}]^{2+}$ (1:0.5 Ru:Fe) in **Figure 3.15**b, there is evidence for electron injection because there is a loss in the MLCT absorbance for Ru^{II} from 450 to 520 nm and Fe^{II} from 520 to 640 nm. Following the laser flash, the bleach feature for Ru^{II} decreases more rapidly than the bleach feature for Fe^{II}.

The time-dependent absorption changes appear to arise from competing electron transfer events following photoexcitation (**Equation 3.7**) and quenching of TiO_2-$\mathbf{Ru^{II}}$* (**Equation 3.8**). They include back electron transfer from $TiO_2(e^-)$ to Ru^{III} (**Equation 3.9**),

interassembly/interlayer electron transfer from Fe^{II} to Ru^{III} (**Equation 3.10**), and back electron transfer (BET) from $TiO_2(e^-)$ to Fe^{III} (**Equation 3.11**). In these reactions, **RuPdvb** and *poly*-$[\mathbf{Fe(v\text{-}tpy)_2}]^{2+}$ are represented by Ru^{II} and Fe^{II}, respectively, and injection by Fe^{II*} is neglected because it is negligible (**Figure 3.14**).

Equation 3.7

$TiO_2|\text{-}\mathbf{Ru^{II}}\text{-}\mathbf{Fe^{II}} + h\nu \rightarrow TiO_2|\text{-}\mathbf{Ru^{II*}}\text{-}\mathbf{Fe^{II}}$

Equation 3.8

$TiO_2|\text{-}\mathbf{Ru^{II*}}\text{-}\mathbf{Fe^{II}} \rightarrow TiO_2(e^-)|\text{-}\mathbf{Ru^{III}}\text{-}\mathbf{Fe^{II}}$

Equation 3.9

$TiO_2(e^-)|\text{-}\mathbf{Ru^{III}}\text{-}\mathbf{Fe^{II}} \rightarrow TiO_2|\text{-}\mathbf{Ru^{II}}\text{-}\mathbf{Fe^{II}}$

Equation 3.10

$TiO_2(e^-)|\text{-}\mathbf{Ru^{III}}\text{-}\mathbf{Fe^{II}} \rightarrow TiO_2(e^-)|\text{-}\ \mathbf{Ru^{II}}\text{-}\mathbf{Fe^{III}}$

Equation 3.11

$TiO_2(e^-)|\text{-}\mathbf{Ru^{II}}\text{-}\mathbf{Fe^{III}} \rightarrow TiO_2|\text{-}\mathbf{Ru^{II}}\text{-}\mathbf{Fe^{II}}$

The spectral changes over time suggest that electron transfer from Fe^{II} to Ru^{III} (**Equation 3.10**) occurs on a time scale of hundreds of nanoseconds. Quantitation is difficult in part because, as noted above, the *nano*$TiO_2|$-**RuPdvb**-*poly*-$[\mathbf{Fe(v\text{-}tpy)_2}]^{2+}$ overlayer structures are inhomogenous in composition with depth in the film. Transient absorption spectral changes

include electron transfer events between localized regions with different Ru^{II}:Fe^{II} ratios. There is also kinetic overlap between intra-assembly $Fe^{II} \rightarrow Ru^{III}$ electron transfer (**Equation 3.10**) and back electron transfer from $TiO_2(e^-)$ to Ru^{III} (**Equation 3.9**) and Fe^{III} (**Equation 3.11**). For **RuP** on TiO_2 back electron transfer extends from the nanosecond to millisecond time scales,[8] and as found for other dynamic processes at nanocrystalline metal oxide interfaces, the kinetics are nonexponential and highly complex.[43,44]

The spectral changes for oxidation/reduction of *poly*-[**Fe(v-tpy)$_2$**]$^{2+}$ can be differentiated from those arising from $Ru^{III/II}$ by measuring the relative electron injection yield and back electron transfer dynamics at 580 nm. This wavelength is the ground state/oxidized state isosbestic point for **RuPdmb**, the optical model for **RuPdvb** after polymerization. Absorption–time kinetic traces at 580 nm following 450 nm excitation are shown in **Figure 3.16**. The data were fit over the first ~10 μs using the triexponential function in **Equation 3.12**. Weighted average lifetime values, ‹τ›, calculated by use of **Equation 3.13** and **Equation 3.14**, are summarized in **Table 3.7**.

Equation 3.12

$$A = \sum_{1}^{3} A_i e^{-k_i t}$$

Equation 3.13

$$\tau_i = \frac{1}{k_i}$$

Equation 3.14

$$\langle \tau \rangle = \frac{\sum_i A_i \tau_i^2}{\sum_i A_i \, \tau_i}$$

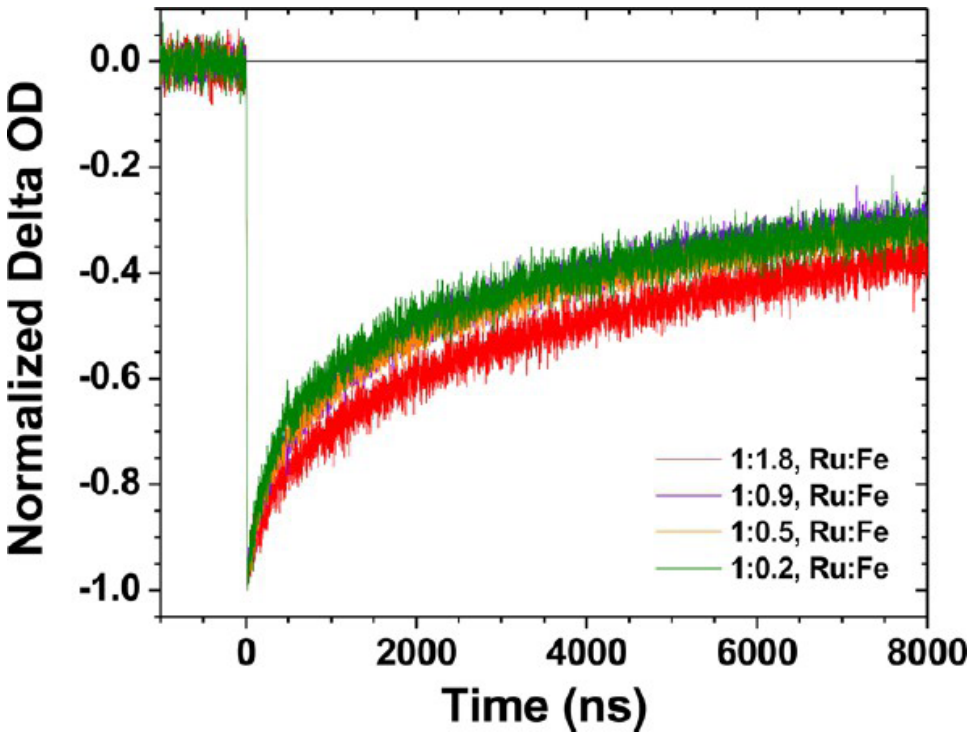

Figure 3.16. Absorption-time traces for *nano*TiO_2|-**RuPdvb**-*poly*-[**Fe(v-tpy)$_2$**]$^{2+}$ with various ratios of Ru to Fe in Ar-deaerated 0.1 M $HClO_4$ aqueous solutions monitored at 580 nm (450 nm excitation, 5.0 mJ pulse^{-1}).

Table 3.7. Net Electron Injection Yields (Based on the Appearance of Fe^{III}), Average Back Electron Transfer Lifetimes, and k_{BET} from Transient Absorption Measurements on *nano*TiO_2|-**RuPdvb**-*poly*-[**Fe(v-tpy)$_2$**]$^{2+}$ as a Function of Ru:Fe Ratio in 0.1 M $HClO_4$ with *nano*TiO_2|-**RuP** as a Reference[a].

Ru:Fe	Φ_{inj}[b]	Lifetime (μs)				k_{BET} ($\times 10^4$ s^{-1})
		t_1 (A_1)	t_2 (A_2)	t_3 (A_3)	‹τ›	
1:0.2	0.15	0.20(1)	1.6(6)	16.5(94)	16.4	6.1
1:0.5	0.35	0.25(1)	1.8(4)	18.5(96)	18.4	5.4
1:0.9	0.30	0.23(1)	1.6(5)	18.2(95)	18.1	5.5
1:1.8	0.20	0.23(1)	1.6(5)	21.3(95)	21.2	4.7
RuP[c]	1.00	0.01(2)	0.8(9)	10.7(89)	10.6	9.4

[a]Excitation at 450 nm, probed at 580 nm. [b]Δϵ for **Fe** at 580 nm is –11,200, for **RuP** at 400 nm is -6,500. [c]Monitored at 400 nm.

In **Figure 3.16**, a bleach feature is present at 580 nm at the earliest observation of ~20 ns. Given the lack of direct injection by Fe^{II*}, this feature is a marker for Ru^{II*} injection (**Equation 3.8**) followed by partial intra-assembly $Fe^{II} \rightarrow Ru^{III}$ electron transfer. Based on these data there is a rapid electron transfer component occurring in less than 20 ns (**Equation 3.10**). The bleach feature for Ru^{II}, **Figure 3.15**, is still present at >20 ns, which shows that another fraction of Ru^{III} sites produced by electron injection undergo relatively slow $Fe^{II} \rightarrow Ru^{III}$ (**Equation 3.10**) electron transfer or return to Ru^{II} by back electron transfer from $TiO_2(e^-)$, **Equation 3.9**.

Return of the bleach to the baseline by $TiO_2(e^-) \rightarrow Fe^{III}$ back electron transfer, **Equation 3.11**, is ~60% complete by 9 μs. As can be seen in **Figure 3.16** and **Table 3.7**, there is a slight trend toward slower back electron transfer as the Ru:Fe ratio is increased from 1:0.2 (k_{BET} = 6.1 $\times 10^4$ s^{-1}) to 1:1.8 (k_{BET} = 4.7 $\times 10^4$ s^{-1}).

Relative electron injection efficiencies (Φ_{inj}) for *nano*TiO_2|-**RuPdvb**-*poly*-[**Fe(v-tpy)$_2$**]$^{2+}$ were estimated by using thin film actinometry with *nano*TiO_2|-**RuP** (Φ_{inj} = 1.0) as the reference.[8,45] Amplitude changes were evaluated 10 ns following 450 nm laser excitation with injection yields calculated by using **Equation 3.15** (see Experimental) with $\Delta\varepsilon = -6{,}500\ M^{-1}\ cm^{-1}$ at 400 nm for **RuP** and $\Delta\varepsilon = -11{,}200\ M^{-1}\ cm^{-1}$ at 580 nm for *poly*-[**Fe(v-tpy)$_2$**]$^{2+}$. The latter were determined by spectroelectrochemical measurements on conductive tin-doped indium oxide nanoparticles (**Figure 3.17**). The results are summarized in **Table 3.7**.

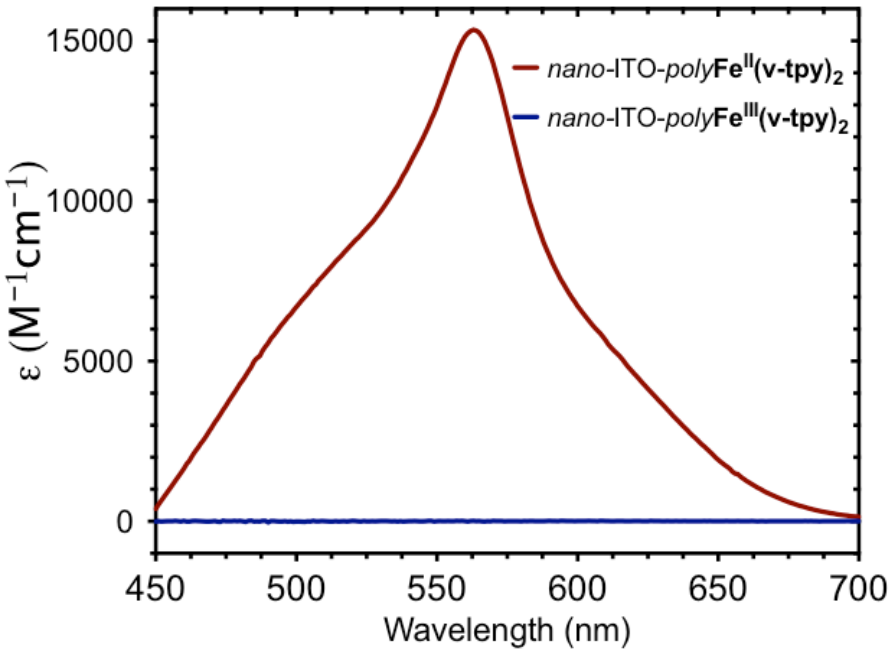

Figure 3.17. Spectroelectrochemistry of *poly*-[**Fe(v-tpy)$_2$**]$^{2+}$ on *nano*ITO in 0.1 M $HClO_4$ with a Pt counter electrode and a Ag/AgCl reference. The potential was slowly increased from 0.2 V to 1.6 V (vs. NHE) to oxidize Fe^{II} to Fe^{III}.

From these data, Φ_{inj} for *nano*TiO_2|-**RuPdvb**-*poly*-[**Fe(v-tpy)$_2$**]$^{2+}$ is significantly lower (≤30%) than Φ_{inj} for *nano*TiO_2|-**RuP** (100%). Since **RuPdvb** is expected to have a near unity electron injection yield in the polymerized film (Φ_{inj}(TiO_2|-**RuPdmb**) = 100%), there is a

significant decrease in Φ_{inj} for *nano*TiO_2|-**RuPdvb**-*poly*-[**Fe(v-tpy)$_2$**]$^{2+}$. It should be noted that the reported net injection yield only accounts for Fe^{III}, and not Ru^{III}, present at 20 ns after the laser flash. Also, photons absorbed by *poly*-[**Fe(v-tpy)$_2$**]$^{2+}$ at 450 nm are largely lost since the *poly*-[**Fe(v-tpy)$_2$**]$^{2+}$ chromophore acts as a nonproductive light absorber/filter. An additional contributing factor may arise from the time scale of the injection measurement. Excitation–injection events followed by back electron transfer on the <20 ns time scale are not included in the experimental Φ_{inj} values.

The transient absorption results demonstrate that electropolymerization can be used to incorporate an electron donor as an overlayer on chromophores preattached to a metal oxide surface. The electron donor facilitates directional electron transfer toward the metal oxide surface and slows deleterious back electron transfer. We are currently investigating more elaborate structures with non-absorbing external donors in the outer layer to prepare chromophore-catalyst assembly structures at the interface for possible DSPEC applications.

3.3. Conclusions

We report here a successful, general strategy for synthesizing and characterizing spatially controlled, multicomponent films on mesoporous *nano*TiO_2. The films were prepared by electropolymerization of [**Fe(v-tpy)$_2$**]$^{2+}$ on both *nano*TiO_2 and **RuPdvb**-derivatized mesoporous *nano*TiO_2. The Ru:Fe ratio in the overlayer structures can be controlled by the number of reductive electrochemical scan cycles. EDS measurements reveal the films to be inhomogeneous in depth with regard to total concentration and Ru:Fe ratio.

The photostability of the *nano*TiO_2|-**RuPdvb**-*poly*-[**Fe(v-tpy)$_2$**]$^{2+}$ interfacial structures is enhanced by factors of up to 30 compared to the surface-bound complex alone. Notably, surface stabilization is enhanced relative to an ALD overlayer strategy based on Al_2O_3.

Based on the results of transient absorbance measurements on *nano*TiO_2|-**RuPdvb**-*poly*-[**Fe(v-tpy)$_2$**]$^{2+}$, excitation of surface-bound Ru^{II} is followed by electron injection and both fast and slow outside-to-inside $Fe^{II} \rightarrow Ru^{III}$ electron transfer. These results show that the electropolymerized overlayer structure facilitates directional electron transfer toward the metal oxide surface and slows back electron transfer from $TiO_2(e^-)$. The generality of the electropolymerized overlayer approach for synthesis of water stable, multicomponent films is notable and is currently being exploited to prepare interfacial structures for electrocatalysis and DSPEC applications.

3.4. Experimental

3.4.1. Sample Preparation

Materials. [Ru(1,4-cyclooctadiene)Cl_2]$_n$,[31,46] 5,5'-divinyl-2,2'-bipyridine,[47] [Ru(bpy)$_2$(4,4'-dpbpy)]$^{2+}$ (**RuP,** chloride salt),[31] and [**Fe(v-tpy)$_2$**][PF_6]$_2$ [25] were synthesized according to previously published procedures. Distilled water was further purified by using a Milli-Q Ultrapure water purification system. All other reagents were ACS grade and used without further purification. Fluoride-doped tin oxide (FTO)-coated glass (Hartford Glass; sheet resistance 15 Ω cm^{-2}) was cut into 10 mm × 40 mm strips and used as the substrate for ZrO_2 and TiO_2 nanoparticle films. Microwave reactions were carried out using a CEM MARS microwave reactor. A CEM HP-500 Plus Teflon-coated microwave vessel (100 mL) was used at a power setting of 400 W. The vessel was rotated and stirred throughout the microwave procedure. The pressure of the reaction vessel was monitored throughout the reaction, and never exceeded 300 PSI.

Metal Oxide Films. *nano*TiO_2[48] films and *nano*ZrO_2[49] films, typically 7 μm thick (~20 nm particle diameter), with a coating area of roughly 10 mm × 15 mm, were synthesized according to literature procedures. Dye adsorption isotherms on *nano*TiO_2 were obtained by soaking the

films in methanol solutions of **RuPdvb**, [Ru(5,5'-dimethyl-2,2'-bipyridine)$_2$(4,4'-dpbpy)]$^{2+}$ (**RuPdmb**), and **RuP** at concentrations of 10, 20, 50, 100, 150, and 200 μM. The slides were then removed, rinsed with methanol, and dried over a stream of nitrogen.

Absorption spectra were obtained by placing the dry derivatized films perpendicular to the detection beam path of the spectrophotometer. The expression, $\Gamma = A(\lambda) \times (\varepsilon(\lambda) \times 1000)^{-1}$, was used to calculate surface coverages.[50] Molar extinction coefficients (ε) in H_2O were used; A(λ) was the absorbance at the MLCT λ_{max}. Maximum surface coverages (Γ_{max}) and surface binding constants (K_{ad}) on TiO_2 for **RuPdvb**, **RuPdmb**, and **RuP** were obtained by use of the Langmuir isotherm (**Equation 3.1**) with [X] the concentration of complex in the loading solution.[32] All subsequent measurements were carried out on films loaded from methanol solutions of 100 μM in ruthenium complex, which gave complete surface coverage ($\Gamma = 8 \times 10^{-8}$ mol cm^{-2}).

3.4.2. Synthesis

Ru(5,5'-divinyl-2,2'-bipyridine)$_2$(Cl)$_2$. This compound was synthesized according to a literature procedure with minor modification.[31] [Ru(1,4-cyclooctadiene)Cl$_2$]$_n$ (0.074 g, 0.24 mmol) and 5,5'-divinyl-2,2'-bipyridine (0.1 g, 0.5 mmol) were added to 1,2-dichlorobenzene (20 mL). The suspension was thoroughly degassed, and then heated to 160 °C for 2 hours under an atmosphere of argon. The reaction was cooled to room temperature and ether (~60 mL) was added. The solid was filtered, washed with ether, dried and collected. This complex was used without further purification (0.134 g, 95%). ^{1}H NMR (600 MHz, DMSO) δ (ppm) 9.96 (s, 2H), 8.65 (d, 2H), 8.49 (d, 2H), 8.28 (d, 2H), 7.91 (d, 2H), 7.48 (s, 2H), 7.00 (dd, 2H), 6.50 (dd, 2H), 6.23 (d, 2H), 5.78 (d, 2H), 5.64 (d, 2H), 5.34 (d, 2H).

[*Ru(5,5'-divinyl-2,2'-bipyridine)$_2$([2,2'-bipyridine]-4,4'-diyldiphosphonic acid)][Cl]$_2$, (**RuPdvb**)*. Ru(5,5'-divinyl-2,2'-bipyridine)$_2$(Cl)$_2$ (0.075 g, 0.13mmol) and tetraethyl [2,2'-

bipyridine]-4,4'-diylbis(phosphonate) (0.054 g, 0.13 mmol) in ethanol (~20 mL) were heated to 160 °C over 5 minutes and then heated for 20 minutes at 160 °C in a microwave reactor. The reaction was cooled, filtered, and taken to dryness by a rotary evaporator. The solid was triturated with ether, collected, and air-dried and used without further purification. The esterified product (0.054 g, 0.053 mmol) was dissolved in anhydrous acetonitrile (~15 mL). Bromotrimethylsilane (0.07 mL, 0.53 mmol) was added, and the reaction was allowed to stir at 40 °C for 3 days under an argon atmosphere. The acetonitrile was removed under vacuum, anhydrous methanol (~15 mL) was added, and the solution was stirred at 40 °C for 30 minutes. The methanol was removed under vacuum, and the resulting solid was triturated with acetone, filtered, and washed with acetone. The solid was further purified by size exclusion chromatography (Sephadex LH-20) with 1:1 methanol:water as eluent. Similar fractions (based on UV-visible absorption spectroscopy) were combined, and the solvent was removed by rotary evaporation. The dark-red solid was triturated with ether, filtered and dried under vacuum (0.041g, 86%). ^{1}H NMR (600 MHz, D_2O) δ (ppm) 8.75 (d, 2H), 8.43 (m, 4H), 8.16 (d, 2H), 8.12 (d, 2H), 7.93 (m, 2H), 7.62 (s, 2H), 7.61 (s, 2H), 7.55 (m, 2H), 6.50 (d, 2H), 6.46 (d, 2H), 5.82 (d, 2H), 5.77 (d, 2H), 5.42 (t, 4H). ^{31}P NMR (D_2O) δ 6.68. HR-ESI-MS (Methanol; 20% H_2O with 1% HCOOH): m/z = 417.0528^{2+} = 834.1056, $[M - 2Cl^-]^{2+}$ = 834.1059. Anal. Found (Calc.) $C_{39}H_{52}Cl_2N_6O_{14}P_2Ru$: C 44.08 (43.99); H 4.93 (4.36); N 7.91 (7.81).

Ru(5,5'-dimethyl-2,2'-bipyridine)$_2$(Cl)$_2$. This complex was synthesized with the same procedure as for Ru(5,5'-divinyl-2,2'-bipyridine)$_2$(Cl)$_2$ but using 5,5'-dimethyl-2,2'-bipyridine (1.19 g, 6.46 mmol). It was isolated in 93% yield (1.79 g).

*[Ru(5,5'-dimethyl-2,2'-bipyridine)$_2$([2,2'-bipyridine]-4,4'-diyldiphosphonic acid)][Cl]$_2$, **(RuPdmb)***. This complex was synthesized by using the same procedure as for [Ru(5,5'-divinyl-

2,2'-bipyridine)$_2$([2,2'-bipyridine]-4,4'-diyldiphosphonic acid)](Cl)$_2$ but with Ru(5,5'-dimethyl-2,2'-bipyridine)$_2$(Cl)$_2$ (0.104 g, 0.17 mmol) as the starting material. The final product was isolated in 80% yield (0.116 g). ^{1}H NMR (400 MHz, D_2O) δ (ppm) 8.70 (d, 2H), 8.33 (d, 4H), 7.84 (d, 4H), 7.78 (m, 2H), 7.50 (d, 4H), 2.15 (s, 12H). ^{31}P NMR (D_2O) δ 6.39. HR-ESI-MS (Methanol; 20% H_2O with 1% HCOOH): m/z = 785.009$^+$, [M – 2Cl$^-$ – H$^+$]$^+$ = 785.103; m/z = 807.0823^{2+} = 1614.1646, [M – 2Cl$^-$ – 2H$^+$ + Na$^+$]$^{2+}$ = 1614.172. Anal. Found (Calc.) for $C_{34}H_{48}Cl_2N_6O_{13}P_2Ru$: C 41.43 (41.56); H 4.70 (4.92); N 8.53 (8.55).

3.4.3. Electrochemical and Spectroscopic Characterization

Electrochemistry. Electrochemical measurements were conducted on a CH Instruments 660D potentiostat with a Pt-mesh or Pt-wire counter electrode, and a Ag/$AgNO_3$ (0.01 M $AgNO_3$/0.1 M tetra-n-butylammonium hexafluorophosphate ([TBA]PF_6) in CH_3CN; -0.09 V vs. $Fc^{+/0}$)[51] or Ag/AgCl (3 M NaCl; 0.198 V vs. NHE) reference electrode. $E_{1/2}$ values were obtained from the peak currents in square-wave voltammograms or from averaging cathodic and anodic potentials at peak current values ($E_{p,c}$ and $E_{p,a}$) in cyclic voltammograms. Reductive electropolymerization was carried out in anhydrous CH_3CN (dried over 3 Å molecular sieves) with 0.1 M [TBA]PF_6 as the supporting electrolyte under an atmosphere of argon. Solutions were deaerated with argon for at least 5 minutes prior to reductive electrochemical cycling.

Scanning electron microscopy (SEM) and energy dispersive X-ray spectroscopy (EDS) results were obtained on a FEI Helios 600 Nanolab Dual Beam System equipped with an Oxford instruments, INCA PentaFET-x3 detector. A cross section was taken of mesoporous *nano*TiO_2 loaded with **RuPdvb** and then reductively cycled 50 or 300 times in the presence of [**Fe(v-tpy)$_2$**]$^{2+}$. Surface images were taken at 20 kV with a 0.69 nA beam current. Three EDS spectra were obtained at the polymer/solution interface (top), in the bulk of TiO_2 nanoparticles (middle),

and at the *nano*TiO_2/FTO interface (bottom) of the cross section (see Associated Content) unless otherwise noted.

Absorption spectra were recorded on an Agilent 8453 UV-visible photo diode array spectrophotometer (adsorption isotherms and spectroelectrochemistry), or a Varian Cary 50 UV-visible spectrophotometer (photostability). Extinction coefficients for the complexes in aqueous H_2O were determined from the absorption spectra of solutions having a known concentration of complex.

Transient absorption (TA) measurements were carried out by inserting derivatized thin films at a 45° angle into a standard 10 mm path length square cuvette containing pH 1 aqueous solutions (0.1 M $HClO_4$). The top of the cuvette was fit with an O-ring seal with a Kontes valve inlet to allow the contents to be purged with Argon. TA experiments were performed by using nanosecond laser pulses produced by a Spectra-Physics Quanta-Ray Lab-170 Nd:YAG laser combined with a VersaScan OPO (532 nm, 5-7 ns, operated at 1 Hz, beam diameter 0.5 cm, ~5 mJ/pulse) integrated into a commercially available Edinburgh LP920 laser flash photolysis spectrometer system. White light probe pulses generated by a pulsed 450 W Xe lamp were passed through the sample, focused into the spectrometer (5 nm bandwidth), then detected by a photomultiplier tube (Hamamatsu R928). Appropriate filters were placed before the detector to reject unwanted scattered light. Detector outputs were processed using a Tektronix TDS3032C Digital Phosphor Oscilloscope interfaced to a PC running Edinburgh's L900 (version 7.0) software package. Single wavelength kinetic data were the result of averaging 50 laser shots and were fit with the Edinburgh software. The data were fit over the first 10 ms by using the tri-exponential function in **Equation 3.12** and the weighted average lifetime ($\langle\tau\rangle$) calculated from

Equation 3.13 and **Equation 3.14**. The results of multiple measurements revealed variations in the kinetic fit parameters of <5% with general trends reproduced in two separate trials.

Electron injection efficiencies (Φ_{inj}) were calculated by using **Equation 3.15** with *nano*TiO_2|-**RuP** as the reference. **RuP** bound to *nano*TiO_2 is known to have an injection yield of 100% in aqueous pH 1 $HClO_4$.[8]

Equation 3.15

$$\Phi_{inj} = \frac{\Delta A_{sam}(\lambda_p)/\Delta\varepsilon_{sam}(\lambda_p)/(1-10^{-A_{sam}(\lambda_{ex})})}{\Delta A_{ref}(\lambda_p)/\Delta\varepsilon_{ref}(\lambda_p)/(1-10^{-A_{ref}(\lambda_{ex})})}$$

In **Equation 3.15**, ΔA is transient absorption amplitude, $\Delta\varepsilon$ is the molar extinction coefficient difference between ground and excited/oxidized states ($\Delta\varepsilon$ = –6,500 M^{-1} cm^{-1} at 400 nm for *nano*TiO_2|-**RuP** and $\Delta\varepsilon$ = –11,200 M^{-1} cm^{-1} at 580 nm for *nano*TiO_2|-*poly*-[**Fe(v-tpy)$_2$**]$^{2+}$). At the probe wavelength, λ_p (= $1 - 10^{(A(\lambda ex))}$) is the sample absorptance at the excitation wavelength (λ_{ex} = 532 nm).

Steady-State Emission. Steady-state emission data were collected at room temperature with an Edinburgh FLS920 spectrometer with emitted light first passing through a 495 nm long-pass color filter, then a single grating (1800 l/mm, 500 nm blaze) Czerny-Turner monochromator (5 nm bandwidth) and finally detected by a Peltier-cooled Hamamatsu R2658P photomultiplier tube. The samples were excited using light output from a housed 450 W Xe lamp / single grating (1800 l/mm, 250 nm blaze) Czerny-Turner monochromator combination with 5 nm bandwidth.

Photostability. Photostability measurements were performed by a previously reported procedure.[9] The light from a Royal Blue (455 nm, fwhm ~30 nm, 475 mW cm^{-2}) Mounted High Power LED (Thorlabs, Inc., M455L2) powered by a T-Cube LED Driver (Thorlabs, Inc.,

LEDD1B) was focused to a 2.5 mm diameter spot size by a focusing beam probe (Newport Corp. 77646) outfitted with a second lens (Newport, Corp 41230). Light output was directed onto the derivatized thin films placed at 45° in a standard 10 mm path length cuvette containing 3 mL of the solutions of interest. The illumination spot was adjusted to coincide both with the thin films and the perpendicular beam path of a Varian Cary 50 UV-visible spectrophotometer. The absorption spectrum (360–800 nm) of the film was obtained every 15 minutes during 16 hours of illumination. The incident light intensity was measured with a thermopile detector (Newport Corp 1918-C meter and 818P-020-12 detector). The solution temperature, 22 ± 2 °C, was consistent throughout the duration of the experiment.

The absorption-time traces at 480 nm could be satisfactorily fit with the biexponential function in **Equation 3.3**. For comparative purposes, the results of the multi-exponential analysis were represented by a single rate constant, the disappearance or desorption rate constant, k_{des}, by calculating the weighted average lifetime (‹τ›) by application of **Equation 3.4**. In **Equation 3.4**, A_i and τ_i are the contributions to the absorbance amplitude and lifetime of component *i*.

3.5. Acknowledgements

K.H. acknowledges support from the UNC EFRC "Center for Solar Fuels", an Energy Frontier Research Center funded by the U.S. Department of Energy, Office of Science, Office of Basic Energy Sciences, under Award No. DE-SC0001011. A.M.L. acknowledges support from the U.S. Department of Energy, Office of Science, Office of Basic Energy Sciences, under Award No. DE-FG02-06ER15788. D.L.A. acknowledges support from a fellowship from the Department of Energy Office of Science Graduate Fellowship Program (DOE SCGF), made possible in part by the American Recovery and Reinvestment Act of 2009, administered by ORISE-ORAU under Contract No. DE-AC05-06OR23100.

3.6. Associated Content

Associated content, including EDS spectra, can be found in Appendix A.

REFERENCES

(1) Hagfeldt, A.; Boschloo, G.; Sun, L.; Kloo, L.; Pettersson, H. *Chem. Rev.* **2010**, *110*, 6595.

(2) Song, W.; Chen, Z.; Brennaman, M. K.; Concepcion, J. J.; Patrocinio, A. O. T.; Murakami Iha, N. Y.; Meyer, T. J. *Pure Appl. Chem.* **2011**, *83*, 749.

(3) Youngblood, W. J.; Lee, S.-H. A.; Maeda, K.; Mallouk, T. E. *Acc. Chem. Res.* **2009**, *42*, 1966.

(4) Xu, Y.; Eilers, G.; Borgström, M.; Pan, J.; Abrahamsson, M.; Magnuson, A.; Lomoth, R.; Bergquist, J.; Polívka, T.; Sun, L.; Sundström, V.; Styring, S.; Hammarström, L.; Åkermark, B. *Chem. Eur. J.* **2005**, *11*, 7305.

(5) Young, K. J.; Martini, L. A.; Milot, R. L.; Snoeberger Iii, R. C.; Batista, V. S.; Schmuttenmaer, C. A.; Crabtree, R. H.; Brudvig, G. W. *Coord. Chem. Rev.* **2012**, *256*, 2503.

(6) Song, W.; Chen, Z.; Glasson, C. R. K.; Hanson, K.; Luo, H.; Norris, M. R.; Ashford, D. L.; Concepcion, J. J.; Brennaman, M. K.; Meyer, T. J. *ChemPhysChem* **2012**, *13*, 2882.

(7) Eisenberg, R.; Gray, H. B. *Inorg. Chem.* **2008**, *47*, 1697.

(8) Hanson, K.; Brennaman, M. K.; Ito, A.; Luo, H.; Song, W.; Parker, K. A.; Ghosh, R.; Norris, M. R.; Glasson, C. R. K.; Concepcion, J. J.; Lopez, R.; Meyer, T. J. *J. Phys. Chem. C* **2012**, *116*, 14837.

(9) Hanson, K.; Brennaman, M. K.; Luo, H.; Glasson, C. R.; Concepcion, J. J.; Song, W.; Meyer, T. J. *ACS Appl. Mater. Interfaces* **2012**, *4*, 1462.

(10) Moore, G. F.; Blakemore, J. D.; Milot, R. L.; Hull, J. F.; Song, H.-e.; Cai, L.; Schmuttenmaer, C. A.; Crabtree, R. H.; Brudvig, G. W. *Energy Environ. Sci.* **2011**, *4*, 2389.

(11) Gao, Y.; Ding, X.; Liu, J.; Wang, L.; Lu, Z.; Li, L.; Sun, L. *J. Am. Chem. Soc.* **2013**, *135*, 4219.

(12) Concepcion, J. J.; Jurss, J. W.; Hoertz, P. G.; Meyer, T. J. *Angew. Chem. Int. Ed.* **2009**, *48*, 9473.

(13) Ashford, D. L.; Song, W.; Concepcion, J. J.; Glasson, C. R. K.; Brennaman, M. K.; Norris, M. R.; Fang, Z.; Templeton, J. L.; Meyer, T. J. *J. Am. Chem. Soc.* **2012**, *134*, 19189.

(14) Hanson, K.; Torelli, D. A.; Vannucci, A. K.; Brennaman, M. K.; Luo, H.; Alibabaei, L.; Song, W.; Ashford, D. L.; Norris, M. R.; Glasson, C. R. K.; Concepcion, J. J.; Meyer, T. J. *Angew. Chem., Int. Ed.* **2012**, *51*, 12782.

(15) Brown, D. G.; Schauer, P. A.; Borau-Garcia, J.; Fancy, B. R.; Berlinguette, C. P. *J. Am. Chem. Soc.* **2013**, *135*, 1692.

(16) Oyama, N.; Anson, F. C. *J. Am. Chem. Soc.* **1979**, *101*, 3450.

(17) Murray, R. W. *Acc. Chem. Res.* **1980**, *13*, 135.

(18) Cosnier, S.; Deronzier, A.; Moutet, J. C. *J. Electroanal. Chem. Interfacial Electrochem.* **1985**, *193*, 193.

(19) Cosnier, S.; Deronzier, A.; Moutet, J. C. *J. Mol. Catal.* **1988**, *45*, 381.

(20) Abruña, H. D. *Coord. Chem. Rev.* **1988**, *86*, 135.

(21) Aranyos, V.; Hjelm, J.; Hagfeldt, A.; Grennberg, H. *J. Chem. Soc., Dalton Trans.* **2001**, 1319.

(22) Abruña, H. D.; Denisevich, P.; Umaña, M.; Meyer, T. J.; Murray, R. W. *J. Am. Chem. Soc.* **1981**, *103*, 1.

(23) Calvert, J. M.; Schmehl, R. H.; Sullivan, B. P.; Facci, J. S.; Meyer, T. J.; Murray, R. W. *Inorg. Chem.* **1983**, *22*, 2151.

(24) Gould, S.; O'Toole, T. R.; Meyer, T. J. *J. Am. Chem. Soc.* **1990**, *112*, 9490.

(25) Ramos Sende, J. A.; Arana, C. R.; Hernandez, L.; Potts, K. T.; Keshevarz-K, M.; Abruña, H. D. *Inorg. Chem.* **1995**, *34*, 3339.

(26) Moss, J. A.; Yang, J. C.; Stipkala, J. M.; Wen, X.; Bignozzi, C. A.; Meyer, G. J.; Meyer, T. J. *Inorg. Chem.* **2004**, *43*, 1784.

(27) Cecchet, F.; Alebbi, M.; Bignozzi, C. A.; Paolucci, F. *Inorg. Chim. Acta* **2006**, *359*, 3871.

(28) Nie, H.-J.; Shao, J.-Y.; Wu, J.; Yao, J.; Zhong, Y.-W. *Organometallics* **2012**, *31*, 6952.

(29) Zhong, Y.-W.; Yao, C.-J.; Nie, H.-J. *Coord. Chem. Rev.* **2013**, *257*, 1357.

(30) Li, M.; Zhang, J.; Nie, H.-J.; Liao, M.; Sang, L.; Qiao, W.; Wang, Z. Y.; Ma, Y.; Zhong, Y.-W.; Ariga, K. *Chem. Commun.* **2013**, *49*, 6879.

(31) Norris, M. R.; Concepcion, J. J.; Glasson, C. R. K.; Fang, Z.; Lapides, A. M.; Ashford, D. L.; Templeton, J. L.; Meyer, T. J. *Inorg. Chem.* **2013**, *52*, 12492.

(32) Langmuir, I. *J. Am. Chem. Soc.* **1918**, *40*, 1361.

(33) Marcus, R. A. *J. Phys. Chem.* **1989**, *93*, 3078.

(34) Ito, A.; Stewart, D. J.; Knight, T. E.; Fang, Z.; Brennaman, M. K.; Meyer, T. J. *J. Phys. Chem. B* **2013**, *117*, 3428.

(35) Katoh, R.; Furube, A.; Yoshihara, T.; Hara, K.; Fujihashi, G.; Takano, S.; Murata, S.; Arakawa, H.; Tachiya, M. *J. Phys. Chem. B* **2004**, *108*, 4818.

(36) Potts, K. T.; Usifer, D. A.; Guadalupe, A.; Abruña, H. D. *J. Am. Chem. Soc.* **1987**, *109*, 3961.

(37) Trammell, S. A.; Meyer, T. J. *J. Phys. Chem. B* **1998**, *103*, 104.

(38) O'Regan, B.; Li, X.; Ghaddar, T. *Energy Environ. Sci.* **2012**, *5*, 7203.

(39) Park, S.-H.; Lim, J.; Song, I. Y.; Atmakuri, N.; Song, S.; Kwon, Y. S.; Choi, J. M.; Park, T. *Adv. Energy Mater.* **2012**, *2*, 219.

(40) Song, W.; Luo, H.; Hanson, K.; Concepcion, J. J.; Brennaman, M. K.; Meyer, T. J. *Energy Environ. Sci.* **2013**, *6*, 1240.

(41) Hanson, K.; Losego, M. D.; Kalanyan, B.; Ashford, D. L.; Parsons, G. N.; Meyer, T. J. *Chem. Mater.* **2013**, *25*, 3.

(42) Juban, E. A.; Smeigh, A. L.; Monat, J. E.; McCusker, J. K. *Coord. Chem. Rev.* **2006**, *250*, 1783.

(43) Durrant, J. R.; Haque, S. A.; Palomares, E. *Coord. Chem. Rev.* **2004**, *248*, 1247.

(44) Piotrowiak, P.; Galoppini, E.; Wei, Q.; Meyer, G. J.; Wiewiór, P. *J. Am. Chem. Soc.* **2003**, *125*, 5278.

(45) Bergeron, B. V.; Kelly, C. A.; Meyer, G. J. *Langmuir* **2003**, *19*, 8389.

(46) Doi, T.; Nagamiya, H.; Kokubo, M.; Hirabayashi, K.; Takahashi, T. *Tetrahedron* **2002**, *58*, 2957.

(47) Liu, Y.; Zhang, S.; Miao, Q.; Zheng, L.; Zong, L.; Cheng, Y. *Macromolecules* **2007**, *40*, 4839.

(48) Lee, S.-H. A.; Abrams, N. M.; Hoertz, P. G.; Barber, G. D.; Halaoui, L. I.; Mallouk, T. E. *J. Phys. Chem. B* **2008**, *112*, 14415.

(49) Song, W.; Glasson, C. R. K.; Luo, H.; Hanson, K.; Brennaman, M. K.; Concepcion, J. J.; Meyer, T. J. *J. Phys. Chem. Lett.* **2011**, *2*, 1808.

(50) Gallagher, L. A.; Serron, S. A.; Wen, X.; Hornstein, B. J.; Dattelbaum, D. M.; Schoonover, J. R.; Meyer, T. J. *Inorg. Chem.* **2005**, *44*, 2089.

(51) Connelly, N. G.; Geiger, W. E. *Chem. Rev.* **1996**, *96*, 877.

CHAPTER 4: WATER OXIDATION BY AN ELECTROPOLYMERIZED CATALYST ON DERIVATIZED MESOPOROUS METAL OXIDE ELECTRODES

4.1. Introduction

Dye-sensitized photoelectrosynthesis cells (DSPECs) offer a potential solution to solar energy storage by using solar energy to directly generate chemical fuels.[1,2] In a DSPEC, the configuration of the chromophore and catalyst is important in enabling rapid electron transfer from the catalyst to the oxidized chromophore following the excitation-electron injection sequence.[3,4]

Multiple strategies have been described for assembling chromophores and catalysts on metal oxide surfaces.[5-12] They typically suffer from difficult synthetic procedures and/or limited stabilities on oxide surfaces.[13,14] Recently, we reported reductive electropolymerization/electro-oligomerization of a vinyl-functionalized polypyridyl complex, [Fe(4'-vinyl-2,2':6',2″-terpyridine)$_2$]$^{2+}$, on bare TiO_2 and on TiO_2 surfaces prederivatized with the vinyl- and phosphonate-functionalized complex, [Ru(5,5'-dvbpy)$_2$(4,4'-dpbpy)]$^{2+}$ (**RuPdvb^{2+}**; 5,5'-dvbpy = 5,5'-divinyl-2,2'-bipyridine; 4,4'-dpbpy = [2,2'-bipyridine]-4,4'-diylbis(phosphonic acid), **Figure 4.1**A).[15,16] The effect of adding the electropolymerized overlayer is dramatic, leading to a 30-fold enhancement in photostability of the surface-bound chromophore relative to the unprotected complex.

Here we describe the utilization of this strategy to introduce the vinyl-functionalized water oxidation catalyst, [Ru(Mebimpy)(5,5'-dvbpy)(OH_2)]$^{2+}$ (**RuOH$_2$$^{2+}$**, Mebimpy = 2,6-bis(1-

methyl-1*H*-benzo[*d*]imidazole-2-yl)pyridine), as the electropolymerized overlayer (**Figure 4.1**A). This procedure provides a basis for preparing stable, catalytically active films both with and without the prebound $\mathbf{RuPdvb}^{2+}$ chromophore on both planar oxide surfaces and in mesoporous, nanoparticle metal oxide films.

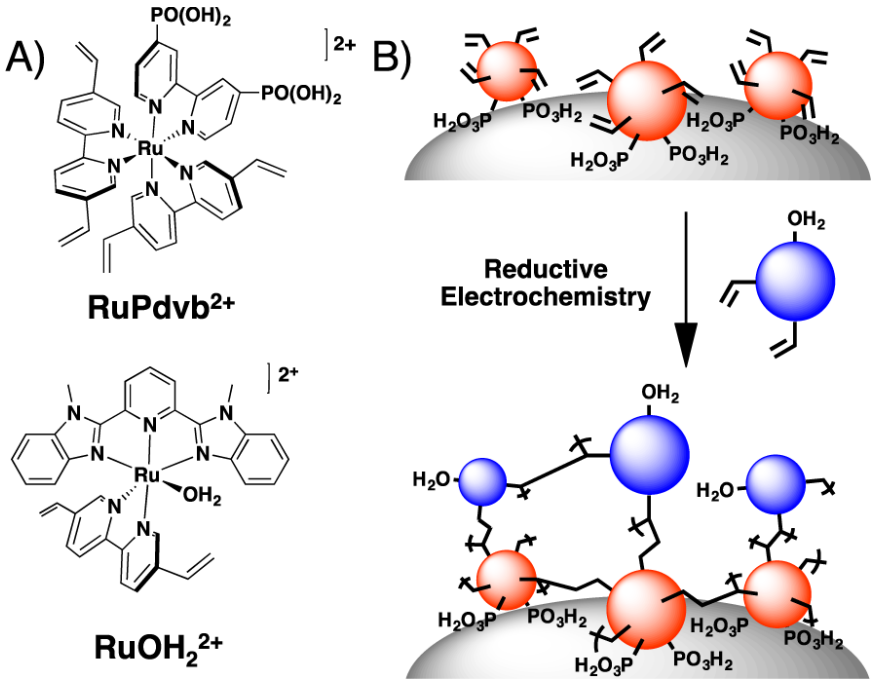

Figure 4.1. A) Structures of $\mathbf{RuPdvb}^{2+}$ and $\mathbf{RuOH_2}^{2+}$. B) Schematic diagram of the surface structure following reductive electropolymerization on *nano*TiO_2|-$\mathbf{RuPdvb}^{2+}$.

4.2. Results and Discussion

The chromophore, $\mathbf{RuPdvb}^{2+}$, and catalyst, $\mathbf{RuOH_2}^{2+}$, were synthesized as previously reported.[5,15] Substitution of coordinated H_2O by CH_3CN was achieved by dissolving $\mathbf{RuOH_2}^{2+}$ in CH_3CN. Vapor diffusion of diethyl ether resulted in X-ray quality crystals of the CH_3CN-substituted complex (**Figure 4.2**). In the structure, the geometry around Ru(II) is a slightly distorted octahedron with bond angles of 174.2° for N1–Ru–N3 and 174.4° for N2–Ru–N6. The length of the vinyl C–C bonds (1.30 Å) and the Ru–N bonds match those of similar complexes.[17]

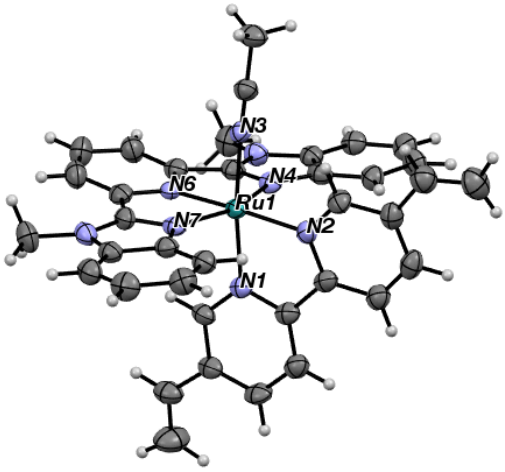

Figure 4.2. Crystal structure of **Ru(NCCH$_3$)$^{2+}$**.

Electropolymerization was conducted in a three-compartment electrochemical cell under an argon atmosphere. All solutions were dried over $MgSO_4$, filtered, and deaerated with argon for 10 minutes before electropolymerization. The working electrodes were planar fluoride-doped tin oxide (FTO), nanocrystalline titanium dioxide (*nano*TiO_2), or nanocrystalline indium tin oxide (*nano*ITO). Working electrodes were either the bare metal oxide or derivatized with **RuPdvb^{2+}** by soaking overnight in methanol solutions of the complex (150 μM).[15] In a typical electropolymerization experiment, the working electrode was cycled in a solution of **RuOH$_2$$^{2+}$** (0.5 mM in complex, 0.1 M [TBA]PF_6/PC; PC = propylene carbonate) from 0 to −1.8 V (vs. $Ag/AgNO_3$) at a scan rate of 100 mV s^{-1} with a 120 s pause between each cycle. PC was used as the electrochemical solvent rather than CH_3CN to avoid displacing the H_2O ligand of **RuOH$_2$$^{2+}$**. Solutions were stirred during and between cycles to promote percolation of **RuOH$_2$$^{2+}$** throughout the mesoporous metal oxides (*nano*ITO and *nano*TiO_2).[15]

Initially, electropolymerization was carried out on FTO electrodes and on FTO derivatized with **RuPdvb^{2+}** (FTO|-**RuPdvb^{2+}**). Surface coverages (Γ) of polymerized **RuOH$_2$$^{2+}$**

on FTO (*poly*$\mathbf{RuOH_2^{2+}}$) were determined by cyclic voltammetry (CV). In these measurements, the integrated charge of the $Ru^{III/II}$ wave and **Equation 4.1** were used to establish Γ in mol cm^{-2}. Surface coverages on FTO|-*poly*$\mathbf{RuOH_2^{2+}}$ and FTO|-$\mathbf{RuPdvb^{2+}}$-*poly*$\mathbf{RuOH_2^{2+}}$ increased linearly with the number of reductive scan cycles (**Figure 4.3**). Under the electropolymerization conditions, one monolayer equivalent (~1×10^{-10} mol cm^{-2} on planar surfaces) of *poly*$\mathbf{RuOH_2^{2+}}$ was deposited every ~2 cycles on both FTO and FTO|-$\mathbf{RuPdvb^{2+}}$. The peak current (i_p) for the *poly*$Ru^{III/II}OH_2$ couple in aqueous 0.1 M $HClO_4$ varied linearly with scan rate for FTO|-$\mathbf{RuPdvb^{2+}}$-*poly*$\mathbf{RuOH_2^{2+}}$ with both 5 and 20 layers of *poly*$\mathbf{RuOH_2^{2+}}$ (**Figure 4.4**), consistent with a non-diffusional surface redox couple.[18]

Equation 4.1

$$\Gamma = \frac{Q}{nFA}$$

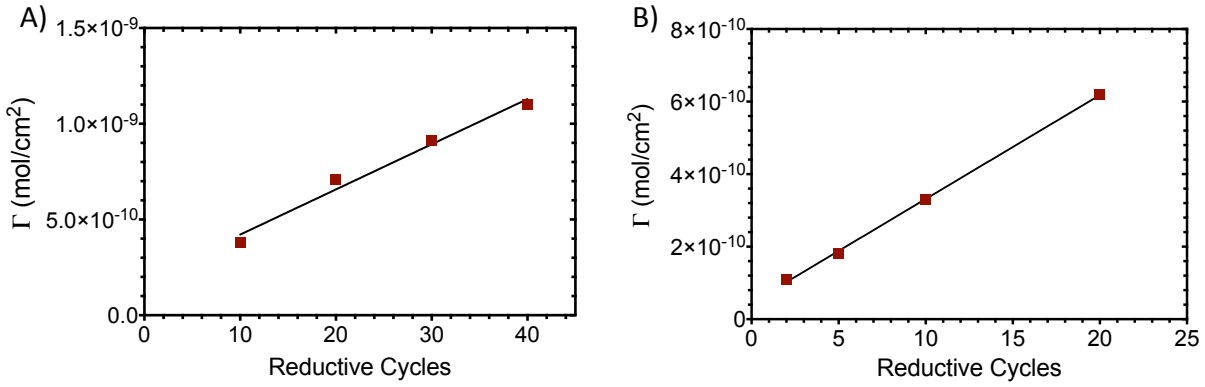

Figure 4.3. Surface coverage of *poly*$\mathbf{RuOH_2^{2+}}$ on A) bare FTO and B) FTO|-$\mathbf{RuPdvb^{2+}}$ as a function of reductive cycles in a 0.5 mM solution of $\mathbf{RuOH_2^{2+}}$ (0.1 M $[TBA]PF_6$/PC). Cycling was performed from 0 to –1.8 V vs. $Ag/AgNO_3$ (ν = 100 mV s^{-1}; Pt counter electrode).

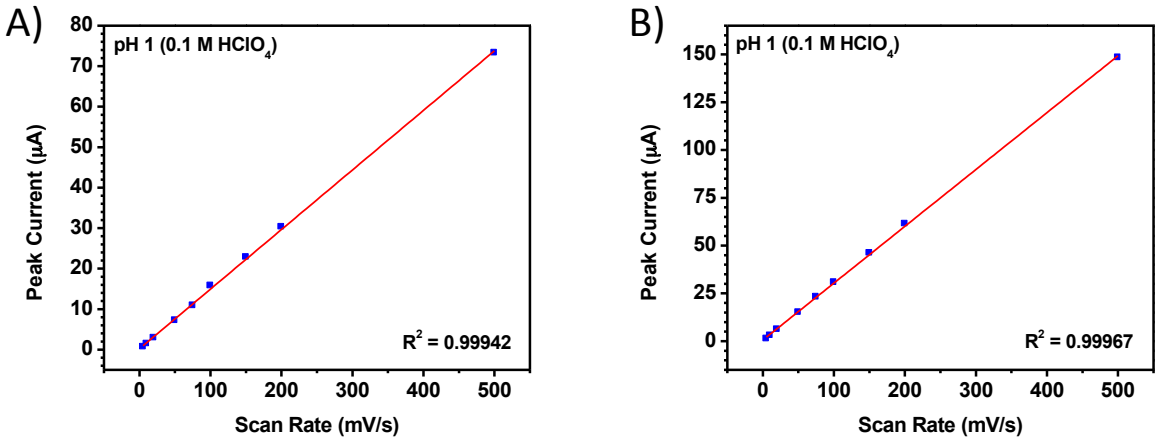

Figure 4.4. Peak current (i_{peak}) for the *poly*$\mathbf{Ru^{III/II}OH_2}$ redox couple as a function of scan rate for samples of FTO|-$\mathbf{RuPdvb^{2+}}$-*poly*$\mathbf{RuOH_2^{2+}}$ with A) 5 monolayer equivalents and B) 20 monolayer equivalents of *poly*$\mathbf{RuOH_2^{2+}}$. CVs were performed in 0.1 M $HClO_4$ with a Pt-wire counter electrode and Ag/AgCl (3 M NaCl) reference electrode.

The pH-dependence of the *poly*$\mathbf{Ru^{III/II}OH_2^{3+/2+}}$ couple on FTO is illustrated in the $E_{1/2}$ vs. pH (Pourbaix) diagram in **Figure 4.5**. Below pH 2.3, the couple is pH independent. Above pH 2.3, $E_{1/2}$ decreases by 51 mV pH^{-1}, suggesting that pK_a = 2.3 for *poly*$\mathbf{Ru^{III}OH_2^{3+}}$. This value is comparable to that of the surface bound catalyst $[Ru(Mebimpy)(4,4'\text{-dpcbpy})(OH_2)]^{2+}$ ($\mathbf{RuPOH_2^{2+}}$: 4,4'-dpcbpy = ([2,2'-bipyridine]-4,4'-diylbis(methylene))bis(phosphonic acid)) on *nano*TiO_2 (pK_a = 2.5).[19] The ensuing *poly*$\mathbf{Ru^{IV}O^{2+}}$/$\mathbf{Ru^{III}OH^{2+}}$ couple is kinetically inhibited and difficult to observe, as documented earlier for related ruthenium complexes.[20] The electrochemical response of the couples is independent of film thickness in FTO|-*poly*$\mathbf{RuOH_2^{2+}}$ in films up to 33 layers (**Figure 4.6**). These results suggest that the environment at the Ru^{II} metal centers in *poly*$\mathbf{RuOH_2^{2+}}$ is open to diffusion of solvent and buffer/electrolyte through the polymer, at least to this level of thickness.

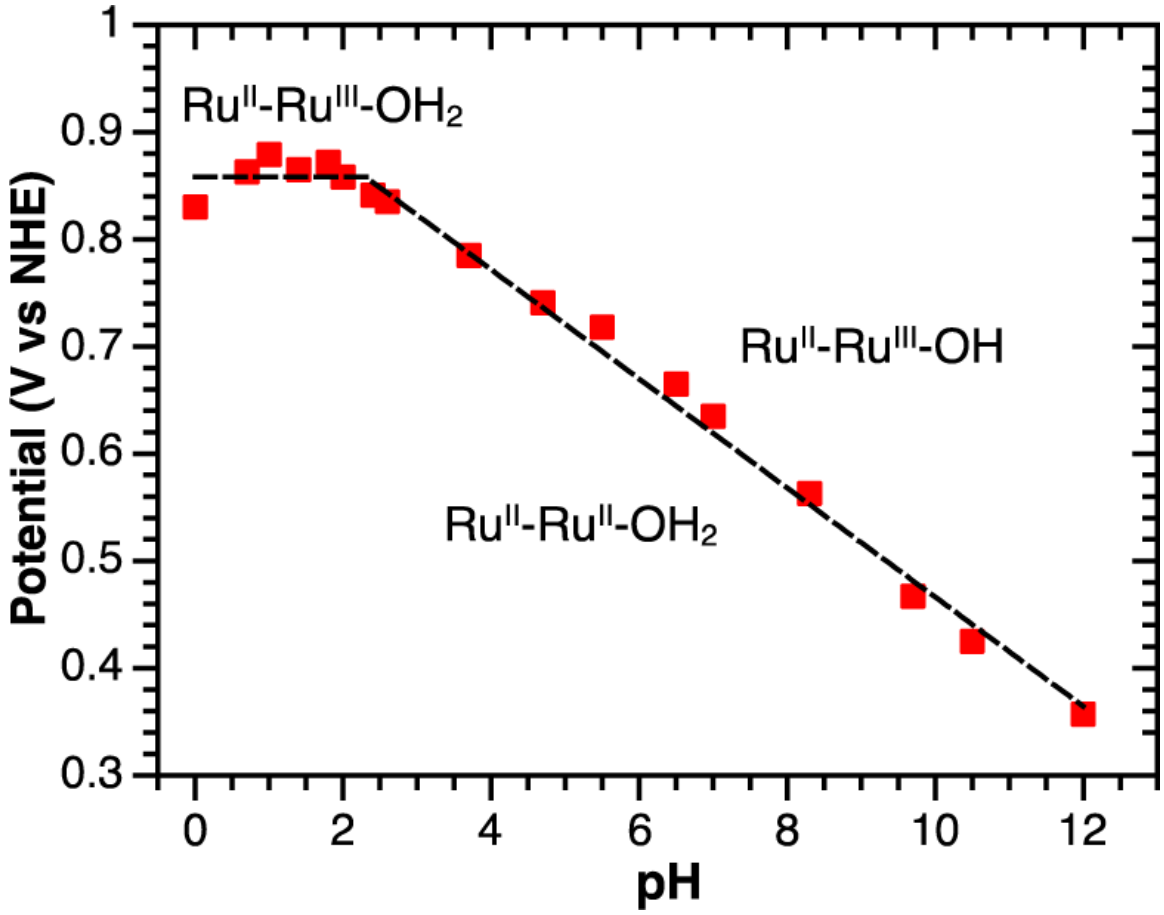

Figure 4.5. $E_{1/2}$ vs. pH diagram for FTO|-**RuPdvb**$^{2+}$-*poly***RuOH$_2$**$^{2+}$ (five layers). $E_{1/2}$ values are cited as potentials at the current maxima in square wave voltammograms. The dashed lines are the fit for the $E_{1/2}$-pH trends for the couples *poly***Ru^{III}OH$_2$**$^{3+}$/**Ru^{II}OH$_2$**$^{2+}$ (~0 mV pH^{-1}) and *poly***Ru^{III}OH**$^{2+}$/**Ru^{II}OH$_2$**$^{2+}$ (51 mV pH^{-1}) with pK_a ≈ 2.3 for *poly*Ru^{III}OH$_2$$^{3+}$ at 23 °C in aqueous 0.5 M $NaClO_4$ with 0.1 M buffer.

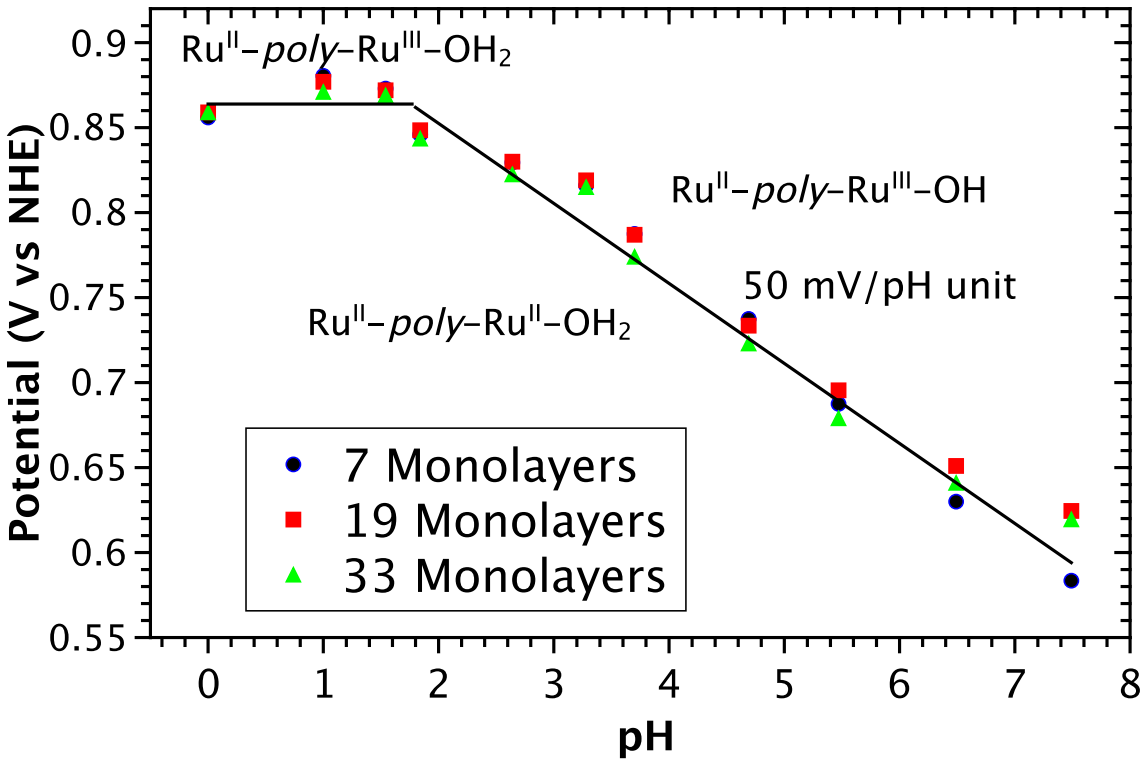

Figure 4.6. $E_{1/2}$ as a function of pH for FTO|-**RuPdvb**$^{2+}$-*poly***RuOH$_2$**$^{2+}$ with 7 (blue circles), 19 (red squares), and 33 (green triangles) monolayer equivalents of *poly***RuOH$_2$**$^{2+}$ deposited onto FTO|-**RuPdvb**$^{2+}$. $E_{1/2}$ values were obtained at peak current maxima in square wave voltammograms. The solid line represents the fit of $E_{1/2}$ values with pH for the **Ru$^{III/II}$(OH$_2$)** and **Ru$^{III/II}$(OH/OH$_2$)** redox couples at 23 °C in 0.5 M $NaClO_4$ and 0.1 M buffer solution.

Electropolymerization was also investigated on *nano*TiO_2 and *nano*TiO_2|-**RuPdvb**$^{2+}$ electrodes (4 to 7 μm thick). The high surface area electrodes allow for UV-visible absorption spectroscopic monitoring of surface coverage based on λ_{max} = 497 nm, $\varepsilon_{497\ nm}$ = 8,200 M^{-1} cm^{-1} for *poly***RuOH$_2$**$^{2+}$. On both surfaces, surface coverage of *poly***Ru^{II}OH$_2$**$^{2+}$ increased linearly with the number of scans (**Figure 4.7**, **Figure 4.8**) for the first 50 reductive cycles. With additional scans, surface coverage continues to increase, but at a slower rate with a plateau reached after ~300 cycles. Surface coverage following 70 and 300 cycles corresponds to one ($\Gamma \approx 7 \times 10^{-8}$ mol cm^{-2} on *nano*TiO_2) and two layers of *poly***Ru^{II}OH$_2$**$^{2+}$, respectively.

A blue-shift in the MLCT absorption maximum from 462 to 453 nm is observed for **RuPdvb**$^{2+}$ in the electropolymerized films (**Figure 4.7**). This shift is consistent with conversion of the π* acceptor vinyl substituents in **RuPdvb**$^{2+}$ to saturated, electron-donating alkyl substituents in the electropolymerized polymers.[15] This observation suggests the formation of direct C–C bonds between surface-bound **RuPdvb**$^{2+}$ and catalyst **RuOH$_2$**$^{2+}$ in the surface assembly.[15,21] No change in the absorption spectrum of *nano*TiO_2|-**RuPdvb**$^{2+}$ was observed following reductive cycling in the absence of **RuOH$_2$**$^{2+}$.

Scanning electron microscopy (SEM) images of *nano*TiO_2|-**RuPdvb**$^{2+}$-*poly***RuOH$_2$**$^{2+}$ films following 60 reductive CVs show that the *nano*TiO_2 films maintain their porosity. A decrease in porosity is observed following 120 reductive cycles. Following 450 reductive cycles, a film of *poly***RuOH$_2$**$^{2+}$ is visible on top of the *nano*TiO_2 substrate. Film formation presumably inhibits diffusion into the pores of the mesoporous oxide, inhibiting further internal polymerization (**Figure 4.7**). Energy-dispersive X-ray spectroscopy (EDS) was used to determine the concentration of Ru at varying depths following 450 reductive scans. These results suggest a relatively uniform concentration of Ru throughout the *nano*TiO_2 substrate.

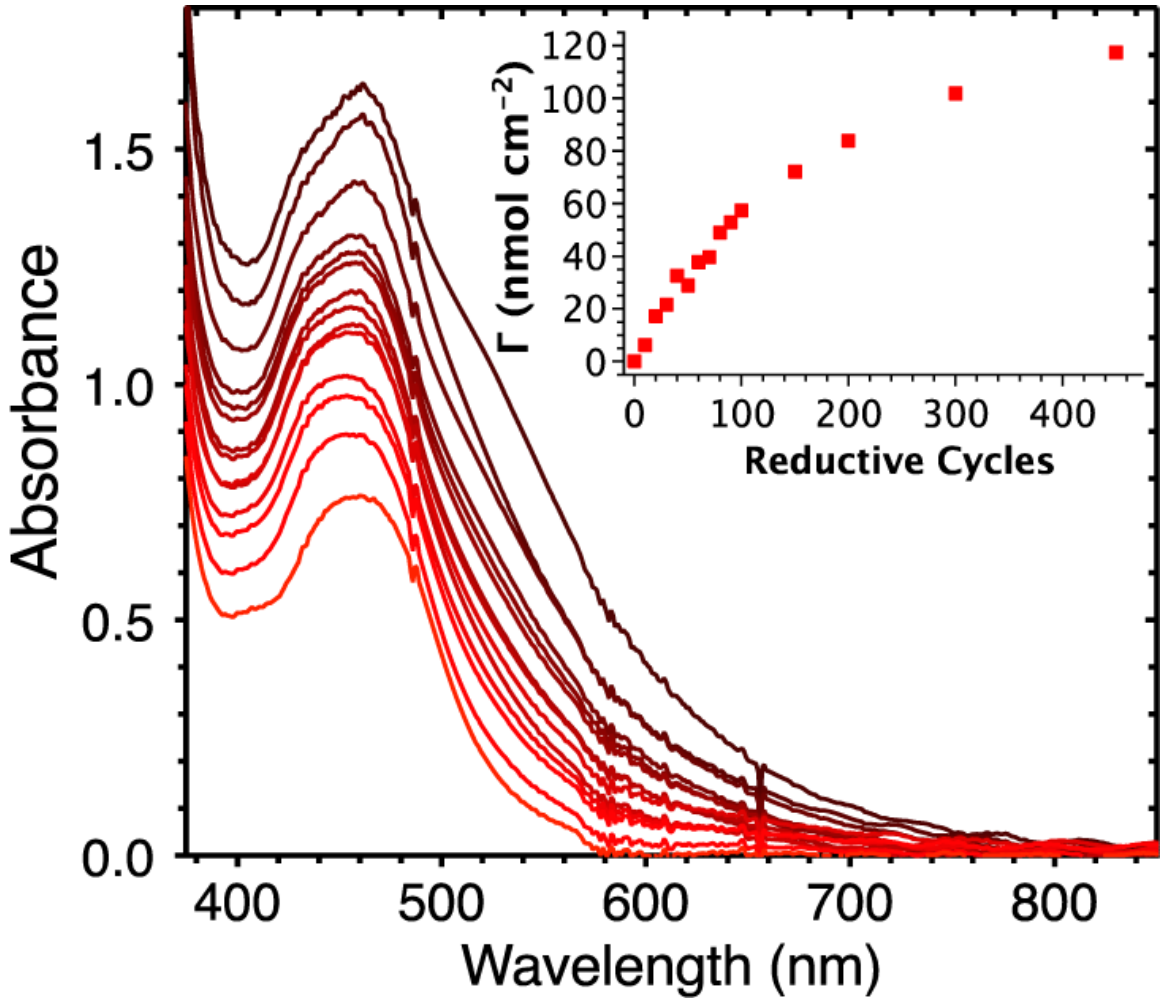

Figure 4.7. UV-visible absorption spectral changes for *nano*TiO_2|-**RuPdvb**$^{2+}$ with an increasing number of reductive scan cycles (0, 10, 20, 30, 40, 50, 60, 70, 80, 90, 100, 150, 200, 300, 450; light red to dark red) in 0.5 mM **RuOH$_2$**$^{2+}$ (0.1 M [TBA]PF_6/PC). Inset: Surface coverage (Γ in nmol cm^{-2}) of *poly***RuOH$_2$**$^{2+}$ versus the number of reductive scan cycles.

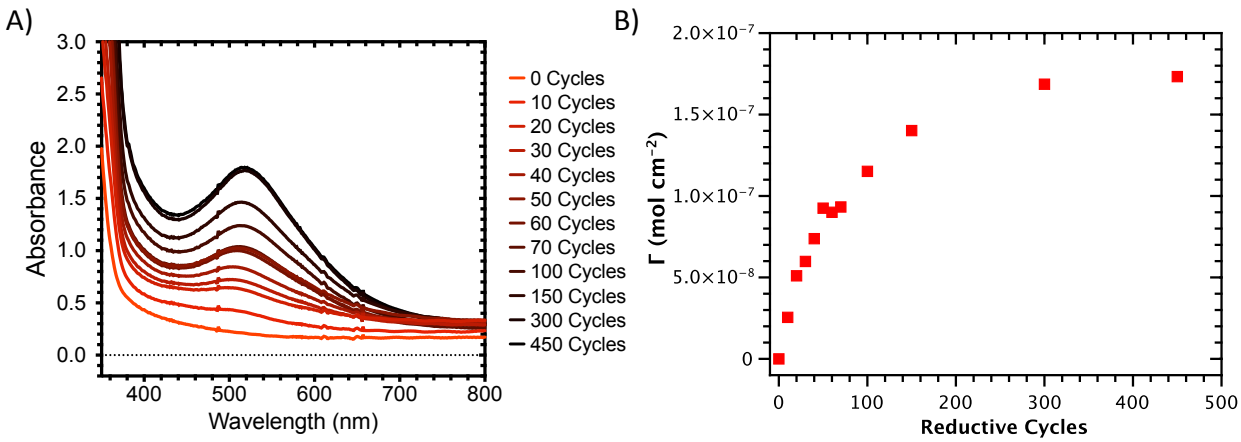

Figure 4.8. A) Changes in UV-visible absorption spectra for *nano*TiO_2 with increasing number of reductive cycles from 0 to –1.8 V (vs. $Ag/AgNO_3$) in 0.5 mM $\mathbf{RuOH_2^{2+}}$ (0.1 M $[TBA]PF_6$/PC). B) Surface coverage of *poly*$\mathbf{RuOH_2^{2+}}$ as a function of reductive cycles.

The photostability of the *nano*TiO_2|-$\mathbf{RuPdvb^{2+}}$-*poly*$\mathbf{RuOH_2^{2+}}$ films was evaluated by a previously published procedure in which the derivatized electrodes were subjected to constant irradiation at 455 nm (fwhm ~30 nm, 475 mW cm^{-2}, ~135 suns at 455 nm).[22] Absorption spectra (360 – 800 nm) of the films were obtained every 15 minutes over 16 hours of irradiation. Results for ~1:1 *nano*TiO_2|-$\mathbf{RuPdvb^{2+}}$-*poly*$\mathbf{RuOH_2^{2+}}$ in aqueous 0.1 M $HClO_4$ demonstrate significant enhancements in surface stability compared to *nano*TiO_2|-$\mathbf{RuP^{2+}}$ ($\mathbf{RuP^{2+}}$ = $Ru(bpy)_2(4,4'\text{-}dpbpy)]^{2+}$, **Figure 4.9**). Following 16 hours of irradiation, the surface coverage of the chromophore in *nano*TiO_2|-$\mathbf{RuP^{2+}}$ decreased by ~70% while only ~10% was lost for *nano*TiO_2|-$\mathbf{RuPdvb^{2+}}$-*poly*$\mathbf{RuOH_2^{2+}}$ (**Figure 4.10**). A 15-fold enhancement of stability was observed for *nano*TiO_2|-$\mathbf{RuPdvb^{2+}}$-*poly*$\mathbf{RuOH_2^{2+}}$ films ($k_{des} = 2.8 \times 10^{-5}$ s^{-1}; k_{des} is the rate constant for loss of the chromophore from the surface) compared to *nano*TiO_2|-$\mathbf{RuP^{2+}}$ ($k_{des} > 30 \times 10^{-5}$ s^{-1}) at pH 4.7 (0.1 M HOAc/NaOAc and 0.5 M $NaClO_4$), **Figure 4.11**.[14,15,22]

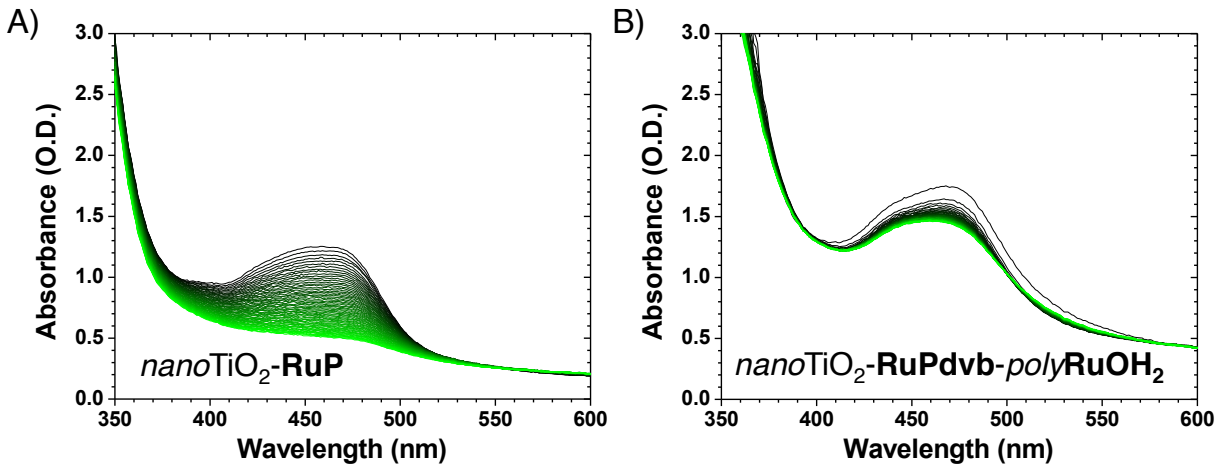

Figure 4.9. Changes in the absorption spectrum of *nano*TiO_2|-RuP^{2+} A) and *nano*TiO_2|-**RuPdvb**$^{2+}$-*poly***RuOH**$_2^{2+}$ following 70 reductive cycles (B, ~1:1 chromophore:catalyst) in aqueous 0.1 M $HClO_4$ under constant 455 nm irradiation (475 mW cm^{-2}) from 0 hours (green) to 16 hours (black) recorded every 15 minutes.

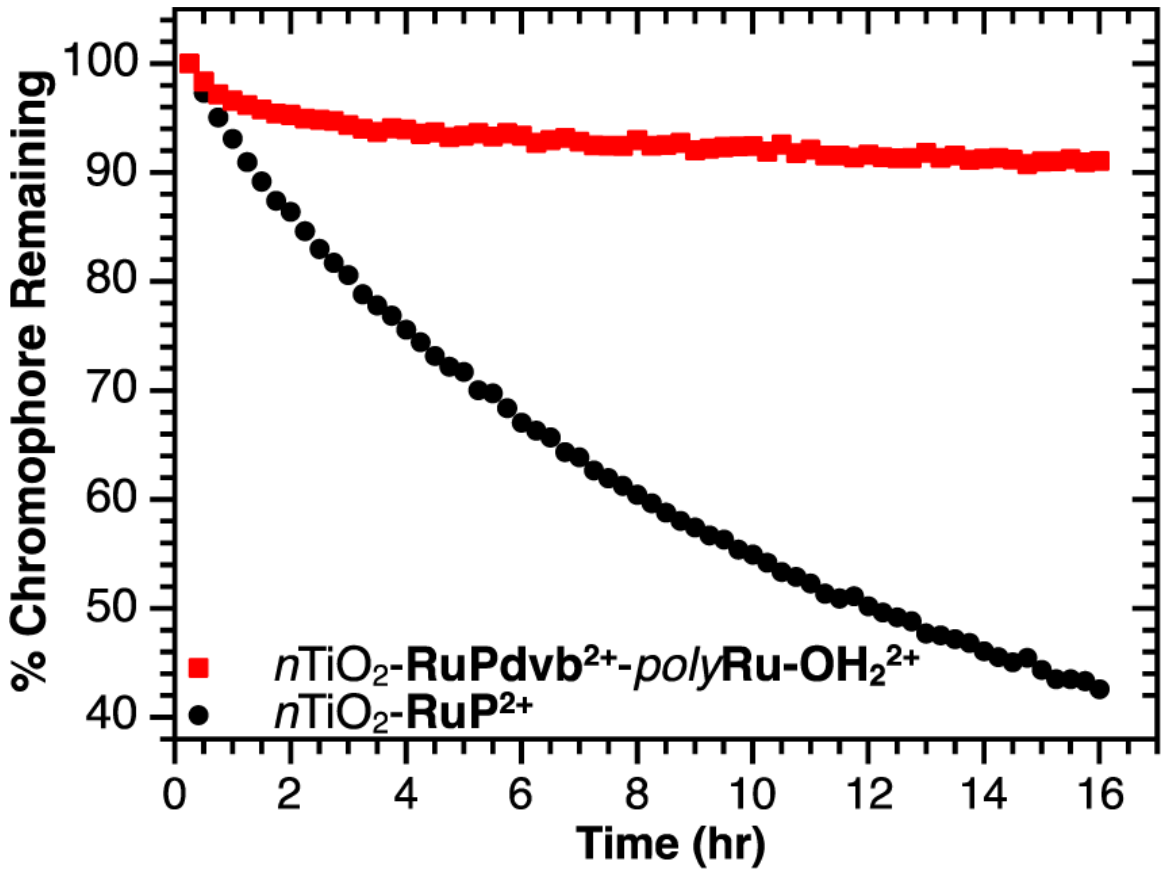

Figure 4.10. Variation of surface coverage as a function of irradiation time at 475 mW cm^{-2} at 455 nm over a 16 hour photolysis period in aqueous 0.1 M $HClO_4$. Loss from the surfaces was monitored by absorbance changes at 453 nm (ε_{453} = 13,500 M^{-1} cm^{-1}).

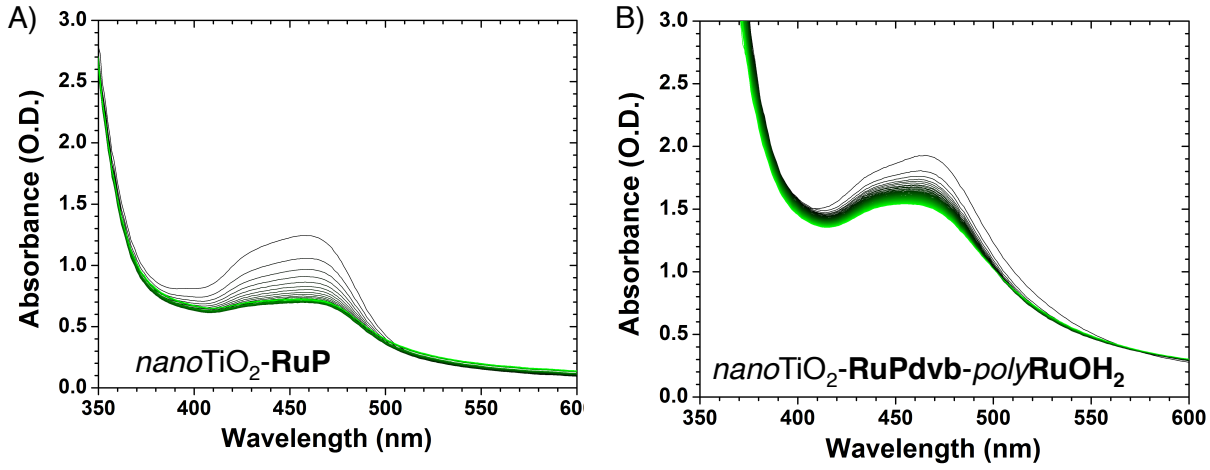

Figure 4.11. Changes in the absorption spectrum of A) *nano*TiO_2|-RuP^{2+}; and B) *nano*TiO_2|-**RuPdvb**$^{2+}$-*poly***RuOH$_2$**$^{2+}$ following 70 reductive cycles (~1:1 chromophore:catalyst) in pH 4.7 (0.1 M HOAc/NaOAc, 0.5 M $NaClO_4$) under constant 455 nm irradiation (475 mW cm^{-2}) from 0 hours (green) to 16 hours (black) recorded every 15 minutes.

Electrocatalytic water oxidation was investigated on *nano*ITO|-**RuPdvb**$^{2+}$-*poly***RuOH$_2$**$^{2+}$ by CV measurements. At pH 4.7 (0.1 M HOAc/NaOAc, 0.5 M $NaClO_4$) oxidative waves appear at $E_{1/2}$ = 0.75 and 1.02 V (vs. NHE) for the –**Ru^{II}-Ru^{III}(OH)**$^{4+}$/–**Ru^{II}-Ru^{II}(OH$_2$)**$^{4+}$ and –**Ru^{II}-Ru^{IV}(O)**$^{4+}$/–**Ru^{II}-Ru^{III}(OH)**$^{4+}$ couples, respectively (**Figure 4.12**). An additional wave appears at $E_{1/2}$ = 1.38 V for the –**Ru^{III}-Ru^{IV}(O)**$^{5+}$/–**Ru^{II}-Ru^{IV}(O)**$^{4+}$ redox couple. Spectroelectrochemical measurements on *nano*ITO|-**RuPdvb**$^{2+}$-*poly***RuOH$_2$**$^{2+}$ in aqueous 0.1 M $HClO_4$ are consistent with the loss of MLCT absorptions in the visible region and with other characteristic spectral changes following oxidation of –**Ru^{II}-Ru^{II}(OH$_2$)**$^{4+}$ to –**Ru^{II}-Ru^{III}(OH$_2$)**$^{5+}$, –**Ru^{II}-Ru^{III}(OH$_2$)**$^{5+}$ to –**Ru^{II}-Ru^{IV}(O)**$^{4+}$, and –**Ru^{II}-Ru^{IV}(O)**$^{4+}$ to –**Ru^{III}-Ru^{IV}(O)**$^{5+}$ (**Figure 4.13**).

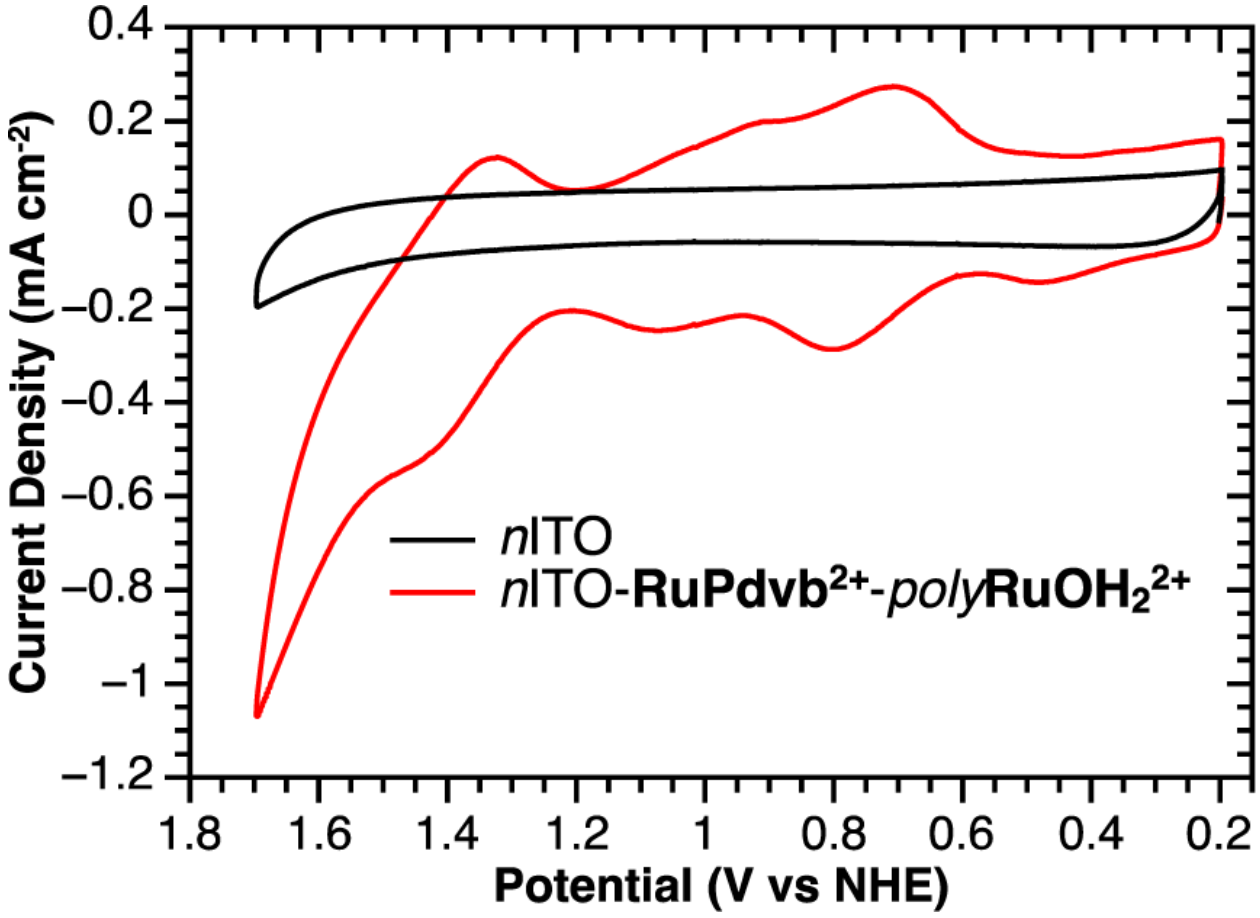

Figure 4.12. Cyclic voltammograms at 20 mV s^{-1} for *nano*ITO|-**RuPdvb**$^{2+}$-*poly***RuOH**$_2^{2+}$ (red) and *nano*ITO (black) in pH 4.7 aqueous solution (0.1 M HOAc/NaOAc, 0.5 M $NaClO_4$); Pt-mesh counter electrode and Ag/AgCl reference electrode (0.197 V vs. NHE).

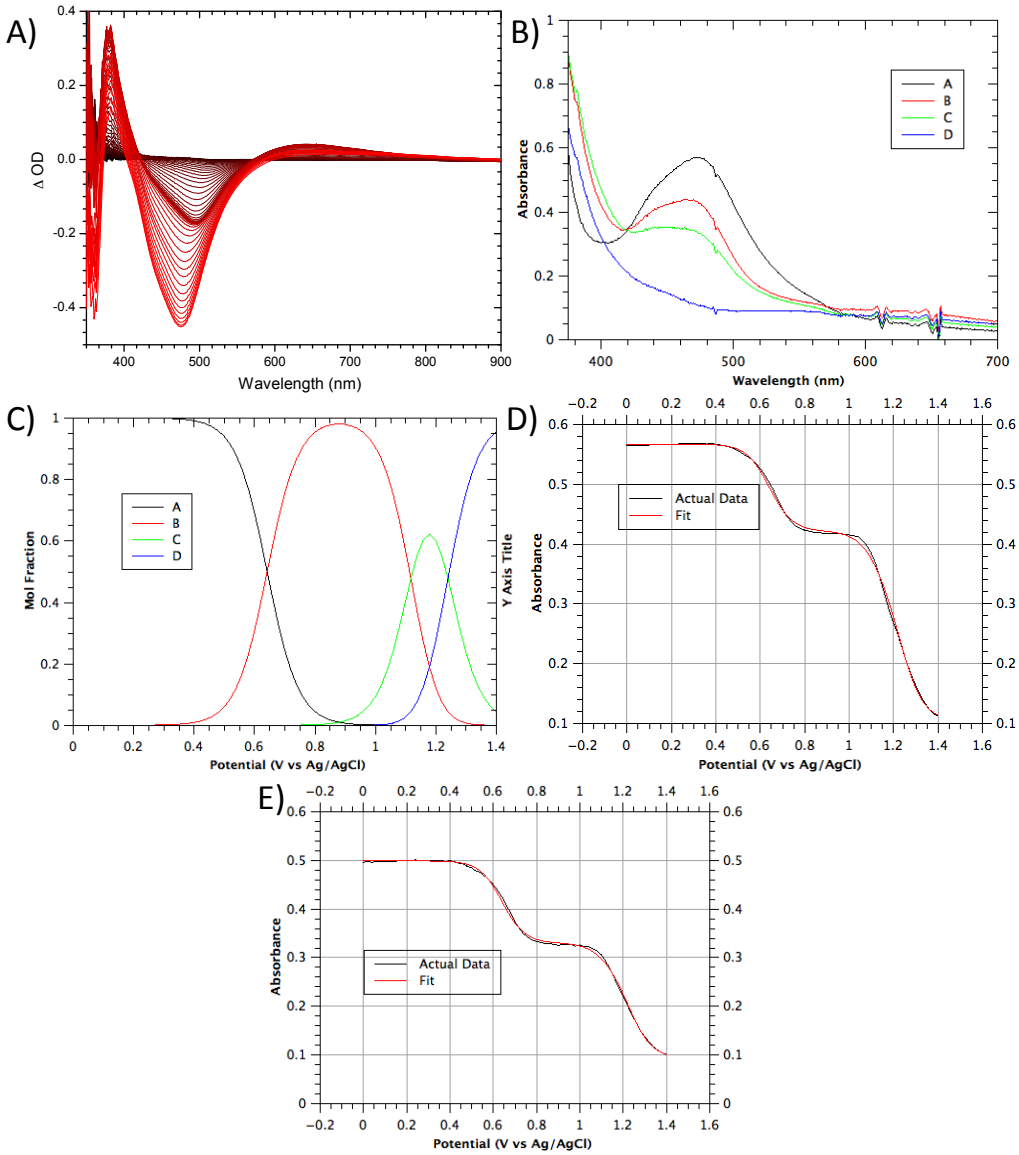

Figure 4.13. A) Spectroelectrochemistry of *nano*ITO|-**RuPdvb**$^{2+}$-*poly***RuOH$_2$**$^{2+}$ in 0.1 M $HClO_4$ with a Pt-mesh counter electrode and Ag/AgCl reference electrode. The *nano*ITO|-**RuPdvb**$^{2+}$-*poly***RuOH$_2$**$^{2+}$ slide was stepped in 0.02 V increments and held for 300 seconds at each potential. Following each potential hold, an absorption spectrum of the slide was obtained. B) Calculated spectra for the multi-wavelength fit to the kinetic model A ⇋ B ⇋ C ⇋ D with A = [–**Ru^{II}-Ru^{II}(OH$_2$)**]$^{4+}$, B = [–**Ru^{II}-Ru^{III}(OH$_2$)**]$^{5+}$, C = [–**Ru^{II}-Ru^{IV}(O)**]$^{4+}$, and D = [–**Ru^{III}-Ru^{IV}(O)**]$^{5+}$. C) Calculated concentration profiles as a function of applied potential (V vs. Ag/AgCl) for the model A ⇋ B ⇋ C ⇋ D. D) Changes in absorption at 476 nm ($\lambda_{max,MLCT}$ for **RuPdvb**$^{2+}$) as function of applied potential in black and calculated fit (red) using the model A ⇋ B ⇋ C ⇋ D. E) Changes in absorption at 491 nm ($\lambda_{max,MLCT}$ for **RuOH$_2$**$^{2+}$) as a function of applied potential in black and calculated fit (red) using the model A ⇋ B ⇋ C ⇋ D. The data was fit using SPECFIT/32 by a series of three sequential Nernstian steps (A ⇋ B ⇋ C ⇋ D).

As shown in **Figure 4.12**, oxidation past the –$\mathbf{Ru^{III}\text{-}Ru^{IV}(O)^{5+}}$/–$\mathbf{Ru^{II}\text{-}Ru^{IV}(O)^{4+}}$ redox couple triggers the onset of catalytic water oxidation. Notably, it occurs at a potential ~200 mV less positive than oxidation to –$\mathbf{Ru^{III}\text{-}Ru^{V}(O)^{6+}}$ which occurs at $E_{p,a} \approx 1.7$ V for the solution-based catalyst.[23] The –$\mathbf{Ru^{III}\text{-}Ru^{V}(O)^{6+}}$/–$\mathbf{Ru^{III}\text{-}Ru^{IV}(O)^{5+}}$ wave in the bilayer is not observable due to the catalytic current. The appearance of the low potential onset suggests that the chromophore $\mathbf{RuPdvb^{2+}}$ in the films behaves as a redox mediator, lowering the overpotential for water oxidation.[24-26] A similar decrease was not observed for *poly*$\mathbf{RuOH_2^{2+}}$ films on *nano*ITO (**Figure 4.14**).

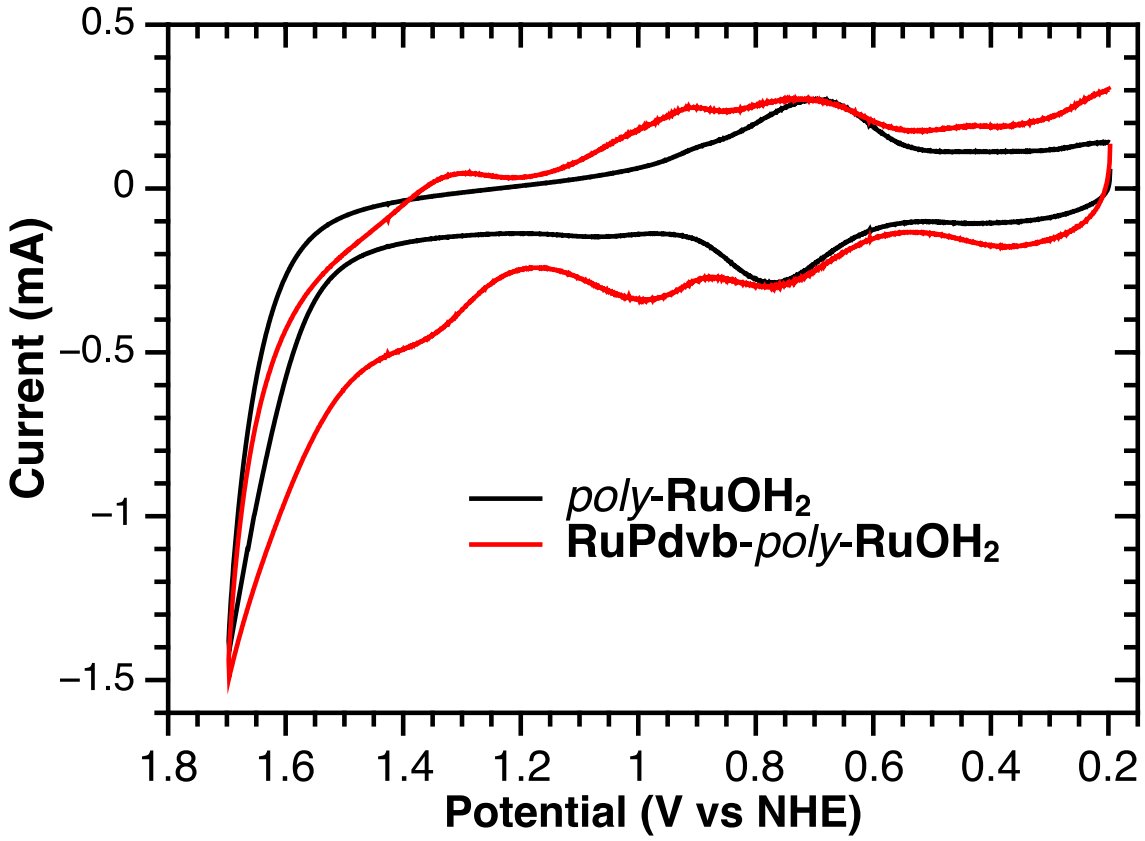

Figure 4.14. CVs at 10 mV s^{-1} of *nano*ITO|-$\mathbf{RuPdvb^{2+}}$-*poly*$\mathbf{RuOH_2^{2+}}$ (red) and *nano*ITO|-*poly*$\mathbf{RuOH_2^{2+}}$ (black) in pH 4.7 (0.1 M HOAc/NaOAc, 0.5 M $NaClO_4$); Pt-mesh counter electrode and Ag/AgCl reference electrode. The traces are normalized to the –$\mathbf{Ru^{III}(OH)/Ru^{II}(OH_2)}$ redox couple.

Rate constants for water oxidation (k_{obs}) at 1.7 V vs. NHE were evaluated at pH 4.7 (0.1 M HOAc/NaOAc, 0.5 M $NaClO_4$) by CV measurements with application of **Equation 4.3** (see Experimental).[20] Based on these data, $k_{obs} = 0.073 \pm 0.030$ s^{-1} for *nano*ITO|-**RuPdvb**$^{2+}$-*poly***RuOH$_2$**$^{2+}$ with a 1:1 chromophore/catalyst ratio (**Figure 4.15**A) and $k_{obs} = 0.060 \pm 0.020$ s^{-1} for *nano*ITO|-*poly***RuOH$_2$**$^{2+}$ (**Figure 4.15**B). Under the same conditions, $k_{obs} = 0.10 \pm 0.010$ s^{-1}, for the monomeric catalyst **RuPOH$_2$**$^{2+}$ on *nano*ITO (**Figure 4.15**C). The comparable k_{obs} suggests that the catalytic properties of the catalyst are not significantly altered in the polymer film. Similar k_{obs} values were obtained on FTO (**Figure 4.16**).

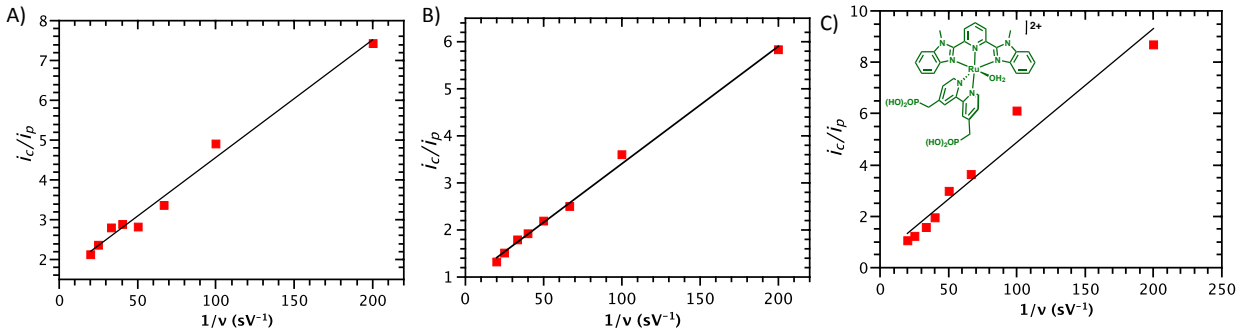

Figure 4.15. Plots of i_c/i_p (i_c is the current at 1.7 V vs. NHE, i_p is the peak current for the –**Ru^{III}(OH)/Ru^{II}(OH$_2$)** redox couple) as a function of ν^{-1} for A) *nano*ITO|-**RuPdvb**$^{2+}$-*poly***RuOH$_2$**$^{2+}$; B) *nano*ITO|-*poly***RuOH$_2$**$^{2+}$ and C) *nano*ITO|-**RuPOH$_2$**$^{2+}$ in pH 4.7 (0.1 M HOAc/NaOAc, 0.5 M $NaClO_4$); Pt-mesh counter electrode and Ag/AgCl reference electrode. Surface coverages for each complex were ~1.1×10^{-8} mol cm^{-2} at 23 °C. The rate constant, k_{obs}, was evaluated from the slope of the each plot.

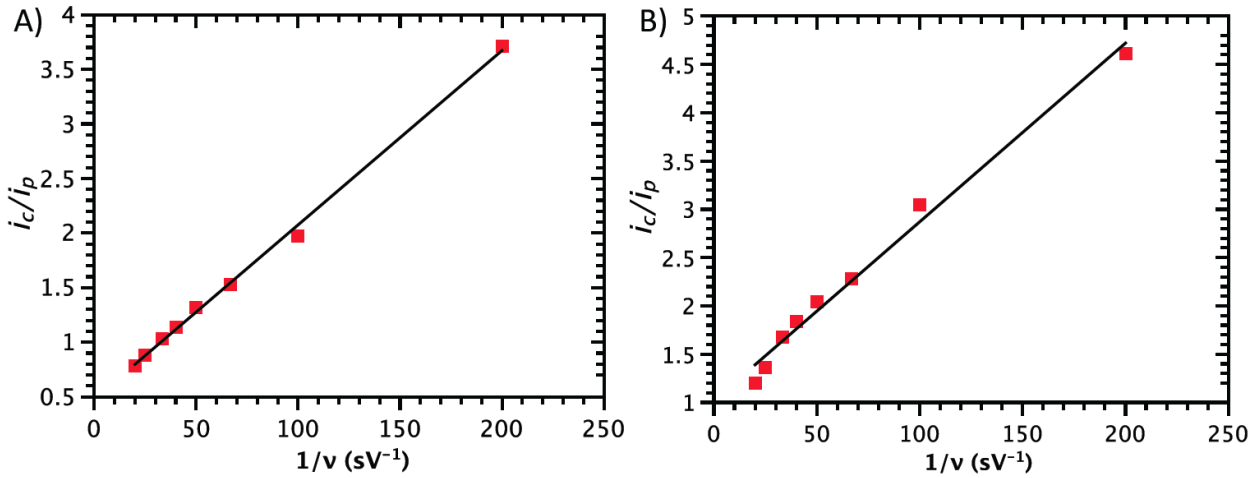

Figure 4.16. Plots of i_c/i_p (i_c is the current at 1.7 V vs. NHE, i_p is the peak current for the –**Ru^{III}(OH)/Ru^{II}(OH$_2$)** redox couple) as a function of ν^{-1} for A) FTO|-*poly***RuOH$_2^{2+}$**; and B) FTO|-**RuPdvb^{2+}**-*poly***RuOH$_2^{2+}$** in pH 4.7 (0.1 M HOAc/NaOAc, 0.5 M $NaClO_4$); Pt-mesh counter electrode and Ag/AgCl reference electrode. Surface coverages for each complex were ~1 × 10^{-10} mol cm^{-2} at 23 °C. The rate constant, k_{obs}, was evaluated from the slope of the each plot.

Controlled potential electrolysis of 1:1 *nano*ITO|-**RuPdvb^{2+}**-*poly***RuOH$_2^{2+}$** at 1.7 V (vs. NHE) in pH 4.7 (0.1 M HOAc/NaOAc, 0.5 M $NaClO_4$, $E°(H_2O \rightarrow 1/2\ O_2 + 2\ H^+ + 2\ e^-) = 0.95$ V vs. NHE at pH 4.7) resulted in a sustained catalytic current with no decrease over a two-hour period (**Figure 4.17**). Oxygen production was quantified by gas chromatography, giving a Faradaic efficiency of 77% (**Figure 4.18**a). During this experiment, the catalytic sites underwent 501 turnovers with a turnover frequency of 0.046 s^{-1} (based on oxygen production), comparable to the rate constants obtained by CV measurements.

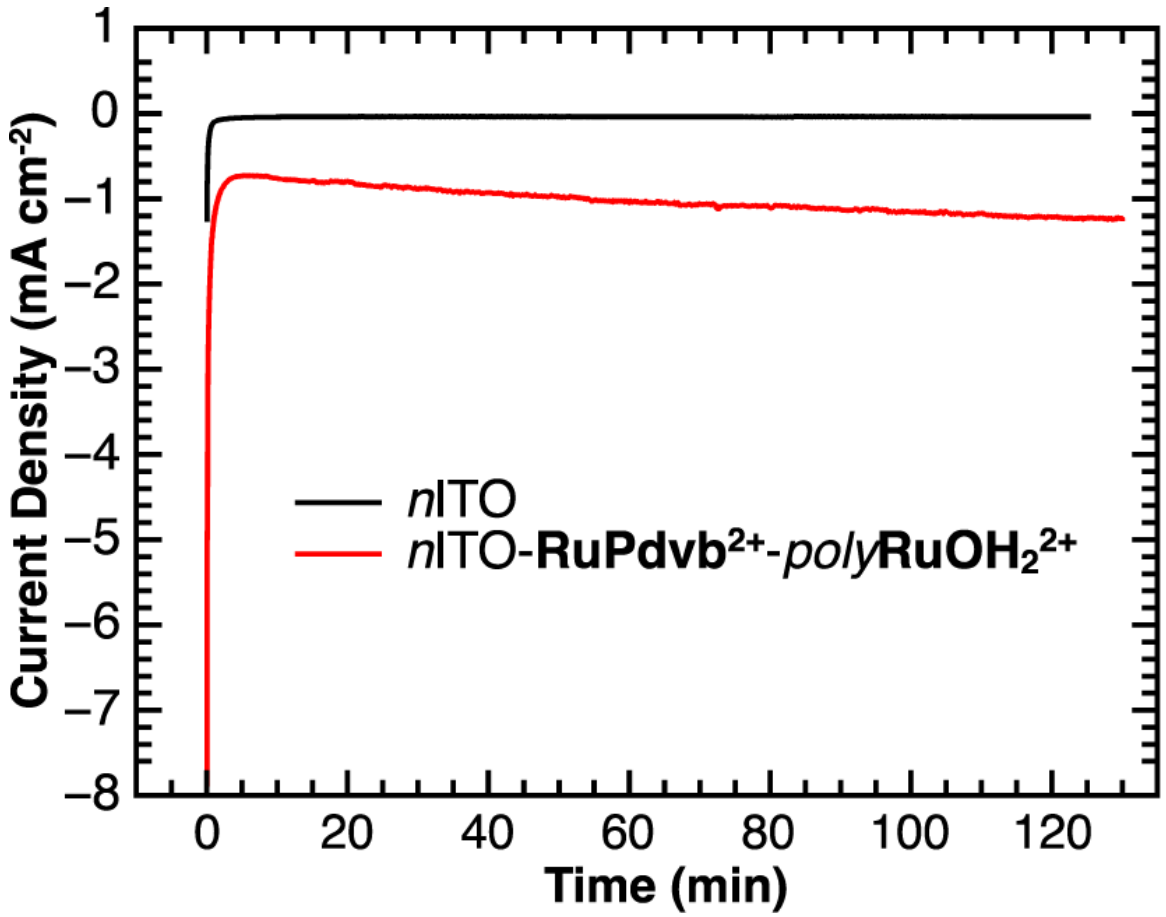

Figure 4.17. Controlled potential electrolysis on 1:1 *nano*ITO|-**RuPdvb**$^{2+}$-*poly***RuOH**$_2^{2+}$ (red) and *nano*ITO (black) at 1.7 V vs. NHE in pH 4.7 aqueous solution (0.1 M HOAc/NaOAc, 0.5 M $NaClO_4$); Pt-mesh counter electrode and Ag/AgCl reference electrode (0.197 V vs. NHE). $\Gamma \approx 1.1 \times 10^{-8}$ mol cm^{-2} for each complex.

Following a two-hour electrolysis period, neither catalyst decomposition nor desorption was observed by CV (**Figure 4.18**b). This observation represents a significant stability enhancement relative to surface-bound **RuPOH**$_2^{2+}$. Despite the presence of the catalyst following the two-hour electrolysis period, the catalyst was observed to experience structural changes. The appearance of a new redox couple ($E_{p,a} \approx 0.3$ V in **Figure 4.18**b) is attributed to conversion of *poly***RuOH**$_2^{2+}$ to *poly***RuOOH**$^{2+}$. This peroxide species is a known intermediate for similar surface-bound water oxidation catalysts.[27-30] These measurements also reveal a

chemical change for surface-bound **RuPdvb**$^{2+}$ over the electrolysis period with characteristic features appearing in the CVs for a surface-bound analogue of *cis*-$[Ru(bpy)_2(OH_2)_2]^{2+}$.[19] Its appearance and activity toward water oxidation catalysis may account for the increase in the magnitude of the catalytic current over time observed during electrolysis (**Figure 4.17**).

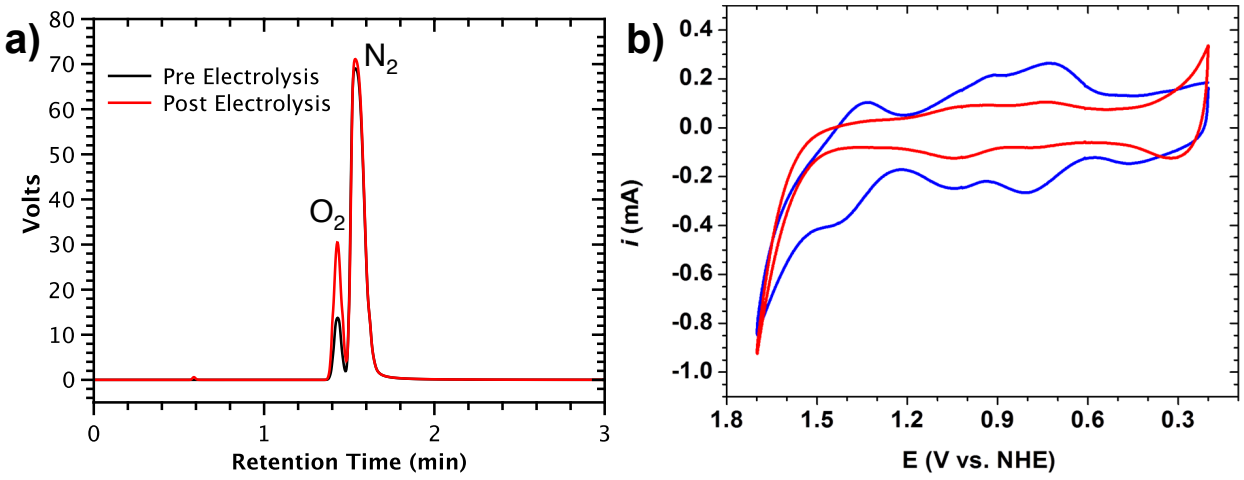

Figure 4.18. a) Gas chromatographs of headspace following electrolysis of blank *nano*ITO (black trace) and *nano*ITO|-**RuPdvb**$^{2+}$-*poly***RuOH$_2$**$^{2+}$ (red trace) at 1.7 V vs. NHE in pH 4.7 aqueous solution (0.1 M HOAc/NaOAc, 0.5 M $NaClO_4$); Pt-mesh counter electrode and Ag/AgCl reference electrode (0.197 V vs. NHE). $\Gamma \approx 1.1 \times 10^{-8}$ mol cm^{-2} for each complex. b) Cyclic voltammograms of *nano*ITO|-**RuPdvb**$^{2+}$-*poly***RuOH$_2$**$^{2+}$ before (blue trace) and after (red trace) a two-hour controlled potential electrolysis under the same conditions as in a).

4.3. Conclusions

Our results are important in describing a general strategy for preparing spatially controlled, multicomponent films and bilayers containing both light harvesting chromophores and water oxidation catalysts on planar and mesoporous nanoparticle metal oxide films. The procedure is general with reductive electropolymerization/assembly formation successfully demonstrated on FTO, *nano*TiO_2, and *nano*ITO and on these surfaces derivatized with **RuPdvb**$^{2+}$. The chromophore/catalyst ratio in the films can be controlled by the number of

reductive CVs scan cycles. The PCET character of the **RuOH$_2^{2+}$** sites in the surface structures is maintained and, on FTO, is independent of film thickness up to 33 layers. Importantly, reactivity toward water oxidation is maintained in both *poly***RuOH$_2^{2+}$** films and **RuPdvb^{2+}**-*poly***RuOH$_2^{2+}$** bilayers on FTO and *nano*ITO with sustained water oxidation catalysis occurring over a 2 h electrolysis period with a Faradaic efficiency of 77% with individual catalyst sites undergoing 501 turnovers and a TOF = 0.046 s^{-1}.

4.4. Experimental

4.4.1. Sample Preparation

Materials and Methods. [Ru(η^6-benzene)(Cl)$_2$]$_2$,[31] 2,6-bis(1-methyl-1H-benzo[d]imidazol-2-yl)pyridine (Mebimpy),[23] and 5,5'-divinyl-2,2'-bipyridine (5,5'-dvbpy)[32] were synthesized as previously reported. Distilled water was further purified by using a Milli-Q Ultrapure water purification system. All other reagents were ACS grade and used without further purification. Fluoride-doped tin oxide (FTO)-coated glass (Hartford Glass; sheet resistance 15 Ω per square), was cut into 10 mm × 40 mm strips and used as the substrate for TiO_2 nanoparticle films. Microwave reactions were carried out using a CEM MARS microwave reactor. A CEM HP-500 Plus Teflon-coated microwave vessel (100 mL) was used at a power setting of 400 W. The vessel was rotated and stirred throughout the microwave procedure. The pressure of the reaction vessel was monitored throughout the reaction, and never exceeded 300 PSI.

Metal Oxide Films. Films of *nano*TiO_2, typically 4 to 7 μm thick (~20 nm particle diameter), with a coating area of roughly 10 mm × 15 mm, were synthesized according to a literature procedure.[33]

Absorption Spectra. Absorption spectra were obtained by placing the dry derivatized films perpendicular to the detection beam path of the spectrophotometer. **Equation 4.2** was used to calculate surface coverages.[34] Molar extinction coefficients (ε) in H_2O were used; A(λ) is the

absorbance at the MLCT λ_{max}. All measurements were carried out on films loaded from methanol solutions of ruthenium complex (150 μM), which gave complete surface coverage ($\Gamma = 8 \times 10^{-8}$ mol cm^{-2}).

Equation 4.2

$$\Gamma = A(\lambda) \times (\varepsilon(\lambda) \times 1000)^{-1}$$

4.4.2. Electrochemical and Photophysical Characterization

Electrochemical Measurements. Electrochemical measurements were conducted on a CH Instruments 660D potentiostat with a Pt-mesh or Pt-wire counter electrode, and a $Ag/AgNO_3$ (0.01 M $AgNO_3$/0.1 M tetra-n-butylammonium hexafluorophosphate ([TBA]PF_6) in CH_3CN; –0.09 V vs. $Fc^{+/0}$)[35] or Ag/AgCl (3 M NaCl; 0.197 V vs. NHE) reference electrode. $E_{1/2}$ values were obtained from the peak currents in square wave voltammograms or from averaging cathodic and anodic potentials at peak current values ($E_{p,c}$ and $E_{p,a}$) in cyclic voltammograms. Reductive electropolymerization was carried out in anhydrous propylene carbonate (dried over $MgSO_4$) with 0.1 M [TBA]PF_6 as the supporting electrolyte under an atmosphere of argon. Solutions were deaerated with argon for at least five minutes prior to reductive electrochemical cycling.

Surface coverages on FTO were calculated using **Equation 4.1** **Equation 4.1**, where Q is the integrated current under the **–$Ru^{III}(OH)/Ru^{II}(OH_2)$** redox couple of ***poly*$RuOH_2^{2+}$**, F is Faraday's constant (96,485 C mol^{-1}), n is the number of electrons transferred (n = 1 unless otherwise indicated), and A is the area of the electrode (~1 cm^2).

Catalysis. Catalytic rate constants for the water oxidation, k_{obs}, were calculated using **Equation 4.3**, where i_{cat} is the catalytic current (in amperes) taken at 1.7 V (vs. NHE), i_{peak} is the

current taken for the –$\mathbf{Ru^{III}(OH)/Ru^{II}(OH_2)}$ redox couple, n_{cat} is the number of electrons involved in the catalytic step (n_{cat} = 4 for H_2O – 4 H^+ – 4 e^- → O_2), R is the ideal gas constant (R = 8.314 J mol^{-1} K^{-1}), T is the temperature (in K), n_p is the number of electrons involved in the –$\mathbf{Ru^{III}(OH)/Ru^{II}(OH_2)}$ redox couple (n = 1), F is Faraday's constant, and ν is the electrochemical scan rate (V s^{-1}).

Equation 4.3

$$\frac{i_{cat}}{i_{peak}} = \left(\frac{4RTn_{cat}}{n_p^2F}\right)\left(\frac{1}{\nu}\right)k_{obs}$$

Scanning Electron Microscopy (SEM) and Energy Dispersive X-ray Spectroscopy (EDS). SEM and EDS results were obtained on a FEI Helios 600 Nanolab Dual Beam System equipped with an Oxford instruments, INCA PentaFET-x3 detector. A cross-section was taken of *nano*TiO_2|-$\mathbf{RuPdvb^{2+}}$ that had been reductively cycled 60, 120, and 300 times in presence of $\mathbf{RuOH_2^{2+}}$. Surface images were taken at 5 kV with a 86 pA beam current. Three EDS spectra were obtained at the *nano*TiO_2/solution interface (top), in the bulk of TiO_2 nanoparticles (middle), and at the *nano*TiO_2/FTO interface (bottom) of the cross section.

Photostability. Photostability measurements were performed by a previously reported procedure.[14] The light from a Royal Blue (455 nm, fwhm ~30 nm, 475 mW cm^{-2}) Mounted High Power LED (Thorlabs, Inc., M455L2) powered by a T-Cube LED Driver (Thorlabs, Inc., LEDD1B) was focused to a 2.5 mm diameter spot size by a focusing beam probe (Newport Corp. 77646) outfitted with a second lens (Newport, Corp 41230). The light output was directed onto the derivatized thin film placed at 45° in a standard 10 mm path length cuvette containing 3 mL of the solution. The illumination spot was adjusted to coincide both with the thin film and the

perpendicular beam path of a Varian Cary 50 UV-visible spectrophotometer. The absorption spectrum (360 – 800 nm) of the film was taken every 15 minutes over 16 hours of illumination. The incident light intensity was measured with a thermopile detector (Newport Corp 1918-C meter and 818P-020-12 detector). The solution temperature, 22 ± 2 °C, was consistent throughout the duration of the experiment.

The absorption-time traces at 400 nm, 450 nm, and 500 nm for the pH 4.6 (0.1 M HOAc/NaOAc, 0.5 M $NaClO_4$) could be satisfactorily fit with the biexponential function (**Equation 4.4**). For comparison purposes, the results of the multi-exponential analysis were represented by a single rate constant by first calculating the weighted average lifetime (‹τ›) using **Equation 4.5**. The three weighted average lifetimes ($\langle\tau\rangle_{400\text{-nm}}$, $\langle\tau\rangle_{450\text{-nm}}$, $\langle\tau\rangle_{500\text{-nm}}$) were then averaged (**Equation 4.6**) to represent desorption as a single rate constant, k_{des}.

Equation 4.4

$$y = A_1 e^{-\frac{1}{\tau_1}x} + A_2 e^{-\frac{1}{\tau_2}x}$$

Equation 4.5

$$\langle\tau\rangle = \frac{\sum A_i \tau_i^2}{\sum A_i \tau_i}$$

Equation 4.6

$$\frac{1}{k_{des}} = \frac{\langle\tau\rangle_{400-nm} + \langle\tau\rangle_{450-nm} + \langle\tau\rangle_{500-nm}}{3}$$

4.4.3. Synthesis

[Ru(5,5'-dvbpy)(η^6-benzene)(Cl)][Cl]. This complex was synthesized according a modified literature procedure.[36] [Ru(η^6-benzene)$(Cl)_2]_2$ (0.24 g, 0.48 mmol) and 5,5'-dvbpy (0.2 g, 0.96 mmol) were dissolved in methanol (~40 mL). The solution was refluxed overnight under an atmosphere of argon. The reaction was cooled, filtered, and the filtrate was taken to dryness by a rotary evaporator. The solid was triturated with ether, collected, and air-dried. This complex was used without further purification (0.42 g, 95%). ^{1}H NMR (400 MHz, DMSO) δ (ppm) 9.64 (s, 2H), 8.63 (d, 2H), 8.48 (d, 2H), 7.05 (dd, 2H), 6.43 (d, 2H), 6.28 (s, 6H), 5.73 (d, 2H).

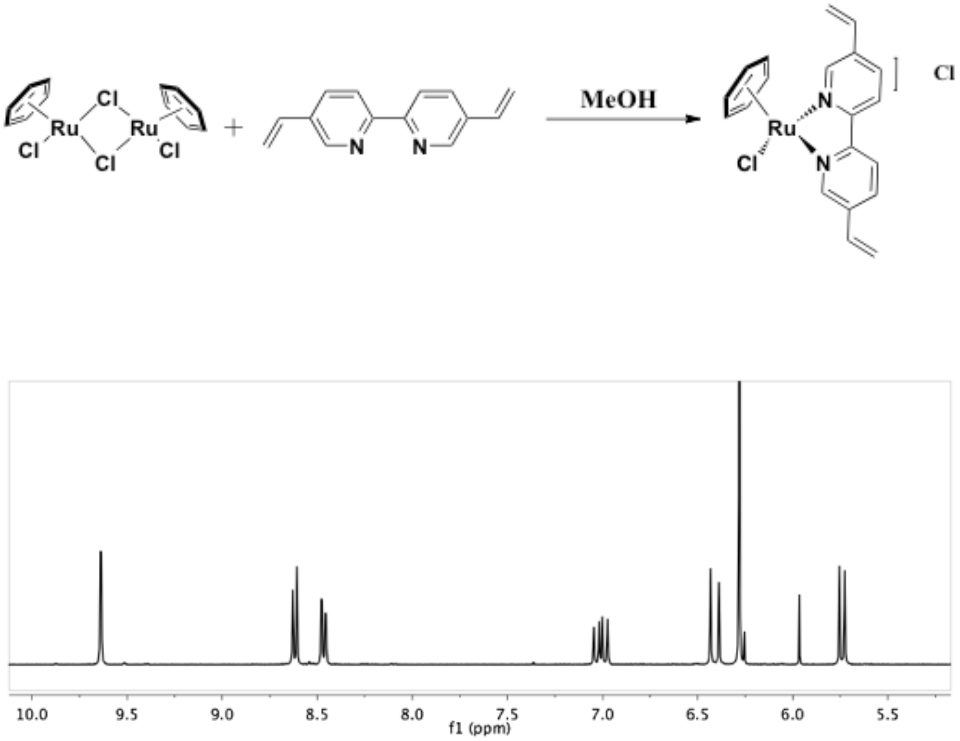

[Ru(Mebimpy)(5,5'-dvbpy)(Cl)][Cl]. This complex was synthesized according a modified literature procedure.[5] [Ru(5,5'-dvbpy)(η^6-benzene)(Cl)][Cl] (0.122 g, 0.27 mmol) and 2,6-bis(1-methyl-1H-benzo[d]imidazol-2-yl)pyridine (0.09 g, 0.27 mmol) were heated at reflux

for 20 minutes at 150 °C in 40 mL ethanol in a microwave reactor. The solution was cooled, then filtered. A saturated solution of LiCl (~15 mL) was added along with additional H_2O (15 mL), and the ethanol was removed by rotary evaporation. The dark purple precipitate was filtered, washed with water and ether, air-dried and collected. This complex was used without further purification (0.169 g, 87%). ^{1}H NMR (600 MHz, d_6-DMSO) δ (ppm) 10.6 (s, 1H), 8.98 (d, 1H), 8.76 (m, 2H), 8.70 (d, 1H), 8.50 (d, 1H), 8.24 (t, 1H), 7.87 (m, 3H), 7.40 (t, 2H), 7.26 (s, 1H), 7.11 (m, 3H), 6.42 (d, 1H), 6.32 (d, 1H), 6.11 (d, 2H), 5.79 (m, 2H), 5.32 (d, 1H), 4.53 (s, 6H).

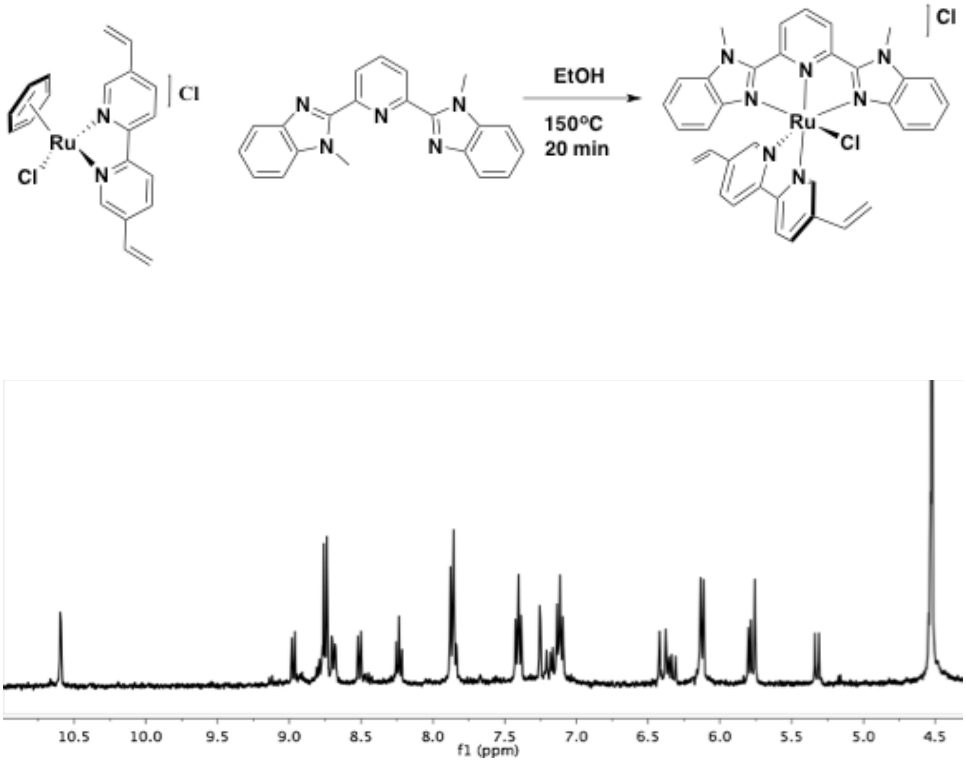

*[Ru(Mebimpy)(5,5'-dvbpy)(OH$_2$)][BF$_4$]$_2$ (**RuOH$_2^{2+}$**)*. [Ru(Mebimpy)(5,5'-dvbpy)(Cl)](Cl) (0.344 g, 0.48 mmol) was dissolved in 1:1 methanol:water (~30 mL) under an atmosphere of argon. A solution of $AgBF_4$ (0.189 g, 0.97 mmol) in H_2O (~10 mL) was added. The solution was refluxed in the dark overnight under an atmosphere of argon. The solution was

cooled, filtered through Celite, and the filtrate was taken to dryness using a rotary evaporator. The crude product was then purified by size-exclusion chromatography (Sephadex LH-20) with 1:1 methanol:water as eluent. Similar fractions (based of UV-visible spectra) were combined, and the solvent was removed by rotary evaporation. The dark red solid was triturated with ether and collected (0.29 g, 73%). ^{1}H NMR (600 MHz, CD_3CN) δ (ppm) 9.97 (s, 1H), 8.60 (m, 4H), 8.34 (t, 1H), 8.19 (d, 1H), 7.82 (dd, 1H), 7.67 (d, 2H), 7.44 (t, 2H), 7.22 (d, 1H), 7.18 (dd, 1H), 7.12 (t, 2H), 6.42 (d, 1H), 6.36 (dd, 1H), 6.23 (d, 2H), 5.80 (d, 1H), 5.69 (d, 1H), 5.33 (d, 1H), 4.41 (s, 6H). Anal. Found (Calc.) for $C_{35}H_{37}B_2F_8N_7O_4Ru$: C 46.83 (47.00), H 3.72 (4.17), N 10.96 (10.96).

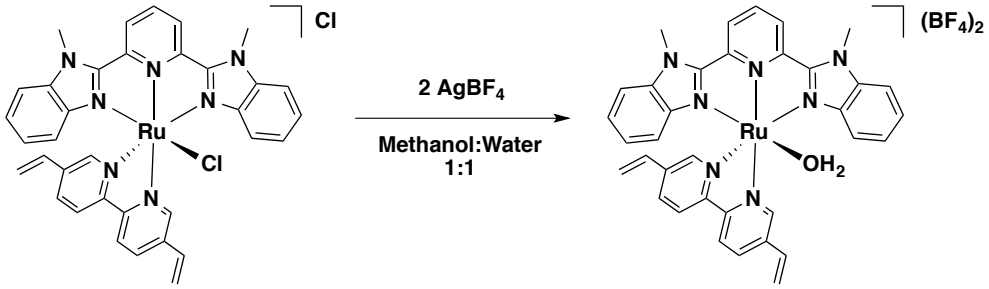

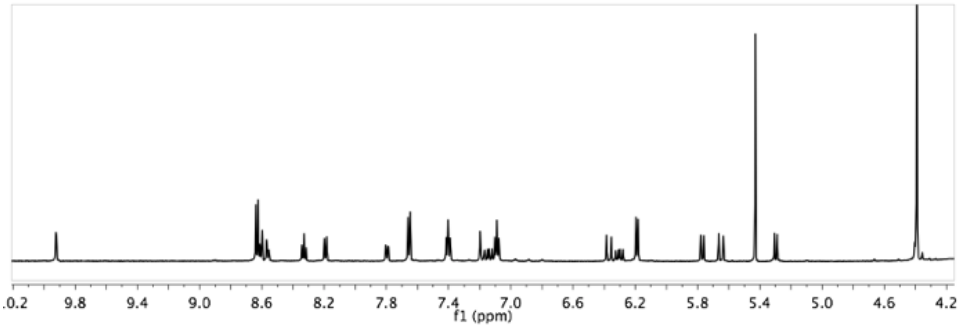

4.5. Acknowledgements

This research was supported by the UNC EFRC Center for Solar Fuels, an Energy Frontier Research Center funded by the U.S. Department of Energy, Office of Science, Office of Basic Energy Sciences, under Award No. DE-SC0001011, supporting A.K.V. and K.H. D.L.A. acknowledges support from the Department of Energy Office of Science Graduate Fellowship Program under Contract No. DE-AC05-06OR23100. A.M.L. acknowledges Government support under FA9550-11-C-0028 and awarded by the DOD, AFOSR, NDSEG Fellowship, 32 CFR 168a. Support is also acknowledged by D.P.H. from the U.S. Department of Energy, Office of Science, Office of Basic Energy Sciences, under Award Number DE-FG02-06ER15788.

4.6. Associated Content

Associated content, including absorption spectra, EDS spectra, and crystal structure information, can be found in Appendix B.

REFERENCES

(1) Grätzel, M. *Nature* **2001**, *414*, 338.

(2) Lewis, N. S.; Nocera, D. G. *Proc. Natl. Acad. Sci. U. S. A.* **2006**, *103*, 15729.

(3) Swierk, J. R.; Mallouk, T. E. *Chem. Soc. Rev.* **2013**, *42*, 2357.

(4) Young, K. J.; Martini, L. A.; Milot, R. L.; Snoeberger Iii, R. C.; Batista, V. S.; Schmuttenmaer, C. A.; Crabtree, R. H.; Brudvig, G. W. *Coord. Chem. Rev.* **2012**, *256*, 2503.

(5) Ashford, D. L.; Song, W.; Concepcion, J. J.; Glasson, C. R. K.; Brennaman, M. K.; Norris, M. R.; Fang, Z.; Templeton, J. L.; Meyer, T. J. *J. Am. Chem. Soc.* **2012**, *134*, 19189.

(6) Concepcion, J. J.; Jurss, J. W.; Hoertz, P. G.; Meyer, T. J. *Angew. Chem. Int. Ed.* **2009**, *48*, 9473.

(7) Hanson, K.; Torelli, D. A.; Vannucci, A. K.; Brennaman, M. K.; Luo, H.; Alibabaei, L.; Song, W.; Ashford, D. L.; Norris, M. R.; Glasson, C. R. K.; Concepcion, J. J.; Meyer, T. J. *Angew. Chem., Int. Ed.* **2012**, *51*, 12782.

(8) Glasson, C. R. K.; Song, W.; Ashford, D. L.; Vannucci, A.; Chen, Z.; Concepcion, J. J.; Holland, P. L.; Meyer, T. J. *Inorg. Chem.* **2012**, *51*, 8637.

(9) Xiang, X.; Fielden, J.; Rodriguez-Cordoba, W.; Huang, Z.; Zhang, N.; Luo, Z.; Musaev, D. G.; Lian, T.; Hill, C. L. *J. Phys. Chem. C* **2013**, *117*, 918.

(10) Gao, Y.; Ding, X.; Liu, J.; Wang, L.; Lu, Z.; Li, L.; Sun, L. *J. Am. Chem. Soc.* **2013**, *135*, 4219.

(11) Moore, G. F.; Blakemore, J. D.; Milot, R. L.; Hull, J. F.; Song, H.-e.; Cai, L.; Schmuttenmaer, C. A.; Crabtree, R. H.; Brudvig, G. W. *Energy Environ. Sci.* **2011**, *4*, 2389.

(12) Mola, J.; Mas-Marza, E.; Sala, X.; Romero, I.; Rodríguez, M.; Viñas, C.; Parella, T.; Llobet, A. *Angew. Chem. Int. Ed.* **2008**, *47*, 5830.

(13) Frischmann, P. D.; Mahata, K.; Wurthner, F. *Chem. Soc. Rev.* **2013**, *42*, 1847.

(14) Hanson, K.; Brennaman, M. K.; Luo, H.; Glasson, C. R.; Concepcion, J. J.; Song, W.; Meyer, T. J. *ACS Appl. Mater. Interfaces* **2012**, *4*, 1462.

(15) Lapides, A. M.; Ashford, D. L.; Hanson, K.; Torelli, D. A.; Templeton, J. L.; Meyer, T. J. *J. Am. Chem. Soc.* **2013**, *135*, 15450.

(16) Moss, J. A.; Yang, J. C.; Stipkala, J. M.; Wen, X.; Bignozzi, C. A.; Meyer, G. J.; Meyer, T. J. *Inorg. Chem.* **2004**, *43*, 1784.

(17) Biner, M.; Buergi, H. B.; Ludi, A.; Roehr, C. *J. Am. Chem. Soc.* **1992**, *114*, 5197.

(18) Bard, A. J.; Faulkner, L. R. *Electrochemical Methods: Fundamentals and Applications, 2nd Edition*; John Wiley & Sons, Inc.: New York, 2001.

(19) Song, W.; Ito, A.; Binstead, R. A.; Hanson, K.; Luo, H.; Brennaman, M. K.; Concepcion, J. J.; Meyer, T. J. *J. Am. Chem. Soc.* **2013**, *135*, 11587.

(20) Vannucci, A. K.; Hull, J. F.; Chen, Z.; Binstead, R. A.; Concepcion, J. J.; Meyer, T. J. *J. Am. Chem. Soc.* **2012**, *134*, 3972.

(21) Calvert, J. M.; Schmehl, R. H.; Sullivan, B. P.; Facci, J. S.; Meyer, T. J.; Murray, R. W. *Inorg. Chem.* **1983**, *22*, 2151.

(22) Hanson, K.; Losego, M. D.; Kalanyan, B.; Ashford, D. L.; Parsons, G. N.; Meyer, T. J. *Chem. Mater.* **2013**, *25*, 3.

(23) Concepcion, J. J.; Jurss, J. W.; Norris, M. R.; Chen, Z.; Templeton, J. L.; Meyer, T. J. *Inorg. Chem.* **2010**, *49*, 1277.

(24) Concepcion, J. J.; Jurss, J. W.; Templeton, J. L.; Meyer, T. J. *Proc. Natl. Acad. Sci. U. S. A.* **2008**, *105*, 17632.

(25) Norris, M. R.; Concepcion, J. J.; Harrison, D. P.; Binstead, R. A.; Ashford, D. L.; Fang, Z.; Templeton, J. L.; Meyer, T. J. *J. Am. Chem. Soc.* **2013**, *135*, 2080.

(26) Norris, M. R.; Concepcion, J. J.; Fang, Z.; Templeton, J. L.; Meyer, T. J. *Angew. Chem. Int. Ed.* **2013**, *52*, 13580.

(27) Vannucci, A. K.; Alibabaei, L.; Losego, M. D.; Concepcion, J. J.; Kalanyan, B.; Parsons, G. N.; Meyer, T. J. *Proc. Natl. Acad. Sci. U. S. A.* **2013**, *110*, 20918.

(28) Chen, Z.; Concepcion, J. J.; Hull, J. F.; Hoertz, P. G.; Meyer, T. J. *Dalton Trans.* **2010**, *39*, 6950.

(29) Concepcion, J. J.; Tsai, M.-K.; Muckerman, J. T.; Meyer, T. J. *J. Am. Chem. Soc.* **2010**, *132*, 1545.

(30) Chen, Z.; Vannucci, A. K.; Concepcion, J. J.; Jurss, J. W.; Meyer, T. J. *Proc. Natl. Acad. Sci. U. S. A.* **2011**, *108*, E1461.

(31) Bennett, M. A.; Smith, A. K. *J. Chem. Soc., Dalton Trans.* **1974**, 233.

(32) Liu, Y.; Zhang, S.; Miao, Q.; Zheng, L.; Zong, L.; Cheng, Y. *Macromolecules* **2007**, *40*, 4839.

(33) Lee, S.-H. A.; Abrams, N. M.; Hoertz, P. G.; Barber, G. D.; Halaoui, L. I.; Mallouk, T. E. *J. Phys. Chem. B* **2008**, *112*, 14415.

(34) Gallagher, L. A.; Serron, S. A.; Wen, X.; Hornstein, B. J.; Dattelbaum, D. M.; Schoonover, J. R.; Meyer, T. J. *Inorg. Chem.* **2005**, *44*, 2089.

(35) Connelly, N. G.; Geiger, W. E. *Chem. Rev.* **1996**, *96*, 877.

(36) Norris, M. R.; Concepcion, J. J.; Glasson, C. R. K.; Fang, Z.; Lapides, A. M.; Ashford, D. L.; Templeton, J. L.; Meyer, T. J. *Inorg. Chem.* **2013**, *52*, 12492.

CHAPTER 5: SYNTHESIS, CHARACTERIZATION, AND WATER OXIDATION BY A MOLECULAR CHROMOPHORE-CATALYST ASSEMBLY PREPARED BY ATOMIC LAYER DEPOSITION. THE "MUMMY" STRATEGY

Reproduced from Lapides, A. M.; Sherman, B. D.; Brennaman, M. K.; Dares, C. J.; Skinner, K. R.; Templeton, J. L.; Meyer, T. J. *Chem. Sci.* **2015**, *6*, 6398 with permission from the Royal Society of Chemistry.

5.1. Introduction

In a Dye-Sensitized Photoelectrosynthesis Cell (DSPEC) for water splitting, a molecular light absorber and catalyst are integrated with a wide bandgap metal oxide semiconductor.[1-3] Typically, the molecular components are either surface-bound on the oxide or covalently linked prior to surface attachment with phosphonate-surface binding used for aqueous stability.[4-6] A number of alternate assembly strategies have been explored including a layer-by-layer technique,[7,8] electro-assembly formation,[9-11] and pre-formed polymer and peptide assemblies.[12]

Although reasonably stable in acidic solutions, phosphonate surface binding is unstable toward hydrolysis as the pH is increased above 5.[13] An additional stability issue arises from decomposition of the oxidized forms of most chromophores under aqueous conditions which also limits DSPEC stability and performance over extended periods.[14-18] Atomic layer deposition (ALD), with thin overlayers of aluminum oxide (Al_2O_3 or AO) or titanium dioxide (TiO_2) added after surface binding, has been used successfully to stabilize phosphonate-surface binding even at high pH.[19-22] We describe here a new ALD-based "mummy" strategy for preparing and stabilizing chromophore-catalyst assemblies. It utilizes ALD for both forming and stabilizing assemblies without the need for covalent or ionic bonds between units. The assembly process is stepwise involving: (1) initial surface binding of a chromophore; (2) embedding the chromophore in a thin layer of deposited oxide; (3) surface binding of a molecular catalyst; and,

finally, (4) thin-layer deposition of an oxide overlayer to stabilize surface binding of the catalyst. Here we describe the application of this strategy to the preparation of a Ru(II) polypyridyl chromophore-catalyst assembly on nanoparticle films of two oxides, tin-doped indium oxide (*nano*ITO) for electrocatalytic water oxidation and titanium dioxide (*nano*TiO_2) for light-assisted photoelectrochemical water oxidation.

5.2. Results and Discussion

5.2.1. Bilayer Formation

The chromophore $[Ru^{II}(4,4'\text{-dpbpy})(2,2'\text{-bipyridine})_2]^{2+}$ (**RuP^{2+}**, **Figure 5.1**a; 4,4'-dpbpy = [2,2'-bipyridine]-4,4'-diylbis(phosphonic acid)) was synthesized as its chloride salt as previously described.[23] Films of *nano*TiO_2 and *nano*ITO were loaded with **RuP^{2+}** by soaking in methanol solutions (~1 mM in complex) overnight to give *nano*TiO_2|–**RuP^{2+}** or *nano*ITO|–**RuP^{2+}**. Surface coverage was estimated by UV-visible absorption measurements with $\varepsilon = 12{,}700$ M^{-1} cm^{-1} at $\lambda_{max} = 458$ nm for a solution analog, although small differences between the solution and surface-bound species are expected.[9,24]

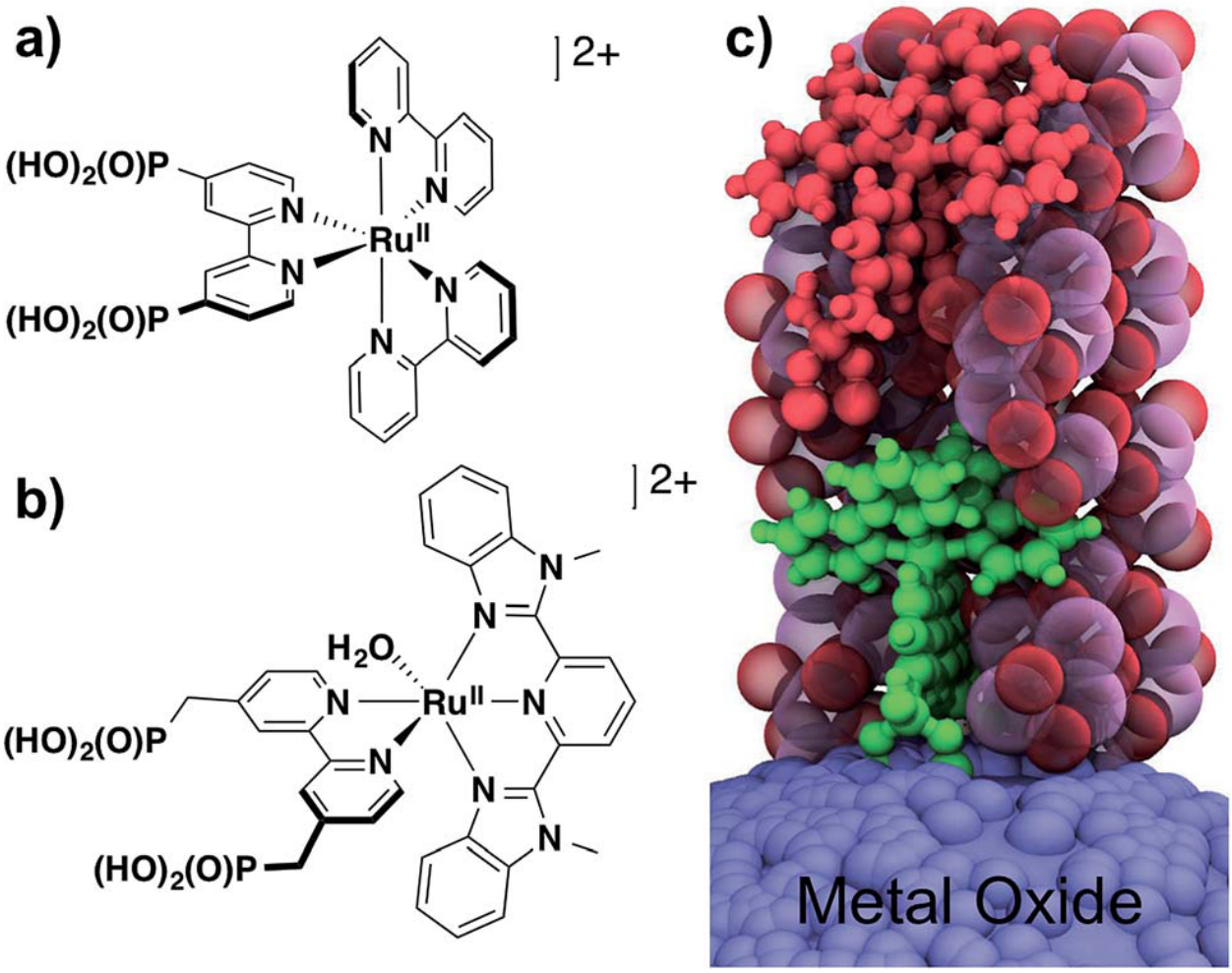

Figure 5.1. Molecular structures of: (a) chromophore, $\mathbf{RuP^{2+}}$; and (b) water oxidation catalyst, $\mathbf{RuCP(OH_2)^{2+}}$. (c) Visualization of the ALD mummy protected surface assembly with $\mathbf{–RuP^{2+}}$ (green molecule) and $\mathbf{–RuCP(OH_2)^{2+}}$ (red molecule) embedded in ~3 nm of Al_2O_3.

ALD overlayers of aluminum oxide (Al_2O_3; AO) were deposited atop derivatized *nano*ITO|$\mathbf{–RuP^{2+}}$ electrodes by sequential pulses of $Al(CH_3)_3$ and H_2O at 150 °C under dynamic vacuum. Ellipsometry performed on a witness Si wafer in the reactor established a deposition rate of ~0.15 nm per cycle with the rate verified by transmission electron microscopy (TEM) measurements on samples of both *nano*ITO and *nano*ITO|$\mathbf{–RuP^{2+}}$. Conformal films were observed on both substrates, suggesting that the adsorbed dye does not hinder conformal Al_2O_3 deposition.

The effect of additional ALD cycles on sequential loading of a second chromophore layer was investigated by UV-visible absorption measurements. In these experiments, *nano*ITO|–**RuP^{2+}** electrodes were subjected to an increasing number of $Al(CH_3)_3/H_2O$ cycles, *x* with *x* = 0, 3, 6, 8, and 10, followed by overnight soaking in the **RuP^{2+}** loading solution. UV-visible absorption spectra were used to monitor the surfaces after each step in the surface synthesis (**Figure 5.2**a). The ratio of **RuP^{2+}** in the outer layer to **RuP^{2+}** in the inner layer was evaluated by taking the ratios of background-subtracted spectra before and after the second loading step. Outer-to-inner ratios at 458 nm are shown in **Figure 5.2**b. The extent of addition of the second **RuP^{2+}** layer was dependent on the number of $Al(CH_3)_3/H_2O$ cycles with a ~1:1 ratio reached at 6 cycles and comparable results obtained for 8 and 10 cycles.

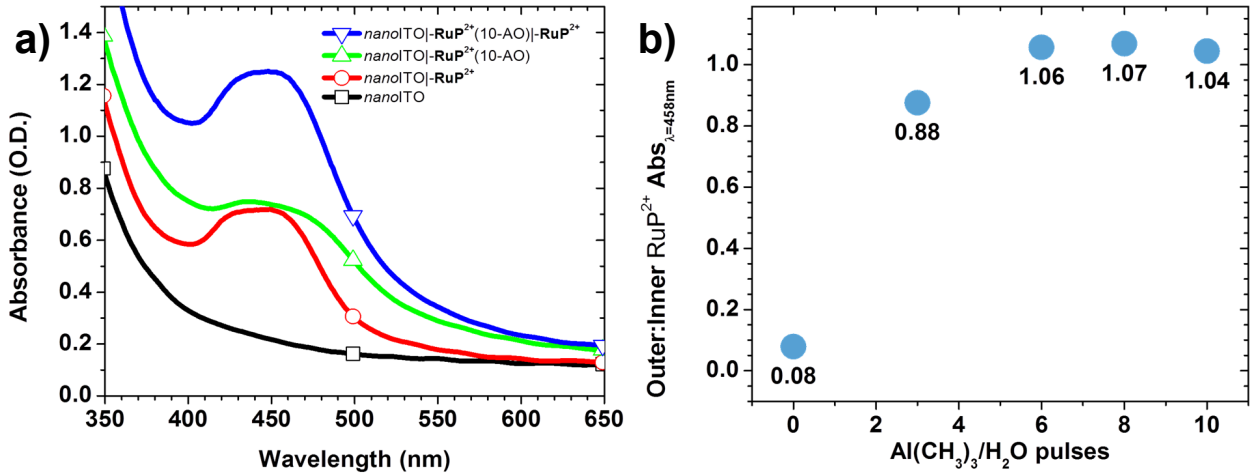

Figure 5.2. (a) Absorption spectra of dry films from the sequential loading procedure leading to *nano*ITO|–**RuP^{2+}**(10-AO)|–**RuP^{2+}**; (b) outer:inner –**RuP^{2+}** ratios as a function of the number of ALD pulses evaluated at 458 nm with background subtraction.

Further Al_2O_3 addition (20 cycles total) caused a decrease in the 1:1 outer-to-inner chromophore-loading ratio. UV-visible absorption measurements comparing outer-to-inner loading on a sample of *nano*TiO_2|–**RuP^{2+}**(20-AO)|–**RuP^{2+}** showed that loading of the outer

chromophore was ~65% that of the inner chromophore (**Figure 5.3**). The decrease in loading could be due to reduced pore size and/or a reduced surface area of the films due to Al_2O_3 deposition.

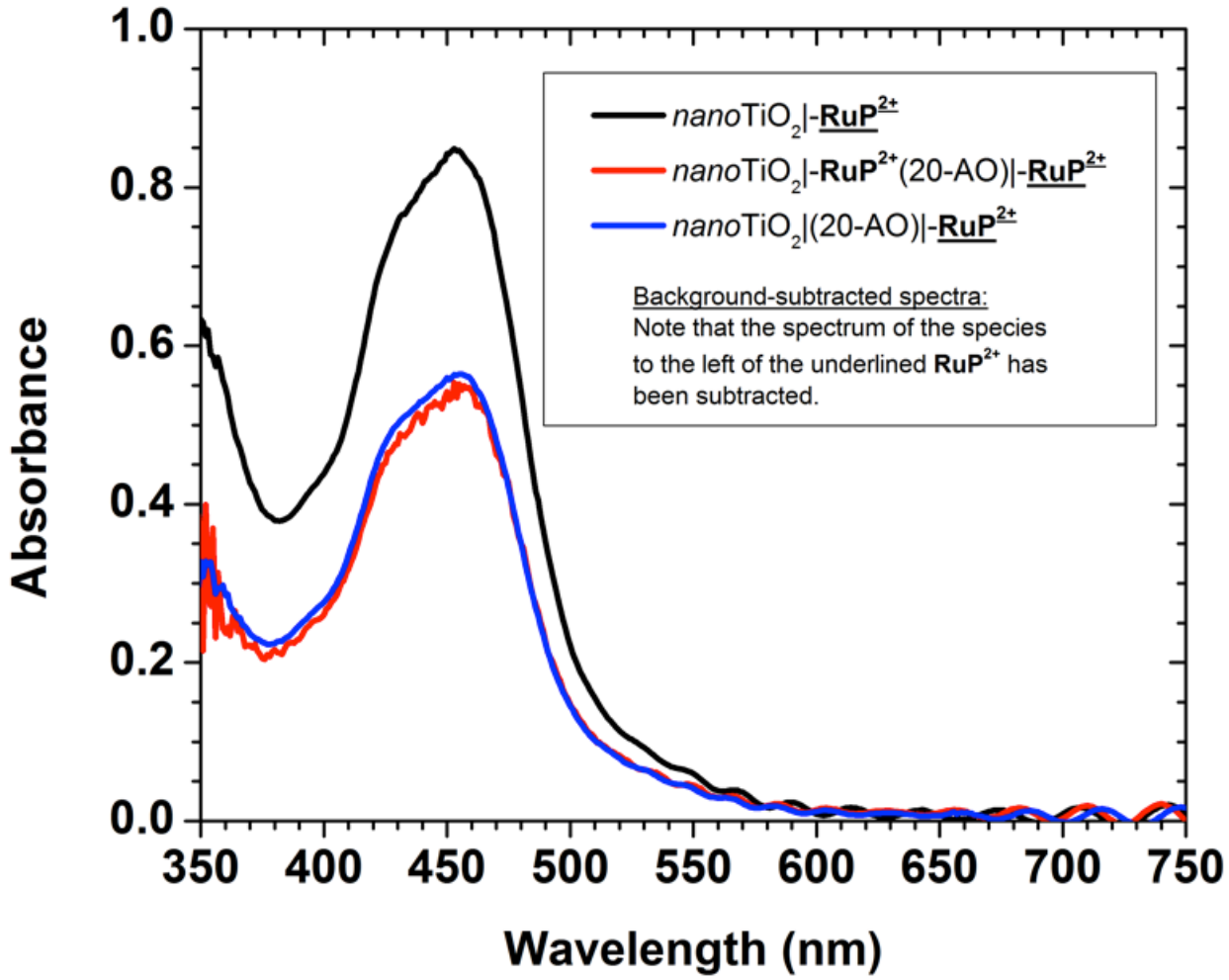

Figure 5.3. Background-subtracted UV-visible absorption spectra of *nano*TiO_2|-**RuP**$^{2+}$(20-AO)|-**RuP**$^{2+}$, *nano*TiO_2|-**RuP**$^{2+}$, and *nano*TiO_2(20-AO)|-**RuP**$^{2+}$. Note that background (i.e. the spectrum of all species to the left of the underlined species in the legend above) has been subtracted from each spectrum as to only present the absorption spectrum of the underlined molecular species.

To investigate pore size further, BET desorption isotherms were used to determine the pore size distribution of modified and unmodified *nano*ITO films for both *nano*ITO and

*nano*ITO(20-AO) (**Figure 5.4**). The mean pore size decreased by ~5 nm upon addition of 20-AO, from 36 nm for *nano*ITO to 31 nm for *nano*ITO(20-AO). This decrease is in good agreement with the expected value (6 nm; 20 cycles at 0.15 nm per cycle on each particle), and could explain the decrease in chromophore loading reflecting waning of nanoparticle voids.

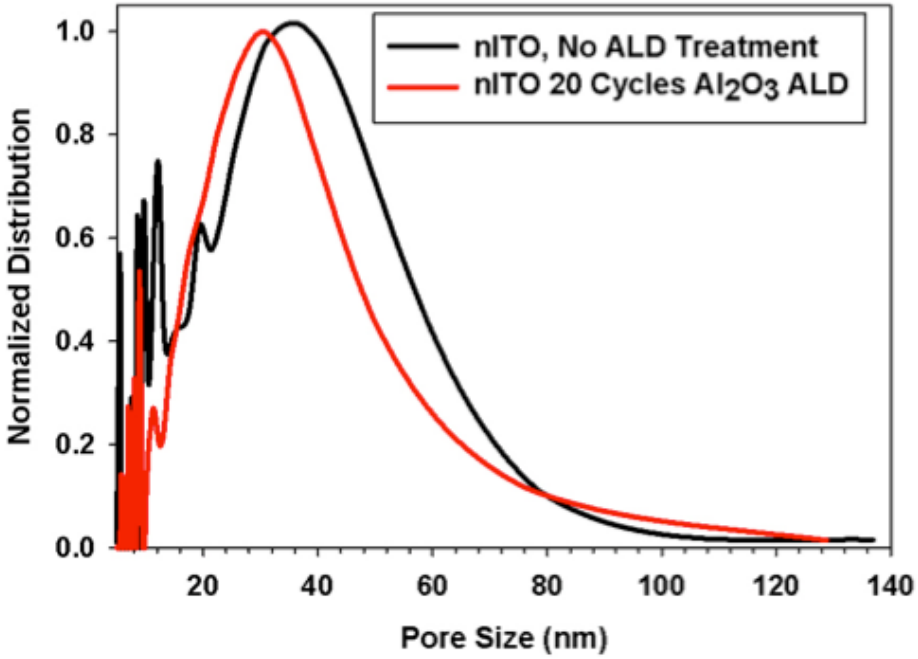

Figure 5.4. Pore size distribution for *nano*ITO (black trace) and *nano*ITO(20-AO) (red trace).

The role of ALD overlayer thickness on the photostability of **RuP^{2+}** surface-bound to nanoTiO$_2$ and on the electrochemical stability of the water oxidation catalyst, [Ru(2,6-bis(1-methyl-1H-benzo[d]imidazol-2-yl)pyridine)(4,4'-dpcbpy)(OH$_2$)]$^{2+}$ (**RuCP(OH$_2$)$^{2+}$**, **Figure 5.1**b; 4,4'-dpcbpy = ([2,2'-bipyridine]-4,4'-diylbis(methylene))bis(phosphonic acid)) on *nano*ITO has been investigated previously.[21,22] For both, maximum stability was achieved for ALD overlayer thicknesses approaching the molecular diameter of **–RuP^{2+}** (~1.3 nm). In synthesizing the chromophore-catalyst assembly, an initial ALD overlayer of 10 Al(CH$_3$)$_3$/H$_2$O cycles (~1.5 nm)

was used to stabilize surface-bound **–RuP^{2+}**. In a second step, **RuCP(OH$_2$)$^{2+}$** (**Figure 5.1**b), as the trifluoromethanesulfonate salt, was loaded from methanol (~1 mM in complex) onto the pre-deposited Al_2O_3 overlayer coating surface-bound **–RuP^{2+}**. In a final step, an additional 10 $Al(CH_3)_3/H_2O$ cycles were deposited to stabilize catalyst surface binding. The second deposition step increased the total thickness of the Al_2O_3 overlayer to ~3 nm, "mummifying" the inner **–RuP^{2+}** complex by addition of Al_2O_3 to a level that was approximately twice the molecular diameter, note **Figure 5.1**c.

5.2.2. Electrochemical characterization

In cyclic voltammetric (CV) scans on the assembly *nano*ITO|**–RuP^{2+}**(10-AO)|**–RuCP(OH$_2$)$^{2+}$**(10-AO) at pH 4.7 in an aqueous sodium acetate buffer (I = 0.1 M; 0.5 M $NaClO_4$) at a scan rate of 20 mV s^{-1}, a broad ($\Delta E_p \approx 0.18$ V) wave at $E_{1/2}$ = 0.73 V vs. NHE appears for the external **–Ru^{III}CP(OH)$^{2+}$/–Ru^{II}CP(OH$_2$)$^{2+}$** couple (**Figure 5.5**, blue trace); this couple is known to have $E_{1/2}$ = 0.75 V at pH 5 on *nano*ITO.[25] Further oxidation with appearance of the **–Ru^{IV}CP(O)$^{2+}$/–Ru^{III}CP(OH)$^{2+}$** couple at $E_{1/2}$ = 1.0 V at pH 5 is not observed on the CV timescale. The inhibition is due to a kinetic effect arising from the proton-coupled electron transfer (PCET) nature of the couple and the insulating Al_2O_3 overlayer.[25]

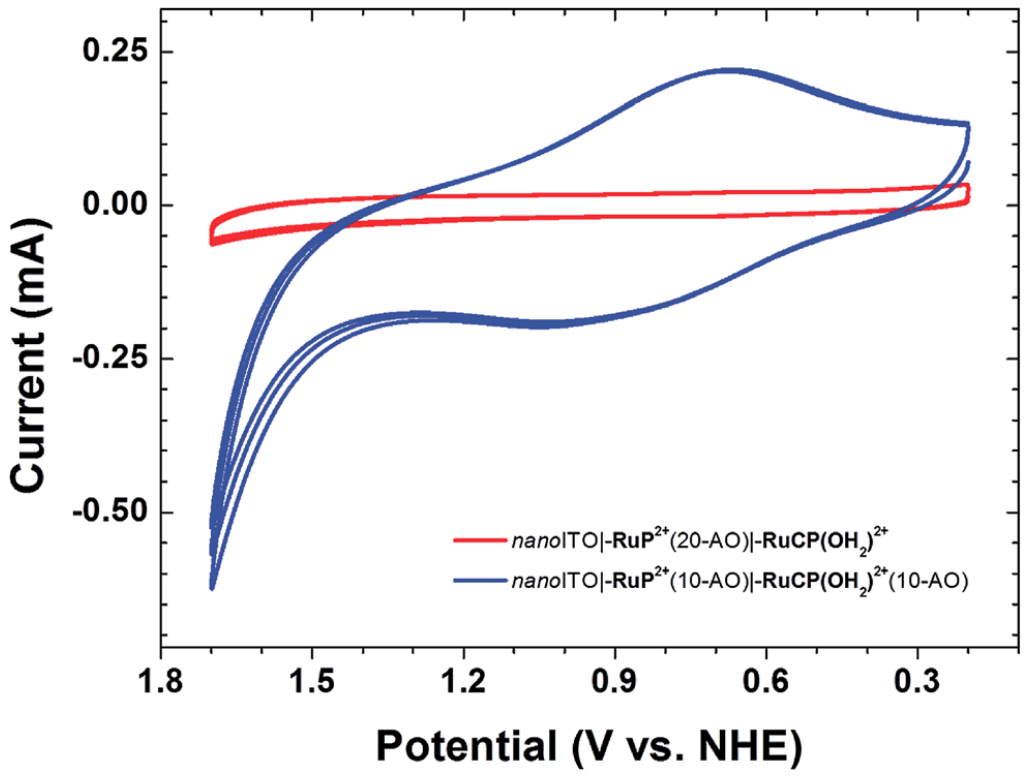

Figure 5.5. CV scans on *nano*ITO|–$\mathbf{RuP^{2+}}$(10-AO)|–$\mathbf{RuCP(OH_2)^{2+}}$(10-AO) (blue trace) and *nano*ITO|–$\mathbf{RuP^{2+}}$(20-AO)|–$\mathbf{RuCP(OH_2)^{2+}}$ (red trace) (conditions: pH 4.7 aqueous sodium acetate (0.1 M); 0.5 M $NaClO_4$; ν = 20 mV s^{-1}; ref = Ag/AgCl; Aux = Pt-mesh).

For the assembly, *nano*ITO|–$\mathbf{RuP^{2+}}$(20-AO)|–$\mathbf{RuCP(OH_2)^{2+}}$, with 20 Al_2O_3 inner layers, there was no electrochemical response at 20 mV s^{-1} (**Figure 5.5**, red trace). The loss of electrochemical activity is presumably due both to the inability of the "buried" chromophore to achieve charge compensation on the time scale of the experiment upon oxidation to –$\mathbf{RuP^{3+}}$, –$\mathbf{RuP^{2+}} - e^- \rightarrow$ –$\mathbf{RuP^{3+}}$, and to slow electron transfer tunneling from the external –$\mathbf{RuCP(OH_2)^{2+}}$ catalyst to the electrode surface.

Oxidation of the external –$\mathbf{RuCP(OH_2)^{2+}}$ catalyst is influenced by the internal chromophore and continues to occur even with an intervening layer of Al_2O_3 without direct surface binding of the chromophore to the underlying *nano*ITO. This effect was demonstrated by CV measurements on an assembly prepared by first depositing 10 layers of Al_2O_3 on *nano*ITO

followed by surface preparation of the assembly as described above. In CV scans of the resulting assembly, *nano*ITO(10-AO)|–**RuP**$^{2+}$(10-AO)|–**RuCP(OH$_2$)**$^{2+}$(10-AO), a broad wave appeared at $E_{1/2} \approx 0.64$ V at pH 8.8 in a $H_2PO_4^-/HPO_4^{2-}$ buffer for the –**Ru^{III}CP(OH)**$^{2+}$/–**Ru^{II}CP(OH$_2$)**$^{2+}$ couple even though the catalyst couple was separated from the surface by 20 cycles (~3 nm) of Al_2O_3.

A spectroelectrochemical experiment was conducted to resolve the broad, overlapping waves for *nano*ITO(10-AO)|–**RuP**$^{2+}$(10-AO)|–**RuCP(OH$_2$)**$^{2+}$(10-AO), the surface-separated mummy sample (**Figure 5.6**). Slow, 180 s electrochemical steps at 0.02 V increments from 0 to 1.7 V vs. NHE with spectrophotometric monitoring revealed a distinct oxidation at $E_{1/2} = 0.66$ V for the –**Ru^{III}CP(OH)**$^{2+}$/–**Ru^{II}CP(OH$_2$)**$^{2+}$ couple, in agreement with the CV data. A second oxidation was revealed at $E_{1/2} = 1.30$ V for the –**RuP**$^{3+/2+}$ couple which was not observed in CV scans at scan rates as slow as 20 mV s^{-1} because of its kinetic inhibition.[9] The spectroelectrochemical results confirm that both chromophore and catalyst are redox active with an important role for long-range electron transfer through Al_2O_3 mediated by the intervening –**RuP**$^{2+}$.

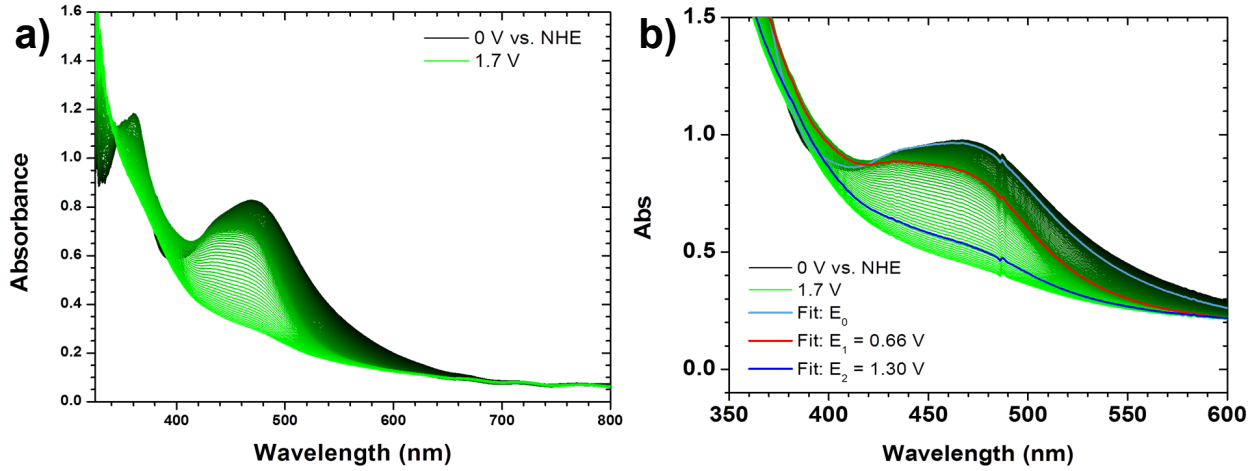

Figure 5.6. Spectroelectrochemistry for *nano*ITO(10-AO)|-**RuP**$^{2+}$(10-AO)|-**RuCP(OH$_2$)**$^{2+}$(10-AO) with bare *nano*ITO(10-AO) subtracted from each spectrum: a) raw data; b) including fit spectra for ground state (light blue), singly-oxidized catalyst (red), and oxidized chromophore-catalyst (dark blue). (Conditions: 0 to 1.7 V vs. NHE, 0.02-V step, 180-s hold per step; pH 8.8 sodium phosphate dibasic (0.1 M), $NaClO_4$ (0.4 M); Ag/AgCl, 3 M NaCl reference electrode; Pt-mesh counter electrode).

5.2.3. Photoelectrochemical hydroquinone dehydrogenation

The "mummy" protected assembly *nano*TiO_2|–**RuP**$^{2+}$(10-AO)|–**RuCP(OH$_2$)**$^{2+}$(10-AO) was investigated as a DSPEC photoanode on *nano*TiO_2. In these experiments a two-compartment cell with a Nafion membrane separator was used with a three-electrode configuration (SCE reference electrode, Pt-mesh counter electrode). The experiments were conducted under N_2 at pH 4.7 in a 0.1 M aqueous sodium acetate buffer in 0.5 M $NaClO_4$ with a ~100 mW cm^{-2} white light source (400 nm long-pass filter). An applied bias of 0.24 V vs. NHE was used to maximize the photocurrent response.

In an initial set of experiments, the photoelectrochemical response of *nano*TiO_2|–**RuP**$^{2+}$(10-AO)|–**RuCP(OH$_2$)**$^{2+}$(10-AO) with added hydroquinone (H_2Q; 20 mM), added as a sacrificial electron donor (**Figure 5.7**a), was compared to *nano*TiO_2|–**RuP**$^{2+}$. Under these

conditions, excitation and injection by *nano*TiO_2|–**RuP^{2+}*** is followed by rapid reduction of *nano*$TiO_2(e^-)$|–**RuP^{3+}** to *nano*$TiO_2(e^-)$|–**RuP^{2+}** by H_2Q (**Equation 5.1**).

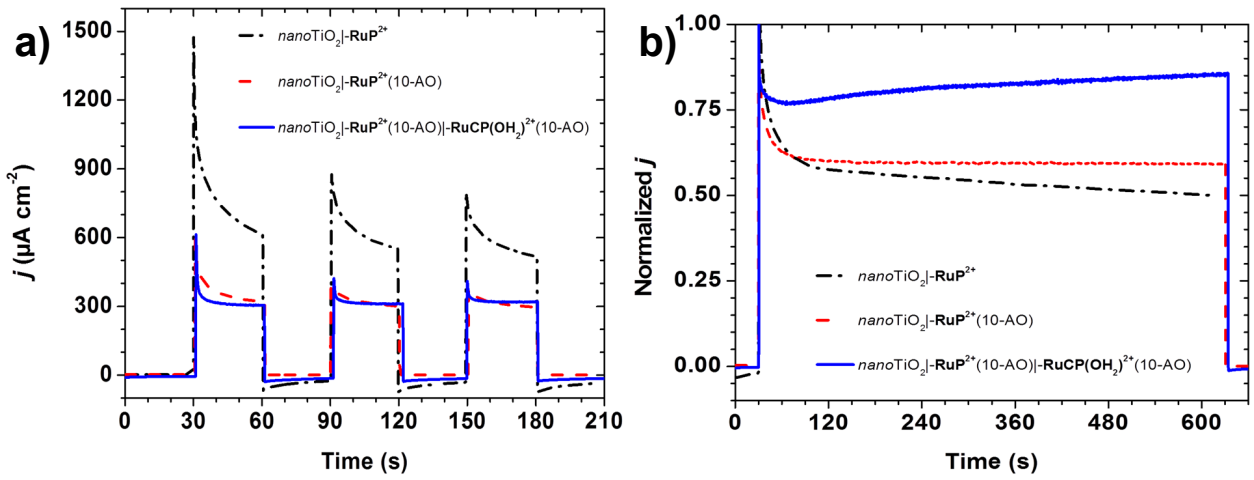

Figure 5.7. (a) Off–on photocurrent–time traces and; (b) normalized photocurrent–time traces under continuous illumination for 10 minutes for *nano*TiO_2|–**RuP^{2+}** (black dash-dot traces), *nano*TiO_2|–**RuP^{2+}**(10-AO) (red dash traces), and *nano*TiO2|–**RuP^{2+}**(10-AO)|–**RuCP(OH$_2$)$^{2+}$**(10-AO) (blue solid traces) with 20 mM added hydroquinone (conditions: I ≈ 100 mW cm^{-2} white light; E_{app} = 0.24 V vs. NHE; pH 4.7 aqueous sodium acetate (0.1 M); 0.5 M $NaClO_4$; ref = SCE; Aux = Pt-mesh).

Equation 5.1

nanoTiO_2|-**Ru^{III}P^{3+}** + $0.5H_2Q$ → *nano*TiO_2|-**Ru^{II}P^{2+}** + $0.5Q + H^+$

For *nano*TiO_2|–**RuP^{2+}**, a large initial photocurrent spike of ~1.5 mA cm^{-2} was observed, arising from surface oxidation of the complex and local capacitance effects, with the photocurrent reaching 0.61 mA cm^{-2} after 30 seconds. Under the same conditions, illumination of *nano*TiO_2|–**RuP^{2+}**(10-AO) resulted in an initial current spike of 0.60 mA cm^{-2} decreasing to 0.32 mA cm^{-2} after 30 seconds. The diminished photocurrent is presumably due to the Al_2O_3 lowering injection yield as discussed previously.[21]

A nearly identical response was observed for the mummified assembly *nano*TiO_2|–**RuP^{2+}**(10-AO)|–**RuCP(OH$_2$)$^{2+}$**(10-AO), with the photocurrent spike reaching 0.61 mA cm^{-2}, falling to 0.31 mA cm^{-2} after 30 seconds. This photocurrent response for the mummified assembly, in which the chromophore is fully buried by Al_2O_3, points to injection by **–RuP^{2+}*** and hole transfer from **–RuP^{3+}** to the catalyst in the outer-layer followed by reduction of **–Ru^{III}CP(OH)$^{2+}$** by H_2Q (**Equation 5.2** and **Equation 5.3**). To validate this explanation, photocurrents for *nano*TiO_2|**–RuP^{2+}**(20-AO), *nano*TiO_2|**–RuP^{2+}**(20-AO)|**–RuCP(OH$_2$)$^{2+}$**), and *nano*TiO_2|**–RuCP(OH$_2$)$^{2+}$**(10-AO) were all negligible at <0.02 mA (**Figure 5.8**). These results point to the importance of the chromophore and the configuration of the mummy-protection in obtaining a significant level of photoelectrochemical activity.

Equation 5.2

nanoTiO_2|-**Ru^{III}P^{3+}**|-**Ru^{II}CP(OH$_2$)$^{2+}$** → *nano*TiO_2|-**Ru^{II}P^{2+}**|-**Ru^{III}CP(OH)$^{2+}$** + H^+

Equation 5.3

nanoTiO_2|-**Ru^{II}P^{2+}**|-**Ru^{III}CP(OH)$^{2+}$** + 0.5H_2Q → *nano*TiO_2|-**Ru^{II}P^{2+}**|-**Ru^{II}CP(OH$_2$)$^{2+}$** + 0.5Q

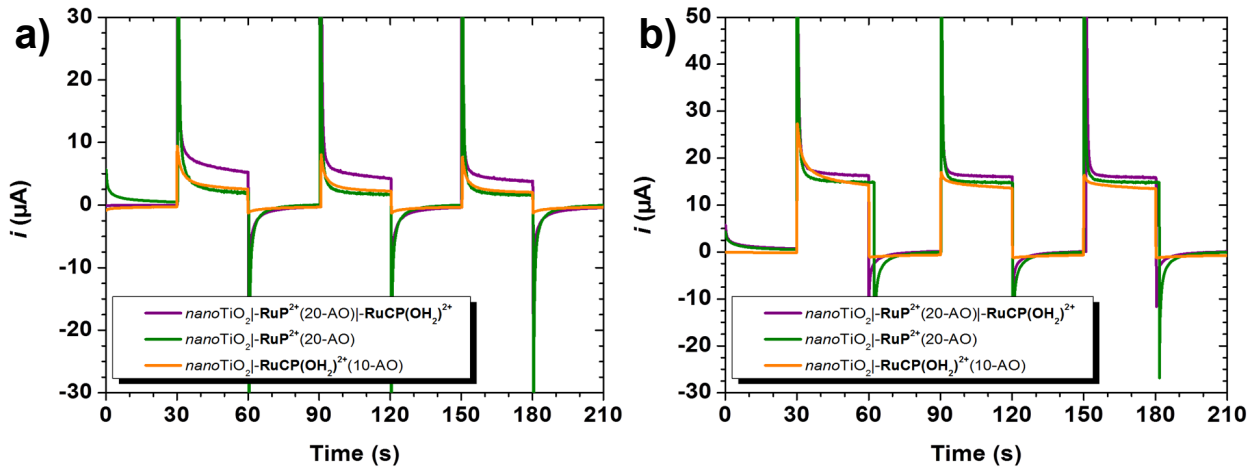

Figure 5.8. Photoelectrochemical "off-on" traces (~100 mW cm^{-2} illumination, 380-nm long-pass filter) of *nano*TiO_2|-**RuP^{2+}**(20-AO)|-**RuCP(OH$_2$)$^{2+}$** (purple traces), *nano*TiO_2|-**RuP^{2+}**(20-AO) (green traces), and *nano*TiO_2|-**RuCP(OH$_2$)$^{2+}$**(10-AO) (orange traces) in pH 4.7 HOAc/NaOAc (0.1 M) buffer a) without; b) with 20 mM hydroquinone added. (Conditions: SCE reference electrode, Pt-mesh counter electrode; solution de-aerated with N_2). NB: The area of each electrode was approximately 1-cm^2.

Longer-term photolyses were undertaken to assess the impact of ALD stabilization on photocurrent performance. Photocurrent–time traces, normalized to their respective initial current spikes, are shown in **Figure 5.7**b. The photocurrent response for *nano*TiO_2|–**RuP^{2+}** decreased to ~57% of the maximum value after two minutes of photolysis with a further decrease to ~50% after ten minutes. With ALD stabilization in *nano*TiO_2|–**RuP^{2+}**(10-AO), the photocurrent decreased to ~60% after two minutes but with less than a 1% decrease between two and ten minutes. This comparison highlights the importance of the ALD overlayer in *nano*TiO_2|–**RuP^{2+}**(10-AO) in inhibiting loss of **–RuP^{2+}** from the surface and, with the addition of H_2Q, rapid reduction of **–RuP^{3+}** to **–RuP^{2+}** in avoiding its decomposition on the surface.[18]

By contrast, for the mummy-protected assembly, *nano*TiO_2|–**RuP^{2+}**(10-AO)|–**RuCP(OH$_2$)$^{2+}$**(10-AO), the normalized photocurrent response increased from 79% to 85% over the final eight minutes of illumination. This "breaking in" period arises from hydrolysis of an

alumina adduct with the catalyst which forms during the ALD process. The adduct forms following exposure of oxide-bound **–RuCP(OH$_2$)$^{2+}$** to pulses of Al(CH$_3$)$_3$ without subsequent re-coordination of the aquo as evidenced by a ~1600 cm^{-1} red shift in the visible MLCT λ_{max} from 487 to 530 nm and a noticeable color change on the surface (**Figure 5.9**, **Figure 5.10**). Subsequent oxidative CV scans through the Ru$^{III/II}$ wave (**Figure 5.10**c), or photoelectrolysis cycles, at pH 4.7 in an aqueous sodium acetate buffer (I = 0.1 M; 0.5 M NaClO$_4$), restore the aquo form of the catalyst, **–Ru^{III}CP(OH)$^{2+}$**. The photocurrent enhancement is due to an enhanced rate of H$_2$Q oxidation by the oxidized catalyst compared to **–RuP^{2+}**.[26]

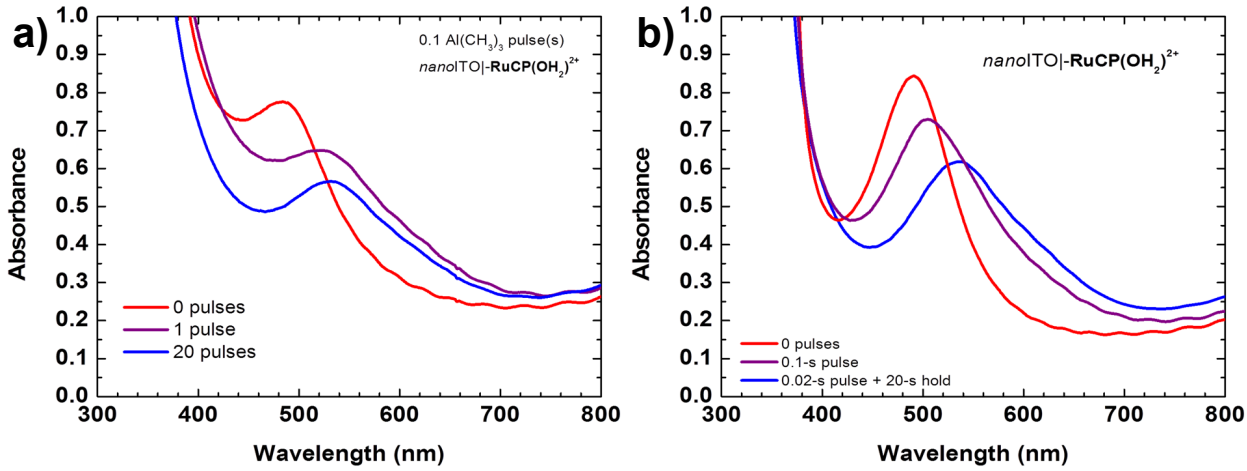

Figure 5.9. UV-visible absorption spectra of *nano*ITO|-**RuCP(OH$_2$)$^{2+}$** following a) single pulses of Al(CH$_3$)$_3$ in the ALD reactor; and b) a single pulse vs. exposing the slide to Al(CH$_3$)$_3$ for 20 seconds. The red shift is attributed to Ru^{II}-OH$_2$ → Ru^{II}-OAl(OH)$_2$.

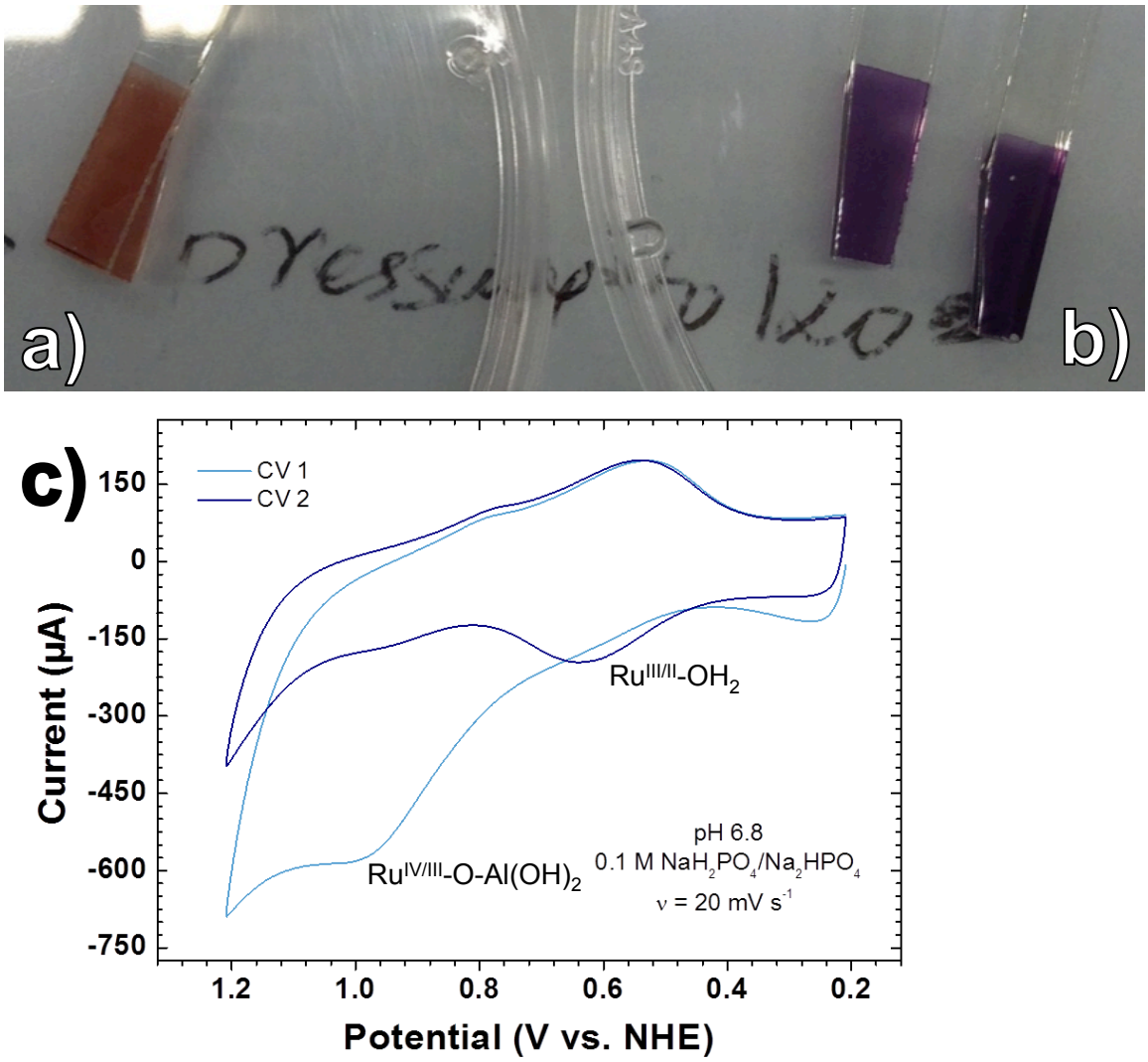

Figure 5.10. Photographs of *nano*ITO|-**RuCP(OH$_2$)$^{2+}$** a) before and b) following exposure to $Al(CH_3)_3$ in the ALD reaction chamber. c) CV scans of *nano*ITO|-**RuCP(OH$_2$)$^{2+}$** + 1 $Al(CH_3)_3$ pulse in 0.1 M sodium phosphate buffer (pH 6.8). The light blue trace is the first scan, while the dark blue trace is the second scan. The pH-dependent couple is attributed to Ru^{II}-OH_2, which is regenerated by the second scan.

5.2.4. Electrocatalytic water oxidation

Electrocatalytic water oxidation was investigated for *nano*ITO|–**RuP^{2+}**(10-AO)|–**RuCP(OH$_2$)$^{2+}$**(10-AO) with *nano*ITO|–**RuP^{2+}**(10-AO) as a control with the same cell configuration as in the photoelectrochemical experiments. Electrolyses were carried out at pH 8.8 sodium phosphate dibasic (I = 0.1 M; 0.4 M $NaClO_4$). O_2 was detected by using a parallel

collector–generator electrode technique (see Chapter 5.4. Experimental, **Figure 5.11**) with real-time detection of O_2 at −0.61 V vs. NHE.[11,27,28] The potential at the working electrode was first held at 0 V vs. NHE for two hours to simulate the dark-current background and reduce trace O_2 in the cell.

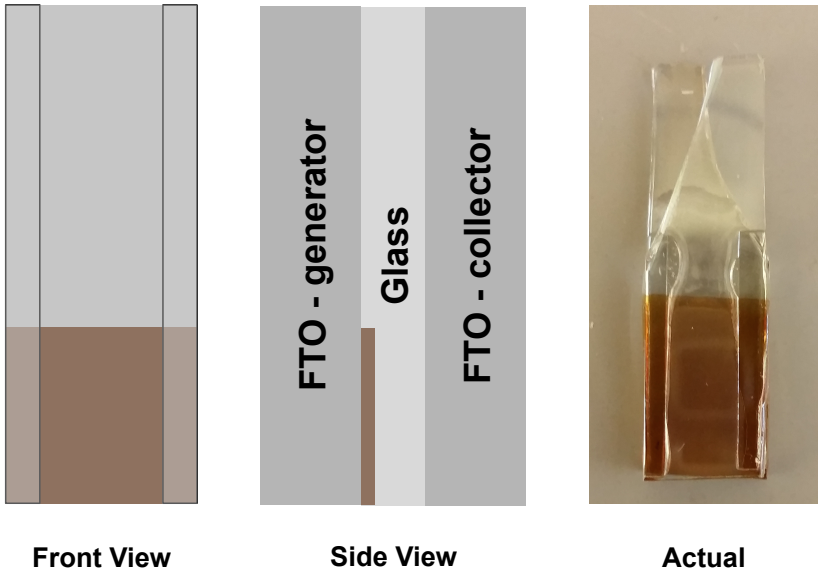

Figure 5.11. Schematic view and photograph of "FTO collector-generator" electrodes.

Water oxidation was initiated by stepping the electrode potential to E_{app} = 1.4 V vs. NHE, past $E_{1/2}$ = 1.3 V for the **–RuP$^{3+/2+}$** couple with the electrolysis continued for two hours.

The appearance of a significant catalytic current at E_{app} = 1.4 V in the current–time trace in **Figure 5.12** is notable, because the onset potential for water oxidation catalysis by **–RuCP(OH$_2$)$^{2+}$** is known to occur at ~1.6 V, near $E_{1/2}$ for the **–Ru^{V}(O)$^{3+/2+}$** catalyst couple.[28] As found earlier for a surface-bound chromophore-catalyst assembly, the low potential onset may be due to concerted electron-atom proton transfer with O-atom transfer to a water molecule

accompanied by single electron transfer to both **–RuP^{3+}** and **–Ru^{IV}CP(O)$^{2+}$** and proton transfer to an external base.[6,22]

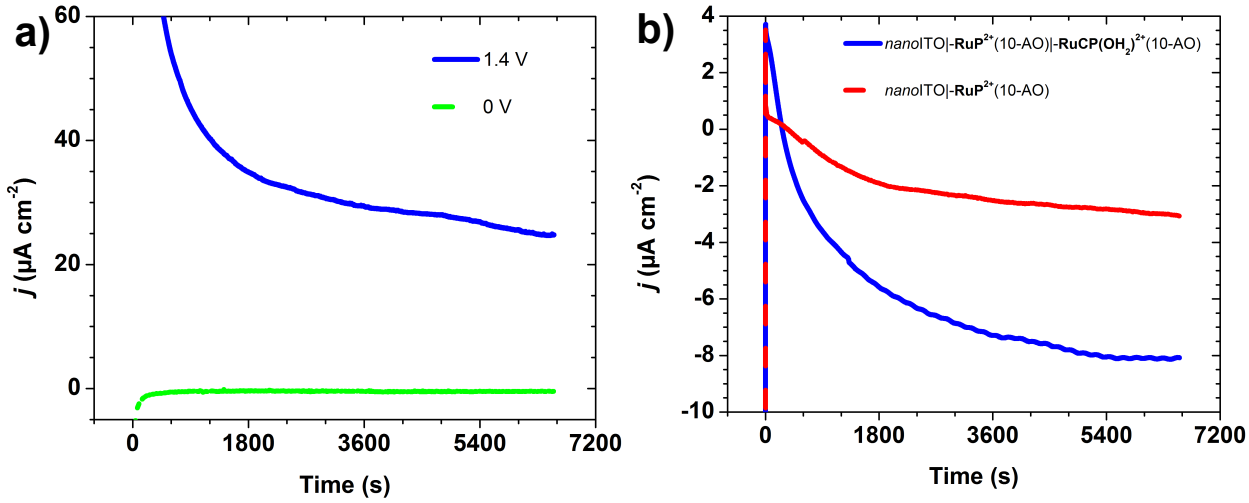

Figure 5.12. (a) Current-time traces for *nano*ITO|-**RuP^{2+}**(10-AO)|-**RuCP(OH$_2$)$^{2+}$**(10-AO) with E_{gen} = 1.4 V (blue trace) and 0 V vs. NHE (green trace); (b) Background (i.e. E_{gen} = 0 V vs. NHE)-subtracted current-time traces for the FTO collector electrode for *nano*ITO|-**RuP^{2+}**(10-AO)|-**RuCP(OH$_2$)$^{2+}$**(10-AO) (blue trace) and *nano*ITO|-**RuP^{2+}**(10-AO) (red trace), with E_{coll} = -0.61 V vs. NHE. Cathodic currents arise from O_2 reduction at the FTO collector electrode (conditions: pH 8.8, 0.1 M $H_2PO_4^-/HPO_4^{2-}$; 0.4 M $NaClO_4$; Ref = SCE; Aux = Pt-mesh).

Currents of >60 μA cm^{-2} were obtained at E_{app} = 1.4 V which slowly decreased to >20 μA cm^{-2} over a two-hour period. Water oxidation catalysis was verified by O_2 detection at the collector electrode compared to the control sample (**Figure 5.12**b). Integration of current passed resulted in a Faradaic efficiency for O_2 evolution of ~23% with the origin of loss presumably due to competitive decomposition of the polypyridyl ligand in the **–Ru^{IV}CP(O)$^{2+}$** form of the catalyst as reported earlier for a related complex.[29]

As calculated by **Equation 5.4**, the turnover frequency (TOF) for water oxidation was 0.014 s^{-1} at E_{app} = 1.4 V. In **Equation 5.4**, $Q_{O2\ reduction}$ (C) is the integrated charge passed for O_2 reduction at the FTO collector electrode, Γ (mol cm^{-2}) is the surface coverage of **RuCP(OH$_2$)$^{2+}$**,

F is Faraday's constant (96,485 C mol^{-1}), n_{cat} = 4 is the electrochemical stoichiometry for water oxidation to O_2, $\eta_{collection}$ = 0.7 is the collection efficiency at the collector electrode,[11] A (cm^2) is the exposed area of the electrode, and t (s) is the electrolysis time. This estimate is a lower limit for water oxidation since surface coverages (Γ) were evaluated by UV-visible measurements and not all of the catalytic sites may be electrochemically active due to the Al_2O_3 overlayer. For comparison, for a closely related chromophore-catalyst assembly with the same catalyst but prepared by an electro-assembly technique, the TOF was 0.046 s^{-1} at E_{app} = 1.7 V in a pH 4.7 aqueous sodium acetate buffer (I = 0.1 M; 0.5 M $NaClO_4$), but with **–Ru^{V}CP(O)$^{3+}$** as the active oxidant rather than **–Ru^{IV}CP(O)$^{2+}$**.[10]

Equation 5.4

$$TOF = \frac{Q_{O_2\ reduction}}{n_{cat}FA\Gamma t\eta_{collection}}$$

5.2.5. Photoelectrochemical water oxidation

Photoelectrochemical water oxidation was investigated for *nano*TiO_2|**–RuP^{2+}**(10-AO)|**–RuCP(OH$_2$)$^{2+}$**(10-AO) by using the same cell configuration as in hydroquinone dehydrogenation studies. The experiments were conducted in pH 8.8 sodium dibasic phosphate (I = 0.1 M; 0.4 M $NaClO_4$) with O_2 detection by the parallel collector–generator technique described earlier.

Short illumination periods (15 minutes) with an intense white light source (~200 mW cm^{-2}, 380 nm long-pass filter) resulted in the photocurrent responses shown in **Figure 5.13** (E_{gen} = 0.64 V; E_{coll} = −0.61 V vs. NHE).

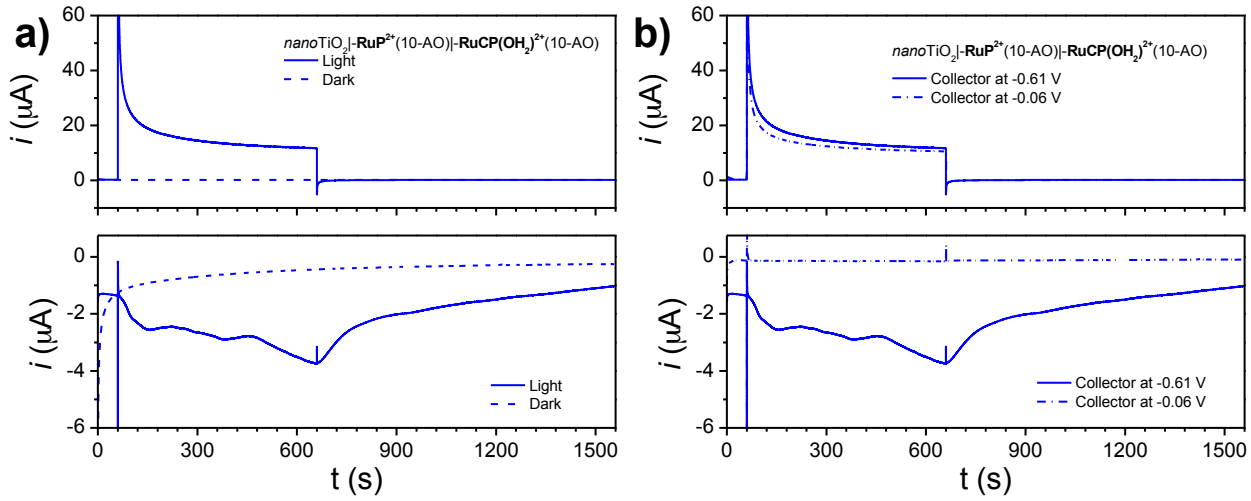

Figure 5.13. (a) Photocurrent-time traces for *nano*TiO_2|-**RuP**$^{2+}$(10-AO)|-**RuCP(OH$_2$)**$_2^{2+}$(10-AO) at the (top) generator electrode and (bottom) collector electrode under illumination (solid traces) and in the dark (dashed traces) with E_{gen} = 0.64 V vs. NHE and E_{coll} = -0.61 V vs. NHE. (b) Photocurrent-time traces for *nano*TiO_2|-**RuP**$^{2+}$(10-AO)|-**RuCP(OH$_2$)**$_2^{2+}$(10-AO) at the (top) generator electrode and (bottom) collector electrode under illumination with E_{gen} = 0.64 V vs. NHE and E_{coll} = –0.61 V vs. NHE (solid traces) or E_{coll} = –0.06 V vs. NHE (dashed traces) (conditions: ~200 mW cm^{-2} white light illumination; 380-nm long-pass filter; pH 8.8, 0.1 M $H_2PO_4^-/HPO_4^{2-}$; 0.4 M $NaClO_4$; Ref = SCE; Aux = Pt-mesh).

Upon illumination, instantaneous photocurrent is produced at the photoanode (generator) electrode. A cathodic current is gradually observed at the collector electrode, indicative of O_2 reduction following diffusion from the generator. Two control assemblies (a non-ALD-protected chromophore-catalyst and a chromophore-only photoanode) did not show productive O_2 current at the collector electrode (**Figure 5.14**).

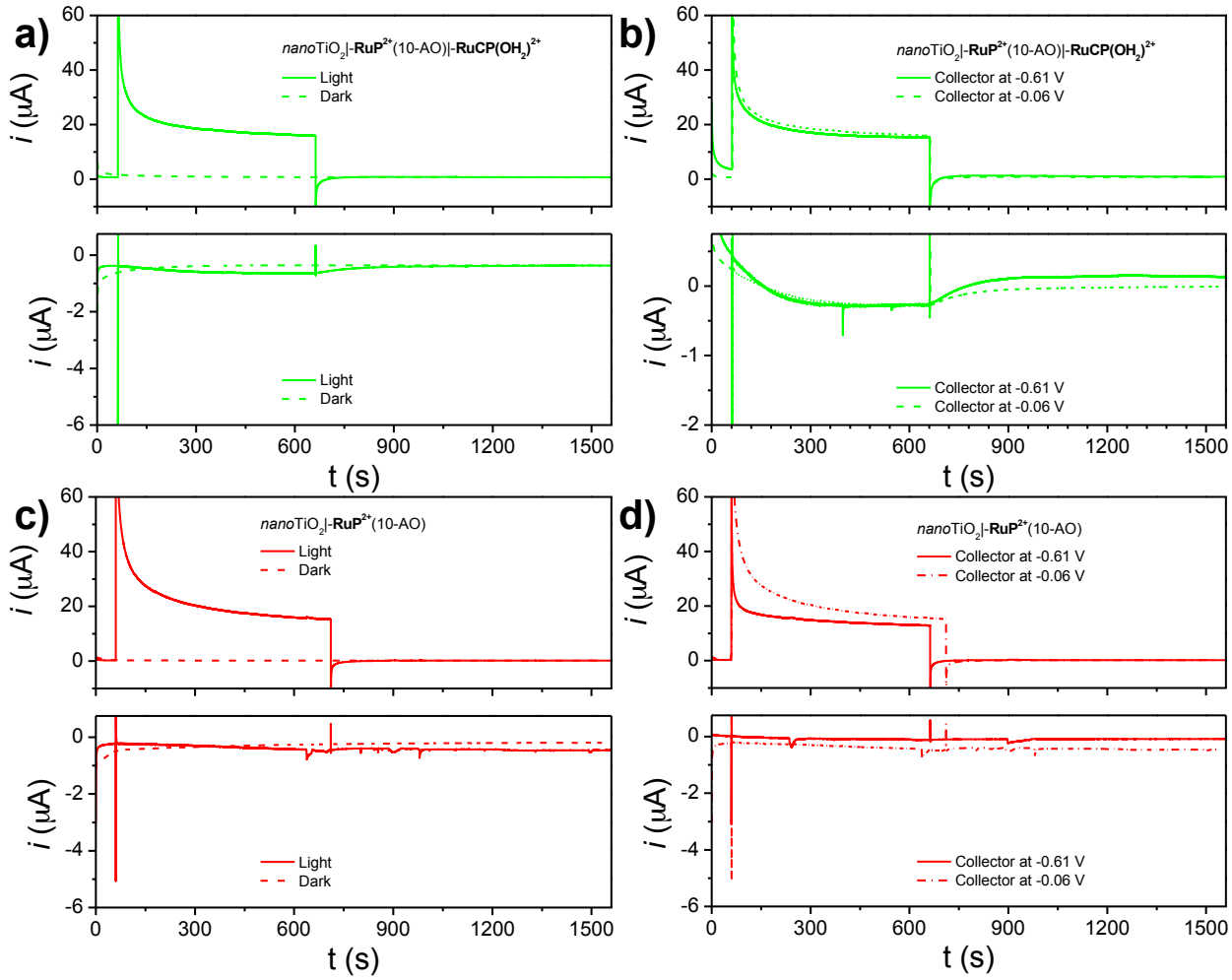

Figure 5.14. a) and c) Photocurrent-time traces for a) *nano*TiO_2|-**RuP**$^{2+}$(10-AO)|-**RuCP(OH$_2$)**$^{2+}$ and c) *nano*TiO_2|-**RuP**$^{2+}$(10-AO) at the (top) generator electrode and (bottom) collector electrode under illumination (solid traces) and in the dark (dashed traces) with E_{gen} = 0.64 V vs. NHE and E_{coll} = -0.61 V vs. NHE. b) and d) Photocurrent-time traces for b) *nano*TiO_2|-**RuP**$^{2+}$(10-AO)|-**RuCP(OH$_2$)**$^{2+}$ and d) *nano*TiO_2|-**RuP**$^{2+}$(10-AO) at the (top) generator electrode and (bottom) collector electrode under illumination with E_{gen} = 0.64 V vs. NHE and E_{coll} = -0.61 V vs. NHE (solid traces) or E_{coll} = -0.06 V vs. NHE (dashed traces). (Conditions: ~200 mW cm^{-2} white light illumination; 380-nm long-pass filter; pH 8.8, 0.1 M $H_2PO_4^-$/HPO_4^{2-}; 0.4 M $NaClO_4$; Ref = SCE; Aux = Pt-mesh).

To ensure the cathodic current at the collector electrode was not due to desorbing, oxidized Ru species, the potential at the collector electrode was raised from −0.61 V to −0.06 V. A potential of −0.06 V is sufficiently negative to reduce Ru(III) → Ru(II), but not sufficient for O_2 reduction. As seen in **Figure 5.13**b, despite similar a similar photocurrent response at the

photoanode generator, no corresponding cathodic current was observed at the collector electrode, suggesting that the cathodic current observed previously is not due to diffusing Ru(III) species.

An extended photoelectrolysis (6 hours) was performed on the mummified assembly (**Figure 5.15**). Under intense white light (~200 mW cm^{-2}, 400 nm long-pass filter), the assembly showed sustained generator and collector current over the course of the six-hour illumination. The generator current decayed instantaneously upon shuttering the light, while the collector current gradually decayed, similar to the current traces observed over shorter time periods. Integration of the current passed allowed for a comparison of the cumulative Faradaic efficiency as a function of time (**Figure 5.16**) by **Equation 5.5**.

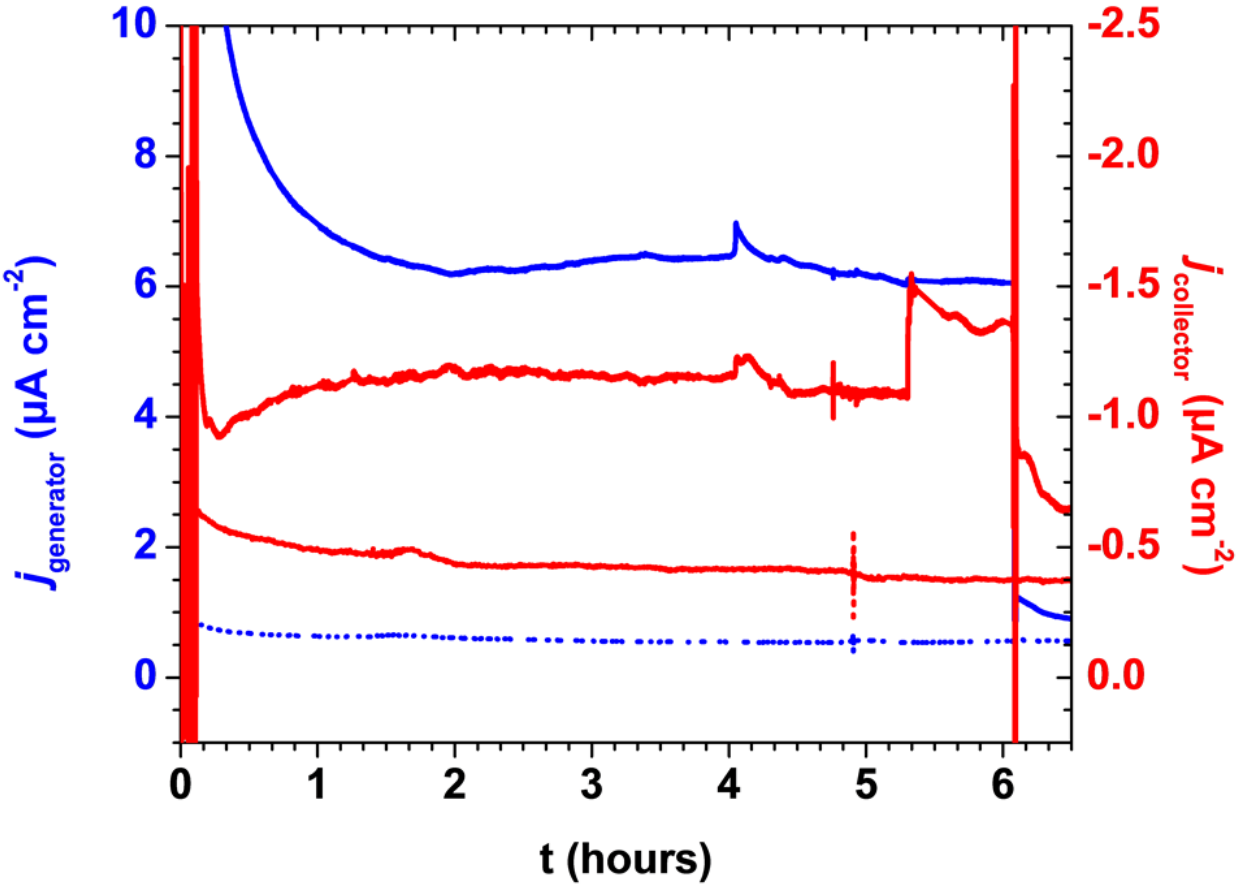

Figure 5.15. Current-time traces for *nano*TiO_2|-**RuP**$^{2+}$(10-AO)|-**RuCP(OH$_2$)**$^{2+}$(10-AO) E_{gen} = 0.64 V and E_{coll} = -0.61 V under illumination. Blue traces (left axis) indicate generator current under illumination (solid) and in the dark (dotted) while red traces (right axis) indicate collector current with the same convention. Cathodic current arises from O_2 reduction at the FTO collector electrode (conditions: ~200 mW cm^{-2} white light illumination; 400-nm long-pass filter; pH 8.8, 0.1 M $H_2PO_4^-$/HPO_4^{2-}; 0.4 M $NaClO_4$; Ref = SCE; Aux = Pt-mesh).

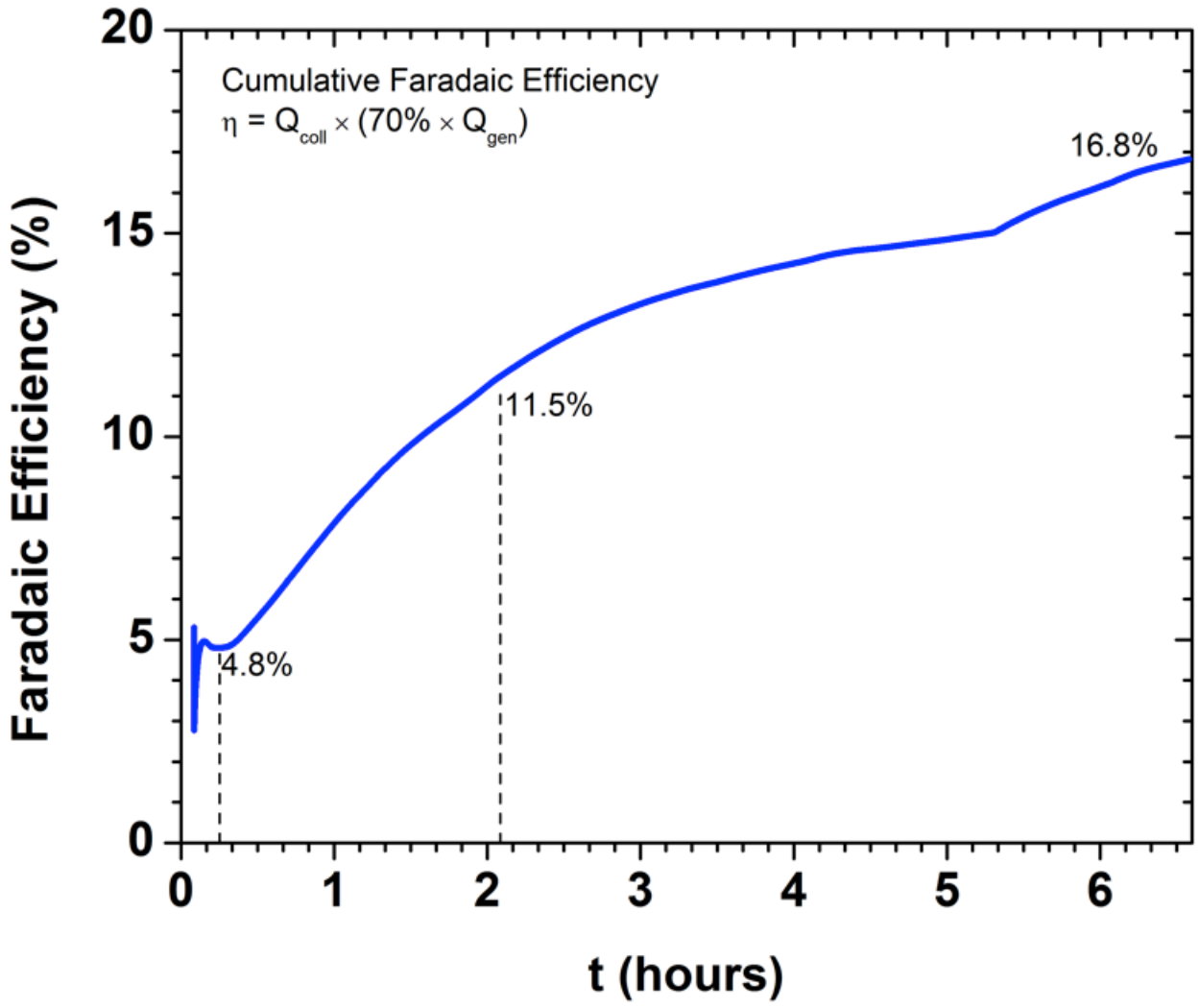

Figure 5.16. Cumulative Faradaic efficiency vs. time trace for *nano*TiO_2|-**RuP**$^{2+}$(10-AO)|-**RuCP(OH$_2$)**$^{2+}$(10-AO) under white light illumination. (Conditions: ~200 mW cm^{-2} white light illumination; 400-nm long-pass filter; pH 8.8, 0.1 M $H_2PO_4^-/HPO_4^{2-}$; 0.4 M $NaClO_4$; Ref = SCE; Aux = Pt-mesh; E_{gen} = 0.64 V vs. NHE and E_{coll} = -0.61 V vs. NHE).

Equation 5.5

$$\eta(t) = \int_0^t j_{collector} / (0.7 \times \int_0^t j_{generator})$$

In **Equation 5.5**, 0.7 is the collection efficiency at the collector electrode, and t is the time (s) of illumination. Over the course of illumination, the Faradaic efficiency is observed to

increase, ultimately reaching 16.8% after 6 hours. As a comparison, a recently reported electro-assembled chromophore-catalyst assembly showed a Faradaic efficiency of 8% for O_2 production for light-assisted water oxidation (100 mW cm^{-2}, 380 nm cut-off filter after 10 minutes of illumination; 4.8% after 10 minutes in the mummified system).[11] This comparison suggests that mummified/ALD-constructed assemblies compare favorably to chromophore-catalyst assemblies constructed by other reported methods.

5.3. Conclusions

We describe here a novel procedure for the direct surface preparation of chromophore-catalyst assemblies based on phosphonate surface binding and ALD deposition of Al_2O_3 overlayers. It features high surface stability and electronically linked chromophore and catalyst pairs without covalent bond formation with an ALD mummy strategy for stabilizing the surface-bound chromophore. Although electron transfer is inhibited on the ALD stabilized surfaces, they do undergo injection and assembly oxidation with sustained photocurrents observed in a DSPEC with added hydroquinone. Electrocatalytic water oxidation is also observed for the mummy assembly with sustained catalytic currents at applied potentials below those required for oxidation of the catalyst to **–Ru^{V}CP(O)$^{3+}$**, apparently by intervention of a concerted electron-atom transfer pathway observed earlier in a covalently linked assembly. Light-assisted water oxidation catalysis has been observed over a continuous six-hour illumination period. Experiments incorporating a more active catalyst are currently underway.

5.4. Experimental

5.4.1. Materials and methods

Materials. De-ionized water was further purified using a Milli-Q Ultrapure water purification system. Additional solvents, hydrochloric acid, and glacial acetic acid were purchased from Fisher Scientific and were used as received. Sodium acetate, sodium phosphate

(monobasic, anhydrous), and sodium phosphate dibasic (anhydrous) were purchased from Sigma-Aldrich, were ACS Reagent grade or better, and were used as received. $[Ru(Mebimpy)(Cl)(\mu\text{-}Cl)]_2$ (Mebimpy = 2,6-bis(1-methyl-1H-benzo[d]imidazol-2-yl)pyridine),[10] 4,4'-dpcbpy,[23] cis-$[Ru(2,2'\text{-bipyridine})_2(Cl)_2]$,[9] and 4,4'-$((EtO)_2(O)P)_2$-2,2'-bipyridine[23] were synthesized according to literature protocols. Fluorine-doped tin oxide (FTO, 15 Ω per square sheet resistance) was purchased from Hartford Glass (Hartford City, IN) and was cleaned by sonication in ethanol (20 min), 0.1 M HCl in ethanol (20 min), and ethanol (20 min) prior to use.

5.4.2. Synthesis of molecular complexes

Synthesis of $\boldsymbol{RuP^{2+}}$.[23] In a 100-mL Teflon microwave vessel, *cis*-$[Ru(2,2'\text{-bipyridine})_2(Cl)_2]$ (227 mg, 4.69×10^{-4} mol) and 4,4'-$((EtO)_2(O)P)_2$-2,2'-bipyridine (201 mg, 4.69×10^{-4} mol) were suspended in water (17 mL). The vessel was placed in a microwave reactor where, following a 5-minute ramping period, it was heated at 140 °C for 10 minutes. The pressure of the vessel did not exceed 300 PSI. The vessel was allowed to cool to room temperature. The suspension was filtered through a Millex GP PES Membrane (0.22 μm). The solvent was removed from the filtrate on a rotary evaporator. The residue was stirred in refluxing 4 M HCl overnight. The solvent was removed on a rotary evaporator. The resulting residue was triturated with ether and collected over a glass frit. The orange-red precipitate was washed with ether and collected (339 mg, 4.23×10^{-4} mol, 90%).

The ^{1}H NMR spectrum matched that of a previously reported sample.

Analytical HPLC (75:25 water:methanol) of the sample indicated ≥ 95% purity, with the likely impurity being $[Ru(2,2'\text{-bipyridine})_3][Cl]_2$, which should not bind to metal oxide electrode surfaces.

Synthesis of $\boldsymbol{RuCP(OH_2)^{2+}}$.[30-32] In a 100-mL Teflon microwave vessel, [Ru(2,6-bis(1-methyl-1*H*-benzo[*d*]imidazol-2-yl)pyridine)(Cl)]$_2$[Cl]$_2$ (41.2 mg, 4.03×10^{-5} mol) and 4,4'-

dpcbpy (27.8 mg, 8.08×10^{-5} mol) were suspended in ethanol (20 mL) and water (10 mL). The vessel was briefly subject to sonication (~1 minute). The vessel was placed in a microwave reactor where, following a 5-minute ramping period, it was heated at 160 °C for 30 minutes. The pressure of the vessel did not exceed 300 PSI. The vessel was allowed to cool to room temperature. The solution was filtered. From the filtrate, the solvent was removed on a rotary evaporator. The residue was dried under vacuum overnight. To the residue, anhydrous methylene chloride (50 mL) was added. The suspension was de-aerated with argon for 15 minutes. With a vent needle in place and under continuous flow of argon (CAUTION: HCl gas is evolved), trifluoromethanesulfonic acid (1.8 mL) was added slowly. The reaction immediately releases HCl (gas). The reaction stirred at room temperature overnight (note: the flow of argon was high enough to vent HCl but low enough as to not evaporate methylene chloride over the time of the experiment). Following the reaction, diethyl ether was added to precipitate the solid, which was collected on a glass frit and washed with diethyl ether (62.4 mg, 5.67×10^{-5} mol, 70%). The ^{1}H NMR spectrum matched that of a previously reported sample. Analytical HPLC (40:60 water:methanol) of the sample revealed three product peaks; however the UV-visible absorption spectrum of each peak was identical.

Complex Loading. Methanol solutions (~1 mM) of $\mathbf{RuP^{2+}}$ and $\mathbf{RuCP(OH_2)^{2+}}$ were used for complex loading. Electrodes (*nano*ITO or *nano*TiO_2) were placed in the solutions to load complexes, typically overnight. Following loading, the electrodes were rinsed with methanol and dried under a stream of air or N_2. Surface coverage was determined using the background-subtracted absorbance values from UV-visible absorption spectra and the following equation: $\Gamma = A(\lambda) \times (\varepsilon(\lambda) \times 1000)^{-1}$.

5.4.3. Nanoparticle TiO_2 films (*nano*TiO_2)

Nanoparticles of TiO_2 were prepared as described previously.[33,34] Nanoparticle paste was spread on FTO glass using the doctor-blade method with 1 layer of Scotch tape. Film thicknesses were approximately 4 μm thick.

5.4.4. Nanoparticle ITO films (*nano*ITO)

Nanoparticles of tin-doped indium oxide (ITO, TC8 DE; 20 wt% dispersion in ethanol) were purchased from Evonik Industries and were prepared as described previously.[35] Nanoparticle paste was spread on FTO glass using the doctor-blade method with 1 layer of Scotch tape. Film thicknesses were approximately 4 μm thick.

5.4.5. BET measurements

The mean pore sizes of *nano*ITO and *nano*ITO(20-AO) were determined using BET desorption isotherms. The electrodes were cut into small (~0.07 cm^2) pieces and placed in a BET sample bulb. The *nano*ITO nanoparticles were not removed from the FTO glass substrate so as to preserve the pore structure, while all glass scoring was made to the backside of the FTO glass substrate. Approximately 8 g of material (which represents a projected area of ~8 cm^2) was placed in the sample bulb and was heated to 140 °C under vacuum for 22 hours using a Quantachrome NOVA 200 system. The samples and sample bulbs cooled to room temperature, after which they were back-filled with helium. Given the majority of the sample mass was FTO glass, specific surface area measurements were not revealing. Using the desorption isotherms with $0.6 < P/P_o < 0.95$, the pore size distribution was determined by Barrett–Joyner–Halenda (BJH) analysis. The mean pore sizes for *nano*ITO and *nano*ITO(20-AO) were 36 nm and 31 nm, respectively.

5.4.6. Atomic layer deposition (ALD)

ALD was performed by using a Cambridge NanoTech Savannah S200 ALD system located in the Chapel Hill Analytical and Nanofabrication Laboratory (CHANL) cleanroom. The reactor was set at 150 °C. Prior to deposition, samples sat in the reactor under continuous nitrogen purge (99.999%, further purified using an Entegris GateKeeper Inert Gas Purifier) at 150 °C for a minimum of 10 minutes. Each deposition cycle consisted of a 0.02 s pulse of trimethylaluminum ($Al(CH_3)_3$, 97% purity), a 20 s exposure in the reactor, a 60 s purge, a 0.02 s pulse of water, a 20 s exposure in the reactor, and a 60 s purge.

5.4.7. FTO collector–generator electrodes

Dual working electrodes were constructed by adapting a technique developed by Mallouk.[11,27] Thin strips of non-conductive glass (~2–3 mm wide, 1 mm thick) were applied to working electrodes (*nano*TiO_2 or *nano*ITO) using epoxy (Loctite Hysol E-00CL) and allowed to cure. FTO was then attached using epoxy such that the conductive side of each electrode faced inward (**Figure 5.11**). The electrolytic solution is drawn between the working electrodes by capillary action.

5.4.8. Electrochemistry

Cyclic voltammetry (CV) and current–time measurements were performed with a CH Instruments potentiostat (model 601D or 660D) or bipotentiostat (model 760E). Typically, a two-compartment glass cell (working electrode and reference/counter electrodes separated by a fine-porosity glass frit) was used. The reference electrode was Ag/AgCl (3 M NaCl, E = 0.2 V vs. NHE). The counter electrode was Pt metal (wire or mesh).

5.4.9. Spectroelectrochemistry

Spectroelectrochemical measurements were performed in a one-compartment glass cuvette with a Ag/AgCl (3 M NaCl) reference electrode and a Pt metal mesh counter electrode.

The reference and counter electrodes were placed behind the working electrode such that contact was made with the non-conductive glass. The working electrode (*nano*ITO) was placed at a 45° angle to the path of the beam. UV-visible absorption spectra were collected with an Agilent 8453 UV-visible photodiode array spectrophotometer. The potential of the working electrode was stepped from −0.2 V to 1.5 V vs. Ag/AgCl (3 M NaCl) with a potential step every 0.02 V. The potential at each step was held for 180 s to achieve equilibrium. Redox potentials were obtained by fitting using SPECFIT/32 software.

5.4.10. Electrocatalysis

Electrocatalytic water oxidation experiments were conducted in a two-compartment cell with the working electrode (nanoITO-FTO dual electrode, see above) and reference (SCE, E = 0.24 V vs. NHE)/counter (Pt mesh) electrodes separated by a Nafion membrane. A bipotentiostat (CHI 760E) was used to poise the potential of the working generator (nanoITO) electrode at a set potential while the working collector (FTO) electrode was poised at −0.61 V vs. NHE for in situ reduction of O_2 as it formed. Prior to electrocatalysis, the buffer solution (pH 8.8, 0.1 M $H_2PO_4^-/HPO_4^{2-}$ in 0.4 M $NaClO_4$) was deaerated with N_2 for ~15 min. A positive stream of N_2 was maintained in the headspace to avoid atmospheric O_2 diffusion into the solution. The potential of the working generator electrode was poised at 0 V vs. NHE for two hours to approximate a dark current trace before immediately stepping the potential to 1.4 V vs. NHE for two hours. Currents were normalized for the geometric areas of the working electrodes.

5.4.11. Photoelectrochemistry (hydroquinone)

Photoelectrochemical experiments were conducted in a two-compartment cell with the working electrode (*nano*TiO_2, working area defined by Hysol E-00CL epoxy) and reference (SCE, E = 0.24 V vs. NHE)/counter (Pt mesh) electrodes separated by a Nafion membrane. A bipotentiostat (CHI 760E) was used to poise the potential of the working electrode (0.24 V vs.

NHE) to maximize hydrogen evolution at the counter electrode. Prior to illumination, the buffer solution (pH 4.7 HOAc/NaOAc, 0.1 M; 0.5 M $NaClO_4$ supporting electrolyte) with added hydroquinone (0.02 M) was de-aerated with N_2 for ~15 min. A positive stream of N_2 was maintained in the headspace to avoid atmospheric O_2 diffusion into the solution. Illumination was provided by a Thor Labs HPLS-30-04 light source. Samples were positioned to receive ~100 mW cm^{-2} (1 sun, 400 to 700 nm) with the light intensity determined with an Oriel Instruments 91150V reference cell. A 400 nm long-pass filter was used to prevent direct bandgap excitation of nanoTiO_2. Preliminary experiments were simple "off–on" illumination cycles with 30 s intervals of dark followed by illumination. Dark and light J–V curves were also obtained at a scan rate of 5 mV s^{-1}. Continuous illumination was performed for 10 minutes. The photocurrent data were normalized to the initial current spike and for the area of nanoTiO_2 illuminated.

5.4.12. Photoelectrochemistry (water oxidation)

Photoelectrochemical experiments for water oxidation were conducted in a two-compartment cell with the working electrode (*nano*TiO_2, working area defined by Hysol 608 epoxy) and reference (SCE, E = 0.24 V vs. NHE)/counter (Pt mesh) electrodes separated by a Nafion membrane. A bipotentiostat (CHI 760E) was used to poise the potential of the working electrode (0.64 V vs. NHE, 1.16 V vs. RHE) to maximize hydrogen evolution at the counter electrode. Prior to illumination, the buffer solution (pH 8.8 NaH_2PO_4/Na_2HPO_4, 0.1 M; 0.4 M $NaClO_4$ supporting electrolyte) was de-aerated with N_2 for ~15 min. A positive stream of N_2 was maintained in the headspace to avoid atmospheric O_2 diffusion into the solution. Illumination was provided by a Thor Labs HPLS-30-04 light source. Samples were positioned to receive ~200 mW cm^{-2} (2 sun, 400 to 700 nm) with the light intensity determined with an Oriel Instruments 91150V reference cell. For short illumination periods (15 minutes), a 380 nm long-pass filter was

used to maximize the photoelectrochemical activity. For long illumination periods (2–6 hours), a 400 nm long-pass filter was used to prevent direct bandgap excitation of nanoTiO_2.

5.5. Acknowledgements

This material is based upon work solely supported as part of the UNC EFRC: Center for Solar Fuels, an Energy Frontier Research Center funded by the U.S. Department of Energy, Office of Science, Office of Basic Energy Sciences under Award Number DE-SC0001011. A.M.L. acknowledges a graduate fellowship supported by the Department of Defense (DoD) through the National Defense Science & Engineering Graduate Fellowship (NDSEG) Program. The authors would like to acknowledge Dr. Bob Geil for assistance with ALD and Dr. Amar Kumbhar for assistance with imaging in the Chapel Hill Analytical and Nanofabrication Laboratory (CHANL).

5.6. Associated Content

Associated content, including SEM images and CVs, can be found in Appendix C.

REFERENCES

(1) Ardo, S.; Meyer, G. J. *Chem. Soc. Rev.* **2009**, *38*, 115.

(2) Swierk, J. R.; Mallouk, T. E. *Chem. Soc. Rev.* **2013**, *42*, 2357.

(3) Young, K. J.; Martini, L. A.; Milot, R. L.; Snoeberger Iii, R. C.; Batista, V. S.; Schmuttenmaer, C. A.; Crabtree, R. H.; Brudvig, G. W. *Coord. Chem. Rev.* **2012**, *256*, 2503.

(4) Song, W.; Vannucci, A. K.; Farnum, B. H.; Lapides, A. M.; Brennaman, M. K.; Kalanyan, B.; Alibabaei, L.; Concepcion, J. J.; Losego, M. D.; Parsons, G. N.; Meyer, T. J. *J. Am. Chem. Soc.* **2014**, *136*, 9773.

(5) Ashford, D. L.; Song, W.; Concepcion, J. J.; Glasson, C. R. K.; Brennaman, M. K.; Norris, M. R.; Fang, Z.; Templeton, J. L.; Meyer, T. J. *J. Am. Chem. Soc.* **2012**, *134*, 19189.

(6) Norris, M. R.; Concepcion, J. J.; Fang, Z.; Templeton, J. L.; Meyer, T. J. *Angew. Chem. Int. Ed.* **2013**, *52*, 13580.

(7) Hanson, K.; Torelli, D. A.; Vannucci, A. K.; Brennaman, M. K.; Luo, H.; Alibabaei, L.; Song, W.; Ashford, D. L.; Norris, M. R.; Glasson, C. R. K.; Concepcion, J. J.; Meyer, T. J. *Angew. Chem., Int. Ed.* **2012**, *51*, 12782.

(8) Ishida, T.; Terada, K.-i.; Hasegawa, K.; Kuwahata, H.; Kusama, K.; Sato, R.; Nakano, M.; Naitoh, Y.; Haga, M.-a. *Appl. Surf. Sci.* **2009**, *255*, 8824.

(9) Lapides, A. M.; Ashford, D. L.; Hanson, K.; Torelli, D. A.; Templeton, J. L.; Meyer, T. J. *J. Am. Chem. Soc.* **2013**, *135*, 15450.

(10) Ashford, D. L.; Lapides, A. M.; Vannucci, A. K.; Hanson, K.; Torelli, D. A.; Harrison, D. P.; Templeton, J. L.; Meyer, T. J. *J. Am. Chem. Soc.* **2014**, *136*, 6578.

(11) Ashford, D. L.; Sherman, B. D.; Binstead, R. A.; Templeton, J. L.; Meyer, T. J. *Angew. Chem. Int. Ed.* **2015**, *54*, 4778.

(12) Bettis, S. E.; Ryan, D. M.; Gish, M. K.; Alibabaei, L.; Meyer, T. J.; Waters, M. L.; Papanikolas, J. M. *J. Phys. Chem. C* **2014**, *118*, 6029.

(13) Hanson, K.; Brennaman, M. K.; Luo, H.; Glasson, C. R.; Concepcion, J. J.; Song, W.; Meyer, T. J. *ACS Appl. Mater. Interfaces* **2012**, *4*, 1462.

(14) Ghosh, P. K.; Brunschwig, B. S.; Chou, M.; Creutz, C.; Sutin, N. *J. Am. Chem. Soc.* **1984**, *106*, 4772.

(15) Hara, M.; Waraksa, C. C.; Lean, J. T.; Lewis, B. A.; Mallouk, T. E. *J. Phys. Chem. A* **2000**, *104*, 5275.

(16) Youngblood, W. J.; Lee, S.-H. A.; Maeda, K.; Mallouk, T. E. *Acc. Chem. Res.* **2009**, *42*, 1966.

(17) Youngblood, W. J.; Lee, S.-H. A.; Kobayashi, Y.; Hernandez-Pagan, E. A.; Hoertz, P. G.; Moore, T. A.; Moore, A. L.; Gust, D.; Mallouk, T. E. *J. Am. Chem. Soc.* **2009**, *131*, 926.

(18) Hyde, J. T.; Hanson, K.; Vannucci, A. K.; Lapides, A. M.; Alibabaei, L.; Norris, M. R.; Meyer, T. J.; Harrison, D. P. *ACS Appl. Mater. Interfaces* **2015**, *7*, 9554.

(19) Son, H.-J.; Prasittichai, C.; Mondloch, J. E.; Luo, L.; Wu, J.; Kim, D. W.; Farha, O. K.; Hupp, J. T. *J. Am. Chem. Soc.* **2013**, *135*, 11529.

(20) Son, H.-J.; Kim, C. H.; Kim, D. W.; Jeong, N. C.; Prasittichai, C.; Luo, L.; Wu, J.; Farha, O. K.; Wasielewski, M. R.; Hupp, J. T. *ACS Appl. Mater. Interfaces* **2015**, *7*, 5150.

(21) Hanson, K.; Losego, M. D.; Kalanyan, B.; Ashford, D. L.; Parsons, G. N.; Meyer, T. J. *Chem. Mater.* **2013**, *25*, 3.

(22) Vannucci, A. K.; Alibabaei, L.; Losego, M. D.; Concepcion, J. J.; Kalanyan, B.; Parsons, G. N.; Meyer, T. J. *Proc. Natl. Acad. Sci. U. S. A.* **2013**, *110*, 20918.

(23) Norris, M. R.; Concepcion, J. J.; Glasson, C. R. K.; Fang, Z.; Lapides, A. M.; Ashford, D. L.; Templeton, J. L.; Meyer, T. J. *Inorg. Chem.* **2013**, *52*, 12492.

(24) O'Donnell, R. M.; Sampaio, R. N.; Li, G.; Johansson, P. G.; Ward, C. L.; Meyer, G. J. *J. Am. Chem. Soc.* **2016**, *138*, 3891.

(25) Vannucci, A. K.; Hull, J. F.; Chen, Z.; Binstead, R. A.; Concepcion, J. J.; Meyer, T. J. *J. Am. Chem. Soc.* **2012**, *134*, 3972.

(26) Binstead, R. A.; McGuire, M. E.; Dovletoglou, A.; Seok, W. K.; Roecker, L. E.; Meyer, T. J. *J. Am. Chem. Soc.* **1992**, *114*, 173.

(27) Lee, S.-H. A.; Zhao, Y.; Hernandez-Pagan, E. A.; Blasdel, L.; Youngblood, W. J.; Mallouk, T. E. *Faraday Discuss.* **2012**, *155*, 165.

(28) Kent, C. A.; Concepcion, J. J.; Dares, C. J.; Torelli, D. A.; Rieth, A. J.; Miller, A. S.; Hoertz, P. G.; Meyer, T. J. *J. Am. Chem. Soc.* **2013**, *135*, 8432.

(29) Roecker, L.; Kutner, W.; Gilbert, J. A.; Simmons, M.; Murray, R. W.; Meyer, T. J. *Inorg. Chem.* **1985**, *24*, 3784.

(30) Concepcion, J. J.; Jurss, J. W.; Norris, M. R.; Chen, Z.; Templeton, J. L.; Meyer, T. J. *Inorg. Chem.* **2010**, *49*, 1277.

(31) Concepcion, J. J.; Binstead, R. A.; Alibabaei, L.; Meyer, T. J. *Inorg. Chem.* **2013**, *52*, 10744.

(32) Concepcion, J. J.; Jurss, J. W.; Hoertz, P. G.; Meyer, T. J. *Angew. Chem. Int. Ed.* **2009**, *48*, 9473.

(33) Song, W.; Ito, A.; Binstead, R. A.; Hanson, K.; Luo, H.; Brennaman, M. K.; Concepcion, J. J.; Meyer, T. J. *J. Am. Chem. Soc.* **2013**, *135*, 11587.

(34) Lee, S.-H. A.; Abrams, N. M.; Hoertz, P. G.; Barber, G. D.; Halaoui, L. I.; Mallouk, T. E. *J. Phys. Chem. B* **2008**, *112*, 14415.

(35) Farnum, B. H.; Morseth, Z. A.; Brennaman, M. K.; Papanikolas, J. M.; Meyer, T. J. *J. Am. Chem. Soc.* **2014**, *136*, 15869.

CHAPTER 6: TRANSIENT ABSORPTION SPECTROSCOPY AND DEVICE CHARACTERIZATION FOR RU(II) POLYPYRIDYL-DERIVATIZED CORE/SHELL PHOTOANODES [1]

6.1. Introduction

Dye-sensitized photoelectrosynthesis cells (DSPECs) offer a solution to solar energy storage by integrating molecular chromophores and catalysts with mesoporous films of wide bandgap oxide semiconductors for light-driven water splitting and carbon dioxide reduction.[1,2] In the simplest case of water splitting, the overall reaction can be divided into two half-reactions: water oxidation at a photoanode (**Equation 6.1**) and proton reduction at a photocathode (**Equation 6.2**).

Equation 6.1

$2H_2O \rightarrow O_2 + 4H^+ + 4e^-$

Equation 6.2

$4H^+ + 4e^- \rightarrow 2H_2$

At the photoanode in a water-splitting DSPEC, oxidation of the catalyst must occur prior to water oxidation. Activation of the catalyst is typically achieved through a series of charge transfer events.[3] First, a molecular chromophore bound to a wide bandgap semiconductor (e.g. TiO_2, SnO_2) absorbs a photon of light, forming a photo-excited state. Electron transfer (a.k.a.

[1] This chapter presents work for a manuscript *in preparation* with co-authors Melissa K. Gish, M. Kyle Brennaman, Byron H. Farnum, Joseph L. Templeton, Thomas J. Meyer, and John M. Papanikolas.

electron injection) can occur from the photo-excited chromophore to the conduction band of the semiconductor, leaving the chromophore oxidized. Hole transfer, or oxidation of the molecular catalyst by the chromophore, can now occur. For O_2 production, this sequence of events must occur four times. The injected electrons can either diffuse to the back contact of the mesoporous semiconductor film or recombine with oxidized molecular species, a deleterious process known as back electron transfer (BET). BET limits the efficiency of DSPEC water oxidation photoanodes by preventing the necessary accumulation of four holes on the catalyst; it is also thought to limit efficiency in dye-sensitized solar cells (DSSCs), which require only single-electron transfer events rather than charge accumulation.[4,5] Despite rapid excited-state electron injection and charge transfer among molecular species bound to TiO_2 nanoparticles ($E_{cb} \approx -0.15$ V vs. NHE at pH 1), BET to the oxidized catalyst still occurs on the microsecond timescale at pH 1.[6,7]

Core/shell oxides are one method for inhibiting BET to oxidized molecules on photoanodes. In a core/shell structure, an underlying material (core) is physically coated with another material. If each material (core and shell) is a distinct metal oxide semiconductor, misalignment of their conduction band edges creates an energy gradient at their interface. This design principle is derived from Nozik's "photochemical diode" in which two semiconductors with mismatched conduction band edges are sandwiched together, forming a rectifying junction.[8] In DSPEC photoanodes, it is advantageous for E_{cb}(core) to be more positive than that of E_{cb}(shell), an arrangement that promotes electron transfer from shell to core (**Figure 6.1**a). The electron effectively becomes "trapped" in the core, leading to long-lived charge separation.

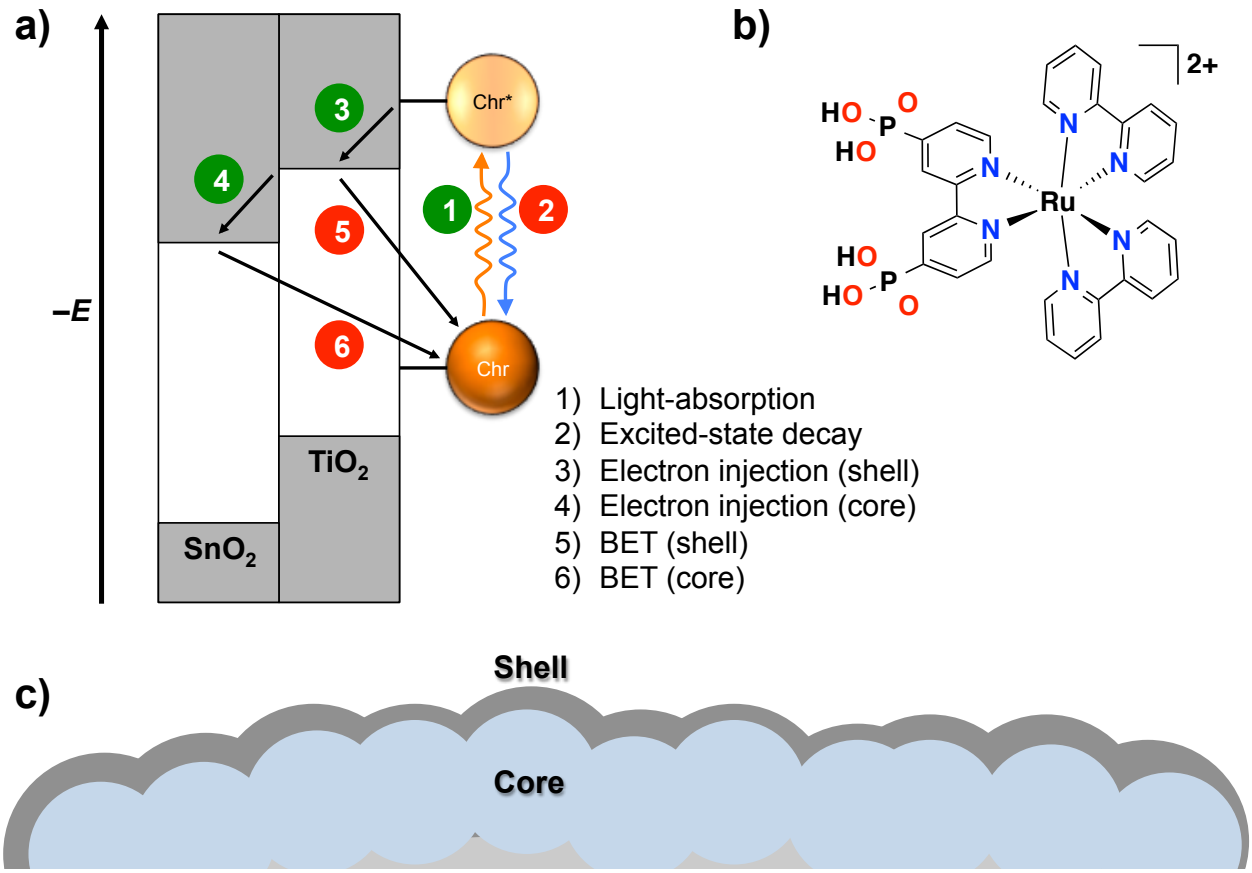

Figure 6.1. a) Schematic depiction of the photophysical processes of excitation and charge transfer occurring at the chromophore-SnO_2/TiO_2 core/shell interface with excitation and forward electron transfer indicated with green numbers and excited-state decay and back electron transfer indicated with red numbers (adapted from reference 9); b) Molecular structure of **RuP**$^{2+}$; c) Schematic depiction of physical core/shell structure.

One commonly employed core/shell structure utilizes a SnO_2 core and TiO_2 shell. While formation of the TiO_2 shell has historically been performed by chemical deposition,[10,11] recently atomic layer deposition (ALD) has allowed for low temperature deposition of conformal, thickness-controlled shells in high aspect ratio structures.[5,12,13] Transient absorption spectroscopy on the nanosecond timescale has been used to investigate the mechanism of charge

recombination in *nano*SnO_2/TiO_2 core shell structures derivatized with the molecular chromophore [Ru(2,2'-bipyridine)$_2$(4,4'-dpbpy)][Cl]$_2$ (**RuP^{2+}**, **Figure 6.1**b; 4,4'-dpbpy = [2,2'-bipyridine]-4,4'-diylbis(phosphonic acid)).[9] In this report, recombination of the injected electron with the oxidized dye occurs by electron tunneling through the TiO_2 for shells less than 3.2 nm thick. For thicker shells, direct recombination from the TiO_2 shell is observed. Despite these promising conclusions, ultrafast transient absorption spectroscopy data for electron injection and recombination with core/shell structures are needed to corroborate the proposed mechanism.

Herein we investigate the electron injection and recombination kinetics from the 250 fs to ms timescale following 480-nm laser excitation of **RuP^{2+}**-derivatized *nano*SnO_2/TiO_2 core/shell electrodes in 0.1 M $HClO_4$. Our results suggest that an ultrafast BET pathway is accessible for *nano*SnO_2/TiO_2|-**RuP^{2+}** core/shell electrodes with TiO_2 shells between 1 and 2 nm thick; however this pathway is not evident for thin (<0.5 nm) shells. Annealing these photoanodes prior to dye loading resulted in a diminished contribution of the ultrafast BET pathway, suggesting the structure and composition of the TiO_2 shell plays a major role in charge separation lifetime on *nano*SnO_2/TiO_2 core/shell photoanodes.

6.2. Results and Discussion

6.2.1. Construction of Core/Shell Electrodes

Core/shell electrodes were constructed by performing ALD of TiO_2 on mesoporous metal oxide films. The thickness of the TiO_2 shell was controlled by varying the number of TiTDMA/H_2O cycles. Shell thickness was estimated by ellipsometry measurements performed on witness Si. Growth characterized for individual electrodes was less than expected; however across all samples the slope (thickness/cycles) was approximately the expected 0.6 Å cycle^{-1} (**Figure 6.2**).[14,15] Slow growth could be attributed to the low temperature (150 °C) used for

deposition.[16] Electrodes were not annealed following TiO_2 deposition (unless otherwise indicated), resulting in amorphous, slightly colored TiO_2 shells.[17]

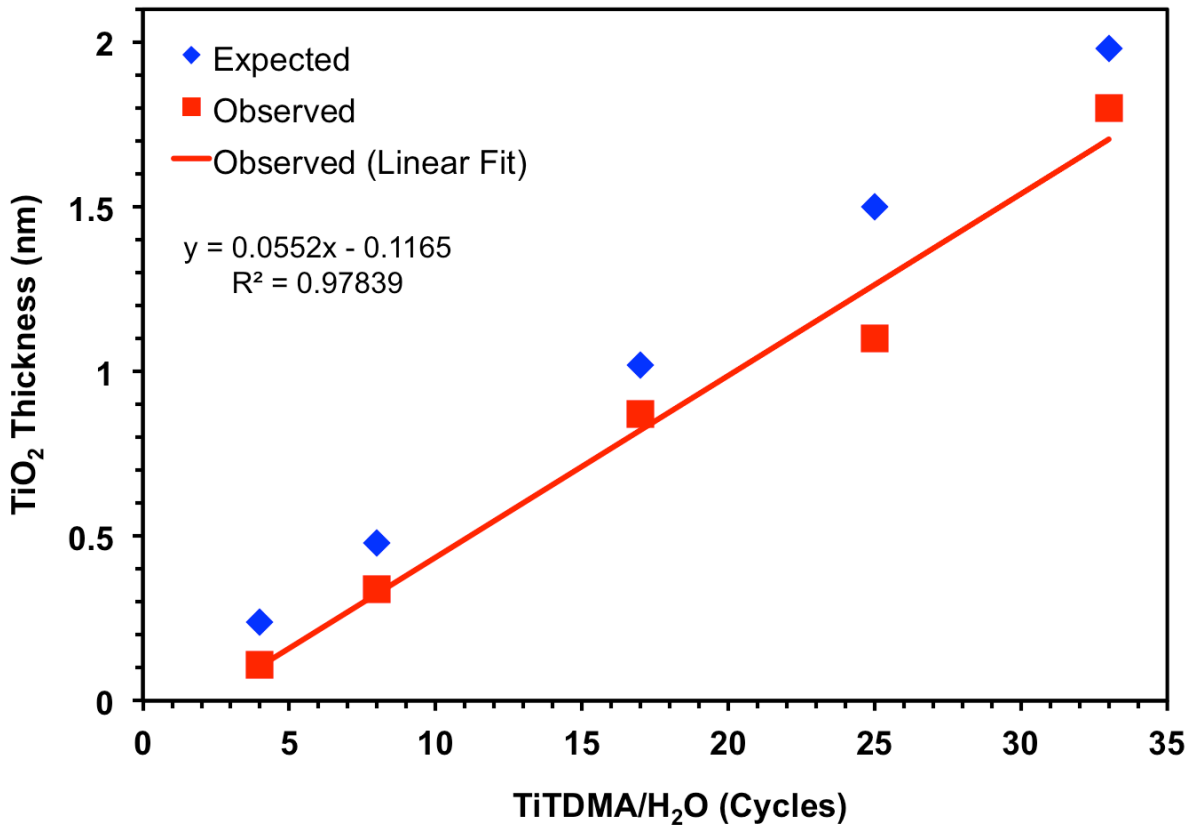

Figure 6.2. Plot of expected (blue diamonds) and observed (red squares) TiO_2 thickness as a function of TiTMDA/H_2O cycles as determined by ellipsometry on planar Si. The red line is a linear fit of the observed data. (conditions: $T_{reactor}$ = 150 °C, T_{TiTDMA} = 75 °C; each reactant was held in the chamber for 20 s, then purged for 60 s)

The molecular chromophore **RuP^{2+}** was synthesized as its chloride salt by literature procedures.[18] Dye loading was achieved by soaking the desired electrode in a methanol solution of **RuP^{2+}** (~1 mM) overnight, followed by rinsing with methanol and drying under a stream of air. The amount of **RuP^{2+}** loaded onto the core/shell electrodes was determined using UV-visible absorption spectroscopy and **Equation 6.3** by subtracting the *nano*MO_x/TiO_2 background

spectrum from the *nano*MO_x/TiO_2|-$\mathbf{RuP^{2+}}$ absorption spectrum.[19] For the unannealed *nano*SnO_2/TiO_2|-$\mathbf{RuP^{2+}}$ electrodes, $\Gamma(\mathbf{RuP^{2+}}) = (5.6 \pm 0.8) \times 10^{-8}$ mol cm^{-2}. For the unannealed *nano*ZrO_2/TiO_2|-$\mathbf{RuP^{2+}}$ electrodes, $\Gamma(\mathbf{RuP^{2+}}) = (5.1 \pm 0.7) \times 10^{-8}$ mol cm^{-2}. These data suggest that similar amounts of $\mathbf{RuP^{2+}}$ are adsorbed to the core/shell electrode films.

Equation 6.3

$$\Gamma = A(\lambda) \times (\varepsilon(\lambda) \times 1000)^{-1}$$

6.2.2. Electron Injection Results

The kinetics and apparent relative yields of electron injection of $\mathbf{RuP^{2+*}}$ on core/shell electrodes of both *nano*SnO_2/TiO_2 and *nano*ZrO_2/TiO_2 as a function of TiO_2 shell thickness (0 to 1.8 nm) in argon-deaerated 0.1 M $HClO_4$ were investigated by transient absorption spectroscopy. Following 480-nm excitation (100 nJ/pulse, 150-fs pulse width), the differences between the white light absorption spectrum with and without excitation (i.e. pump on and pump off) were monitored from 200 fs to 1.3 ns. There are two main features of the transient absorption spectrum of $\mathbf{RuP^{2+*}}$ on TiO_2: a positive feature for a $bpy^{\bullet-}$ radical (λ_{max} = 380 nm) and a negative ground state bleach (GSB; λ_{max} = 450 nm) corresponding to the MLCT transition of $\mathbf{RuP^{2+}}$ (**Equation 6.4**).[20] Injection of photo-excited electrons into the semiconductors' conduction bands was evaluated by monitoring the π-π* absorption feature of the reduced bpy ligand characteristic of the excited state of $\mathbf{RuP^{2+}}$, namely $\mathbf{RuP^{2+*}}$, at 376 nm. Excited-state electron injection occurs from the surface-bound 4,4'-$dpbpy^{\bullet-}$ ligand (**Equation 6.5**),[21] causing the $bpy^{\bullet-}$ absorbance to decay as injection occurs. The GSB intensity is maintained throughout the injection process because the metal center remains oxidized. The pump wavelength used in all transient absorption

experiments (λ_{pump} = 480 nm) was chosen to minimize direct excitation of TiO_2 by a high-energy visible absorption apparent in the films upon deposition of TiO_2 via the TiTDMA precursor.

Equation 6.4

$$MO_x|\text{-}Ru^{II}(4,4'\text{-dpbpy})(bpy)_2^{2+} + h\nu \rightarrow MO_x|\text{-}Ru^{III}(4,4'\text{-dpbpy}^{\bullet-})(bpy)_2^{2+}$$

Equation 6.5

$$MO_x|\text{-}Ru^{III}(4,4'\text{-dpbpy}^{\bullet-})(bpy)_2^{2+} \rightarrow MO_x(e^-)|\text{-}Ru^{III}(4,4'\text{-dpbpy})(bpy)_2^{3+}$$

Normalized transient absorption kinetics for *nano*ZrO_2/TiO_2|-**RuP^{2+}** as a function of TiO_2 shell thickness (from 0 nm to 1.3 nm) are shown in **Figure 6.3**. The kinetic data were fit to a biexponential decay function (**Equation 6.6**) and the fit parameters are summarized in **Table 6.1**. In **Equation 6.3**, τ_1 and τ_2 represent the lifetimes of fast and slow components of decay, respectively, A_1 and A_2 their relative contributions to decay, and y_0 the offset for absorption by the $bpy^{\bullet-}$, or presumably where the t_∞ value of absorption lies.

In the simplest case of *nano*ZrO_2|-**RuP^{2+}** (**Figure 6.3**, light blue squares), a positive feature is observed at λ_{probe} = 376 nm following laser excitation. After ~1.2 ns, approximately 80% of this feature is maintained. For a related $[Ru(bpy)_3]^{2+}$-like complex surface-bound to *nano*ZrO_2, a single-exponential decay function fit the offset (y_0) to 0.87 (**Table 6.1**).[22] In contrast, for *nano*TiO_2|-**RuP^{2+}** under similar conditions, this same positive feature decays below $\Delta A = 0$ in under 100 ps.[20] The large, positive offset fit values for *nano*ZrO_2|-**RuP^{2+*}** suggests minimal excited-state electron injection from **RuP^{2+*}** to the conduction band of *nano*ZrO_2. **RuP^{2+*}** does not have sufficient energy to inject into the conduction band of ZrO_2, which is

positioned about –1 V vs. NHE at pH 1.[23] The excited-state oxidation potential for **RuP**$^{2+*}$, $E°'(Ru^{III/II*})$, is –0.76 V vs. NHE.[19]

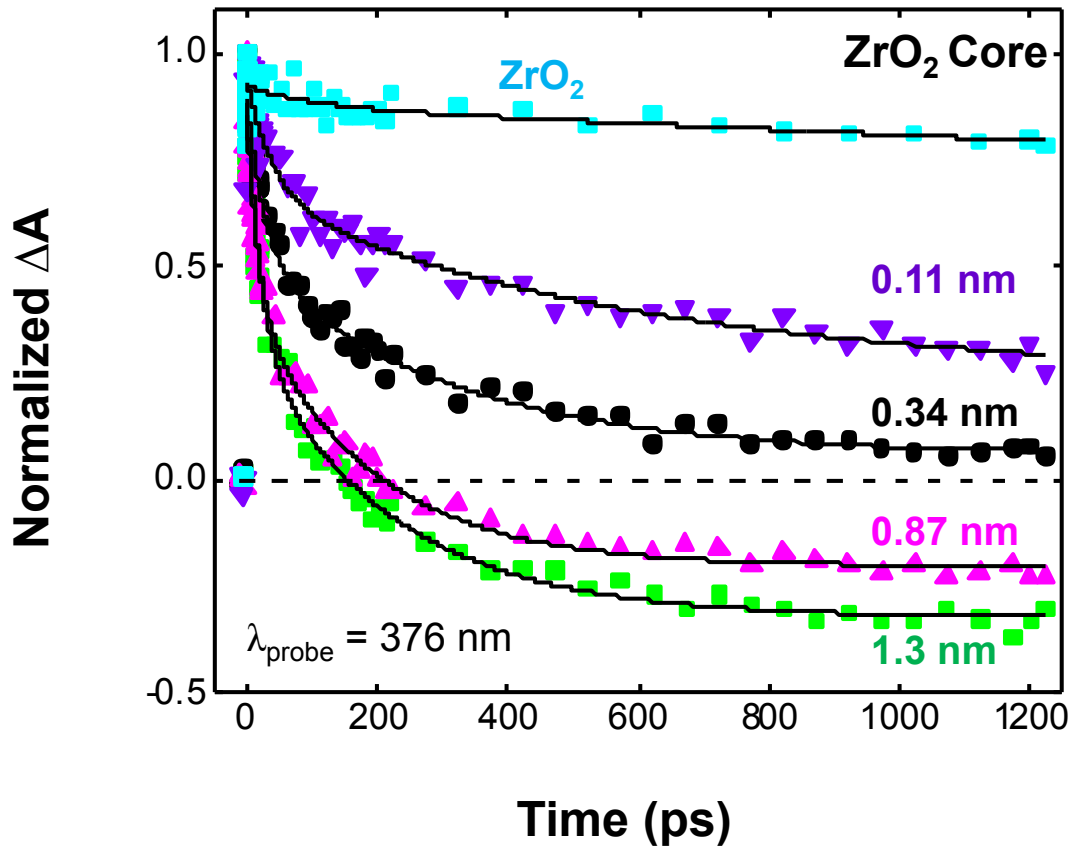

Figure 6.3. Normalized transient absorption kinetics for *nano*ZrO_2/TiO_2|-**RuP**$^{2+}$ as a function of TiO_2 shell thickness monitored at λ_{probe} = 376 nm. (conditions: 0.1 M $HClO_4$; λ_{pump} = 480 nm; 100 nJ/pulse)

Equation 6.6

$$y = y_0 + A_1 e^{-\frac{x}{\tau_1}} + A_2 e^{-\frac{x}{\tau_2}}$$

Table 6.1. Summary of Biexponential Fit Parameters for *nano*ZrO_2/TiO_2|-**RuP**$^{2+}$ Monitored at λ_{probe} = 376 nm Following λ_{pump} = 480 nm Laser Excitation as a Function of TiO_2 Thickness

TiO_2 Shell Thickness (nm)	y_0	A_1	A_2	Lifetime (ps)	
				τ_1	τ_2
0[a]	0.9(0.12)	0.03(0.02)	-	10(17.6)	-
0.11	0.24(0.058)	0.27(0.039)	0.42(0.037)	40(10.6)	600(218.8)
0.34	0.06(0.016)	0.37(0.038)	0.46(0.032)	30(4.69)	300(52.9)
0.87	–0.20(0.015)	0.45(0.068)	0.62(0.060)	18(3.88)	190(30.1)
1.3	–0.33(0.019)	0.58(0.062)	0.65(0.064)	22(3.91)	220(40.1)
nanoTiO_2 [a]	–0.3(0.14)	0.6(0.31)	0.69(0.03)	19(1.5)	200(18.5)

[a] Data for a related complex from reference [22]

As the thickness of the TiO_2 shell increases on *nano*ZrO_2/TiO_2|-**RuP**$^{2+}$, the fast and slow components of decay lifetime tend to decrease. For the thinnest (0.11 nm) TiO_2 shell investigated, τ_1 = 40.4 ps and τ_2 = 586.8 ps; for the thickest (1.3 nm) TiO_2 shell investigated, τ_1 = 21.7 ps and τ_2 = 220.5 ps. Additionally, the offset value decreases as TiO_2 shell thickness increases, from 0.87 for bare *nano*ZrO_2 to –0.325 for *nano*ZrO_2/TiO_2(1.3-nm). In fact, all modeled decay parameters for *nano*ZrO_2/TiO_2(1.3-nm)|-**RuP**$^{2+}$ closely resemble those fit for a related $[Ru(bpy)_3]^{2+}$-like complex surface-bound to bare *nano*TiO_2 (**Table 6.1**).[22]

Normalized transient absorption kinetics for *nano*SnO_2/TiO_2|-**RuP**$^{2+}$ as a function of TiO_2 shell thickness (from 0 nm to 1.8 nm) are shown in **Figure 6.4**. The kinetic data were fit to a biexponential decay function (**Equation 6.6**) and the fit parameters are summarized in **Table 6.2**. As with *nano*ZrO_2/TiO_2|-**RuP**$^{2+}$ electrodes, laser excitation produces an excited state at λ_{probe} = 376 nm, which then decays over time. For the simplest case of *nano*SnO_2|-**RuP**$^{2+}$, both lifetime components are fast (τ_1 = 4 ps; τ_2 = 25 ps), and the offset is negative (y_0 = –0.422). These data

represent a rapid disappearance of λ_{probe} = 376 nm absorbance with an ultimate bleach of the $bpy^{\bullet-}$.

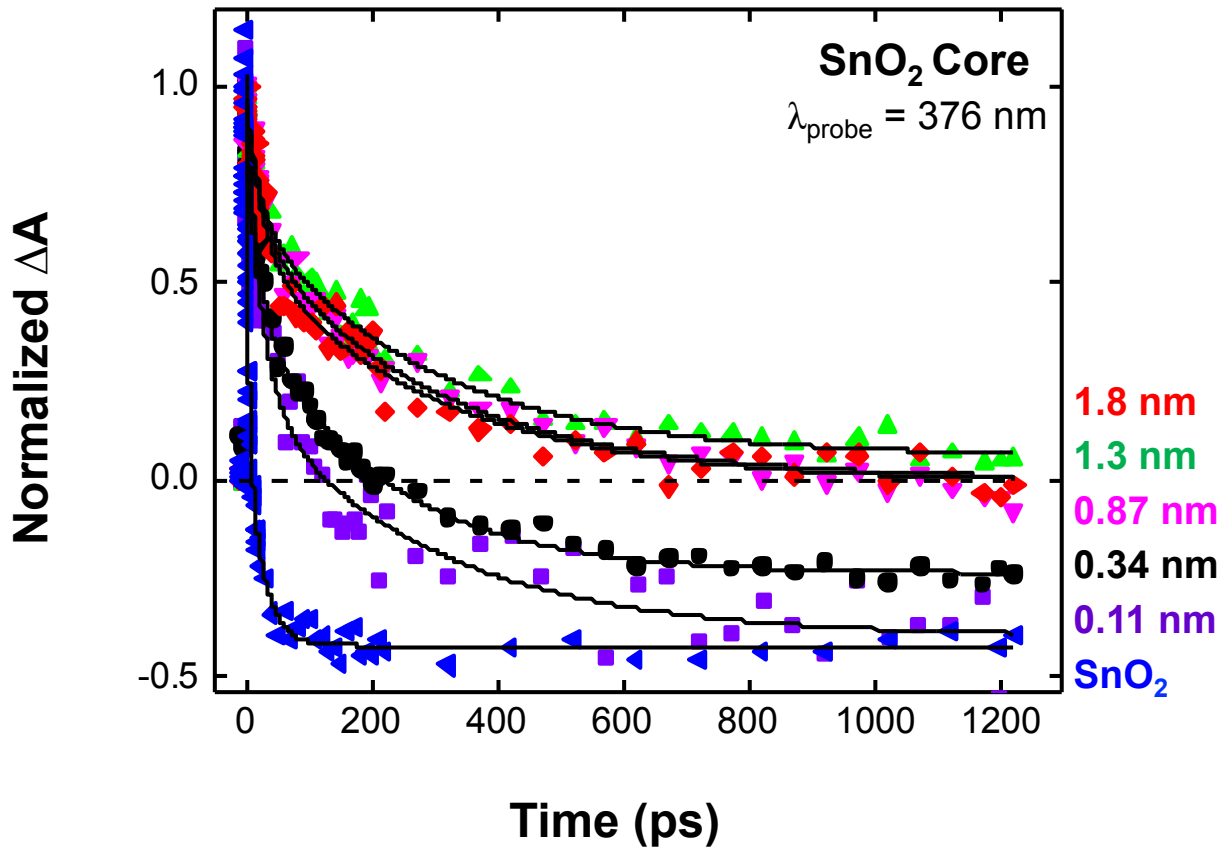

Figure 6.4. Normalized transient absorption kinetics for *nano*SnO_2/TiO_2|-**RuP**$^{2+}$ as a function of TiO_2 shell thickness monitored at λ_{probe} = 376 nm. (conditions: 0.1 M $HClO_4$; λ_{pump} = 480 nm; 100 nJ/pulse)

Table 6.2. Summary of Biexponential Fit Parameters for *nano*SnO_2/TiO_2|-**RuP**$^{2+}$ Monitored at λ_{probe} = 376 nm Following λ_{pump} = 480 nm Laser Excitation as a Function of TiO_2 Thickness

TiO_2 Shell Thickness (nm)	y_0	A_1	A_2	Lifetime (ps)	
				τ_1	τ_2
0	–0.422(0.006)	0.86(0.059)	0.60(0.061)	3.8(0.31)	25(3.2)
0.11	–0.4[a]	0.70(0.088)	0.61(0.90)	27(6.1)	290(62.9)
0.34	–0.239(0.0097)	0.51(0.036)	0.67(0.034)	21(2.2)	210(19.5)
0.87	0[a]	0.33(0.044)	0.63(0.045)	27(6.3)	290(30.2)
1.3	0.06(0.016)	0.29(0.037)	0.62(0.032)	22(4.7)	280(36.1)
1.8	–0.008(0.025)	0.39(0.060)	0.58(0.050)	28(6.7)	300(64.3)

[a] Parameter fixed prior to fit.

Upon addition of TiO_2 (0.11 to 1.8 nm), both lifetimes increase (τ_1 > 20 ps; τ_2 > 200 ps); however, there is not a trend of increase as the TiO_2 shell thickness increases. Instead, the relative contributions (A_1 and A_2) of each component appear to change as TiO_2 shell thickness increases. Contribution of the slow component (A_2) remains between 0.6 and 0.7 across all shell thickness values; contribution of the fast component (A_1) decreases as the shell thickness increases. Additionally, the offset value y_0 appears to increase as TiO_2 shell thickness increases.

The effects of annealing the core/shell electrodes prior to dye loading on the decay kinetics at λ_{probe} = 376 nm were also investigated. Films of both *nano*SnO_2 and *nano*ZrO_2 were derivatized with TiO_2 (0.34 and 0.87 nm thick shells) and annealed under ambient atmosphere at 450 °C (30 minutes; 45-minute ramp to temperature; multiple-hour cool down). The films were then loaded with **RuP**$^{2+}$ and the decay kinetics at λ_{probe} = 376 nm were monitored following laser excitation at λ_{pump} = 480 nm, fit to a biexponential decay function (**Equation 6.6**), and compared to unannealed electrodes with similar TiO_2 shells (**Table 6.3**, **Figure 6.5**).

Table 6.3. Summary of Biexponential Fit Parameters for *nano*MO_x/TiO_2|-**RuP**$^{2+}$ Monitored at λ_{probe} = 376 nm Following λ_{pump} = 480 nm Laser Excitation with Annealed Electrodes

TiO_2 Shell Thickness (nm)		y_0	A_1	A_2	Lifetime (ps)	
					τ_1	τ_2
SnO_2 core	0.34	–0.50(0.0136)	0.72(0.041)	0.65(0.037)	23(2.0)	250(29.1)
	0.87	0[a]	0.64(0.046)	0.62(0.043)	22(2.5)	230(30.6)
ZrO_2 core	0.34	0.08(0.0155)	0.37(0.045)	0.48(0.040)	22(4.3)	250(45.7)
	0.87	–0.30(0.0123)	0.59(0.052)	0.67(0.050)	15(2.2)	170(20.4)

[a] Parameter fixed prior to fit.

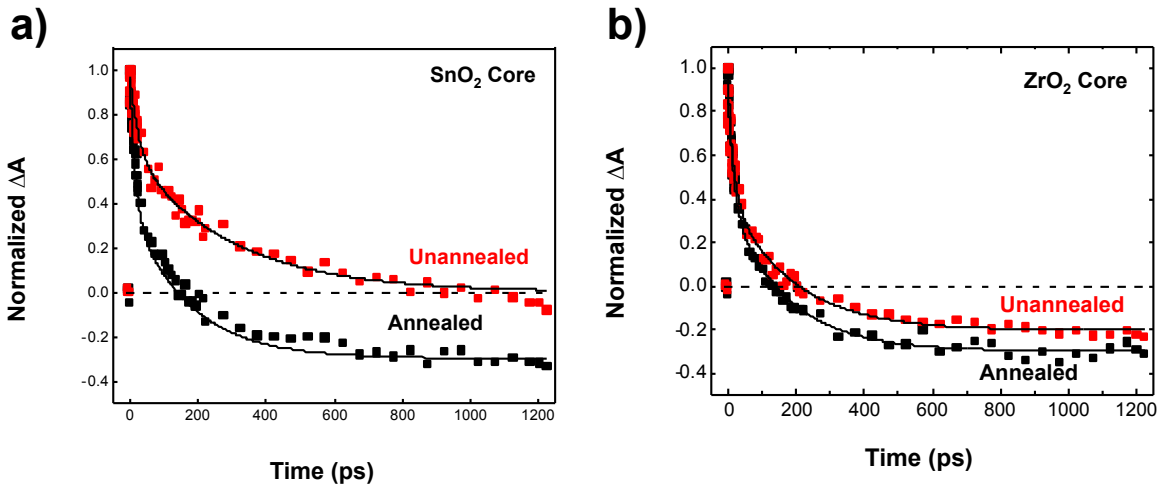

Figure 6.5. Normalized transient absorption kinetics for a) *nano*SnO_2/TiO_2(0.87-nm)|-**RuP**$^{2+}$; and b) *nano*ZrO_2/TiO_2(0.87-nm)|-**RuP**$^{2+}$ for unannealed (red squares) and annealed (black squares) photoanodes. (conditions: 0.1 M $HClO_4$; λ_{pump} = 480 nm; λ_{probe} = 376 nm; 100 nJ/pulse; annealing conditions: 450 °C for 30 minutes, following 45-minute ramp)

The decay traces for a 0.87-nm thick TiO_2 shell on both *nano*SnO_2 and *nano*ZrO_2 are shown in **Figure 6.5** for both annealed and unannealed films. Qualitatively, decay appears to occur more rapidly following annealing for a *nano*SnO_2 core, but remains relatively unchanged following annealing for a *nano*ZrO_2 core. The ΔA value for *nano*SnO_2/TiO_2(0.87-nm)|-**RuP**$^{2+}$

electrode is approximately 0 after 1.2 ns for the unannealed film, but drops to approximately –0.35 for the annealed film, similar to the y_0 fit parameter for a related $[Ru(bpy)_3]^{2+}$-like complex surface-bound to bare *nano*TiO_2 (–0.34).[22]

6.2.3. Electron Injection Discussion

Decay of absorbance at λ_{probe} = 376 nm suggests excited-state electron injection from $\mathbf{RuP^{2+*}}$ into the conduction band of the metal oxide semiconductor or excited-state relaxation of $\mathbf{RuP^{2+*}}$ back to $\mathbf{RuP^{2+}}$. Decay kinetics for *nano*ZrO_2|-$\mathbf{RuP^{2+}}$ highlight that relaxation occurs slowly relative to excited-state electron injection, because injection does not occur for $\mathbf{RuP^{2+*}}$ on ZrO_2. As increasing amounts of TiO_2 are deposited on *nano*ZrO_2, excited-state electron injection becomes more favorable as demonstrated qualitatively by the decrease in y_0 as TiO_2 thickness increases for *nano*ZrO_2/TiO_2|-$\mathbf{RuP^{2+}}$.

Excited-state electron injection for $\mathbf{RuP^{2+*}}$ is rapid on *nano*SnO_2, with injection time constants of τ_1 = 4 ps and τ_2 = 25 ps. Deposition of TiO_2 shows the rate of injection, but not gradually; instead both time constants increase (τ_1 > 20 ps; τ_2 > 200 ps) for shells between 0.11 and 1.8 nm thick. The relative contribution of each injection time constant does change gradually, with the τ_1 becoming a smaller contributor as TiO_2 thickness increases. The time constants are similar to those reported for a related $[Ru(bpy)_3]^{2+}$-like complex surface-bound to bare *nano*TiO_2 (τ_1 = 19.3 ps; τ_2 = 201.7 ps).[22] The similarity of these times suggests that $\mathbf{RuP^{2+*}}$ injects into TiO_2 states on *nano*SnO_2/TiO_2 core/shell electrodes.

The increase in offset value, y_0, as TiO_2 shell thickness increases is surprising, especially given the offset value of –0.34 for *nano*TiO_2|-$\mathbf{RuP^{2+}}$. It suggests that the apparent injection yield decreases with increasing thickness of TiO_2 compared to nanocrystalline films, where Φ_{inj} = 1.0 for *nano*SnO_2 and *nano*TiO_2.[21,24] However, it is important to note that a superposition of the oxidized chromophore and the ground state exists at λ_{probe} = 376 nm. We have demonstrated that

apparent injection yield increases on *nano*ZrO_2/TiO_2 core/shell electrodes with increasing thickness so this process should not be hindered on a *nano*SnO_2/TiO_2 core/shell where the excited-state oxidation potential of $\mathbf{RuP^{2+}}$ is sufficient to inject into either the core or the shell. Instead, it is possible that the ground-state chromophore is restored faster on the *nano*SnO_2/TiO_2 core/shell than on *nano*TiO_2 or *nano*SnO_2 alone. A possible explanation for this phenomenon is ultrafast BET following electron injection. Ultrafast BET could occur if electron injection does not occur exclusively into the conduction band of the TiO_2 shell, but into surface-localized trap states with energy levels positive to that of the TiO_2 conduction band. The existence of these trap states is plausible for several reasons: TiO_2 deposited by ALD tends to be amorphous,[17] TiO_2 deposited specifically using the TiTDMA precursor is known to be hole-conducting possibly due to low-energy, mid-bandgap trap states,[25-28] and the TiO_2 shells exhibit a visible, high-energy coloration that could be caused by excitation from the TiO_2 valence band to mid-bandgap states positive that of the conduction band. Electron injection to these trap states could hinder or prevent electron diffusion to remote surface sites; in this scenario, BET to the oxidized chromophore could be rapid due to the proximity of the surface-localized electron and $\mathbf{RuP^{3+}}$.

Annealing the electrodes at 450 °C results in a phase transition from amorphous to anatase.[29,30] Annealing the TiO_2 deposited from the TiTDMA precursor has also been shown to diminish the hole-conducting properties of the TiO_2, which likely removes the mid-bandgap trap states.[26] Removal of the mid-bandgap trap states allows for electron diffusion from the site of injection to remote surface sites.

Comparison of the normalized transient absorption kinetics for annealed and unannealed films of *nano*SnO_2/TiO_2(0.87-nm)|-$\mathbf{RuP^{2+}}$ (**Figure 6.5**) suggests improved charge separation for the annealed films. However, this improvement does not appear to be due to a change in surface

states. No difference in decay kinetics is observed for annealed or unannealed *nano*ZrO_2/TiO_2(0.87-nm)|-$\mathbf{RuP^{2+}}$ electrodes. Therefore, the improvement observed for *nano*SnO_2/TiO_2 could be due to improved interaction of materials along the SnO_2/TiO_2 interface.

6.2.4. Recombination Results

The recombination kinetics of $\mathbf{RuP^{2+}}$ on core/shell photoanodes of both *nano*SnO_2/TiO_2 and *nano*ZrO_2/TiO_2 as a function of TiO_2 shell thickness (0 to 1.8 nm) following 480 nm (100 nJ/pulse, 150 fs pulse width) excitation in argon-deaerated 0.1 M $HClO_4$ were investigated by transient absorption spectroscopy. Monitoring was performed at λ_{probe} = 430 nm, which corresponds to the ground-state bleach of the $\mathbf{RuP^{2+}}$ MLCT.[21] This bleach is maintained on *nano*TiO_2 and *nano*SnO_2 following electron injection from the 4,4'-dpbpy$^{\bullet-}$ to the semiconductor conduction band, because the chromophore remains oxidized (as $\mathbf{Ru^{III}P^{3+}}$). The disappearance of the bleach can be attributed to reduction of $\mathbf{RuP^{3+}}$ to $\mathbf{RuP^{2+}}$ i.e. to the restoration of the ground-state chromophore.

Normalized transient absorption kinetics for *nano*ZrO_2/TiO_2|-$\mathbf{RuP^{2+}}$ as a function of TiO_2 shell thickness (0 to 1.3 nm) are shown in **Figure 6.6**. The kinetic data were fit either to a triexponential decay function (**Equation 6.7**) or to a biexponential decay function (**Equation 6.6**), and the fit parameters are summarized in **Table 6.4**. In **Equation 6.7**, τ_i represents a lifetime of recombination, A_i represents its relative contribution to recombination, and y_0 represents the offset (or t_∞ value) of absorbance at λ_{probe} = 430 nm. In all cases, y_0 was fixed at 0, as decay should occur to baseline.

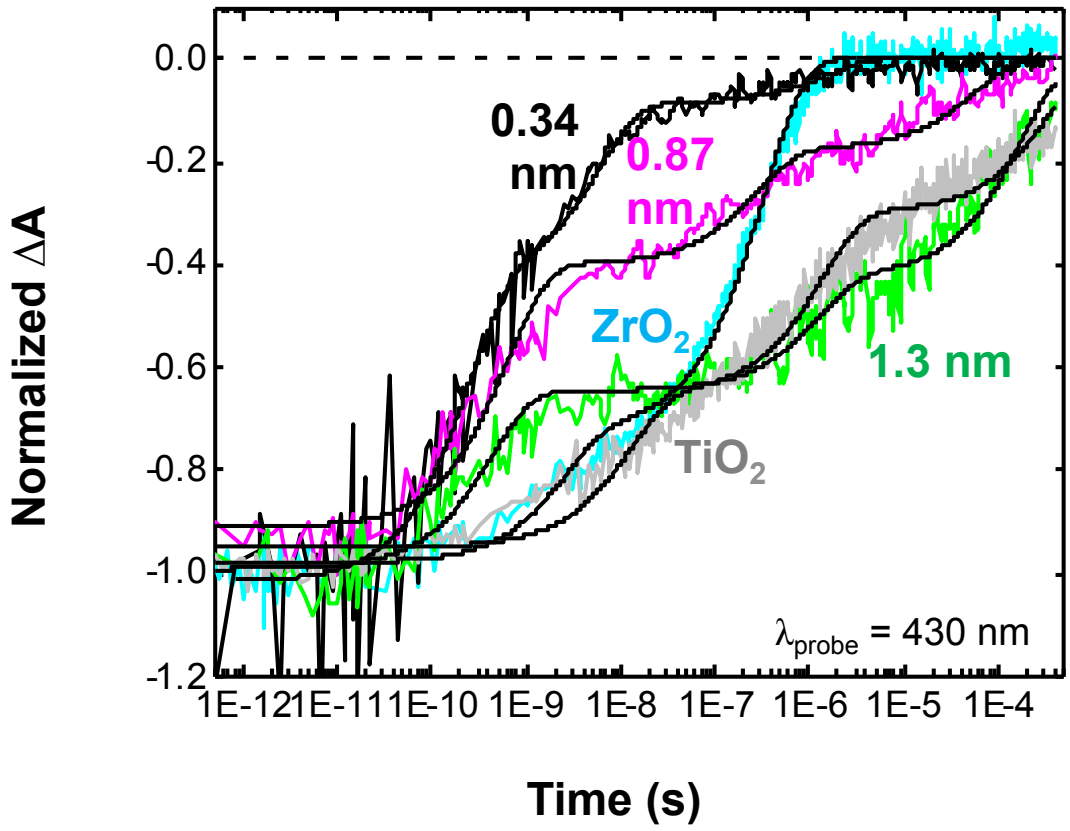

Figure 6.6. Normalized decay kinetics vs. pump-probe time monitored at 430 nm for *nano*ZrO_2/TiO_2|-**RuP**$^{2+}$ as a function of TiO_2 shell thickness (0 to 1.3 nm). The numeric labels in the figure refer to the TiO_2 shell thickness, while the ZrO_2 and TiO_2 labels indicate a film of bare nanoparticles loaded with **RuP**$^{2+}$. (conditions: 0.1 M $HClO_4$; λ_{pump} = 480 nm; λ_{probe} = 430 nm; 100 nJ/pulse)

Equation 6.7

$$y = y_0 + A_1 e^{-\frac{x}{\tau_1}} + A_2 e^{-\frac{x}{\tau_2}} + A_3 e^{-\frac{x}{\tau_3}}$$

Table 6.4. Summary of Multi-Exponential Fit Parameters for *nano*ZrO_2/TiO_2|-**RuP**$^{2+}$ Monitored at λ_{probe} = 430 nm Following λ_{pump} = 480 nm Laser Excitation as a Function of TiO_2 Thickness

TiO_2 Shell Thickness (nm)	**y_0**	**A_1**	**A_2**	**A_3**	**Lifetime**		
					τ_1	**τ_2**	**τ_3**
nanoZrO_2	0	-0.258 (0.005)	-0.721 (0.004)	-	2.6 ns (0.22)	330 ns (5.3)	-
nanoTiO_2	0	-0.297 (0.006)	-0.353 (0.006)	-0.299 (0.004)	12.7 ns (0.9)	1.36 μs (0.068)	340 μs (20.1)
0.34	0	-0.58 (0.017)	-0.35 (0.017)	-0.088 (0.005)	240 ps (17.7)	5.8 ns (0.58)	1.5 μs (0.26)
0.87	0	-0.510 (0.006)	-0.222 (0.005)	-0.177 (0.003)	630 ps (28.4)	280 ns (18.6)	57 μs (3.75)
1.3	0	-0.346 (0.009)	-0.222 (0.006)	-0.422 (0.006)	430 ps (40.4)	1.3 μs (0.11)	178 μs (7.4)

Absorption-time data (λ_{probe} = 430 nm) were fit to a biexponential decay function for *nano*ZrO_2|-**RuP**$^{2+}$. Decay occurs rapidly, with lifetimes (and relative contributions) of τ_1 = 2.6 ns (26%) and τ_2 = 330 ns (74%). In contrast, decay for *nano*TiO_2|-**RuP**$^{2+}$ (fit to a triexponential decay function) occurs more gradually, with lifetimes (and relative contributions) of τ_1 = 12.7 ns (31%), τ_2 = 1.36 μs (37%), and τ_3 = 340 μs (32%).

Absorption-time data (λ_{probe} = 430 nm) were fit to a triexponential decay function for *nano*ZrO_2/TiO_2|-**RuP**$^{2+}$ for TiO_2 shell thickness values of 0.34, 0.87, and 1.3 nm. Qualitatively, τ_2 and τ_3 both increase with TiO_2 shell thickness; τ_1 does not appear to correlate with TiO_2 shell thickness. Additionally, the relative contributions of recombination lifetimes appear to shift as TiO_2 thickness increases. For the thinnest shell (0.34 nm), the largest contribution comes from the fastest lifetime (A_1). The same is true of the intermediate shell (0.87 nm). However, the thickest shell (1.3 nm) shows the slowest lifetime (A_3) having the largest contribution to recombination.

Normalized transient absorption kinetics for *nano*SnO_2/TiO_2|-**RuP**$^{2+}$ as a function of TiO_2 shell thickness (0 to 1.8 nm) are shown in **Figure 6.7**. The kinetic data were fit either to a quad-exponential decay function (**Equation 6.8**) or to a triexponential decay function (**Equation 6.7**), and the fit parameters are summarized in **Table 6.5**. As with the fit parameters for *nano*ZrO_2|-**RuP**$^{2+}$, in all cases, y_0 was fixed at 0, as decay should occur to baseline. Absorption spectra were blanked on the ground-state complexes prior to laser excitation.

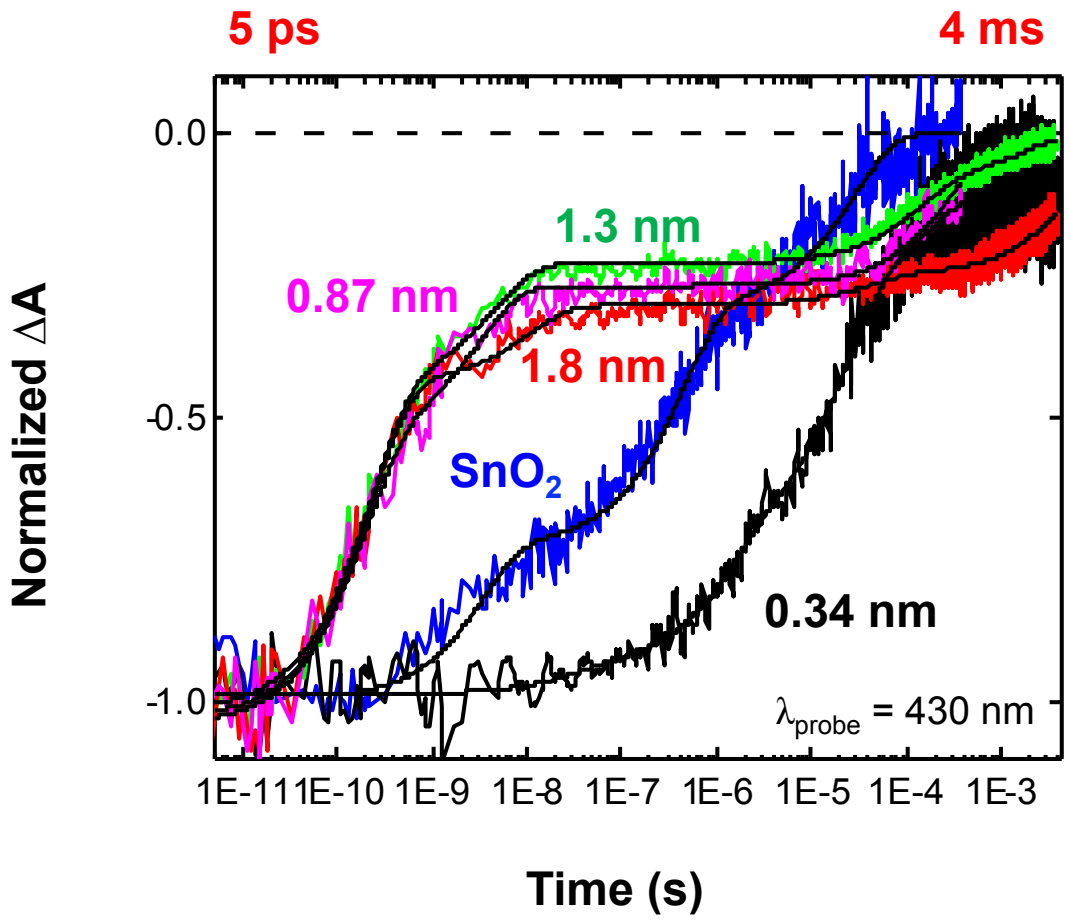

Figure 6.7. Normalized decay kinetics vs. pump-probe time monitored at 430 nm for *nano*SnO_2/TiO_2|-**RuP**$^{2+}$ as a function of TiO_2 shell thickness (0 to 1.8 nm). The numeric labels in the figure refer to the TiO_2 shell thickness, while the SnO_2 label indicates a film of bare nanoparticles loaded with **RuP**$^{2+}$. (conditions: 0.1 M $HClO_4$; λ_{pump} = 480 nm; λ_{probe} = 430 nm; from 200 fs to 400 μs: 100 nJ/pulse; for 400 μs to 4 ms: 1 mJ/pulse; the short (<400 μs) and long (>400 μs) timescales were normalized to each other)

Equation 6.8

$$y = y_0 + A_1 e^{-\frac{x}{\tau_1}} + A_2 e^{-\frac{x}{\tau_2}} + A_3 e^{-\frac{x}{\tau_3}} + A_4 e^{-\frac{x}{\tau_4}}$$

Table 6.5. Summary of Multi-Exponential Fit Parameters for *nano*SnO_2/TiO_2|-**RuP**$^{2+}$ Monitored at λ_{probe} = 430 nm Following λ_{pump} = 480 nm Laser Excitation as a Function of TiO_2 Thickness

TiO_2 Shell Thick-ness (nm)	y_0	A_1	A_2	A_3	A_4	Lifetime			
						τ_1	τ_2	τ_3	τ_4
SnO_2	0	-0.27 (0.012)	-0.423 (0.008)	-0.301 (0.006)	-	3.4 ns (0.4)	44 ns (2.3)	28 μs (1.6)	-
0.34	0	-0.049 (0.009)	-0.22 (0.013)	-0.44 (0.013)	-0.18 (0.01)	30 ns (15.2)	1.3 μs (0.18)	23 μs (1.5)	190 μs (10)
0.87	0	-0.49 (0.014)	-0.27 (0.014)	-0.267 (0.0014)	-	200 ps (11)	3.2 ns (0.294)	330 μs (12)	-
1.3	0	-0.57 (0.005)	-0.219 (0.005)	-0.146 (0.0007)	-0.0821 (0.0006)	220 ps (4.4)	4.6 ns (0.18)	139 μs (1.7)	1.87 ms (0.017)
1.8	0	-0.54 (0.004)	-0.123 (0.004)	-0.049 (0.0009)	-0.223 (0.0003)	222 ps (4.9)	10.5 ns (0.66)	42 μs (2.4)	6.6 ms (0.33)

Absorption-time data (λ_{probe} = 430 nm) were fit to a triexponential decay function for *nano*SnO_2|-**RuP**$^{2+}$. The lifetimes for decay (with relative contributions in parentheses) were τ_1 = 3.4 ns (27%), τ_2 = 43.9 ns (43%), and τ_3 = 28 μs (30%), and there was nearly quantitative decay to baseline by 400 μs ($t_{1/2} \approx$ 33 ns). Qualitatively, decay is smooth, with little indication of transition from one decay regime to another (e.g. from a regime of fast decay to a regime of slower decay).

Absorption-time data (λ_{probe} = 430 nm) were fit to a quad-exponential decay function for *nano*SnO_2/TiO_2|-**RuP**$^{2+}$ for TiO_2 shell thickness values of 0.34, 1.3 and 1.8 nm, and to a

triexponential decay function for a TiO_2 shell thickness of 0.87 nm. Data for 0.34-, 1.3-, and 1.8-nm thick shells were fit out to 4 ms, while data for the 0.87-nm thick shell were fit only to 400 μs.

For the thinnest TiO_2 shell (0.34 nm), the lifetimes for decay are τ_1 = 31.5 ns (6%), τ_2 = 1.3 μs (25%), τ_3 = 22.6 μs (50%), and τ_4 = 194 μs (20%). As compared with *nano*SnO_2|-**RuP**$^{2+}$ decay kinetics, there is a smaller contribution from the fastest lifetime (only about a 6% contribution for the 0.34-nm thick TiO_2 shell whereas A_1(*nano*SnO_2|-**RuP**$^{2+}$) represented about a 27% contribution to decay). As with *nano*SnO_2|-**RuP**$^{2+}$ decay kinetics, decay appears smooth, with little indication of transition from one decay regime to another. However, decay appears to occur more slowly with the 0.34-nm thick TiO_2 shell, with $t_{1/2} \approx 6.6$ μs.

The thicker shells (0.87, 1.3, and 1.8 nm) qualitatively show altered decay behavior compared to bare *nano*SnO_2 and the thin 0.34-nm thick shell. Whereas decay appeared smooth, with little indication of a regime change for the bare and thin-shelled photoanodes, distinct regime shifts are evident for the thicker-shelled photoanodes. Rapid decay appears to occur for each photoanode, followed by a plateau-region with slow further decay of the ground-state bleach. As a comparison to the decay lifetimes (and relative contributions) for *nano*SnO_2/TiO_2(0.34 nm)|-**RuP**$^{2+}$, the decay lifetimes (and relative contributions) for *nano*SnO_2/TiO_2(0.34 nm)|-**RuP**$^{2+}$ are τ_1 = 221.6 ps (58%), τ_2 = 10.5 ns (13%), τ_3 = 42 μs (5%), and τ_4 = 6.6 ms (24%). The fastest decay lifetime, on the ps-timescale, is also the most heavily weighted; this observation holds true for the 0.87-nm thick shell (τ_1 = 197.6 ps (48%)) and the 1.3-nm thick shell (τ_1 = 222 ps (50%)) as well.

As with monitoring decay kinetics at λ_{probe} = 376 nm, the effects of annealing the core/shell electrodes prior to dye loading on the decay kinetics at λ_{probe} = 430 nm were

investigated. Films of both *nano*SnO_2 and *nano*ZrO_2 were derivatized with TiO_2 (0.34- and 0.87-nm thick shells) and annealed under ambient atmosphere at 450 °C (30 minutes; 45-minute ramp to temperature; multiple-hour cool down). The films were then loaded with **RuP**$^{2+}$ and the decay kinetics at λ_{probe} = 430 nm were monitored following laser excitation at λ_{pump} = 480 nm (**Figure 6.12**, **Figure 6.9**, **Figure 6.8**) and fit to a triexponential decay function (**Table 6.6**).

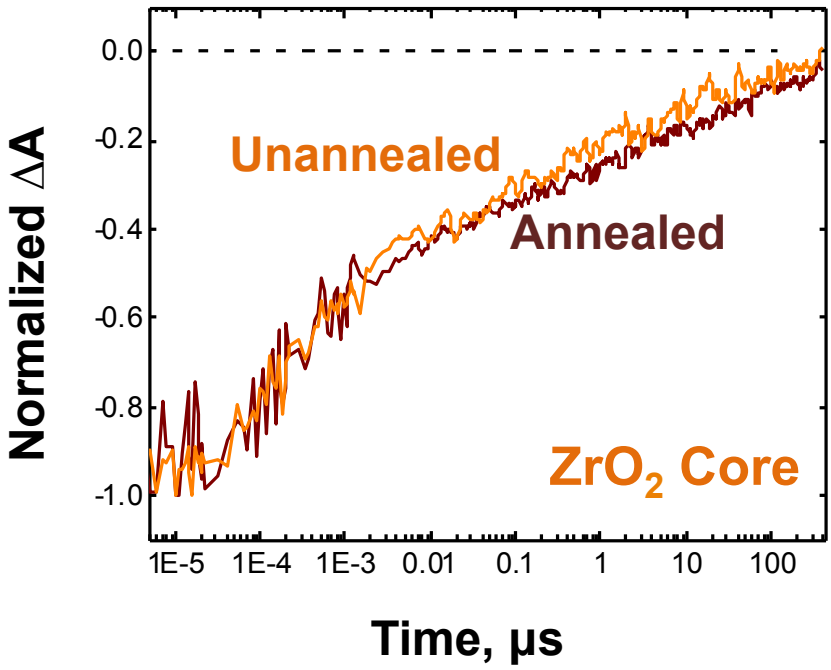

Figure 6.8. Normalized decay kinetics for unannealed (orange trace) and annealed (dark orange trace) *nano*ZrO_2/TiO_2(0.87-nm)|-**RuP**$^{2+}$. (conditions: 0.1 M $HClO_4$; λ_{pump} = 480 nm; λ_{probe} = 430 nm; 100 nJ/pulse; annealing conditions: 450 °C for 30 minutes, following 45-minute ramp)

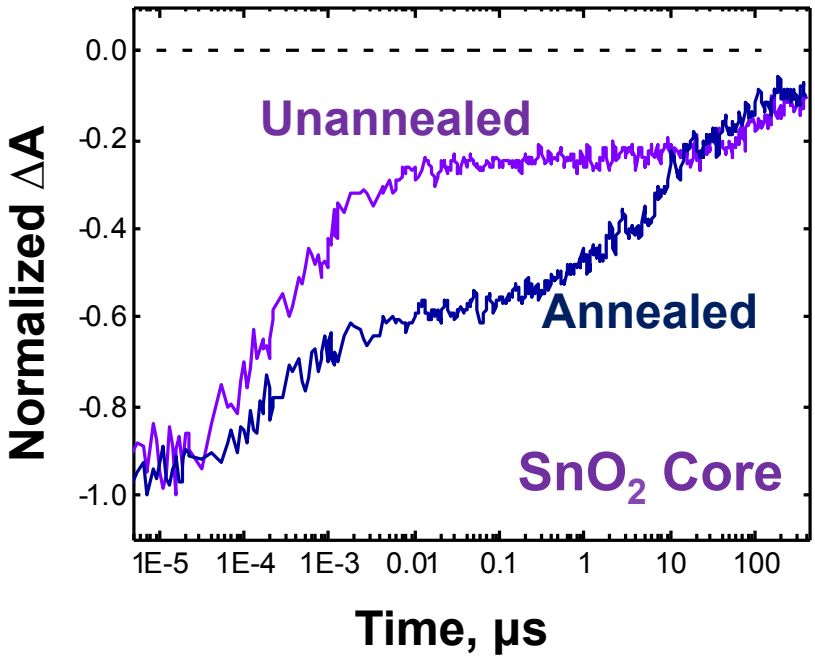

Figure 6.9. Normalized decay kinetics for unannealed (purple trace) and annealed (dark blue trace) *nano*SnO_2/TiO_2(0.87-nm)|-**RuP**$^{2+}$. (conditions: 0.1 M $HClO_4$; λ_{pump} = 480 nm; λ_{probe} = 430 nm; 100 nJ/pulse; annealing conditions: 450 °C for 30 minutes, following 45-minute ramp)

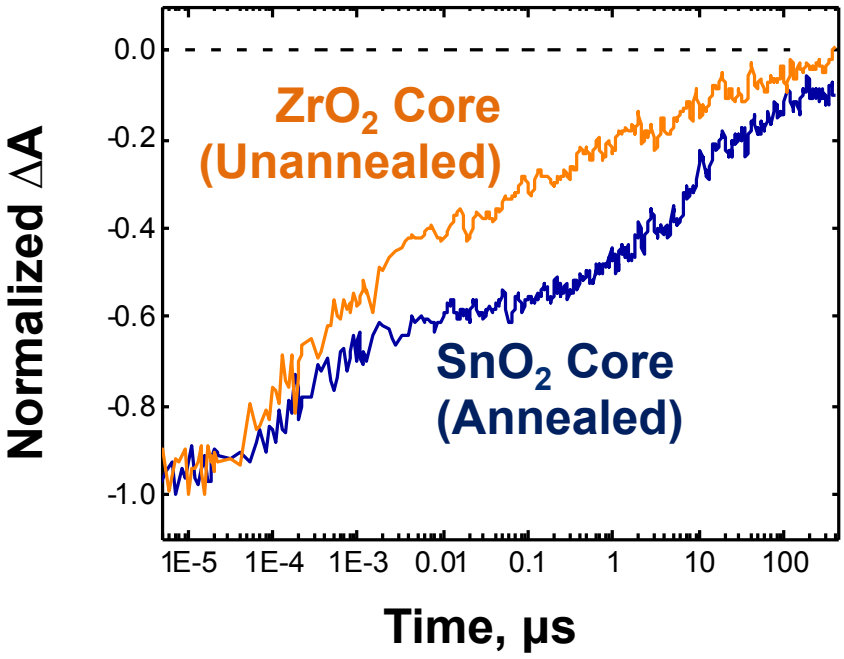

Figure 6.10. Normalized decay kinetics for unannealed *nano*ZrO_2/TiO_2(0.87-nm)|-**RuP**$^{2+}$ (orange trace) and annealed *nano*SnO_2/TiO_2(0.87-nm)|-**RuP**$^{2+}$ (dark blue trace). (conditions: 0.1 M $HClO_4$; λ_{pump} = 480 nm; λ_{probe} = 430 nm; 100 nJ/pulse; annealing conditions: 450 °C for 30 minutes, following 45-minute ramp)

Table 6.6. Summary of Triexponential Fit Parameters for *nano*MO_x/TiO_2|-**RuP**$^{2+}$ Monitored at λ_{probe} = 430 nm Following λ_{pump} = 480 nm Laser Excitation with Annealed Electrodes

Core	TiO_2 Shell Thickness (nm)	y_0	A_1	A_2	A_3	Lifetime τ_1	Lifetime τ_2	Lifetime τ_3
SnO_2	0.34	0	-0.23 (0.009)	-0.413 (0.009)	-0.195 (0.006)	43 ns (4.3)	2.1 μs (0.12)	170 μs (15.4)
	0.87	0	-0.356 (0.006)	-0.35 (0.006)	-0.217 (0.005)	670 ps (38)	5.3 μs (0.22)	260 μs (18.1)
ZrO_2	0.34	0	-0.638 (0.008)	-0.225 (0.008)	-0.06 (0.002)	420 ps (15.4)	21 ns (1.4)	32 μs (4.5)
	0.87	0	-0.487 (0.007)	-0.203 (0.005)	-0.201 (0.004)	640 ps (33.6)	550 ns (43)	120 μs (8.0)

Little change in decay kinetics as the result of annealing is observed for *nano*ZrO_2/TiO_2|-**RuP**$^{2+}$ photoanodes. For the case of *nano*ZrO_2/TiO_2(0.87 nm)|-**RuP**$^{2+}$, the unannealed photoanode exhibits decay lifetimes (and relative contributions) of τ_1 = 633 ps (56%), τ_2 = 284 ps (24%), and τ_3 = 57 μs (19%), while the annealed photoanode exhibits decay lifetimes (and relative contributions) of τ_1 = 640 ps (55%), τ_2 = 546 ps (23%), and τ_3 = 120 μs (23%).

The decay kinetics observed for *nano*SnO_2/TiO_2|-**RuP**$^{2+}$ photoanodes change significantly as the result of annealing. For the case of *nano*SnO_2/TiO_2(0.87 nm)|-**RuP**$^{2+}$, the unannealed photoanode exhibits decay lifetimes (and relative contributions) of τ_1 = 197.6 ps (48%), τ_2 = 3.19 ns (26%), and τ_3 = 334 μs (26%), while the annealed photoanode exhibits decay

lifetimes (and relative contributions) of τ_1 = 670 ps (39%), τ_2 = 5.3 μs (38%), and τ_3 = 260 μs (24%). For these two photoanodes, the lifetimes of fast decay (τ_1 and τ_2) both increase for the annealed film, indicative of slower decay. Additionally, the relative contribution increases for τ_2 in the annealed film relative to the unannealed film, further indicating a shift to slower decay. Curiously, the lifetime of slow decay (τ_3) decreases for the annealed film, indicating faster decay at longer time points.

6.2.5. Recombination Discussion

As demonstrated previously, $\mathbf{RuP^{2+*}}$ does not inject an electron into the conduction band of *nano*ZrO_2; therefore, the decay process observed at λ_{probe} = 430 nm for *nano*ZrO_2|-$\mathbf{RuP^{2+}}$ is due to excited-state relaxation (**Equation 6.9**). Although different degree-exponential equations were used to fit the decay data, the fastest component of decay for *nano*ZrO_2/TiO_2(0.34 nm)|-$\mathbf{RuP^{2+}}$ (τ_1 = 243 ps; 57%) is both faster and a larger contributor to decay than the faster component of decay for *nano*ZrO_2|-$\mathbf{RuP^{2+}}$ (τ_1 = 2.6 ns; 26%). Comparison of the $t_{1/2}$ values for each process also suggests much faster decay on *nano*ZrO_2/TiO_2(0.34 nm)|-$\mathbf{RuP^{2+}}$ ($t_{1/2}$ = 456 ps) than on *nano*ZrO_2|-$\mathbf{RuP^{2+}}$ ($t_{1/2}$ = 121 ns).

Equation 6.9

$$ZrO_2\text{-}Ru^{III}(4,4'\text{-}dpbpy^{\bullet-})(bpy)_2^{2+} \rightarrow ZrO_2\text{-}Ru^{II}(4,4'\text{-}dpbpy)(bpy)_2^{2+}$$

In the absence of electron injection, surface binding of $\mathbf{RuP^{2+}}$ to TiO_2 instead of ZrO_2 should not cause excited state relaxation to occur faster. The discrepancy in recombination lifetimes is then likely due to excited-state electron injection into TiO_2 for *nano*ZrO_2/TiO_2(0.34 nm)|-$\mathbf{RuP^{2+}}$. From the half-life data, the recombination process appears about three orders of magnitude faster than relaxation of the excited state. Intuitively, electron injection to the TiO_2

shell conduction band (**Equation 6.10**) should result in slower recombination due to the separation of the electron and the oxidized chromophore. However, these results point to an ultrafast BET process (**Equation 6.11**) that occurs following excited-state electron injection. There are a limited number of states available in a thin shell of TiO_2 since the electron cannot inject into ZrO_2. As such, the dominant pathway for the injected electron, which would normally undergo a random walk within *nano*TiO_2 prior to recombination,[2] is to immediately recombine with an oxidized chromophore.

Equation 6.10

$ZrO_2/TiO_2|\text{-}Ru^{III}(4,4'\text{-}dpbpy^{\bullet-})(bpy)_2^{2+} \rightarrow ZrO_2/TiO_2(e^-)|\text{-}Ru^{III}(4,4'\text{-}dpbpy)(bpy)_2^{3+}$

Equation 6.11

$ZrO_2/TiO_2(e^-)|\text{-}Ru^{III}(4,4'\text{-}dpbpy)(bpy)_2^{3+} \rightarrow ZrO_2/TiO_2|\text{-}Ru^{II}(4,4'\text{-}dpbpy)(bpy)_2^{2+}$

As the thickness of the TiO_2 shell is increased for *nano*$ZrO_2/TiO_2|$-$\mathbf{RuP^{2+}}$ photoanodes, the recombination behavior shifts from favoring an ultrafast BET process to resembling the random walk recombination kinetics of $\mathbf{RuP^{2+}}$ on *nano*TiO_2. Qualitatively, the kinetic data for *nano*ZrO_2/TiO_2(1.3 nm)|-$\mathbf{RuP^{2+}}$ appear to overlap those of *nano*$TiO_2|$-$\mathbf{RuP^{2+}}$. Quantitatively, the $t_{1/2}$ values for the two decay traces are similar (1.26 μs and 761 ns, respectively). As with the injection kinetics on *nano*ZrO_2/TiO_2, the similarity in recombination behavior can be attributed to an increase in the density of states in the TiO_2 shell. These data suggest that sufficiently thick TiO_2 shells (≥1.3 nm) on a *nano*ZrO_2 core allow for recombination behavior similar to that of *nano*TiO_2 photoanodes.

From the electron injection data, electron injection is rapid from $\mathbf{RuP^{2+*}}$ to *nano*SnO_2 (**Equation 6.12**). If quantitative injection is assumed (i.e. $\Phi_{inj} = 1.0$),[24] then decay monitored at λ_{probe} = 430 nm can be attributed completely to recombination of the electron in the SnO_2 conduction band to the oxidized chromophore, $\mathbf{RuP^{3+}}$ (**Equation 6.13**).

Equation 6.12

$SnO_2|\text{-}Ru^{III}(4,4'\text{-dpbpy}^{\bullet-})(bpy)_2^{2+} \rightarrow SnO_2(e^-)|\text{-}Ru^{III}(4,4'\text{-dpbpy})(bpy)_2^{3+}$

Equation 6.13

$SnO_2(e^-)|\text{-}Ru^{III}(4,4'\text{-dpbpy})(bpy)_2^{3+} \rightarrow SnO_2|\text{-}Ru^{II}(4,4'\text{-dpbpy})(bpy)_2^{2+}$

For *nano*SnO_2/TiO_2(0.34 nm)|-$\mathbf{RuP^{2+}}$, recombination to the ground state appears to occur more slowly than for *nano*SnO_2|-$\mathbf{RuP^{2+}}$. The fastest decay lifetime, τ_1, increases with the addition of the thin TiO_2 shell, while its overall contribution to decay decreases (from 3.4 ns, 27% without the 0.34-nm TiO_2 shell to 31.5 ns, 6% with the 0.34-nm TiO_2 shell). The $t_{1/2}$ increases as well, from 33 ns without the shell to 6.6 μs with the shell.

The improvement in recombination lifetime is attributable to the TiO_2 shell. Excited-state electron injection could occur from $\mathbf{RuP^{2+*}}$ to either the TiO_2 shell (**Equation 6.14**; suggested by *nano*ZrO_2/TiO_2) or directly to the SnO_2 core (**Equation 6.15**). In the event of injection to the TiO_2 conduction band (**Equation 6.14**), electron transfer from the conduction band of TiO_2 to the conduction band of SnO_2 (**Equation 6.16**) is a downhill process by ~300 mV.[31] Recombination of the electron to the oxidized chromophore can occur either from TiO_2 (**Equation 6.17**) or SnO_2 (**Equation 6.18**). The slow recombination process observed with the thin 0.34-nm TiO_2 shell on SnO_2 suggests that recombination is occurring from SnO_2 (**Equation**

6.18), which is consistent both with previous work on *nano*SnO_2/TiO_2 core/shell photoanodes,[9] and with the recombination results on *nano*ZrO_2/TiO_2(0.34 nm). If the electron were localized on TiO_2, ultrafast BET would be expected.

Equation 6.14

$$SnO_2/TiO_2|\text{-}Ru^{III}(4,4'\text{-}dpbpy^{\bullet-})(bpy)_2^{2+} \rightarrow SnO_2/TiO_2(e^-)|\text{-}Ru^{III}(4,4'\text{-}dpbpy)(bpy)_2^{3+}$$

Equation 6.15

$$SnO_2/TiO_2|\text{-}Ru^{III}(4,4'\text{-}dpbpy^{\bullet-})(bpy)_2^{2+} \rightarrow SnO_2(e^-)/TiO_2|\text{-}Ru^{III}(4,4'\text{-}dpbpy)(bpy)_2^{3+}$$

Equation 6.16

$$SnO_2/TiO_2(e^-)|\text{-}Ru^{III}(4,4'\text{-}dpbpy)(bpy)_2^{3+} \rightarrow SnO_2(e^-)/TiO_2|\text{-}Ru^{III}(4,4'\text{-}dpbpy)(bpy)_2^{3+}$$

Equation 6.17

$$SnO_2/TiO_2(e^-)|\text{-}Ru^{III}(4,4'\text{-}dpbpy)(bpy)_2^{3+} \rightarrow SnO_2/TiO_2|\text{-}Ru^{II}(4,4'\text{-}dpbpy)(bpy)_2^{2+}$$

Equation 6.18

$$SnO_2(e^-)/TiO_2|\text{-}Ru^{III}(4,4'\text{-}dpbpy)(bpy)_2^{3+} \rightarrow SnO_2/TiO_2|\text{-}Ru^{II}(4,4'\text{-}dpbpy)(bpy)_2^{2+}$$

Thicker shells of TiO_2 on *nano*SnO_2 do not result in slower recombination kinetics. Instead, for shells of TiO_2 thicker than 0.87 nm on *nano*SnO_2, kinetic decay splits into distinct fast and slow regimes (**Figure 6.7**). The fastest decay lifetimes and relative contributions of those lifetimes to overall decay kinetics for 0.87-, 1.3-, and 1.8-nm thick shells of TiO_2 on *nano*SnO_2 are similar, with τ_1 = 197.6 ps (48%), 222 ps (56%), and 221.6 ps (58%), respectively

and τ_2 = 3.19 ns (26%), 4.6 ns (22%), and 10.5 ns (13%), respectively. These data suggest rapid recombination at early time points, and perhaps a similar mechanism of recombination given the similarity of the decay data. Following rapid decay, recombination appears to plateau, with τ_3 = 334 μs (26%), 139 μs (14%), and 42 μs (5%), respectively, for 0.87-, 1.3-, and 1.8-nm thick shells of TiO_2 on *nano*SnO_2. For 1.3- and 1.8-nm thick TiO_2 shells, a fourth lifetime, τ_4, was fit as well, with τ_4 = 1.87 ms (8%) and 6.6 ms (24%), respectively.

These data suggest that recombination for thick TiO_2 shells is largely dominated by fast decay. Between 70% and 80% of the decay lifetime contribution is on the nanosecond timescale, or faster, for TiO_2 shells between 0.87 nm and 1.8 nm thick. Also, fast recombination appears to be thickness-independent. However, following the fast decay regimes, recombination slows dramatically. The *nano*SnO_2/TiO_2(1.8 nm)|-**RuP**$^{2+}$ photoanode provides the starkest example. The two fastest lifetimes, τ_1 and τ_2, account for a combined 71% of observed decay (decay that is presumably complete by 10.5 ns). However, the slowest lifetime, τ_4, still accounts for 24% of decay, and extends to 6.6 ms, nearly six orders of magnitude longer than the two fast components. The slow components, τ_3 and τ_4, appear to be TiO_2 thickness-dependent, with increasing lifetime as TiO_2 thickness increases.

One possible explanation for this behavior is the presence of surface-localized trap states for the as-deposited TiO_2. A schematic explanation is shown in **Figure 6.11**. For thin shells of TiO_2 on *nano*SnO_2 (**Figure 6.11**a), electron injection from **RuP**$^{2+*}$ could occur to either the TiO_2 conduction band or to trap states that are energetically positive of the conduction band. Trap states could also be thermally populated following injection to the TiO_2 conduction band. However, for trap states energetically negative of the SnO_2 conduction band, electron transfer could still occur from TiO_2 trap states to SnO_2. Recombination would then occur through

tunneling as previously observed.[9] For thick shells of TiO_2 (**Figure 6.11**b), injection from $\mathbf{RuP^{2+*}}$ could still occur to either trap states or the TiO_2 conduction band. If the TiO_2 shell is sufficiently thick, electron mobility from trap states through the TiO_2 "bulk" to the underlying SnO_2 core could be disfavored as it would be an uphill process to the conduction band. The injected electrons would remain localized on the TiO_2 surface, promoting the ultrafast BET observed for *nano*ZrO_2/TiO_2(0.34 nm)|-$\mathbf{RuP^{2+}}$ photoanode. The $t_{1/2}$ value for *nano*ZrO_2/TiO_2(0.34 nm)|-$\mathbf{RuP^{2+}}$ (456 ps) is in the middle of the $t_{1/2}$ value range for *nano*SnO_2/TiO_2|-$\mathbf{RuP^{2+}}$ (675, 298, and 109 ps for 0.87-, 1.3-, and 1.8-nm thick TiO_2 shells, respectively), furthering suggesting electron localization at the TiO_2 surface.

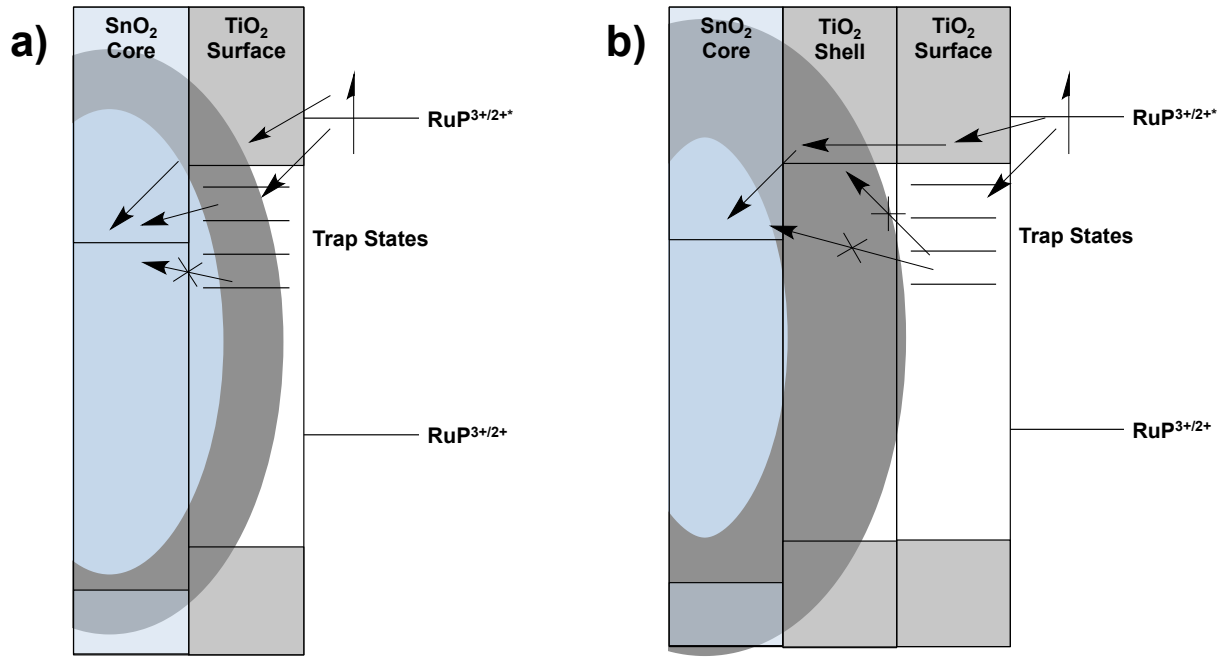

Figure 6.11. Proposed scheme comparing electron transfer on *nano*SnO_2/TiO_2|-$\mathbf{RuP^{2+}}$ with a) thin TiO_2 shells and b) thick TiO_2 shells.

Comparison of the recombination kinetics for unannealed films of *nano*SnO_2/TiO_2 and *nano*ZrO_2/TiO_2 with TiO_2 shells of different thickness (0.34 and 1.3 nm) are shown in **Figure**

6.12. The comparison of *nano*SnO_2/TiO_2 and *nano*ZrO_2/TiO_2 with a 0.34-nm thick shell (**Figure 6.12**a) supports the hypothesis of electron transfer from TiO_2 to SnO_2 for thin TiO_2 shells. Qualitatively, recombination is many orders of magnitude more rapid on *nano*ZrO_2/TiO_2 than on *nano*SnO_2/TiO_2. However, comparison of *nano*SnO_2/TiO_2 and *nano*ZrO_2/TiO_2 with a 1.3-nm thick shell (**Figure 6.12**b) does not necessarily support the notion of surface-localized trap states for thick shells of TiO_2. For TiO_2 shells of the same thickness, a rapid BET component is expected regardless of the underlying metal oxide core. However, rapid BET is not observed for *nano*ZrO_2/TiO_2(1.3 nm). Comparing $t_{1/2}$ for the fit data shows an approximately four order of magnitude longer-lived charge separation for *nano*ZrO_2/TiO_2(1.3 nm) ($t_{1/2}$ = 1.26 μs) than for *nano*SnO_2/TiO_2(1.3 nm) ($t_{1/2}$ = 298 ps).

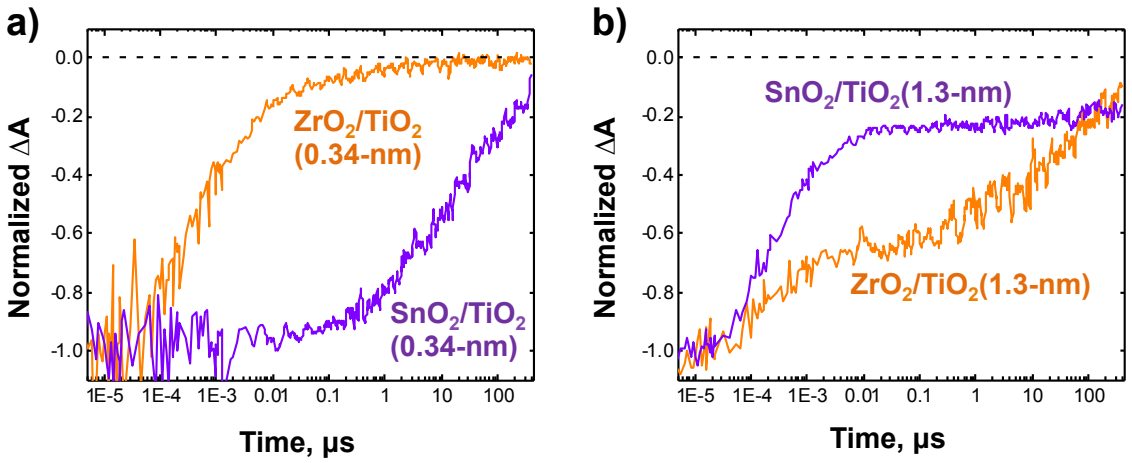

Figure 6.12. Normalized decay kinetics for unannealed MO_x/TiO_2|-**RuP**$^{2+}$ for MO_x = ZrO_2 (orange traces) and MO_x = SnO_2 (purple traces) for a) 0.34-nm thick TiO_2 shell; and b) 1.3-nm thick TiO_2 shell. (conditions: 0.1 M $HClO_4$; λ_{pump} = 480 nm; λ_{probe} = 430 nm; 100 nJ/pulse)

The dramatic improvement of charge separation lifetime on *nano*ZrO_2/TiO_2 compared to *nano*SnO/TiO_2 for thick TiO_2 shells could be due to crystallinity differences in the underlying

core nanoparticles and the effect of this crystallinity during the TiO_2 deposition process. The phase composition of the ALD substrate has been shown, under certain circumstances, to affect the phase composition of the resulting ALD layer.[16,32,33] It is possible that ALD of TiO_2 performed on the *nano*ZrO_2 results in a more defect-free and trap-state-free TiO_2 overlayer. In this event, diffusion to remote surface locations on *nano*ZrO_2/TiO_2 with thick TiO_2 shells could become more probable. Further investigation into the density of states, particularly of trap states, for TiO_2 overlayers deposited on both *nano*ZrO_2 and *nano*SnO_2 substrates is required.

Recombination kinetics for annealed photoanodes of *nano*SnO_2 and *nano*ZrO_2 were investigated for 0.34 and 0.87-nm thick TiO_2 shells. Recombination kinetics for *nano*ZrO_2/TiO_2(0.87 nm)|-$\mathbf{RuP^{2+}}$ are shown in **Figure 6.8** and recombination kinetics for *nano*SnO_2/TiO_2(0.87 nm)|-$\mathbf{RuP^{2+}}$ are shown in **Figure 6.9**. Qualitatively, **Figure 6.8** shows that annealing does not significantly alter the recombination kinetics for $\mathbf{RuP^{2+}}$ on *nano*ZrO_2/TiO_2 core/shell photoanodes.

The same is untrue for *nano*SnO_2/TiO_2 core/shell photoanodes. Comparison of the unannealed and annealed kinetic traces in **Figure 6.9** shows a dramatic decrease in rapid recombination for the annealed film. The fastest lifetime for the unannealed film (τ_1 = 198 ps (48%)) increases in lifetime and decreases in contribution for the annealed film (τ_1 = 670 ps (39%)). The annealed photoanode has a significantly longer intermediate lifetime as well (τ_2 = 5.3 μs (38%) annealed; τ_2 = 3.19 ns (26%) unannealed). However, at long lifetime, the unannealed film outperforms the annealed film (τ_3 = 260 μs (24%) annealed; τ_3 = 334 μs (26%) unannealed). These data are consistent with annealing reducing the number of surface-localized trap sites and improving the crystallinity of the TiO_2 shell,[29,30] thereby reducing the number of buried trap sites as well. A reduced number of trap sites, both at the solution/TiO_2 interface and

in the TiO_2 "bulk" near the SnO_2/TiO_2 interface, could improve electron mobility from the TiO_2 conduction band to the SnO_2 conduction band, resulting in the improved recombination kinetics that are observed. These data further highlight the necessity of determining the density of states for TiO_2 overlayers deposited on both *nano*SnO_2 and *nano*ZrO_2 cores.

6.2.6. Photoelectrochemistry

Photoelectrochemical (PEC) comparisons were performed on photoanodes derivatized with $\mathbf{RuP^{2+}}$. In these experiments, the working electrode (the photoanode) was separated from the reference electrode (Ag/AgCl, saturated NaCl; E(vs. NHE) = 0.197 V) and the counter electrode (Pt mesh) using a Nafion membrane and a custom-built, two-compartment glass cell. The core/shell electrodes were coated with an inert, opaque epoxy to define a working area for illumination and limit background reactions at the FTO back contact.[34] The electrolyte was 0.1 M $HClO_4$. Hydroquinone (0.02 M) was added a sacrificial reducing agent.[35] The electrolytic solution was deaerated by bubbling N_2 for at least 15 minutes prior to illumination, and a constant N_2 flow was maintained over the headspace of the working compartment throughout experimentation. Illumination was provided by a white light source positioned to output ~100 mW cm^{-2} (similar to the level of solar irradiance) on the photoanodes.

Photoanodes of *nano*SnO_2|-$\mathbf{RuP^{2+}}$ ($\Gamma \approx 3.6 \times 10^{-8}$ mol cm^{-2}) and *nano*TiO_2|-$\mathbf{RuP^{2+}}$ ($\Gamma \approx 7.4 \times 10^{-8}$ mol cm^{-2}) were illuminated for 3 cycles in a 30 s on/30 s off pattern (**Figure 6.13**). Bare films of nanoparticles were used to establish a benchmark for photoelectrochemical activity of $\mathbf{RuP^{2+}}$ in the presence of hydroquinone in 0.1 M $HClO_4$. Following immersion of the photoanode in solution and deaeration, the working electrode was held at 0.4 V vs. Ag/AgCl in the dark for 30 seconds. After 30 seconds, with bias still applied, the working electrode was illuminated. A current spike was observed for both *nano*SnO_2|-$\mathbf{RuP^{2+}}$ and *nano*TiO_2|-$\mathbf{RuP^{2+}}$ (609 and 300 μA cm^{-2}, respectively). The spike decayed gradually over 30 seconds of illumination

(567 and 277 μA cm^{-2}, respectively) until the light source was shuttered, at which point the current for each photoanode dropped to approximately 0. The off/on cycle was repeated twice more, with similar spikes and relaxations during illumination as observed initially. For each off/on cycle, the photocurrent level observed for *nano*SnO_2|-**RuP**$^{2+}$ was approximately twice of that observed for *nano*TiO_2|-**RuP**$^{2+}$. This observation does not account for the near doubling of **RuP**$^{2+}$ surface coverage on *nano*TiO_2 compared to *nano*SnO_2.

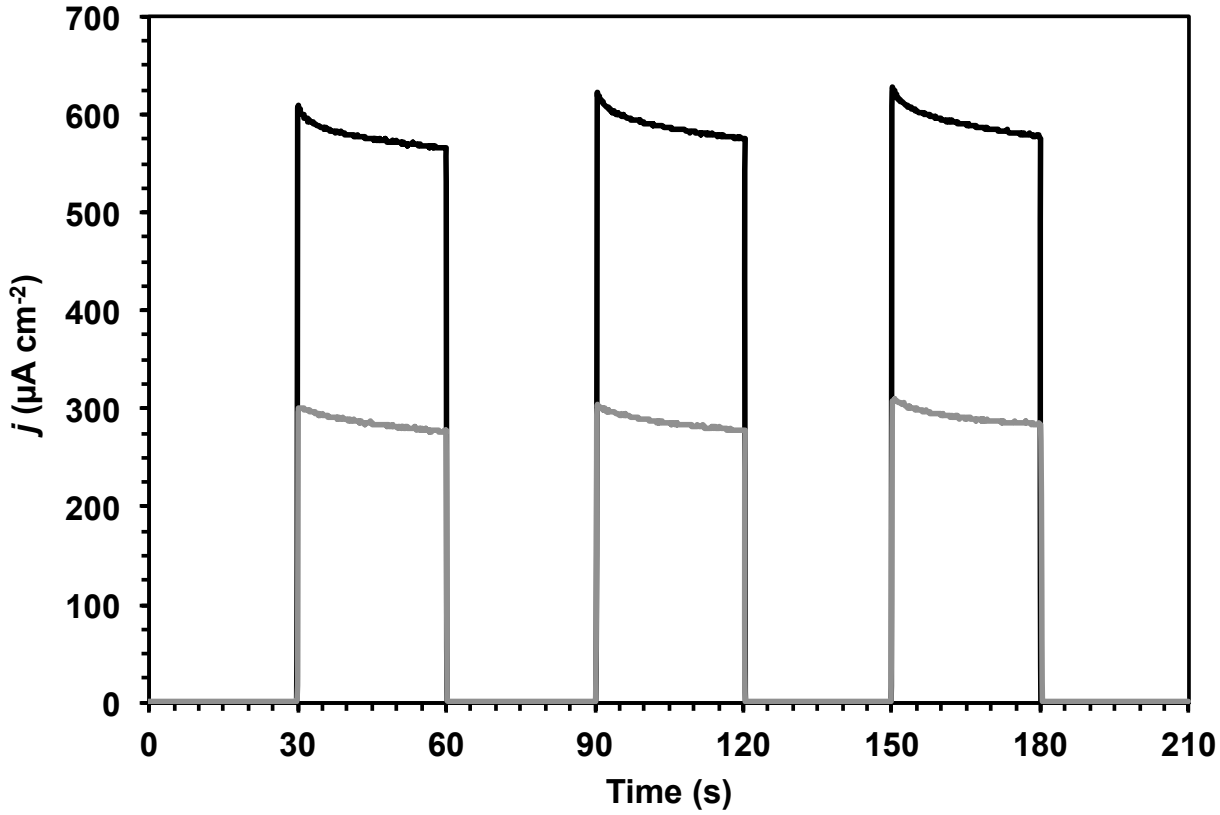

Figure 6.13. Light-on/light-off photocurrent-time traces for *nano*SnO_2|-**RuP**$^{2+}$ (black) and *nano*TiO_2|-**RuP**$^{2+}$ (gray) in the presence of hydroquinone (0.02 M). (conditions: ~100 mW cm^{-2} white light; 400-nm long-pass cutoff filter; E_{app} = 0.4 V vs. Ag/AgCl; 0.1 M $HClO_4$; ref = Ag/AgCl, sat. NaCl; aux = Pt)

Photoanodes of *nano*SnO_2/TiO_2|-**RuP**$^{2+}$, with 0.34-, 0.87-, and 1.3-nm thick TiO_2 shells, were illuminated under the same conditions as *nano*SnO_2|-**RuP**$^{2+}$ and *nano*TiO_2|-**RuP**$^{2+}$. The results are shown in **Figure 6.14**. The *nano*SnO_2|-**RuP**$^{2+}$ photocurrent trace is shown for comparison. As the thickness of the TiO_2 shell increases, the observed photocurrent increases as well. Additionally, the photocurrent level for each photoanode is higher than that of bare *nano*SnO_2|-**RuP**$^{2+}$. For example, the initial spike of the first illumination results in photocurrent levels of 771, 892, and 1,474 μA cm^{-2} for 0.34-, 0.87-, and 1.3-nm thick TiO_2 shells, respectively (recall 609 μA cm^{-2} for *nano*SnO_2|-**RuP**$^{2+}$). This trend continues throughout illumination, and over multiple off/on cycles. Increases in photocurrent for core/shell photoanodes compared to bare electrodes have been observed previously.[13,36]

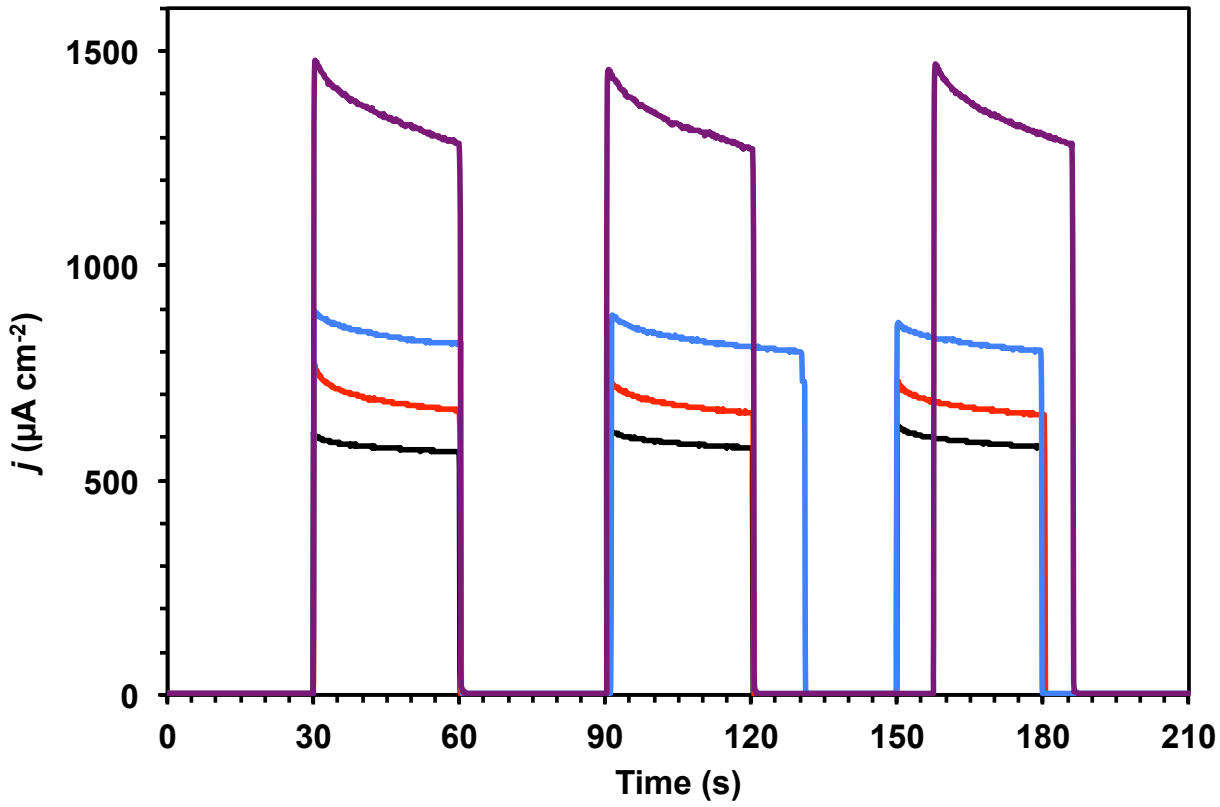

Figure 6.14. Light-on/light-off photocurrent-time traces for *nano*SnO_2/TiO_2|-**RuP**$^{2+}$ with TiO_2 shell thickness of 0.34 nm (red), 0.87 nm (blue), 1.3 nm (purple), and *nano*SnO_2|-**RuP**$^{2+}$ (black) in the presence of hydroquinone (0.02 M). (conditions: ~100 mW cm^{-2} white light; 400-nm long-pass cutoff filter; E_{app} = 0.4 V vs. Ag/AgCl; 0.1 M $HClO_4$; ref = Ag/AgCl, sat. NaCl; aux = Pt)

To ensure that the increase in photocurrent observed for *nano*SnO_2/TiO_2|-**RuP**$^{2+}$ core/shell photoanodes was not solely attributable to the ALD-TiO_2 overlayer, films of *nano*ZrO_2/TiO_2|-**RuP**$^{2+}$, with 0.34-, 0.87-, and 1.3-nm thick TiO_2 shells, were investigated as photoanodes as well. Little photocurrent is expected for these electrodes, because (as shown above) minimal electron injection is observed for **RuP**$^{2+*}$ on *nano*ZrO_2. In line with this hypothesis, <20 μA cm^{-2} of photocurrent is observed for even the thickest (1.3 nm) TiO_2 shell on *nano*ZrO_2, and <10 μA cm^{-2} is observed for the two thin shells (0.34 and 0.87 nm) (**Figure 6.15**).

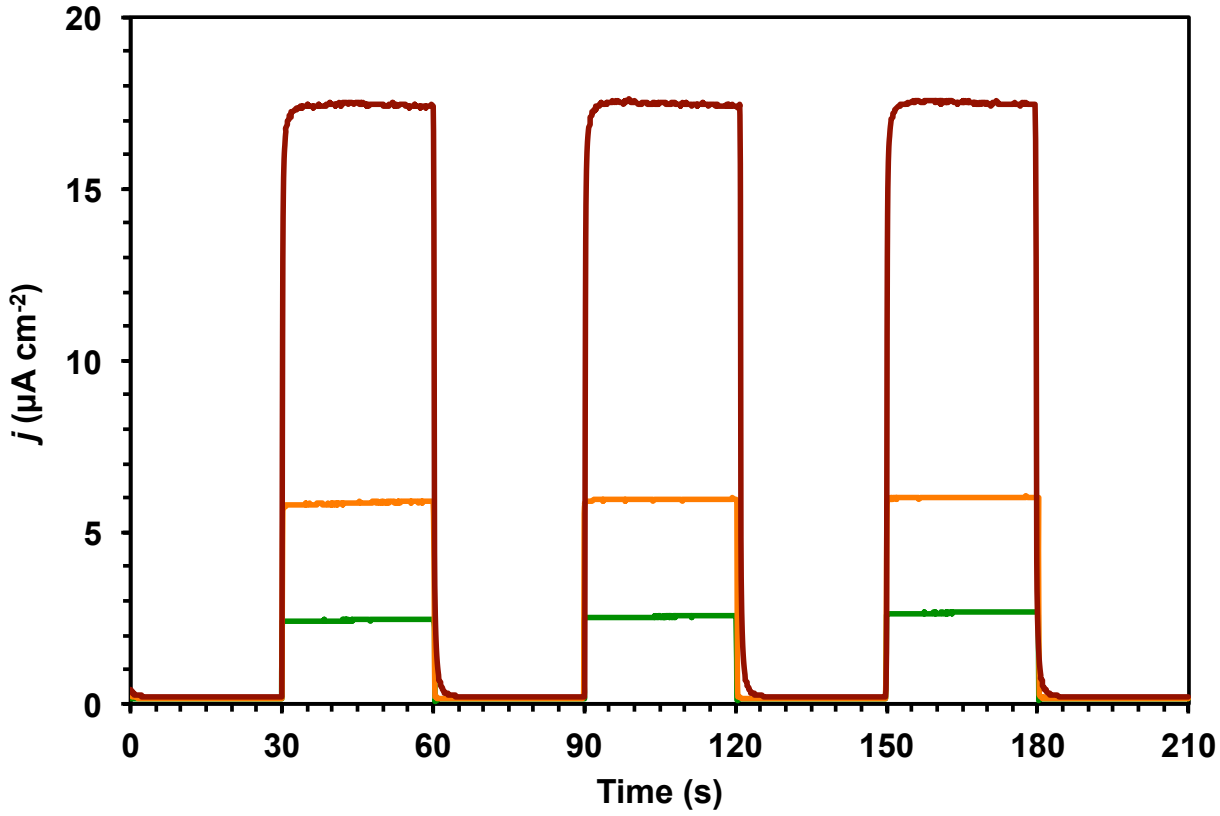

Figure 6.15. Light-on/light-off photocurrent-time traces for *nano*ZrO_2/TiO_2|-**RuP**$^{2+}$ with TiO_2 shell thickness of 0.34 nm (green), 0.87 nm (orange), and 1.3 nm (dark red) in the presence of hydroquinone (0.02 M). (conditions: ~100 mW cm^{-2} white light; 400-nm long-pass cutoff filter; E_{app} = 0.4 V vs. Ag/AgCl; 0.1 M $HClO_4$; ref = Ag/AgCl, sat. NaCl; aux = Pt)

These data provide some insight into the PEC reactions occurring at core/shell photoanodes. The small photocurrent observed for *nano*ZrO_2/TiO_2|-**RuP**$^{2+}$ electrodes demonstrates that electron injection is necessary for quenching of the oxidized chromophore by hydroquinone. Additionally, the deposition of TiO_2 by itself does not lead to the dramatic increase in photocurrent observed for *nano*SnO_2/TiO_2|-**RuP**$^{2+}$ electrodes compared to *nano*SnO_2|-**RuP**$^{2+}$, because similar increases in photocurrent are not observed for *nano*ZrO_2/TiO_2|-**RuP**$^{2+}$ electrodes.

The dramatic increase in photocurrent for *nano*SnO_2/TiO_2|-**RuP**$^{2+}$ electrodes compared to *nano*SnO_2|-**RuP**$^{2+}$ is promising from a device standpoint. However, these photocurrent data cannot be directly compared to the transient absorption kinetic data due to the applied bias in the PEC experiments. Future work on bias-dependent transient absorption (with and without an added sacrificial reducing agent) is required. Still, the improvement observed employing the core/shell *nano*SnO_2/TiO_2|-**RuP**$^{2+}$ electrodes over bare films of *nano*SnO_2|-**RuP**$^{2+}$ or *nano*TiO_2|-**RuP**$^{2+}$ is in line with similar reports from the literature and points to the potential for *nano*SnO_2/TiO_2 core/shell electrodes in future photoanode applications.[12,13,36,37]

6.3. Conclusions

Transient absorption spectroscopy was used to elucidate the electron injection and recombination kinetics for **RuP**$^{2+}$ on core/shell photoanodes with TiO_2 shells of varying thickness. For TiO_2 shells of comparable thickness to those typically employed in DSPEC photoanodes (>1 nm), ultrafast BET is observed, and half of recombination complete after only a few hundred picoseconds. However, approximately 20% to 30% of the chromophore remains oxidized out to the millisecond timescale. This behavior suggests at least two mechanisms of recombination: ultrafast BET from surface-localized defect sites and a long-lived tunneling process from the SnO_2 core through TiO_2 to the oxidized chromophore.[9]

Annealing the *nano*SnO_2/TiO_2 core/shell electrodes prior to dye loading significantly impacts both electron injection and recombination. In the case of recombination, the ultrafast BET component decreases, with a longer-lived intermediate state. However, at longer (i.e. millisecond) timescales, the unannealed films outperform their annealed counterparts. An explanation for the observed improvement is the removal of defect sites on the TiO_2 surface and throughout the TiO_2 shell "bulk." Detailed density of states measurements before and after annealing would provide valuable insight into the energetics of the TiO_2 shell.

Photoelectrochemical experiments using *nano*SnO_2/TiO_2|-**RuP**$^{2+}$ core/shell electrodes in the presence of hydroquinone as a sacrificial reducing agent corroborate the TiO_2 shell thickness dependence observed for DSPEC devices reported in the literature. However, further investigation of bias-dependent transient absorption spectroscopy is needed to compare the observations made herein with electron injection and recombination. These studies could provide valuable insight into the construction of core/shell photoanodes under conditions similar to those in operating DSPEC devices.

6.4. Experimental

Materials. Deionized water was further purified using a Milli-Q Ultrapure water purification system. Perchloric acid (99.999%) was purchased from Sigma-Aldrich and was used as received. Nanoparticle films of tin oxide (*nano*SnO_2) were constructed according to literature procedures.[31,36] Nanoparticle films of zirconium oxide (*nano*ZrO_2) were constructed according to literature procedures.[38,39] Thin shells of titanium dioxide were deposited on *nano*SnO_2 or *nano*ZrO_2 using atomic layer deposition (ALD). The molecular chromophore [Ru(2,2'-bipyridine)$_2$(4,4'-dpbpy)][Cl]$_2$ (**RuP**$^{2+}$) was synthesized according to a literature procedure.[18,19] Dye-sensitized electrodes for transient absorption spectroscopy were constructed by soaking the nanoparticle films in a methanol solution of **RuP**$^{2+}$ (~1 mM) in the dark overnight (~14 hours). After the soak period, the electrodes were rinsed with methanol and dried under a stream of air. The electrodes were stored in the dark. Dye-sensitized electrodes for photoelectrochemical experiments were constructed identically to those for transient absorption spectroscopy, followed by masking with an opaque epoxy. Loctite Hysol 9462 epoxy was applied to dye-sensitized electrodes to define an exposed working area. The epoxy cured overnight (~14 hours) at room temperature. Photographs were taken of the electrodes, and working areas were determined using ImageJ software.

Atomic layer deposition (ALD). ALD was performed using a Cambridge NanoTech Savannah S200 ALD system located in the Chapel Hill Analytical Nanofabrication Laboratory (CHANL) cleanroom. The reactor temperature was set at 150 °C. The cylinder containing the titanium dioxide precursor, tetrakis(dimethylamido)titanium(IV) (TiTDMA, 99.999%, Sigma Aldrich), was set to 75 °C. Both the reactor and the TiTDMA cylinder were warmed to temperature and allowed to equilibrate for approximately an hour prior to use. Prior to deposition, samples sat in the reactor under continuous nitrogen purge (99.999%, further purified using an Entegris GateKeeper Inert Gas Purifier) for a minimum of 10 minutes. Each deposition cycle consisted of a 1-s pulse of TiTDMA, a 20-s exposure in the reactor, a 60-s purge, a 0.02-s pulse of H_2O, a 20-s exposure in the reactor, and a 60-s purge. The thickness of TiO_2 deposited was determined by ellipsometry performed on a piece of witness Si in the reactor using a J. A. Woollam Variable Angle Spectroscopic Ellipsometer.

Transient Absorption. Femtosecond transient absorption spectra were obtained using a pump-probe configuration. The 775 nm (1 kHz repetition rate, 150 fs pulse width) output of a chirped pulse amplifier (Clark-MXR 2001) was split into two beams. A large portion of the regenerative amplifier output (90%) was sent through a home-built optical parametric amplifier (OPA) where the signal (~1250 nm) is mixed with residual 775 nm in a 2-mm thick β-$BaBO_3$ (BBO) crystal through sum frequency generation to produce the 480 nm pump pulse. The probe pulse (325 nm to 800 nm) was generated in a rotating CaF_2 window through supercontinuum generation. Pump and probe polarizations were set to magic angle and focused to a 150 μm spot size at the sample. The time between pump and probe was controlled by a mechanical delay stage. Using a neutral density filter, the pump pulse was set to 100 nJ/pulse. Pump-induced changes in the white light continuum were collected at a fiber optic coupled multichannel

spectrometer with a CMOS sensor with a sensitivity of 0.1 mOD. A mechanical chopper synchronized with the laser chopped the pump beam at 500 Hz.

Transient absorption measurements in the ps to μs range were collected using the same pump pulse as the femtosecond experiment, while the white light probe pulse was generated in a diode-pumped photonic crystal fiber. The time delay between pump and probe was electronically controlled (Ultrafast Systems). The data were collected using the same CMOS sensor.

Transient absorption data collected with time delays >400 μs were obtained by placing the electrode at a 45° angle in a 10-mm cuvette containing 0.1 M $HClO_4$. The top of the cuvette was fit with an O-ring and Kontes valve for purging with argon and were sealed immediately after purging. Samples were purged with argon for at least 45 minutes prior to experiments. Measurements were performed using a Spectra-Physics Quanta-Ray Lab-170 Nd:YAG Laser combined with a VersaScan OPO (488 nm, 5 to 7 ns, operated at 1 Hz, beam diameter 0.5 cm, 1 mJ/pulse) integrated with an Edinburgh LP920 laser flash photolysis spectrometer system. White probe light was generated using a 450 W Xe lamp in pulsed mode. Two filters (380-nm long-pass) were placed in the probe beam to prevent direct bandgap excitation of the semiconductors. A glan-laser polarizer (Thorlabs GL-10A) set to 54.7° (the "magic angle") was placed in the probe beam (after the sample) to eliminate anisotropy effects. Light was detected using a photomultiplier tube (PMT; Hamamatsu R928). A Tektronix oscilloscope (model TDS-3032, 300 MHz) was used to record the PMT output and to ensure the pulsed probe source did not exceed 600 mV baseline signal assessed without laser excitation. The PMT was housed in a PMT housing wired with only five dynodes and biased at 600 V. Laser scatter and luminescence were removed by subtracting waveforms collected with laser light but not probe light from those collected with both laser light and probe light incident on the sample. A notch filter was placed

after the sample but before the monochromator to reject laser scatter. Experiment synchronization was achieved by the Edinburgh L900 software. Data sets were the result of 25 to 100 averages. A mechanical shutter (part of the Edinburgh system) was fixed in the path of the probe beam and was open for <50 ms per each 1 Hz pulse to minimize each sample's exposure to light.

Photoelectrochemical Experiments. Photoelectrochemical experiments were conducted in a homemade, two-compartment cell described elsewhere.[35,36] The working, dye-sensitized electrode was separated from the reference electrode (Ag/AgCl, saturated NaCl) and counter electrode (Pt mesh) by a Nafion membrane. A potentiostat (CH Instruments 760E) was used to poise the potential of the working electrode. The electrolytic solution was 0.1 M $HClO_4$ with 0.02 M hydroquinone added as a sacrificial electron donor. Prior to experiments, the working compartment was deaerated with N_2 for a minimum of 15 minutes. A positive stream of N_2 was maintained in the headspace to avoid atmospheric O_2 diffusion into the solution. Illumination was provided by a Thor Labs HPLS-30-04 light source. Samples were positioned to receive ~100 mW cm^{-2} (1 sun, 400 to 700 nm) with the light intensity determined with an Oriel Instruments 91150V reference cell. A 400-nm long-pass filter was employed to minimize direct bandgap excitation of the underlying semiconductors.

6.5. Acknowledgements

This material is based upon work solely supported as part of the UNC EFRC: Center for Solar Fuels, an Energy Frontier Research Center funded by the U.S. Department of Energy, Office of Science, Office of Basic Energy Sciences under Award Number DE-SC0001011. I acknowledge a graduate fellowship supported by the Department of Defense (DoD) through the National Defense Science & Engineering Graduate Fellowship (NDSEG) Program. I would further like to acknowledge Melissa K. Gish for her acquisition and workup of the transient

absorption spectroscopy data as well as discussion, interpretation, and editing of the information presented in this chapter. M. Kyle Brennanman (transient absorption, editing), Byron H. Farnum (providing *nano*ZrO_2 electrodes), Benjamin D. Sherman (editing), and Bob Geil (assistance with and maintenance of CHANL ALD equipment) also deserve acknowledgement.

REFERENCES

(1) Alstrum-Acevedo, J. H.; Brennaman, M. K.; Meyer, T. J. *Inorg. Chem.* **2005**, *44*, 6802.

(2) Ashford, D. L.; Gish, M. K.; Vannucci, A. K.; Brennaman, M. K.; Templeton, J. L.; Papanikolas, J. M.; Meyer, T. J. *Chem. Rev.* **2015**, *115*, 13006.

(3) House, R. L.; Iha, N. Y. M.; Coppo, R. L.; Alibabaei, L.; Sherman, B. D.; Kang, P.; Brennaman, M. K.; Hoertz, P. G.; Meyer, T. J. *Journal of Photochemistry and Photobiology C: Photochemistry Reviews* **2015**, *25*, 32.

(4) Hamann, T. W.; Farha, O. K.; Hupp, J. T. *J. Phys. Chem. C* **2008**, *112*, 19756.

(5) Alibabaei, L.; Farnum, B. H.; Kalanyan, B.; Brennaman, M. K.; Losego, M. D.; Parsons, G. N.; Meyer, T. J. *Nano Lett.* **2014**, *14*, 3255.

(6) Ashford, D. L.; Song, W.; Concepcion, J. J.; Glasson, C. R. K.; Brennaman, M. K.; Norris, M. R.; Fang, Z.; Templeton, J. L.; Meyer, T. J. *J. Am. Chem. Soc.* **2012**, *134*, 19189.

(7) Wang, L.; Ashford, D. L.; Thompson, D. W.; Meyer, T. J.; Papanikolas, J. M. *J. Phys. Chem. C* **2013**, *117*, 24250.

(8) Nozik, A. J. *Appl. Phys. Lett.* **1977**, *30*, 567.

(9) Knauf, R. R.; Kalanyan, B.; Parsons, G. N.; Dempsey, J. L. *J. Phys. Chem. C* **2015**, *119*, 28353.

(10) Bedja, I.; Kamat, P. V. *J. Phys. Chem.* **1995**, *99*, 9182.

(11) Chappel, S.; Chen, S.-G.; Zaban, A. *Langmuir* **2002**, *18*, 3336.

(12) Alibabaei, L.; Brennaman, M. K.; Norris, M. R.; Kalanyan, B.; Song, W.; Losego, M. D.; Concepcion, J. J.; Binstead, R. A.; Parsons, G. N.; Meyer, T. J. *Proc. Natl. Acad. Sci. U. S. A.* **2013**, *110*, 20008.

(13) Alibabaei, L.; Sherman, B. D.; Norris, M. R.; Brennaman, M. K.; Meyer, T. J. *Proc. Natl. Acad. Sci. U. S. A.* **2015**, *112*, 5899.

(14) Schuisky, M.; Hårsta, A.; Aidla, A.; Kukli, K.; Kiisler, A. A.; Aarik, J. *J. Electrochem. Soc.* **2000**, *147*, 3319.

(15) Hanson, K.; Losego, M. D.; Kalanyan, B.; Parsons, G. N.; Meyer, T. J. *Nano Lett.* **2013**, *13*, 4802.

(16) Iancu, A. T.; Logar, M.; Park, J.; Prinz, F. B. *ACS Appl. Mater. Interfaces* **2015**, *7*, 5134.

(17) Aarik, J.; Aidla, A.; Uustare, T.; Sammelselg, V. *J. Cryst. Growth* **1995**, *148*, 268.

(18) Norris, M. R.; Concepcion, J. J.; Glasson, C. R. K.; Fang, Z.; Lapides, A. M.; Ashford, D. L.; Templeton, J. L.; Meyer, T. J. *Inorg. Chem.* **2013**, *52*, 12492.

(19) Lapides, A. M.; Ashford, D. L.; Hanson, K.; Torelli, D. A.; Templeton, J. L.; Meyer, T. J. *J. Am. Chem. Soc.* **2013**, *135*, 15450.

(20) Bettis, S. E.; Hanson, K.; Wang, L.; Gish, M. K.; Concepcion, J. J.; Fang, Z.; Meyer, T. J.; Papanikolas, J. M. *J. Phys. Chem. A* **2014**, *118*, 10301.

(21) Hanson, K.; Brennaman, M. K.; Ito, A.; Luo, H.; Song, W.; Parker, K. A.; Ghosh, R.; Norris, M. R.; Glasson, C. R. K.; Concepcion, J. J.; Lopez, R.; Meyer, T. J. *J. Phys. Chem. C* **2012**, *116*, 14837.

(22) Bettis, S. E.; Ryan, D. M.; Gish, M. K.; Alibabaei, L.; Meyer, T. J.; Waters, M. L.; Papanikolas, J. M. *J. Phys. Chem. C* **2014**, *118*, 6029.

(23) Katoh, R.; Furube, A.; Yoshihara, T.; Hara, K.; Fujihashi, G.; Takano, S.; Murata, S.; Arakawa, H.; Tachiya, M. *J. Phys. Chem. B* **2004**, *108*, 4818.

(24) Knauf, R. R.; Brennaman, M. K.; Alibabaei, L.; Norris, M. R.; Dempsey, J. L. *J. Phys. Chem. C* **2013**, *117*, 25259.

(25) Chen, Y. W.; Prange, J. D.; Dühnen, S.; Park, Y.; Gunji, M.; Chidsey, C. E. D.; McIntyre, P. C. *Nat Mater* **2011**, *10*, 539.

(26) Hu, S.; Shaner, M. R.; Beardslee, J. A.; Lichterman, M.; Brunschwig, B. S.; Lewis, N. S. *Science* **2014**, *344*, 1005.

(27) Lichterman, M. F.; Carim, A. I.; McDowell, M. T.; Hu, S.; Gray, H. B.; Brunschwig, B. S.; Lewis, N. S. *Energy Environ. Sci.* **2014**, *7*, 3334.

(28) McDowell, M. T.; Lichterman, M. F.; Carim, A. I.; Liu, R.; Hu, S.; Brunschwig, B. S.; Lewis, N. S. *ACS Appl. Mater. Interfaces* **2015**, *7*, 15189.

(29) Habibi, M. H.; Talebian, N.; Choi, J.-H. *Dyes and Pigments* **2007**, *73*, 103.

(30) Mathews, N. R.; Morales, E. R.; Cortés-Jacome, M. A.; Toledo Antonio, J. A. *Solar Energy* **2009**, *83*, 1499.

(31) Green, A. N. M.; Palomares, E.; Haque, S. A.; Kroon, J. M.; Durrant, J. R. *J. Phys. Chem. B* **2005**, *109*, 12525.

(32) Gorbenko, O. Y.; Samoilenkov, S. V.; Graboy, I. E.; Kaul, A. R. *Chem. Mater.* **2002**, *14*, 4026.

(33) Emery, J. D.; Schlepütz, C. M.; Guo, P.; Riha, S. C.; Chang, R. P. H.; Martinson, A. B. F. *ACS Appl. Mater. Interfaces* **2014**, *6*, 21894.

(34) Chen, Z.; Dinh, H. N.; Miller, E. *Photoelectrochemical Water Splitting: Standards, Experimental Methods, and Protocols*; Springer-Verlag New York, 2013.

(35) Lapides, A. M.; Sherman, B. D.; Brennaman, M. K.; Dares, C. J.; Skinner, K. R.; Templeton, J. L.; Meyer, T. J. *Chem. Sci.* **2015**, *6*, 6398.

(36) Sherman, B. D.; Ashford, D. L.; Lapides, A. M.; Sheridan, M. V.; Wee, K.-R.; Meyer, T. J. *J. Phys. Chem. Lett.* **2015**, *6*, 3213.

(37) Wee, K.-R.; Sherman, B. D.; Brennaman, M. K.; Sheridan, M. V.; Nayak, A.; Alibabaei, L.; Meyer, T. J. *J. Mater. Chem. A.* **2016**, *4*, 2969.

(38) O'Regan, B.; Moser, J.; Anderson, M.; Grätzel, M. *J. Phys. Chem.* **1990**, *94*, 8720.

(39) Heimer, T. A.; D'Arcangelis, S. T.; Farzad, F.; Stipkala, J. M.; Meyer, G. J. *Inorg. Chem.* **1996**, *35*, 5319.

APPENDIX A: STABILIZATION OF A RUTHENIUM(II) POLYPYRIDYL DYE ON NANOCRYSTALLINE TiO_2 BY AN ELECTROPOLYMERIZED OVERLAYER

Element	Weight%	Atomic%
Si K	0.45	0.8
Ti K	91.6	95.09
Fe K	1.18	1.05
Ru L	3.12	1.54
Sn L	3.65	1.53
Totals	100	

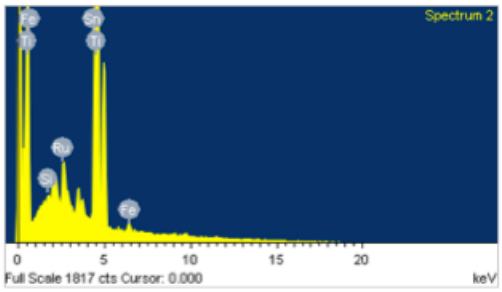

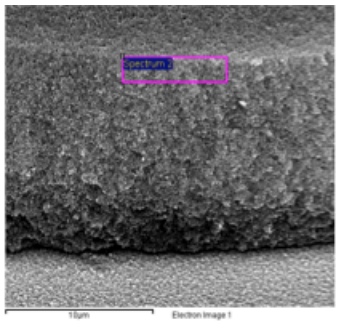

Element	Weight%	Atomic%
Si K	0.55	1
Ti K	87.92	93.53
Fe K	0.68	0.62
Ru L	2.59	1.31
Sn L	8.27	3.55
Totals	100	

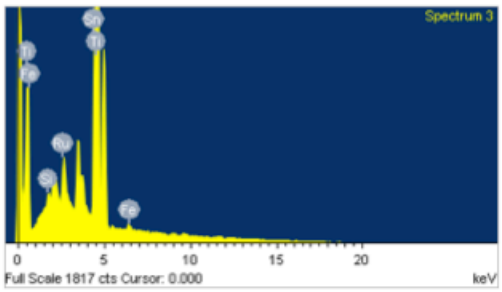

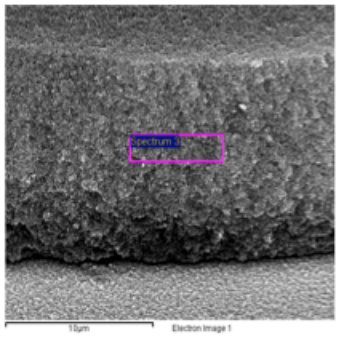

Element	Weight%	Atomic%
Si K	2.26	4.78
Ti K	62.07	77
Fe K	0.41	0.43
Ru L	1.5	0.88
Sn L	33.76	16.9
Totals	100	

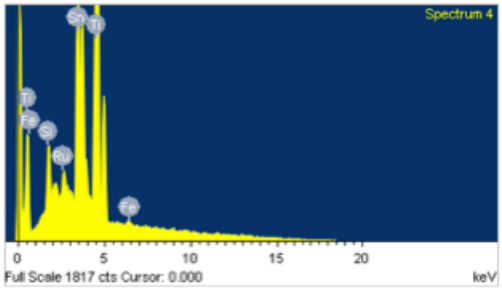

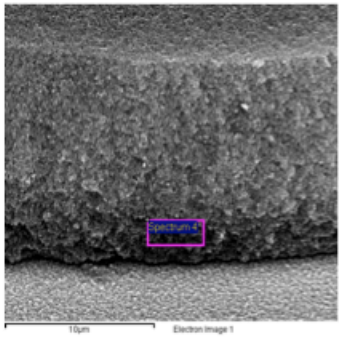

Figure A.1. EDS spectra (middle) and the tabulated results (left) for *nano*TiO_2|-**RuPdvb**-*poly*[**Fe(v-tpy)$_2$**]$^{2+}$ (50 cycles) at various depths that are indicated by the pink rectangle (far right).

Element	Weight%	Atomic%
Si K	1	1.77
Ti K	89.65	93.58
Fe K	1.34	1.2
Ru L	1	0.5
Sn L	7.02	2.96
Totals	100	

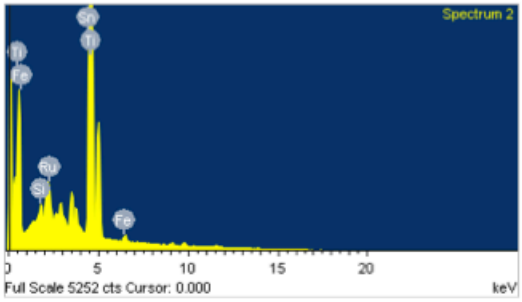

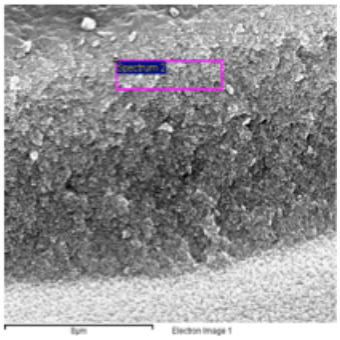

Element	Weight%	Atomic%
Si K	1.42	2.76
Ti K	75.78	86.29
Fe K	0.76	0.75
Ru L	0.94	0.51
Sn L	21.1	9.7
Totals	100	

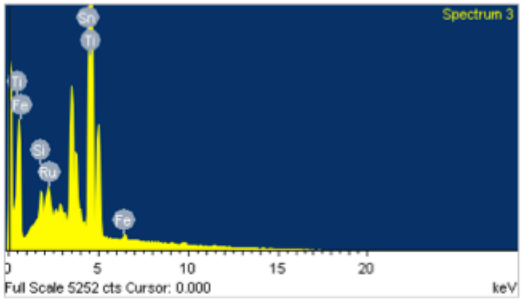

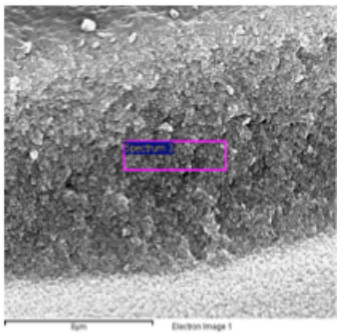

Element	Weight%	Atomic%
Si K	5.89	13.55
Ti K	43.34	58.44
Fe K	0.52	0.6
Ru L	0.68	0.43
Sn L	49.57	26.98
Totals	100	

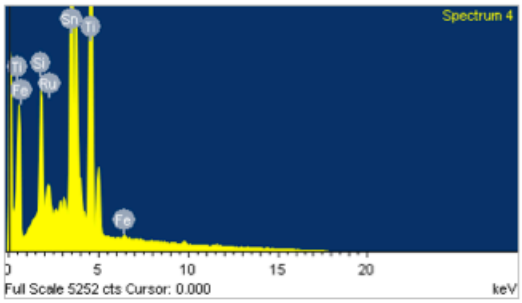

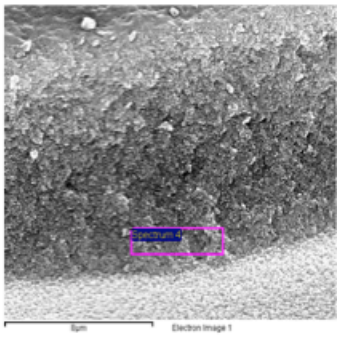

Figure A.2. EDS spectra (middle) and the tabulated results (left) for *nano*TiO_2|-**RuPdvb**-*poly*[**Fe(v-tpy)$_2$**]$^{2+}$ (300 cycles) at various depths that are indicated by the pink rectangle (far right).

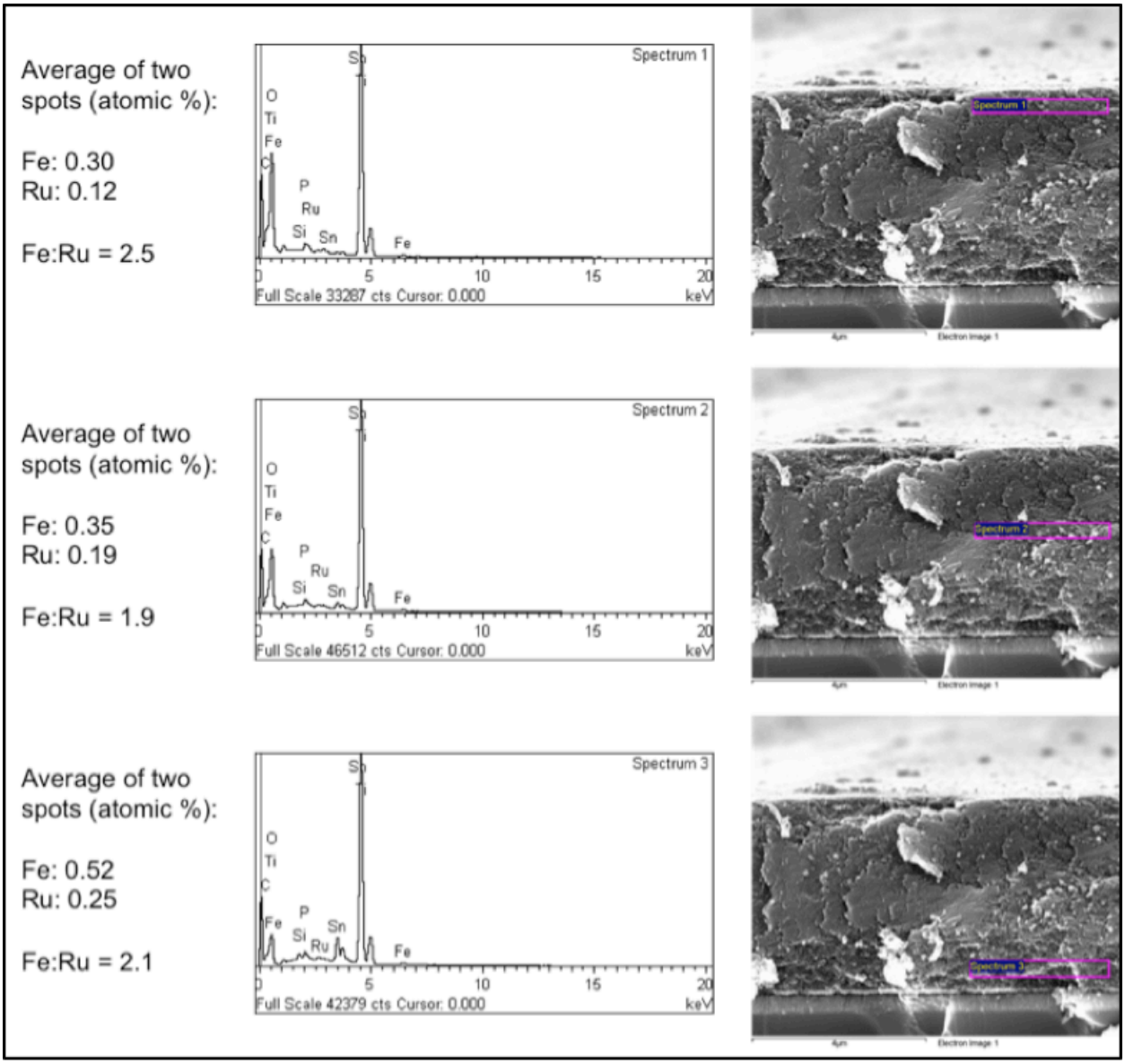

Figure A.3. EDS spectra (middle) and the tabulated results (left) for Fe and Ru obtained for *nano*TiO_2|-**RuPdvb**-*poly*[**Fe(v-tpy)$_2$**]$^{2+}$ (50 cycles) at various depths that are indicated by the pink rectangle (far right). This film was formed by soaking a *nano*TiO_2|-**RuPdvb** slide in [**Fe(v-tpy)$_2$**]$^{2+}$ (0.5 mM in 0.1 M [TBA]PF_6/CH_3CN) for over 24 hours prior to electropolymerization, then stirring during electropolymerization and resting the film for 60 seconds in between each electropolymerization cycle.

APPENDIX B: WATER OXIDATION BY AN ELECTROPOLYMERIZED CATALYST ON DERIVATIZED MESOPOROUS METAL OXIDE ELECTRODES

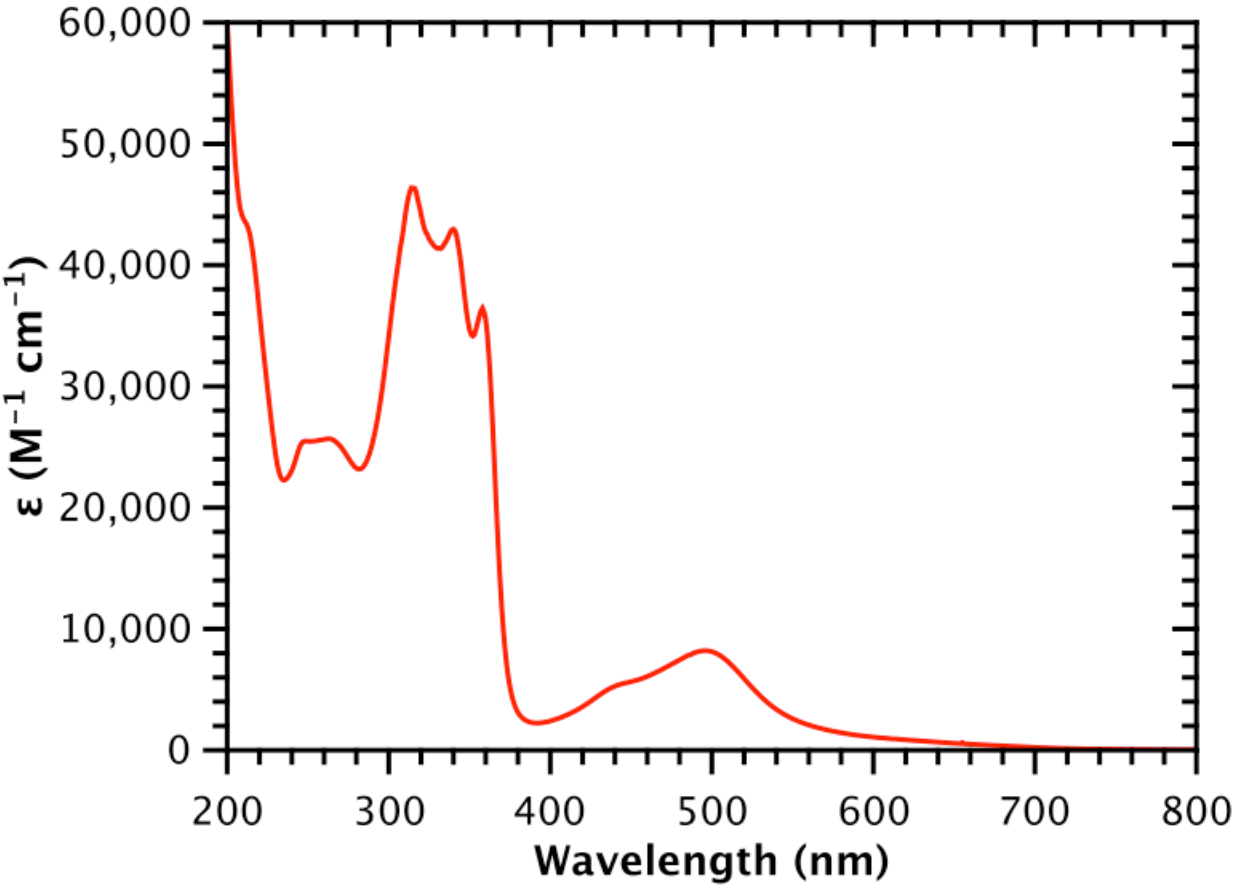

Figure B.1. Absorption spectrum of $\mathbf{RuOH_2^{2+}}$ at room temperature in H_2O.

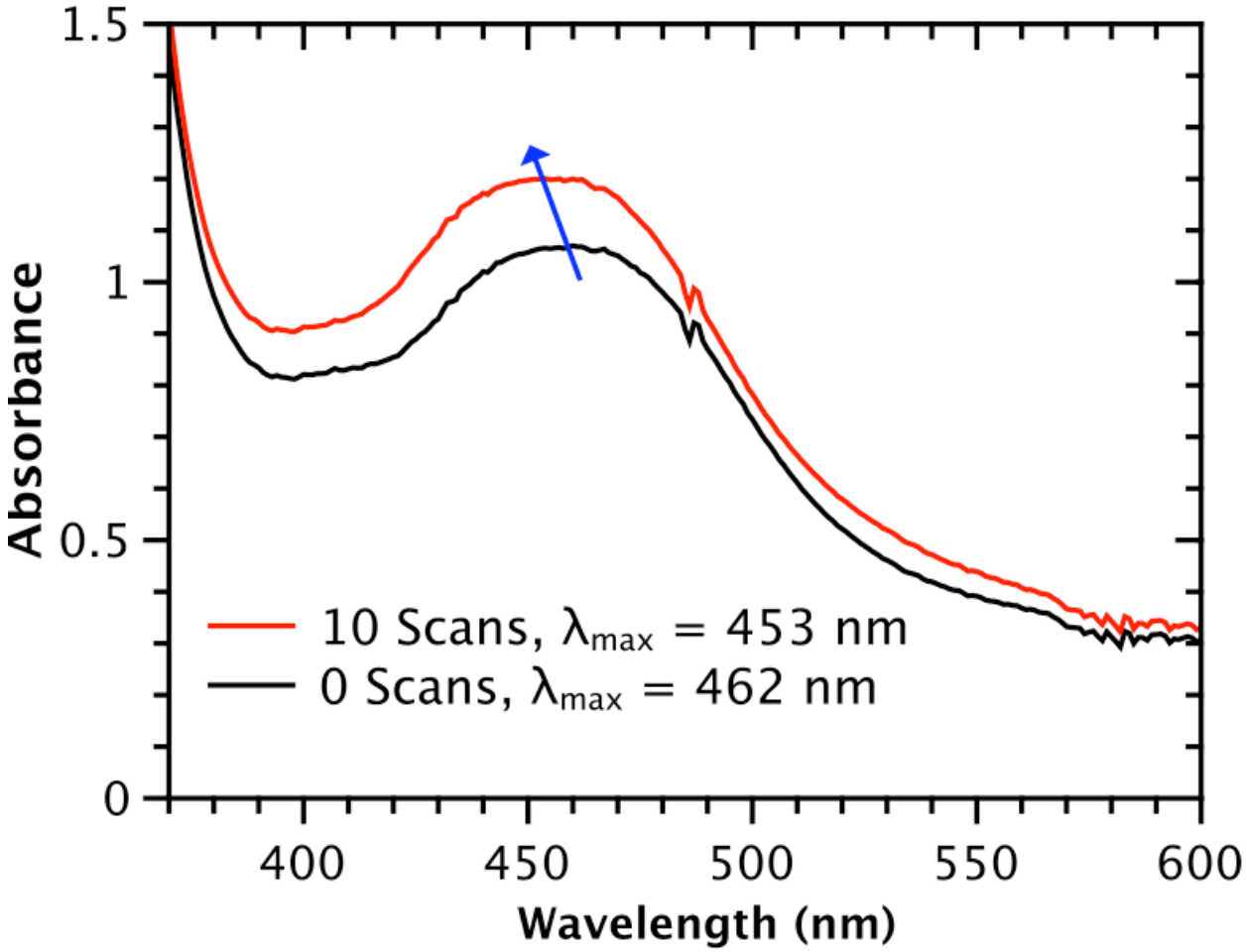

Figure B.2. UV-visible absorption spectra of *nano*TiO_2|-**RuPdvb**$^{2+}$ before (black) and after (red) 10 reductive cycles from 0 to –1.8 V (vs. $Ag/AgNO_3$) in a PC solution of 0.5 mM **RuOH$_2$**$^{2+}$, Pt counter, and $Ag/AgNO_3$ reference electrode.

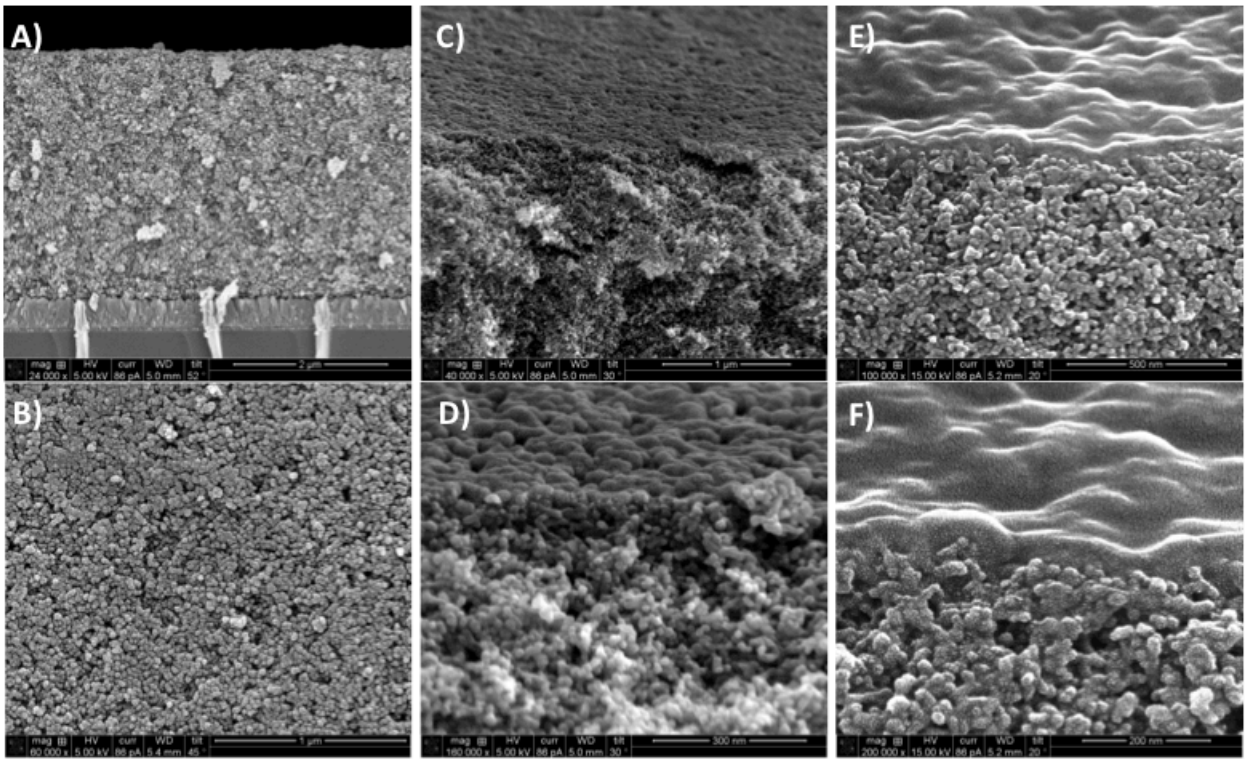

Figure B.3. Cross-sectional SEM images of the *nano*TiO_2|-**RuPdvb**$^{2+}$ films following 60 (A and B), 120 (C and D), and 450 (E and F) reductive cycles in a PC solution containing 0.5 mM **RuOH$_2$**$^{2+}$.

Element	Weight%	Atomic%
C K	12.07	19.68
O K	54.70	66.98
Ti K	32.03	13.10
Ru L	1.19	0.23
Totals	100.00	

Element	Weight%	Atomic%
C K	7.64	14.27
O K	46.42	65.14
Ca K	0.42	0.23
Ti K	41.90	19.64
Ru L	1.06	0.24
Sn L	2.56	0.48
Totals	100.00	

Element	Weight%	Atomic%
C K	5.44	11.44
O K	40.44	63.91
Si K	1.81	1.63
Ti K	37.62	19.85
Ru L	0.91	0.23
Sn L	13.78	2.93
Totals	100.00	

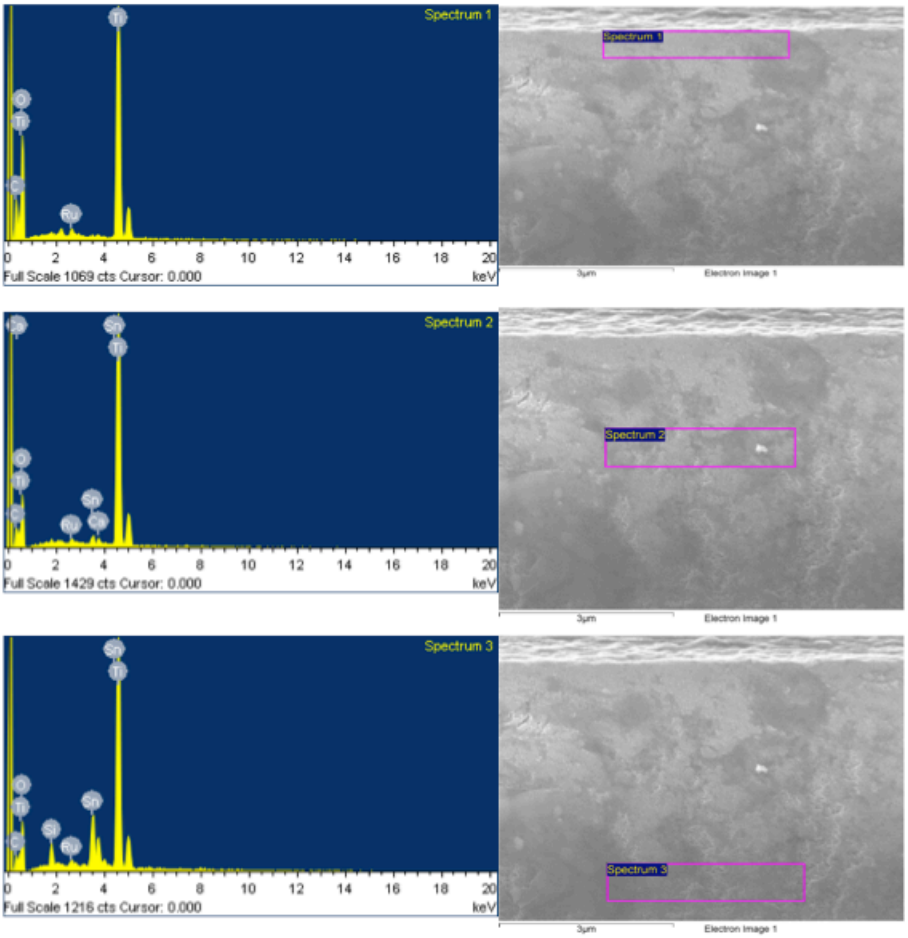

Figure B.4. EDS spectra (middle) and the tabulated results (left) obtained for *nano*TiO_2|-**RuPdvb**-*poly***RuOH$_2$** following 450 reductive cycles at various depths that are indicated by the pink rectangle (right).

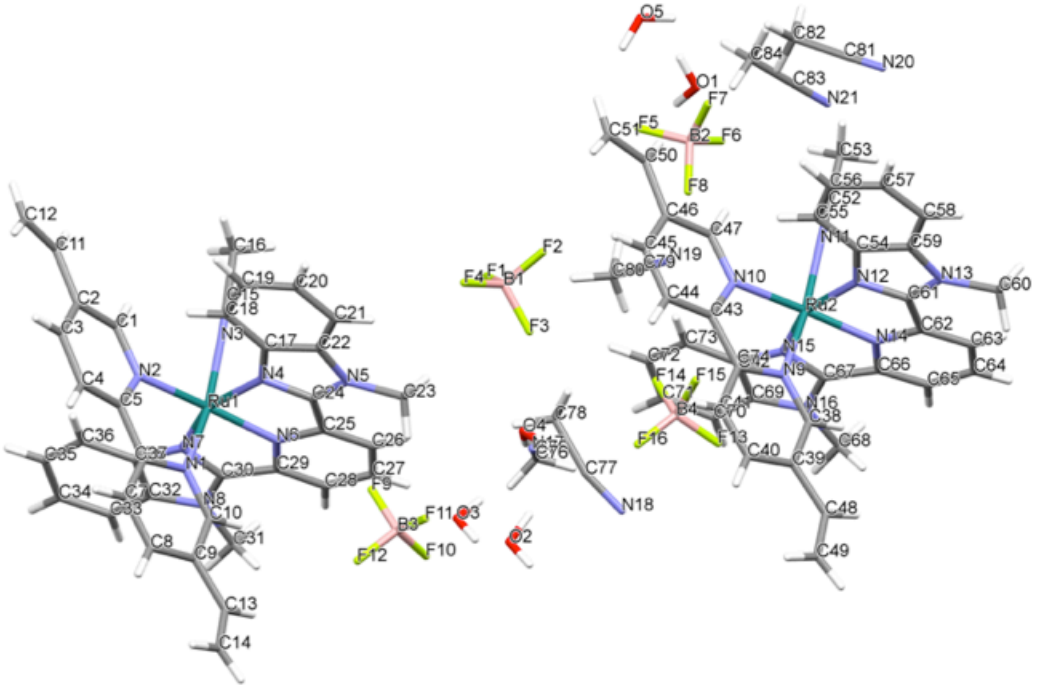

Figure B.5. Refined crystal structure

Table B.1. Crystal data and structure refinement for DLA-3-216 (**$RuOH_2^{2+}$**)

Identification code	DLA-3-216
Empirical formula	$C_{84}H_{89}B_4F_{16}N_{21}O_5Ru_2$
Formula weight	2022.14
Temperature/K	100.15
Crystal system	monoclinic
Space group	P21/c
a/Å	19.0462(4)
b/Å	25.0845(6)
c/Å	19.0686(4)
α/°	90
β/°	92.458(2)
γ/°	90
Volume/$Å^3$	9101.9(3)
Z	4
ρcalc/mg mm^{-3}	1.476
m/mm^{-1}	3.511
F(000)	4128.0
Crystal size/mm^3	0.461 × 0.13 × 0.042
2Θ range for data collection	4.644 to 140.488°

Index ranges	$-19 \leq h \leq 23, -29 \leq k \leq 30, -20 \leq l \leq 22$
Reflections collected	66621
Independent reflections	16885[R(int) = 0.0785]
Data/restraints/parameters	16885/18/1197
Goodness-of-fit on F^2	1.014
Final R indexes [I>=2σ (I)]	R1 = 0.0687, wR2 = 0.1660
Final R indexes [all data]	R1 = 0.1148, wR2 = 0.1920
Largest diff. peak/hole / e $Å^{-3}$	1.03/-0.69

Table B.2. Fractional Atomic Coordinates ($\times 10^4$) and Equivalent Isotropic Displacement Parameters ($Å^2 \times 10^3$) for DLA-3-216. U_{eq} is defined as 1/3 of the trace of the orthogonalised U_{IJ} tensor.

Atom	x	y	z	U(eq)
Ru1	9389.8(2)	2275.1(2)	4468.3(2)	30.23(13)
N1	10388(3)	2239(2)	4892(2)	32.1(11)
N2	9470(3)	1473(2)	4712(3)	33.5(11)
N3	8384(3)	2203(2)	4075(3)	32.2(11)
N4	9013(3)	2529(2)	5417(2)	31.6(11)
N5	8751(3)	3226(2)	6092(3)	37.0(12)
N6	9367(2)	3065(2)	4330(3)	30.1(10)
N7	9746(2)	2350(2)	3460(2)	32.0(11)
N8	10076(3)	2896(2)	2611(3)	38.3(12)
C1	8969(3)	1091(3)	4602(3)	38.1(14)
C2	8997(4)	592(3)	4921(4)	40.9(15)
C3	9574(4)	484(3)	5369(3)	44.2(16)
C4	10102(4)	857(3)	5462(3)	40.8(15)
C5	10049(3)	1346(3)	5121(3)	35.3(13)
C6	10586(3)	1764(3)	5181(3)	35.2(13)
C7	11244(3)	1690(3)	5502(3)	40.7(15)
C8	11716(3)	2111(3)	5540(3)	42.5(16)
C9	11526(3)	2609(3)	5255(3)	37.4(14)
C10	10857(3)	2647(3)	4924(3)	35.7(13)
C11	8422(4)	208(3)	4766(4)	51.1(18)
C12	8327(4)	-245(3)	5092(5)	59(2)
C13	11981(3)	3081(3)	5292(4)	47.7(17)
C14	12581(4)	3118(4)	5636(5)	67(2)
C15	7823(3)	2139(3)	3876(3)	36.6(14)
C16	7105(3)	2054(3)	3609(4)	50.2(18)
C17	8783(3)	2334(3)	6047(3)	37.0(14)
C18	8673(3)	1812(3)	6275(3)	39.2(14)
C19	8396(4)	1745(3)	6927(3)	43.7(16)
C20	8253(4)	2189(3)	7357(3)	42.9(16)
C21	8356(3)	2706(3)	7147(3)	37.4(14)
C22	8618(3)	2772(3)	6481(3)	34.4(13)
C23	8692(4)	3773(3)	6353(4)	49.5(17)

C24	8975(3)	3065(3)	5460(3)	34.9(13)
C25	9117(3)	3383(3)	4835(3)	35.1(14)
C26	9008(4)	3919(3)	4727(4)	43.7(16)
C27	9160(4)	4136(3)	4072(4)	47.5(17)
C28	9430(4)	3811(3)	3567(4)	45.3(16)
C29	9535(3)	3275(3)	3704(3)	36.0(14)
C30	9796(3)	2855(3)	3242(3)	36.0(14)
C31	10282(4)	3383(3)	2246(4)	48.5(18)
C32	10210(3)	2389(3)	2386(3)	36.6(14)
C33	10482(4)	2193(3)	1769(4)	45.2(16)
C34	10546(4)	1660(3)	1704(4)	50.3(18)
C35	10329(4)	1297(3)	2239(4)	46.9(17)
C36	10059(3)	1482(3)	2851(3)	40.1(15)
C37	9999(3)	2037(3)	2913(3)	36.3(14)
Ru2	5109.5(2)	7343.9(2)	5400.8(2)	29.41(12)
N9	6128(3)	7325(2)	5793(2)	32.3(11)
N10	5228(3)	6536(2)	5600(3)	31.6(11)
N11	4094(3)	7282.4(19)	5029(2)	29.8(10)
N12	4743(3)	7567(2)	6363(3)	33.7(11)
N13	4433(3)	8232(2)	7066(3)	40.0(13)
N14	5056(3)	8136(2)	5291(3)	33.1(11)
N15	5447(3)	7450(2)	4391(3)	31.3(11)
N16	5775(3)	8011(2)	3557(3)	36.5(12)
C38	6565(3)	7737(3)	5840(3)	37.5(14)
C39	7247(3)	7701(3)	6125(3)	39.6(14)
C40	7474(4)	7212(3)	6373(4)	49.0(18)
C41	7037(4)	6779(3)	6323(4)	47.1(17)
C42	6350(3)	6838(3)	6019(3)	38.2(14)
C43	5855(3)	6396(3)	5942(3)	37.3(14)
C44	5957(4)	5885(3)	6180(4)	45.8(17)
C45	5452(4)	5504(3)	6073(4)	50.6(18)
C46	4829(4)	5634(3)	5702(4)	45.3(16)
C47	4748(3)	6155(3)	5477(3)	36.4(14)
C48	7679(3)	8190(3)	6167(4)	45.8(17)
C49	8321(4)	8232(4)	6439(5)	73(3)
C50	4246(4)	5254(3)	5559(4)	52.3(18)
C51	4212(5)	4774(3)	5819(5)	63(2)
C52	3525(3)	7246(3)	4840(3)	35.5(14)
C53	2804(3)	7206(3)	4576(4)	46.1(17)
C54	4509(3)	7344(3)	6974(3)	36.4(14)
C55	4420(3)	6816(3)	7172(3)	37.5(14)
C56	4141(4)	6723(3)	7825(4)	45.2(16)
C57	3966(3)	7146(3)	8270(3)	48.5(18)
C58	4047(3)	7671(3)	8077(4)	44.2(16)
C59	4320(3)	7762(3)	7421(3)	38.9(15)
C60	4317(4)	8771(3)	7346(4)	47.8(17)

C61	4673(3)	8096(3)	6430(3)	36.8(14)
C62	4806(3)	8434(3)	5821(4)	39.0(15)
C63	4678(4)	8974(3)	5720(4)	47.6(17)
C64	4805(4)	9204(3)	5080(4)	49.4(17)
C65	5081(4)	8902(3)	4549(4)	44.8(16)
C66	5215(3)	8365(3)	4674(3)	35.6(14)
C67	5481(3)	7958(3)	4198(3)	34.1(13)
C68	5949(4)	8519(3)	3204(4)	49.1(18)
C69	5884(3)	7505(3)	3312(3)	35.4(13)
C70	6159(3)	7321(3)	2689(3)	38.6(14)
C71	6187(3)	6779(3)	2600(3)	41.7(15)
C72	5962(3)	6421(3)	3118(3)	38.0(14)
C73	5711(3)	6606(3)	3741(3)	34.7(13)
C74	5680(3)	7152(2)	3836(3)	31.1(13)
F1	5366(5)	4858(3)	1401(4)	145(3)
F2	5060(4)	5121(4)	2481(4)	148(3)
F3	5983(6)	5364(4)	2068(5)	190(5)
F4	5832(7)	4528(4)	2325(5)	219(6)
B1	5556(6)	4944(4)	2061(6)	66(3)
F5	3297(4)	5388(2)	3471(4)	116(3)
F6	2949(3)	6231(2)	3350(3)	70.0(14)
F7	2873(3)	5803(3)	4389(3)	110(3)
F8	3931(3)	6014(3)	3992(3)	97(2)
B2	3260(5)	5862(4)	3816(6)	59(2)
F9	8750(8)	4519(4)	1913(5)	226(7)
F10	9202(4)	5303(2)	1749(3)	111(3)
F11	9056(5)	4987(2)	2827(3)	119(3)
F12	9764(5)	4617(5)	2170(7)	232(7)
B3	9166(6)	4875(4)	2159(5)	58(2)
F13	7913(4)	6646(2)	7888(3)	94(2)
F14	7400(3)	5890(2)	7503(3)	77.9(15)
F15	7496(3)	6080(3)	8664(3)	103(2)
F16	8454(3)	5862(2)	8149(3)	79.6(15)
B4	7837(6)	6131(5)	8005(6)	67(3)
O1	2055(4)	6007(3)	1981(3)	91(2)
O2	9418(8)	5558(8)	4784(8)	294(10)
O3	9770(4)	4787(3)	6002(5)	247(8)
O4	8870(4)	4778(3)	7896(5)	192(6)
O5	3548(4)	4102(3)	9153(5)	109(3)
N17	7953(10)	5525(5)	4077(8)	176(7)
C75	7819(8)	5663(5)	3483(10)	114(6)
C76	7677(7)	5804(6)	2763(9)	145(7)
N18	8802(5)	6266(4)	6208(5)	99(3)
C77	8551(7)	5790(6)	6190(7)	107(4)
C78	8032(12)	5308(8)	6086(12)	246(11)
N19	6443(6)	5234(4)	9575(6)	104(3)

C79	6518(6)	5107(4)	9003(8)	91(4)
C80	6576(7)	4968(5)	8239(7)	126(5)
N20	2979(5)	6447(4)	9831(5)	89(3)
C81	2948(5)	6103(4)	9472(5)	66(2)
C82	2888(6)	5636(4)	8989(6)	88(3)
N21	2687(4)	6640(3)	6156(4)	72(2)
C83	2703(4)	6221(4)	6364(5)	59(2)
C84	2718(6)	5683(4)	6633(8)	122(5)

Table B.3. Anisotropic Displacement Parameters ($Å^2 \times 10^3$) for DLA-3-216. The Anisotropic displacement factor exponent takes the form: $-2\pi^2[h^2a^{*2}U_{11}+...+2hka \times b \times U_{12}]$

Atom	U_{11}	U_{22}	U_{33}	U_{23}	U_{13}	U_{12}
Ru1	26.2(2)	40.2(3)	24.1(2)	3.47(17)	-0.49(16)	-0.24(19)
N1	31(3)	43(3)	22(3)	0.0(19)	1.4(19)	3(2)
N2	34(3)	38(3)	29(3)	6(2)	6(2)	3(2)
N3	32(3)	37(3)	27(3)	2.8(19)	0(2)	4(2)
N4	32(3)	40(3)	23(3)	-2.4(19)	-2.7(19)	-1(2)
N5	35(3)	43(3)	33(3)	-1(2)	5(2)	2(2)
N6	21(2)	36(3)	32(3)	7(2)	-2.4(19)	-2(2)
N7	24(2)	51(3)	21(3)	1(2)	-0.6(18)	0(2)
N8	33(3)	51(3)	31(3)	7(2)	0(2)	-8(2)
C1	40(4)	44(4)	29(3)	2(2)	-5(3)	-3(3)
C2	48(4)	35(3)	41(4)	2(3)	7(3)	0(3)
C3	60(4)	41(4)	32(4)	4(3)	7(3)	7(3)
C4	43(4)	47(4)	33(4)	4(3)	3(3)	4(3)
C5	33(3)	46(4)	27(3)	1(2)	2(2)	7(3)
C6	33(3)	48(4)	25(3)	-2(2)	0(2)	4(3)
C7	40(4)	47(4)	35(4)	3(3)	3(3)	7(3)
C8	33(3)	65(5)	29(4)	2(3)	-8(3)	6(3)
C9	31(3)	59(4)	22(3)	1(3)	0(2)	-2(3)
C10	26(3)	50(4)	31(3)	1(3)	1(2)	-6(3)
C11	51(4)	48(4)	54(5)	0(3)	3(3)	-2(3)
C12	64(5)	45(4)	70(6)	-5(4)	11(4)	-9(4)
C13	33(3)	70(5)	40(4)	-3(3)	-2(3)	-3(3)
C14	48(5)	67(6)	83(7)	-8(4)	-22(4)	-4(4)
C15	31(3)	46(4)	33(3)	1(2)	3(3)	3(3)
C16	31(3)	70(5)	49(5)	0(3)	-3(3)	-2(3)
C17	28(3)	55(4)	28(3)	-2(3)	3(2)	-1(3)
C18	41(4)	46(4)	30(4)	4(3)	1(3)	-2(3)
C19	52(4)	52(4)	28(4)	0(3)	9(3)	-3(3)
C20	50(4)	51(4)	27(3)	2(3)	8(3)	6(3)
C21	38(3)	47(4)	27(3)	-3(3)	-1(2)	2(3)
C22	30(3)	45(4)	28(3)	1(2)	-2(2)	-2(3)
C23	63(5)	49(4)	37(4)	-4(3)	7(3)	2(4)
C24	28(3)	46(4)	31(3)	-1(2)	-1(2)	-2(3)
C25	30(3)	51(4)	24(3)	2(2)	0(2)	2(3)

C26	45(4)	41(4)	46(4)	4(3)	8(3)	-2(3)
C27	60(5)	40(4)	42(4)	9(3)	2(3)	-3(3)
C28	50(4)	47(4)	39(4)	11(3)	2(3)	-9(3)
C29	29(3)	50(4)	29(3)	5(3)	-5(2)	0(3)
C30	33(3)	46(4)	29(3)	9(2)	1(2)	-2(3)
C31	59(5)	49(4)	38(4)	5(3)	12(3)	-12(3)
C32	30(3)	50(4)	30(3)	1(3)	0(2)	-1(3)
C33	43(4)	61(5)	32(4)	5(3)	2(3)	-4(3)
C34	54(4)	66(5)	30(4)	-8(3)	4(3)	1(4)
C35	49(4)	48(4)	43(4)	-4(3)	0(3)	0(3)
C36	37(3)	50(4)	33(4)	3(3)	0(3)	-1(3)
C37	29(3)	49(4)	32(4)	3(3)	0(2)	3(3)
Ru2	29.1(2)	36.0(2)	23.0(2)	1.35(17)	-0.37(16)	-0.63(19)
N9	32(3)	39(3)	25(3)	1.2(19)	0.6(19)	2(2)
N10	34(3)	33(3)	27(3)	2.7(18)	3(2)	1(2)
N11	30(3)	32(3)	27(3)	1.1(18)	3.2(19)	0(2)
N12	29(3)	43(3)	28(3)	-3(2)	-5(2)	-4(2)
N13	40(3)	47(3)	33(3)	-11(2)	-3(2)	2(3)
N14	28(3)	41(3)	31(3)	-5(2)	-1(2)	-3(2)
N15	30(3)	38(3)	26(3)	3.8(19)	0.5(19)	-3(2)
N16	36(3)	41(3)	33(3)	6(2)	1(2)	-8(2)
C38	33(3)	49(4)	31(3)	-3(3)	1(2)	3(3)
C39	39(3)	54(4)	25(3)	-4(3)	1(2)	-1(3)
C40	34(4)	73(5)	40(4)	2(3)	-2(3)	3(3)
C41	44(4)	60(5)	37(4)	5(3)	0(3)	13(3)
C42	37(3)	51(4)	26(3)	4(2)	0(3)	2(3)
C43	41(4)	42(4)	29(3)	3(2)	5(3)	8(3)
C44	40(4)	55(4)	43(4)	13(3)	5(3)	9(3)
C45	57(5)	42(4)	54(5)	9(3)	9(4)	3(3)
C46	54(4)	42(4)	41(4)	4(3)	12(3)	0(3)
C47	40(3)	39(3)	31(3)	0(2)	9(3)	4(3)
C48	35(4)	67(5)	35(4)	-6(3)	-2(3)	-4(3)
C49	53(5)	82(7)	84(7)	-1(5)	-9(5)	-9(5)
C50	60(5)	45(4)	52(5)	-3(3)	8(4)	-3(4)
C51	78(6)	44(5)	66(6)	3(4)	-2(4)	-14(4)
C52	39(4)	44(4)	24(3)	2(2)	3(2)	4(3)
C53	28(3)	69(5)	41(4)	1(3)	-1(3)	-3(3)
C54	27(3)	57(4)	25(3)	-3(3)	-4(2)	4(3)
C55	34(3)	55(4)	24(3)	-5(2)	-3(2)	3(3)
C56	41(4)	61(5)	33(4)	0(3)	1(3)	-3(3)
C57	32(3)	90(6)	24(4)	-3(3)	4(3)	-4(3)
C58	29(3)	67(5)	36(4)	-9(3)	-5(3)	3(3)
C59	32(3)	52(4)	33(4)	-7(3)	-6(2)	-1(3)
C60	48(4)	47(4)	48(4)	-14(3)	-2(3)	3(3)
C61	31(3)	43(4)	36(4)	-5(3)	0(3)	-5(3)
C62	30(3)	43(4)	44(4)	-6(3)	2(3)	-5(3)

C63	48(4)	44(4)	51(5)	-4(3)	8(3)	-2(3)
C64	55(4)	37(4)	57(5)	1(3)	5(3)	-1(3)
C65	48(4)	40(4)	46(4)	1(3)	-5(3)	-8(3)
C66	33(3)	39(3)	35(4)	5(2)	0(3)	-7(3)
C67	27(3)	47(4)	28(3)	8(2)	-7(2)	-1(3)
C68	57(4)	47(4)	44(4)	16(3)	3(3)	-11(3)
C69	34(3)	44(4)	28(3)	5(2)	-1(2)	-2(3)
C70	33(3)	58(4)	25(3)	6(3)	4(2)	-2(3)
C71	40(4)	59(4)	27(3)	3(3)	4(3)	5(3)
C72	36(3)	46(4)	32(4)	-4(3)	1(3)	2(3)
C73	30(3)	47(4)	27(3)	5(2)	2(2)	4(3)
C74	27(3)	42(3)	24(3)	4(2)	-1(2)	0(2)
F1	234(10)	129(7)	68(5)	-27(4)	-28(5)	-55(6)
F2	131(7)	195(9)	122(7)	32(6)	55(5)	53(6)
F3	247(11)	203(10)	124(7)	-90(7)	61(7)	-134(9)
F4	365(16)	134(8)	156(9)	11(6)	1(9)	169(10)
B1	87(8)	52(6)	59(6)	-13(4)	-4(5)	23(5)
F5	121(5)	67(4)	157(7)	-26(4)	-42(5)	12(4)
F6	73(3)	69(3)	69(3)	16(2)	19(3)	7(3)
F7	93(4)	133(6)	106(5)	67(4)	52(4)	37(4)
F8	80(4)	165(6)	45(3)	20(3)	-12(3)	-58(4)
B2	55(5)	47(5)	75(7)	9(4)	21(5)	3(4)
F9	376(17)	190(10)	108(7)	20(6)	-34(9)	-186(11)
F10	248(8)	44(3)	41(3)	4(2)	4(4)	-19(4)
F11	242(9)	66(4)	51(4)	15(3)	35(4)	31(5)
F12	155(9)	297(14)	253(13)	153(11)	105(9)	130(9)
B3	73(7)	47(5)	56(6)	-10(4)	10(5)	6(5)
F13	155(6)	66(4)	59(4)	10(3)	-42(4)	-9(4)
F14	105(4)	74(4)	52(3)	-6(2)	-22(3)	-9(3)
F15	82(4)	155(7)	72(4)	-8(4)	-2(3)	-23(4)
F16	76(4)	77(4)	85(4)	10(3)	-13(3)	-1(3)
B4	53(5)	82(8)	66(7)	-17(5)	-7(5)	-4(5)
O1	120(6)	86(5)	67(5)	-4(4)	13(4)	24(4)
O2	188(14)	510(30)	186(16)	16(17)	6(12)	-103(16)
O3	265(16)	206(14)	262(17)	72(12)	-78(14)	-176(13)
O4	206(12)	88(7)	291(16)	-36(9)	120(11)	-12(8)
O5	62(4)	75(5)	189(9)	-7(5)	-12(5)	-6(4)
N17	300(20)	79(9)	157(14)	-7(8)	84(15)	4(11)
C75	127(11)	56(7)	166(16)	7(8)	73(12)	8(7)
C76	116(11)	134(14)	192(18)	58(12)	67(11)	56(10)
N18	96(6)	92(6)	106(6)	12(5)	-15(5)	9(5)
C77	113(6)	107(6)	102(6)	0(4)	7(4)	-14(4)
C78	249(14)	229(14)	262(14)	-10(9)	51(9)	-23(9)
N19	100(8)	102(8)	110(9)	22(6)	14(7)	31(6)
C79	69(7)	62(7)	144(12)	11(7)	33(8)	2(5)
C80	153(13)	81(9)	148(13)	-36(8)	57(10)	-40(9)

N20	99(7)	83(7)	84(7)	-16(5)	-12(5)	8(5)
C81	64(6)	67(6)	68(6)	1(4)	15(4)	8(5)
C82	119(9)	61(6)	88(8)	-7(5)	45(7)	-5(6)
N21	79(5)	76(6)	62(5)	0(4)	3(4)	7(4)
C83	56(5)	56(5)	67(6)	-2(4)	13(4)	-2(4)
C84	105(9)	57(7)	208(16)	37(8)	53(10)	21(6)

Table B.4. Bond Lengths for DLA-3-216.

Atom	Atom	Length/Å	Atom	Atom	Length/Å
Ru1	N1	2.035(5)	N13	C59	1.382(9)
Ru1	N2	2.069(5)	N13	C60	1.472(8)
Ru1	N3	2.036(5)	N13	C61	1.358(8)
Ru1	N4	2.075(5)	N14	C62	1.358(8)
Ru1	N6	1.998(5)	N14	C66	1.356(8)
Ru1	N7	2.076(5)	N15	C67	1.329(8)
N1	C6	1.359(8)	N15	C74	1.383(7)
N1	C10	1.358(8)	N16	C67	1.374(8)
N2	C1	1.362(8)	N16	C68	1.486(8)
N2	C5	1.360(8)	N16	C69	1.371(8)
N3	C15	1.129(8)	C38	C39	1.389(9)
N4	C17	1.384(7)	C39	C40	1.379(10)
N4	C24	1.350(8)	C39	C48	1.475(10)
N5	C22	1.388(8)	C40	C41	1.369(10)
N5	C23	1.466(8)	C41	C42	1.415(9)
N5	C24	1.357(8)	C42	C43	1.459(9)
N6	C25	1.353(8)	C43	C44	1.371(9)
N6	C29	1.357(8)	C44	C45	1.366(10)
N7	C30	1.338(8)	C45	C46	1.394(10)
N7	C37	1.406(8)	C46	C47	1.382(9)
N8	C30	1.341(8)	C46	C50	1.480(10)
N8	C31	1.468(8)	C48	C49	1.312(10)
N8	C32	1.370(9)	C50	C51	1.305(10)
C1	C2	1.392(9)	C52	C53	1.446(9)
C2	C3	1.390(10)	C54	C55	1.389(9)
C2	C11	1.477(10)	C54	C59	1.407(9)
C3	C4	1.379(10)	C55	C56	1.394(9)
C4	C5	1.391(9)	C56	C57	1.409(10)
C5	C6	1.465(9)	C57	C58	1.378(10)
C6	C7	1.385(9)	C58	C59	1.394(9)
C7	C8	1.386(10)	C61	C62	1.468(9)
C8	C9	1.403(9)	C62	C63	1.390(9)
C9	C10	1.401(8)	C63	C64	1.380(10)
C9	C13	1.467(10)	C64	C65	1.387(10)
C11	C12	1.312(10)	C65	C66	1.390(9)
C13	C14	1.297(10)	C66	C67	1.469(9)
C15	C16	1.456(9)	C69	C70	1.397(8)

C17	C18	1.399(9)	C69	C74	1.402(8)
C17	C22	1.419(9)	C70	C71	1.371(9)
C18	C19	1.381(8)	C71	C72	1.414(9)
C19	C20	1.417(9)	C72	C73	1.381(8)
C20	C21	1.372(9)	C73	C74	1.384(9)
C21	C22	1.394(8)	F1	B1	1.312(12)
C24	C25	1.468(8)	F2	B1	1.339(12)
C25	C26	1.375(9)	F3	B1	1.331(14)
C26	C27	1.405(9)	F4	B1	1.263(12)
C27	C28	1.377(10)	F5	B2	1.362(11)
C28	C29	1.382(9)	F6	B2	1.398(11)
C29	C30	1.472(9)	F7	B2	1.352(10)
C32	C33	1.395(9)	F8	B2	1.362(11)
C32	C37	1.409(9)	F9	B3	1.270(13)
C33	C34	1.349(10)	F10	B3	1.331(11)
C34	C35	1.439(10)	F11	B3	1.330(11)
C35	C36	1.375(9)	F12	B3	1.310(12)
C36	C37	1.402(9)	F13	B4	1.319(13)
Ru2	N9	2.049(5)	F14	B4	1.381(11)
Ru2	N10	2.073(5)	F15	B4	1.446(12)
Ru2	N11	2.038(5)	F16	B4	1.372(12)
Ru2	N12	2.069(5)	N17	C75	1.20(2)
Ru2	N14	2.000(5)	C75	C76	1.43(2)
Ru2	N15	2.074(5)	N18	C77	1.287(15)
N9	C38	1.329(8)	C77	C78	1.57(2)
N9	C42	1.356(8)	N19	C79	1.150(16)
N10	C43	1.381(8)	C79	C80	1.507(17)
N10	C47	1.336(8)	N20	C81	1.100(12)
N11	C52	1.130(8)	C81	C82	1.491(12)
N12	C54	1.383(8)	N21	C83	1.125(11)
N12	C61	1.340(8)	C83	C84	1.443(12)

Table B.5. Bond Angles for DLA-3-216

Atom	Atom	Atom	Angle/°	Atom	Atom	Atom	Angle/°
N1	Ru1	N2	79.0(2)	C38	N9	Ru2	126.0(4)
N1	Ru1	N3	172.1(2)	C38	N9	C42	119.5(6)
N1	Ru1	N4	91.16(19)	C42	N9	Ru2	114.5(4)
N1	Ru1	N7	91.99(18)	C43	N10	Ru2	114.8(4)
N2	Ru1	N4	97.3(2)	C47	N10	Ru2	126.7(4)
N2	Ru1	N7	105.8(2)	C47	N10	C43	118.3(5)
N3	Ru1	N2	93.2(2)	C52	N11	Ru2	178.2(5)
N3	Ru1	N4	89.61(19)	C54	N12	Ru2	140.4(5)
N3	Ru1	N7	90.36(19)	C61	N12	Ru2	113.0(4)
N4	Ru1	N7	156.9(2)	C61	N12	C54	106.5(5)
N6	Ru1	N1	96.4(2)	C59	N13	C60	125.2(6)
N6	Ru1	N2	173.9(2)	C61	N13	C59	106.8(6)

N6	Ru1	N3	91.43(19)	C61	N13	C60	128.0(6)
N6	Ru1	N4	78.8(2)	C62	N14	Ru2	119.1(4)
N6	Ru1	N7	78.1(2)	C66	N14	Ru2	119.9(4)
C6	N1	Ru1	116.0(4)	C66	N14	C62	120.8(6)
C10	N1	Ru1	125.9(4)	C67	N15	Ru2	113.6(4)
C10	N1	C6	118.1(5)	C67	N15	C74	106.6(5)
C1	N2	Ru1	127.2(4)	C74	N15	Ru2	139.7(4)
C5	N2	Ru1	114.0(4)	C67	N16	C68	126.4(6)
C5	N2	C1	118.0(5)	C69	N16	C67	106.7(5)
C15	N3	Ru1	176.4(5)	C69	N16	C68	126.9(6)
C17	N4	Ru1	141.5(4)	N9	C38	C39	123.3(6)
C24	N4	Ru1	112.3(4)	C38	C39	C48	118.5(6)
C24	N4	C17	106.3(5)	C40	C39	C38	117.7(7)
C22	N5	C23	124.6(6)	C40	C39	C48	123.7(6)
C24	N5	C22	107.6(5)	C41	C40	C39	120.0(7)
C24	N5	C23	127.7(6)	C40	C41	C42	119.7(7)
C25	N6	Ru1	119.8(4)	N9	C42	C41	119.6(6)
C25	N6	C29	120.0(6)	N9	C42	C43	117.4(6)
C29	N6	Ru1	119.8(4)	C41	C42	C43	123.0(6)
C30	N7	Ru1	113.8(4)	N10	C43	C42	113.4(6)
C30	N7	C37	105.6(5)	C44	C43	N10	120.1(6)
C37	N7	Ru1	140.6(5)	C44	C43	C42	126.5(6)
C30	N8	C31	127.9(6)	C45	C44	C43	121.0(7)
C30	N8	C32	107.3(5)	C44	C45	C46	119.4(7)
C32	N8	C31	124.5(6)	C45	C46	C50	123.9(7)
N2	C1	C2	123.5(6)	C47	C46	C45	117.4(7)
C1	C2	C11	119.0(7)	C47	C46	C50	118.7(7)
C3	C2	C1	117.3(6)	N10	C47	C46	123.7(7)
C3	C2	C11	123.7(6)	C49	C48	C39	126.6(8)
C4	C3	C2	119.9(6)	C51	C50	C46	125.1(8)
C3	C4	C5	120.1(6)	N11	C52	C53	178.1(7)
N2	C5	C4	121.0(6)	N12	C54	C55	131.4(6)
N2	C5	C6	115.0(6)	N12	C54	C59	108.0(6)
C4	C5	C6	124.0(6)	C55	C54	C59	120.5(6)
N1	C6	C5	114.5(5)	C54	C55	C56	117.3(6)
N1	C6	C7	121.8(6)	C55	C56	C57	121.4(7)
C7	C6	C5	123.7(6)	C58	C57	C56	121.9(6)
C6	C7	C8	119.6(6)	C57	C58	C59	116.4(6)
C7	C8	C9	120.1(6)	N13	C59	C54	106.8(6)
C8	C9	C13	123.9(6)	N13	C59	C58	130.6(7)
C10	C9	C8	116.7(6)	C58	C59	C54	122.5(7)
C10	C9	C13	119.4(6)	N12	C61	N13	111.9(6)
N1	C10	C9	123.6(6)	N12	C61	C62	118.4(6)
C12	C11	C2	126.0(8)	N13	C61	C62	129.6(6)
C14	C13	C9	126.0(8)	N14	C62	C61	110.4(6)
N3	C15	C16	179.1(7)	N14	C62	C63	119.9(6)

N4	C17	C18	131.1(6)	C63	C62	C61	129.6(6)
N4	C17	C22	108.6(6)	C64	C63	C62	119.5(7)
C18	C17	C22	120.2(6)	C63	C64	C65	120.3(7)
C19	C18	C17	117.5(6)	C64	C65	C66	118.4(7)
C18	C19	C20	121.1(7)	N14	C66	C65	120.9(6)
C21	C20	C19	122.7(6)	N14	C66	C67	109.8(5)
C20	C21	C22	116.1(6)	C65	C66	C67	129.2(6)
N5	C22	C17	105.8(5)	N15	C67	N16	111.4(6)
N5	C22	C21	131.8(6)	N15	C67	C66	118.3(5)
C21	C22	C17	122.4(6)	N16	C67	C66	130.4(6)
N4	C24	N5	111.7(6)	N16	C69	C70	131.5(6)
N4	C24	C25	118.7(6)	N16	C69	C74	107.0(5)
N5	C24	C25	129.4(6)	C70	C69	C74	121.6(6)
N6	C25	C24	109.9(6)	C71	C70	C69	116.8(6)
N6	C25	C26	121.7(6)	C70	C71	C72	121.9(6)
C26	C25	C24	128.4(6)	C73	C72	C71	120.9(6)
C25	C26	C27	118.4(6)	C72	C73	C74	117.6(6)
C28	C27	C26	119.4(7)	N15	C74	C69	108.2(6)
C27	C28	C29	120.0(6)	N15	C74	C73	130.7(5)
N6	C29	C28	120.4(6)	C73	C74	C69	121.1(6)
N6	C29	C30	110.2(6)	F1	B1	F2	117.1(11)
C28	C29	C30	129.3(6)	F1	B1	F3	106.3(10)
N7	C30	N8	112.7(6)	F3	B1	F2	100.3(9)
N7	C30	C29	117.5(5)	F4	B1	F1	109.8(10)
N8	C30	C29	129.7(6)	F4	B1	F2	109.1(11)
N8	C32	C33	132.3(6)	F4	B1	F3	114.0(13)
N8	C32	C37	107.2(6)	F5	B2	F6	107.5(9)
C33	C32	C37	120.5(7)	F7	B2	F5	109.6(8)
C34	C33	C32	117.7(6)	F7	B2	F6	110.8(7)
C33	C34	C35	122.1(7)	F7	B2	F8	111.7(9)
C36	C35	C34	121.1(7)	F8	B2	F5	107.3(8)
C35	C36	C37	116.2(6)	F8	B2	F6	109.8(7)
N7	C37	C32	107.2(6)	F9	B3	F10	113.5(10)
C36	C37	N7	130.5(6)	F9	B3	F11	112.3(10)
C36	C37	C32	122.3(6)	F9	B3	F12	100.7(11)
N9	Ru2	N10	79.4(2)	F11	B3	F10	114.0(8)
N9	Ru2	N12	91.89(19)	F12	B3	F10	109.9(10)
N9	Ru2	N15	90.87(19)	F12	B3	F11	105.2(10)
N10	Ru2	N15	105.06(19)	F13	B4	F14	112.3(10)
N11	Ru2	N9	174.2(2)	F13	B4	F15	106.8(9)
N11	Ru2	N10	94.82(19)	F13	B4	F16	114.6(9)
N11	Ru2	N12	88.75(19)	F14	B4	F15	106.5(8)
N11	Ru2	N15	90.79(18)	F16	B4	F14	114.1(9)
N12	Ru2	N10	98.1(2)	F16	B4	F15	101.3(9)
N12	Ru2	N15	156.8(2)	N17	C75	C76	177.1(16)
N14	Ru2	N9	96.0(2)	N18	C77	C78	162.0(16)

N14	Ru2	N10	174.5(2)	N19	C79	C80	176.0(14)
N14	Ru2	N11	89.7(2)	N20	C81	C82	178.6(12)
N14	Ru2	N12	78.8(2)	N21	C83	C84	179.5(11)
N14	Ru2	N15	78.0(2)				

Table B.6. Torsion Angles for DLA-3-216.

A	B	C	D	Angle/°	A	B	C	D	Angle/°
Ru1	N1	C6	C5	1.8(7)	Ru2	N9	C38	C39	178.6(4)
Ru1	N1	C6	C7	-178.4(5)	Ru2	N9	C42	C41	-177.8(5)
Ru1	N1	C10	C9	176.4(4)	Ru2	N9	C42	C43	1.5(7)
Ru1	N2	C1	C2	-164.6(5)	Ru2	N10	C43	C42	-7.2(6)
Ru1	N2	C5	C4	165.2(5)	Ru2	N10	C43	C44	171.8(5)
Ru1	N2	C5	C6	-13.5(6)	Ru2	N10	C47	C46	-171.6(5)
Ru1	N4	C17	C18	-5.1(12)	Ru2	N12	C54	C55	-1.1(11)
Ru1	N4	C17	C22	178.1(5)	Ru2	N12	C54	C59	-178.4(5)
Ru1	N4	C24	N5	-177.9(4)	Ru2	N12	C61	N13	-180.0(4)
Ru1	N4	C24	C25	6.9(7)	Ru2	N12	C61	C62	4.5(7)
Ru1	N6	C25	C24	6.7(7)	Ru2	N14	C62	C61	5.2(7)
Ru1	N6	C25	C26	-171.6(5)	Ru2	N14	C62	C63	-171.5(5)
Ru1	N6	C29	C28	171.1(5)	Ru2	N14	C66	C65	170.2(5)
Ru1	N6	C29	C30	-6.8(7)	Ru2	N14	C66	C67	-5.9(7)
Ru1	N7	C30	N8	175.3(4)	Ru2	N15	C67	N16	173.7(4)
Ru1	N7	C30	C29	-5.6(7)	Ru2	N15	C67	C66	-6.1(7)
Ru1	N7	C37	C32	-174.2(5)	Ru2	N15	C74	C69	-174.8(5)
Ru1	N7	C37	C36	5.4(11)	Ru2	N15	C74	C73	7.3(11)
N1	C6	C7	C8	0.8(10)	N9	C38	C39	C40	-0.4(9)
N2	C1	C2	C3	-0.5(10)	N9	C38	C39	C48	-178.3(6)
N2	C1	C2	C11	179.8(6)	N9	C42	C43	N10	3.8(8)
N2	C5	C6	N1	7.9(8)	N9	C42	C43	C44	-175.1(6)
N2	C5	C6	C7	-172.0(6)	N10	C43	C44	C45	1.3(10)
N4	C17	C18	C19	-176.0(6)	N12	C54	C55	C56	-177.3(6)
N4	C17	C22	N5	0.3(7)	N12	C54	C59	N13	1.0(7)
N4	C17	C22	C21	178.5(5)	N12	C54	C59	C58	178.6(6)
N4	C24	C25	N6	-8.9(8)	N12	C61	C62	N14	-6.3(8)
N4	C24	C25	C26	169.3(6)	N12	C61	C62	C63	170.0(7)
N5	C24	C25	N6	176.8(6)	N13	C61	C62	N14	179.1(6)
N5	C24	C25	C26	-5.0(11)	N13	C61	C62	C63	-4.5(12)
N6	C25	C26	C27	0.2(10)	N14	C62	C63	C64	0.1(11)
N6	C29	C30	N7	8.0(8)	N14	C66	C67	N15	7.8(8)
N6	C29	C30	N8	-173.2(6)	N14	C66	C67	N16	-172.0(6)
N8	C32	C33	C34	-179.6(7)	N16	C69	C70	C71	-179.0(6)
N8	C32	C37	N7	-0.8(7)	N16	C69	C74	N15	0.3(7)
N8	C32	C37	C36	179.6(6)	N16	C69	C74	C73	178.5(5)
C1	N2	C5	C4	-4.9(9)	C38	N9	C42	C41	2.0(9)
C1	N2	C5	C6	176.4(5)	C38	N9	C42	C43	-178.7(5)

C1	C2	C3	C4	-2.3(10)	C38	C39	C40	C41	1.2(10)
C1	C2	C11	C12	-170.4(8)	C38	C39	C48	C49	177.7(8)
C2	C3	C4	C5	1.5(10)	C39	C40	C41	C42	-0.4(10)
C3	C2	C11	C12	9.8(12)	C40	C39	C48	C49	-0.1(12)
C3	C4	C5	N2	2.3(10)	C40	C41	C42	N9	-1.2(10)
C3	C4	C5	C6	-179.2(6)	C40	C41	C42	C43	179.5(6)
C4	C5	C6	N1	-170.7(6)	C41	C42	C43	N10	-176.9(6)
C4	C5	C6	C7	9.4(10)	C41	C42	C43	C44	4.2(10)
C5	N2	C1	C2	4.1(9)	C42	N9	C38	C39	-1.2(9)
C5	C6	C7	C8	-179.3(6)	C42	C43	C44	C45	-179.8(6)
C6	N1	C10	C9	-1.8(9)	C43	N10	C47	C46	3.2(9)
C6	C7	C8	C9	0.0(10)	C43	C44	C45	C46	1.5(11)
C7	C8	C9	C10	-1.6(9)	C44	C45	C46	C47	-1.9(10)
C7	C8	C9	C13	177.9(6)	C44	C45	C46	C50	-179.7(7)
C8	C9	C10	N1	2.6(9)	C45	C46	C47	N10	-0.5(10)
C8	C9	C13	C14	-6.4(12)	C45	C46	C50	C51	7.4(12)
C10	N1	C6	C5	-179.8(5)	C47	N10	C43	C42	177.4(5)
C10	N1	C6	C7	0.0(9)	C47	N10	C43	C44	-3.6(9)
C10	C9	C13	C14	173.1(8)	C47	C46	C50	C51	-170.4(8)
C11	C2	C3	C4	177.5(6)	C48	C39	C40	C41	179.0(6)
C13	C9	C10	N1	-177.0(5)	C50	C46	C47	N10	177.5(6)
C17	N4	C24	N5	1.6(7)	C54	N12	C61	N13	2.6(7)
C17	N4	C24	C25	-173.7(5)	C54	N12	C61	C62	-172.9(5)
C17	C18	C19	C20	-2.1(10)	C54	C55	C56	C57	-0.9(10)
C18	C17	C22	N5	-176.9(6)	C55	C54	C59	N13	-176.7(5)
C18	C17	C22	C21	1.2(9)	C55	C54	C59	C58	0.9(9)
C18	C19	C20	C21	2.2(11)	C55	C56	C57	C58	1.5(11)
C19	C20	C21	C22	-0.5(10)	C56	C57	C58	C59	-0.9(10)
C20	C21	C22	N5	176.4(7)	C57	C58	C59	N13	176.7(6)
C20	C21	C22	C17	-1.2(9)	C57	C58	C59	C54	-0.3(9)
C22	N5	C24	N4	-1.4(7)	C59	N13	C61	N12	-2.0(7)
C22	N5	C24	C25	173.2(6)	C59	N13	C61	C62	172.9(6)
C22	C17	C18	C19	0.5(9)	C59	C54	C55	C56	-0.2(9)
C23	N5	C22	C17	-176.2(6)	C60	N13	C59	C54	-178.7(6)
C23	N5	C22	C21	5.9(11)	C60	N13	C59	C58	4.0(11)
C23	N5	C24	N4	175.3(6)	C60	N13	C61	N12	177.2(6)
C23	N5	C24	C25	-10.1(11)	C60	N13	C61	C62	-7.9(11)
C24	N4	C17	C18	175.7(7)	C61	N12	C54	C55	175.3(6)
C24	N4	C17	C22	-1.1(7)	C61	N12	C54	C59	-2.1(7)
C24	N5	C22	C17	0.6(7)	C61	N13	C59	C54	0.5(7)
C24	N5	C22	C21	-177.3(6)	C61	N13	C59	C58	-176.8(6)
C24	C25	C26	C27	-177.7(6)	C61	C62	C63	C64	-175.9(7)
C25	N6	C29	C28	-2.2(9)	C62	N14	C66	C65	-4.5(9)
C25	N6	C29	C30	179.9(5)	C62	N14	C66	C67	179.4(5)
C25	C26	C27	C28	-1.7(11)	C62	C63	C64	C65	-2.1(11)
C26	C27	C28	C29	1.3(11)	C63	C64	C65	C66	0.8(11)

C27	C28	C29	N6	0.7(10)	C64	C65	C66	N14	2.5(10)
C27	C28	C29	C30	178.1(7)	C64	C65	C66	C67	177.7(6)
C28	C29	C30	N7	-169.7(6)	C65	C66	C67	N15	-167.9(6)
C28	C29	C30	N8	9.2(12)	C65	C66	C67	N16	12.4(11)
C29	N6	C25	C24	-179.9(5)	C66	N14	C62	C61	179.9(5)
C29	N6	C25	C26	1.8(9)	C66	N14	C62	C63	3.2(9)
C30	N7	C37	C32	1.4(7)	C67	N15	C74	C69	2.4(7)
C30	N7	C37	C36	-179.0(7)	C67	N15	C74	C73	-175.5(6)
C30	N8	C32	C33	178.3(7)	C67	N16	C69	C70	179.1(7)
C30	N8	C32	C37	-0.2(7)	C67	N16	C69	C74	-2.8(7)
C31	N8	C30	N7	-172.6(6)	C68	N16	C67	N15	-174.7(6)
C31	N8	C30	C29	8.5(11)	C68	N16	C67	C66	5.1(10)
C31	N8	C32	C33	-7.6(11)	C68	N16	C69	C70	-1.6(11)
C31	N8	C32	C37	173.9(6)	C68	N16	C69	C74	176.5(6)
C32	N8	C30	N7	1.2(7)	C69	N16	C67	N15	4.6(7)
C32	N8	C30	C29	-177.7(6)	C69	N16	C67	C66	-175.6(6)
C32	C33	C34	C35	1.5(11)	C69	C70	C71	C72	-1.3(10)
C33	C32	C37	N7	-179.5(6)	C70	C69	C74	N15	178.6(6)
C33	C32	C37	C36	0.8(10)	C70	C69	C74	C73	-3.2(9)
C33	C34	C35	C36	-1.5(12)	C70	C71	C72	C73	-0.7(10)
C34	C35	C36	C37	1.0(10)	C71	C72	C73	C74	0.7(9)
C35	C36	C37	N7	179.7(6)	C72	C73	C74	N15	178.9(6)
C35	C36	C37	C32	-0.7(10)	C72	C73	C74	C69	1.2(9)
C37	N7	C30	N8	-1.7(7)	C74	N15	C67	N16	-4.4(7)
C37	N7	C30	C29	177.4(5)	C74	N15	C67	C66	175.8(5)
C37	C32	C33	C34	-1.2(10)	C74	C69	C70	C71	3.2(9)

Table B.7. Hydrogen Atom Coordinates ($Å \times 10^4$) and Isotropic Displacement Parameters ($Å^2 \times 10^3$) for DLA-3-216

Atom	x	y	z	U(eq)
H1	8579	1170	4292	46
H3	9605	153	5610	53
H4	10501	780	5760	49
H7	11372	1353	5695	49
H8	12169	2062	5760	51
H10	10725	2976	4710	43
H11	8092	298	4398	61
H12A	8644	-352	5464	71
H12B	7940	-467	4955	71
H13	11822	3387	5040	57
H14A	12762	2821	5896	80
H14B	12840	3441	5629	80
H16A	7109	1918	3127	75
H16B	6847	2392	3613	75
H16C	6873	1794	3906	75
H18	8784	1514	5993	47

H19	8300	1396	7090	52
H20	8078	2127	7809	51
H21	8255	3001	7438	45
H23A	8285	3947	6119	74
H23B	9120	3971	6254	74
H23C	8631	3766	6861	74
H26	8833	4137	5087	52
H27	9078	4503	3978	57
H28	9544	3955	3126	54
H31A	10604	3291	1877	73
H31B	10517	3627	2581	73
H31C	9862	3556	2035	73
H33	10617	2426	1407	54
H34	10741	1519	1293	60
H35	10372	924	2168	56
H36	9921	1247	3210	48
H38	6403	8073	5670	45
H40	7935	7175	6580	59
H41	7193	6441	6492	57
H44	6387	5795	6423	55
H45	5524	5153	6249	61
H47	4327	6248	5220	44
H48	7470	8506	5979	55
H49A	8553	7928	6635	88
H49B	8553	8567	6441	88
H50	3868	5368	5254	63
H51A	4579	4645	6126	75
H51B	3819	4554	5701	75
H53A	2779	6979	4158	69
H53B	2626	7563	4454	69
H53C	2516	7051	4938	69
H55	4544	6531	6875	45
H56	4067	6366	7972	54
H57	3788	7068	8716	58
H58	3923	7956	8376	53
H60A	3871	8912	7149	72
H60B	4703	9005	7217	72
H60C	4300	8753	7858	72
H63	4503	9184	6089	57
H64	4704	9571	5004	59
H65	5176	9058	4109	54
H68A	5518	8681	3002	74
H68B	6273	8448	2829	74
H68C	6171	8764	3547	74
H70	6319	7560	2344	46
H71	6362	6640	2178	50

H72	5985	6048	3035	46
H73	5565	6367	4093	42
H1A	2243	5949	1581	136
H1B	1832	5723	2110	136
H2A	9648	5789	5046	441
H2B	8975	5643	4756	441
H3A	9391	4954	5854	371
H4A	9001	5017	8206	288
H4B	8883	4915	7477	288
H3B	10004	4987	6304	288
H5A	3999	4053	9143	164
H5B	3461	4352	9453	164
H76A	8084	5714	2489	218
H76B	7585	6187	2728	218
H76C	7265	5606	2580	218
H78A	7711	5377	5681	369
H78B	7762	5264	6508	369
H78C	8301	4982	6004	369
H80A	6105	4944	8014	189
H80B	6816	4625	8199	189
H80C	6845	5246	8008	189
H82A	3250	5660	8641	132
H82B	2422	5636	8750	132
H82C	2952	5307	9260	132
H84A	2572	5435	6257	183
H84B	2395	5654	7018	183
H84C	3196	5595	6806	183

B.1. Experimental Information for Crystal Structure

Single crystals of $C_{84}H_{89}B_4F_{16}N_{21}O_5Ru_2$ [DLA-3-216] were grown by solution diffusion of diethyl ether into a $\mathbf{RuOH_2^{2+}}$ solution in CH_3CN resulting in CH_3CN coordination. A suitable crystal was selected and placed on a 'Bruker APEX-II CCD' diffractometer. The crystal was kept at 100.15 K during data collection. Using Olex2 [1], the structure was solved with the olex2.solve [2] structure solution program using Charge Flipping and refined with the ShelXL [3] refinement package using Least Squares minimisation.

[1] O. V. Dolomanov, L. J. Bourhis, R. J. Gildea, J. A. K. Howard and H. Puschmann, OLEX2: a complete structure solution, refinement and analysis program. J. Appl. Cryst. (2009). 42, 339-341.

[2] olex2.solve (L.J. Bourhis, O.V. Dolomanov, R.J. Gildea, J.A.K. Howard, H. Puschmann, in preparation, 2011)

[3] SHELXL, G.M. Sheldrick, Acta Cryst. (2008). A64, 112-122

Crystal structure determination of [DLA-3-216]

Crystal Data for $C_{84}H_{89}B_4F_{16}N_{21}O_5Ru_2$ (M =2022.14): monoclinic, space group $P2_1/c$ (no. 14), a = 19.0462(4) Å, b = 25.0845(6) Å, c = 19.0686(4) Å, β = 92.458(2)°, V = 9101.9(3) $Å^3$, Z = 4, T = 100.15 K, μ(CuKα) = 3.511 mm^{-1}, ρ_{calc} = 1.476 g/mm^3, 66621 reflections measured ($4.644 \leq 2\Theta \leq 140.488$), 16885 unique ($R_{int}$ = 0.0785) which were used in all calculations. The final R_1 was 0.0687 ($I > 2\sigma(I)$) and wR_2 was 0.1920 (all data).

This report has been created with Olex2, compiled on Apr 9 2013 14:10:59.

APPENDIX C: SYNTHESIS, CHARACTERIZATION, AND WATER OXIDATION BY A MOLECULAR CHROMOPHORE-CATALYST ASSEMBLY PREPARED BY ATOMIC LAYER DEPOSITION. THE "MUMMY" STRATEGY

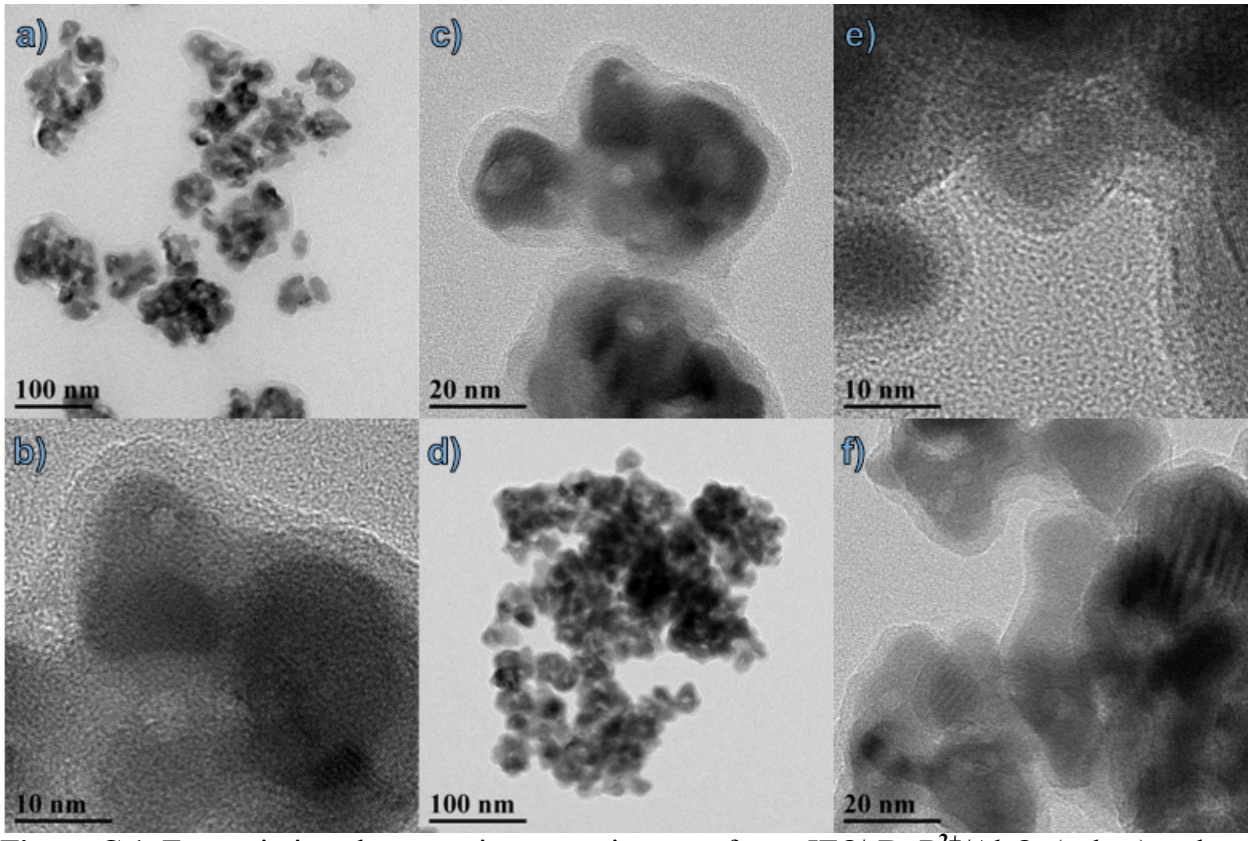

Figure C.1. Transmission electron microscopy images of *nano*ITO|-**RuP**$^{2+}$/Al_2O_3 (a, b, c) and *nano*ITO/Al_2O_3 (d, e, f) core/shell structure (core = *nano*ITO|-**RuP**$^{2+}$ or *nano*ITO; shell = Al_2O_3). The Al_2O_3 shell was formed by 20 cycles of $Al(CH_3)_3/H_2O$.

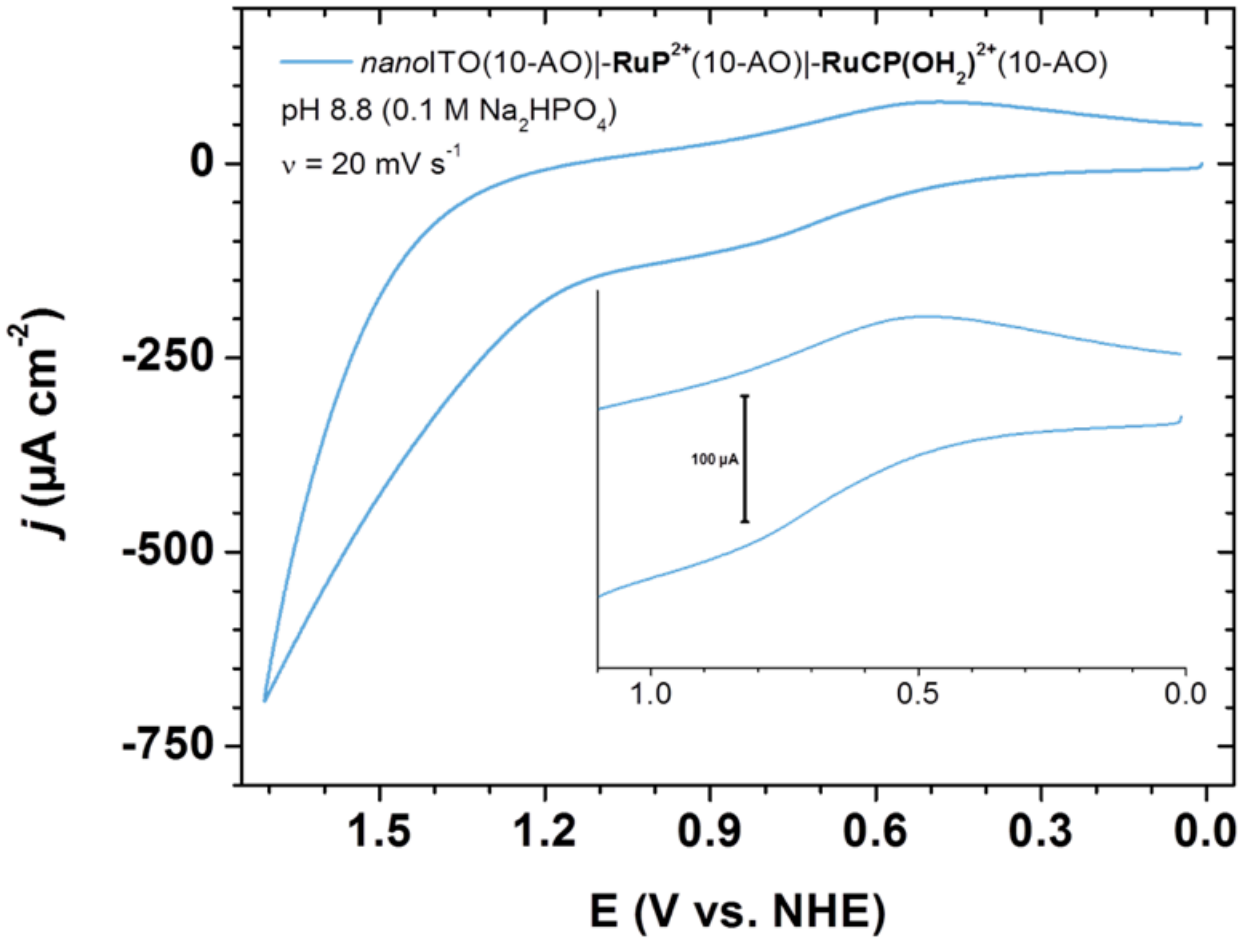

Figure C.2. CV scan at pH 8.8 of *nano*ITO(10-AO)|-**RuP**$^{2+}$(10-AO)|-**RuCP(OH$_2$)**$^{2+}$(10-AO) (Conditions: ν = 20 mV s^{-1}; Ag/AgCl, 3 M NaCl reference electrode; Pt-mesh counter electrode).

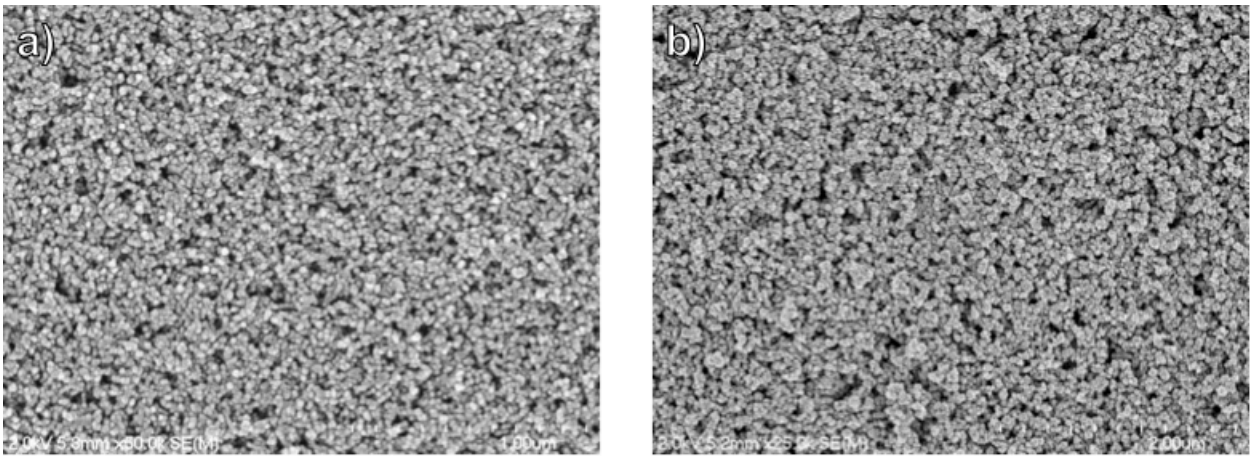

Figure C.3. SEM images of (a) *nano*TiO_2 and (b) *nano*ITO.